**The Dissertation Committee for Ali Mohamed Helwa Certifies that this is the approved version of the following dissertation:**

# PREDICTING THE BEHAVIOR OF A DRILLED SHAFT WALL RETAINING HIGHLY EXPANSIVE SOIL

**Committee:**

Robert B. Gilbert, Supervisor

Kenneth H. Stokoe, II

John L. Tassoulas

Shin-Tower Wang

Jorge G. Zornberg

# PREDICTING THE BEHAVIOR OF A DRILLED SHAFT WALL RETAINING HIGHLY EXPANSIVE SOIL

**by**

**Ali Mohamed Helwa, B.CIVIL.ENGR; M.PUBLIC.WORKS.ENGR.**

**Dissertation**

Presented to the Faculty of the Graduate School of

The University of Texas at Austin

in Partial Fulfillment

of the Requirements

for the Degree of

**Doctor of Philosophy**

**The University of Texas at Austin**

**May 2016**

# Dedication

To

Hoda Shaaban

# Acknowledgements

"These kinds of personal explanations of success don't work… We do owe something to parentage and patronage… But in fact they are invariably the beneficiaries of hidden advantages and extraordinary opportunities and cultural legacies that allow them to learn and work hard and make sense of the world in ways others cannot…We pretend that success is exclusively a matter of individual merit. But there's nothing in any of the histories we've looked at so far to suggest things are that simple."

*Malcolm Gladwell, Outliers*

The author is grateful to be blessed with the act of God that made him a benefiter of great advantages and opportunities; on top of these opportunities is the opportunity to work with Prof. Robert Gilbert, who doesn't only excel as an academician but also as a mentor with a great heart full of life lessons. The author is grateful to God for blessing him with parents, namely, Hoda Shabaan and M. Fawzi Helwa, and his sister, Amira Helwa, who provided continuous encouragement through better and worse times.

The author would also like to thank Drs. Jorge G. Zornberg, Kenneth H. Stokoe, Shin-Tower Wang, and John L. Tassoulas for their contributions to the development and review of this research. The author thanks his colleagues Amr Morsy, Hande Gerkus, M. Hisham Moawad, Hazem Hossam, and Shehab Wissa for showing a good friendship material through bitter times.

**Predicting the Behavior of a Drilled Shaft Wall Retaining Highly Expansive Soil**

Ali Mohamed Helwa, Ph.D.

The University of Texas at Austin, 2016

Supervisor: Robert B. Gilbert

A full scale drilled shaft retaining wall was constructed in the highly expansive soil of Manor, Texas, to advance our understanding of the behavior of walls in highly expansive soils. The wall was monitored for a total period of four years; during the monitored period the state of Texas experienced severe drought conditions and the retained soil was inundated via a manmade pond. The monitored wall did not experience a point of fixity, instead, the wall experienced global movement towards the excavated side. Analytical predictions of the wall during short-term and long-term conditions miss-predicted the deflection and bending moment profiles, and could not estimate the wall behavior during transition state towards the long-term conditions.

The Reese wall was simulated in a numerical model using the Finite Element method. A framework is developed in this study that can describe the swelling behavior of soil. The framework relies on two soil properties, first, a relationship between effective degree of saturation and effective stress, second, a relationship between stiffness, effective stress and voids ratio. Comparison between measured and predicted deflection and bending moment profiles showed that the proposed framework could result in reasonable deflection and bending moment predictions during dry and inundated saturation conditions.

The predicted short-term deflection and bending moment profiles best matched the measured profiles when a constitutive model that accounts for small strain stiffness non-linearity was adopted. The numerical model was used to segregate the superimposed wall deflection profile obtained during long-term conditions. The study concluded that the short-term conditions accounts for 20%, dissipation of the excess pore-pressures accounts for 30%, the additional hydrostatic pressures accounts for 10%, saturation change related factors accounts for 15%, and change in soil properties on the excavation side accounts for 25% of the total deflection.

Parametric analyses concluded that the short-term and long-term behaviors of the Reese wall are not very sensitive to building stiffer and deeper walls. The long-term behavior of the Reese wall is sensitive to construction season, the hardening properties of soil, and the relationship between effective stresses and effective degree of saturation.

# Table of Contents

## List of Figures

# List of Tables

# CHAPTER 1: INTRODUCTION

Expansive soils are characterized as partially saturated high-plasticity soils subjected to increase in the soil degree of saturation. The severity of soil expansiveness is function of characteristic soil parameters such as soil plasticity and state parameters such as the degree of saturation and confining stresses. The behavior of the expansive soils in proximity to structural elements ought to be addressed as a soil structure interaction problem; because, the presence of structural elements restrains the expansive behavior of the soils.

Currently, walls retaining expansive soils are designed to withstand an estimated design load; there is high level of uncertainty in these estimated design loads. This high level of uncertainty could outcome in walls that are either unsafe or over-conservative. As example of unsafe wall, two cases of wall failures have been detected since 2009 in the state of Texas. One failure took place during construction Smith (2009) and the other took place during long-term conditions Adil Haque and Bryant (2011). In regards to over-conservative, the FHWA/TX-130/0-6603-2 TXDoT report indicated that the current design procedures of walls retaining expansive soils might be resulting in over conservative walls.

A full scale wall was built in Manor, Texas, in a soil profile that is characterized as expansive soil. The wall was monitored for four consecutive years during which the site location experienced severe drought conditions and the retained soil profile was subjected to manmade inundation cycles.

This study adopts the measured wall behavior as a benchmark in developing a framework for analyzing the behavior of walls retaining expansive soils, subjected to variation in the degree of saturation. The framework describes the pore-water pressure of

partially saturated soils as a function of the soil saturation. The study relies on common laboratory tests to estimate the negative pore-water pressure of partially saturated soil, which is intended to make this approach of practical value.

## 1.1 OBJECTIVES

The objectives of this study are:

1. Advance understanding about modeling the behavior of high-plasticity partially saturated clays in interaction with retaining walls.
2. Develop a framework for predicting the deflections and bending moments in retaining walls constructed in expansive clays.
3. Assess sources of uncertainties in describing the behavior of expansive clays and quantify the sensitivity of the predicted behavior of retaining walls to these uncertainties.
4. Provide guidance to designers for developing efficient and reliable solutions for walls retaining expansive clays.

## 1.2 METHODOLOGY

The objectives of this research will be accomplished according to the following methodology:

1. Develop a numerical model for a monitored full-scale test wall, using Finite Element Method (FEM).
2. Evaluate the accuracy of the predictions of wall performance from the numerical model with the field measurements during short-term and long-term conditions.

3. Formulate a framework that describes the behavior of expansive clays. The framework adopts an effective stress definition that accounts for the inter-particle physiochemical stresses of high-plasticity clays.
4. Perform a sensitivity analysis with the numerical model to estimate the wall response to conditions other than the field conditions and gain understanding about the behavior of walls retaining expansive soils in different conditions.

## 1.3 ORGANIZATION

Chapter 2 presents background information about the size of the problem, sources of uncertainty in design loads of retaining walls, recent failures of retaining walls in Texas. Chapter 3 describes a project of a full-scale wall that was built to provide some insight about the behavior of walls in expansive soils. Measurements obtained from the full-scale wall is used as a benchmark to evaluate the accuracy of behavior prediction methods. Chapter 4 presents analytical predictions of the wall behavior during short-term and long-term conditions. Chapter 5 presents the characteristics of a more complicated prediction of wall behavior; which, adopts the Finite Element method in simulating a numerical model of the full-scale wall. The study is then divided into two sections.

Section I (Chapters 6 and 7) addresses the behavior of retaining walls during short-term conditions. Chapter 6 presents the characteristics of the Finite Element model during the short-term conditions and evaluates the accuracy of the numerical model by comparing the predicted response to the measured response. Chapter 7 presents the sensitivity analyses of the behavior during short-term conditions.

Section II (Chapters 8, 9, 10, 11) addresses the behavior of retaining walls during long-term conditions, including wetting and drying of the retained soil, i.e., permanent walls. Chapter 8 presents the development of a framework that describes the changes in

the soil properties of partially saturated soil during variation in the degree of saturation. The framework adopts Lu and Likos (2007)'s definition of effective stresses and attributed the swelling properties of expansive soils to the changes in the effective stress and the soil stiffness. Later in the chapter the framework is implemented in simple one dimensional swell tests and the applicability of the framework is evaluated. Chapter 9 implements the developed framework in the numerical model of a wall constructed in expansive soil; the predicted wall behavior is compared to the measured wall behavior and the applicability of the framework is evaluated. Chapter 10 presents the sensitivity of the long-term behavior of walls to soil properties and wall design parameters. Chapter 11 presents a summary of the research study and highlights the conclusions and recommendations for future work.

# CHAPTER 2: BACKGROUND

The objectives of this chapter are, first, to illustrate the difficulties generally associated with predicting the behavior of the expansive clay soil; then focus on the difficulties associated with predicting the behavior of expansive clay soils interacting with retaining walls.

## 2.1 EXPANSIVE SOILS

Structural elements constructed in partially saturated high-plasticity clays are subjected to changes in the pore-water pressure, during the transition to long-term conditions, in addition to the dissipation of excess pore-water pressure. These changes are due to variation in the soil saturation visa-a-vis changes in the boundary condition of the ground water. Walls constructed in partially saturated high-plasticity clays encounter stresses higher than the long-term drained stresses, i.e., stresses after dissipation of excess pore-water pressure; these additional stresses are often attributed to the loss of pore-water suction that is accompanied with changes in the degree of saturation. Practitioners adopt a range of assumptions to account for the additional stresses due to variation in the degree of saturation; however, there is no consensus on the right way to account for these additional stresses, and the current assumptions could be under or over conservative.

Swelling soils are characterized as partially saturated, overconsolidated soils with high plasticity; as the weight percentage of clay size <0.002mm and the soil plasticity increase, the swell potential increases (Figure 2.1, Figure 2.2). As the high plasticity clay soil becomes more saturated the soil swells and structural elements interacting with this soil are affected. The soil swell potential is a function of the variation in the degree of saturation experienced by the soil; soils subjected to severe variations in the degree of

saturation are most susceptible to large swelling strains and subsequent impacts to structures.

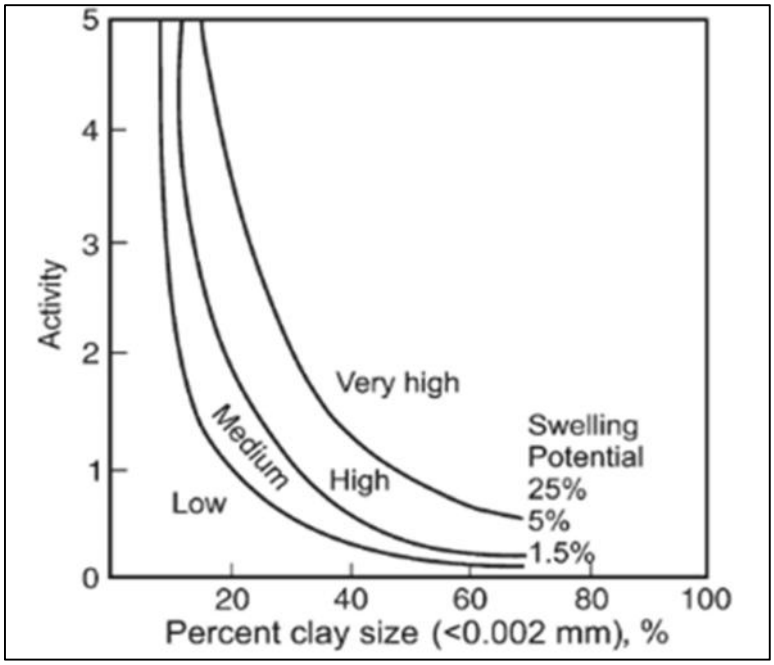


Figure 2.1: Soil swell potential (Seed et al. 1962)

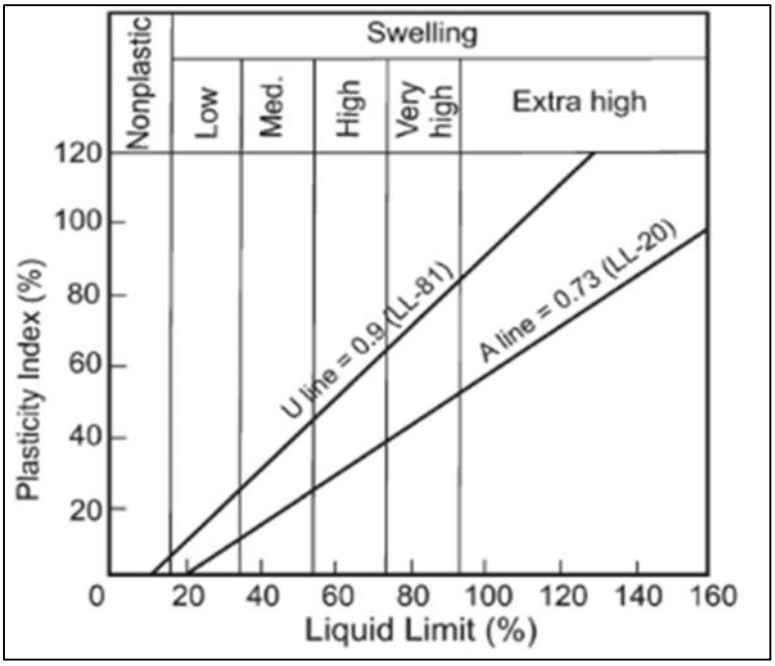


Figure 2.2: Soil swell potential (Dakshanamurthy and Raman 1973)

Soils with high swell potential spread over the Mid-North to mid-South states and the states along the Gulf of Mexico (Figure 2.3). The areas classified as areas with high swell potential are characterized as areas where highly swelling soils composes 50% or more of the underlining soil.

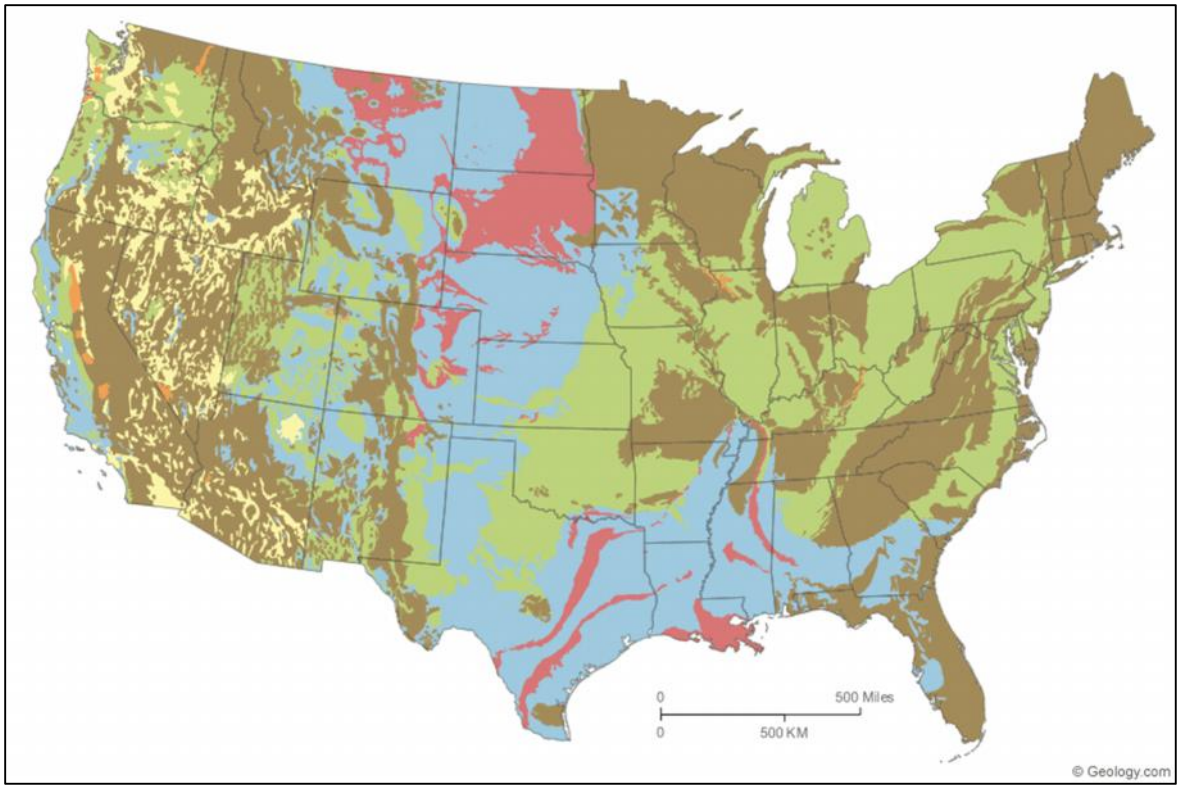


Figure 2.3: Location of swelling clays in the United States (www.Geology.com)

| | |
|---|---|
| | Over 50 percent of these areas are underlain by soils with abundant clays of high swelling potential. |
| | Less than 50 percent of these areas are underlain by soils with clays of high swelling potential. |
| | Over 50 percent of these areas are underlain by soils with abundant clays of slight to moderate swelling potential. |
| | Less than 50 percent of these areas are underlain by soils with abundant clays of slight to moderate swelling potential. |
| | These areas are underlain by soils with little to no clays with swelling potential. |
| | Data insufficient to indicate the clay content or the swelling potential of soils |

The state of Texas has two corridors of high swell potential soil extending from the southern state border to the North-Eastern state border (Figure 2.4). The interstate highways overlap with the areas classified as susceptible to high swell potential (Figure 2.4). The overlap between the interstate highways and the high swelling soil means that retaining walls along the sides of the interstate crossings are founded in high swelling soils.

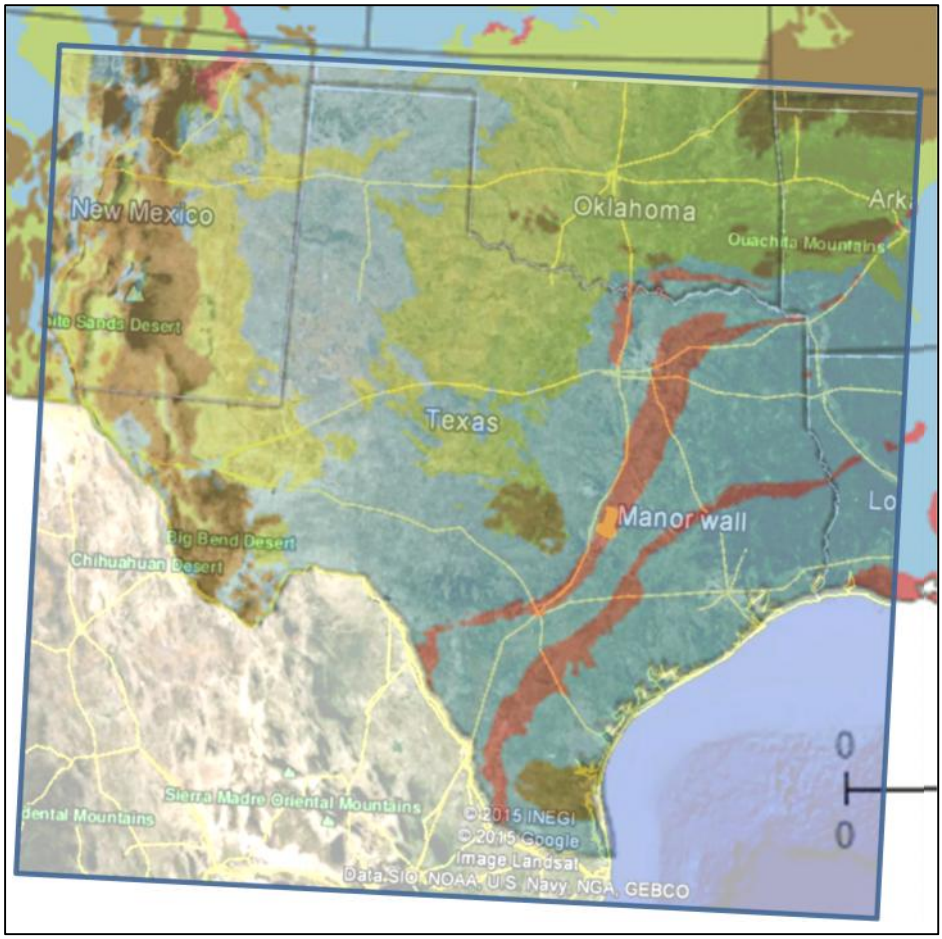


Figure 2.4: Highways map relative to regions with high swell potential

Describing the behavior of walls constructed in high-plasticity partially saturated clay is challenging because of the uncertainties in describing soil behaviors, including soil

anisotropy, strength, and stiffness. Unreliable presentation of the soil behavior could produce walls that are either under or over designed. Sources of uncertainties of high-plasticity clays are discussed in this section.

### 2.1.1 Anisotropy

High-plasticity clay particles are flaky particles with high specific surface area; specific surface area is defined as the ratio between the total surface areas of clay particles to one unit of mass. The higher the specific surface area of the soil the higher the anisotropy. Soils with high specific surface area are identified by their high Atterberg limits. Figure 2.5 presents an electronic microscopic images of high plasticity clay, the figure shows that the flaky nature of the high plasticity clay.

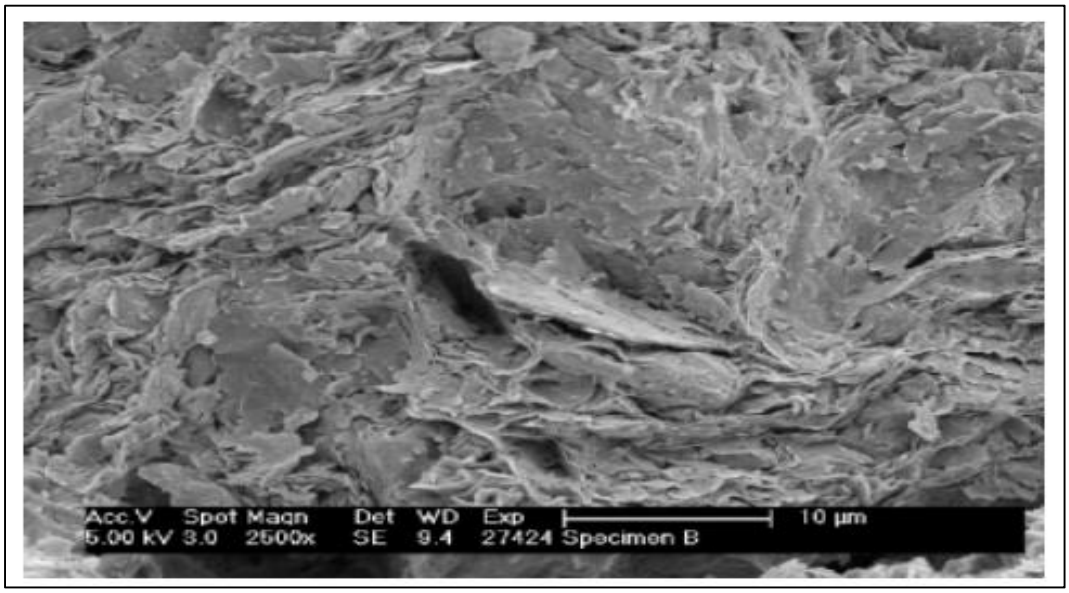


Figure 2.5: Electronic microscopic images of high plasticity clay (Gasparre et al. 2007)

Kayyal (1991) studied the sensitivity of particles orientation of high plasticity clays to cyclic wetting and drying and consolidation pressure. Figure 2.6 presents the particles orientation index with respect to the consolidation pressure after wetting and drying cycles. The orientation index is defined as the ratio between the intensity of basal reflections to the intensity of a non-basal reflection measured in an X-ray diffractometer; where a higher orientation index (O.I) corresponds to a more oriented structure. The study concluded that the particles orientation increases as the consolidation pressure increases for both wetting and drying conditions. Therefore, the anisotropy of the soil is sensitive to the loads and depth of the soil. The difference between the wet and dry conditions is insignificant at small consolidation pressure and is more observed at higher consolidation pressures.

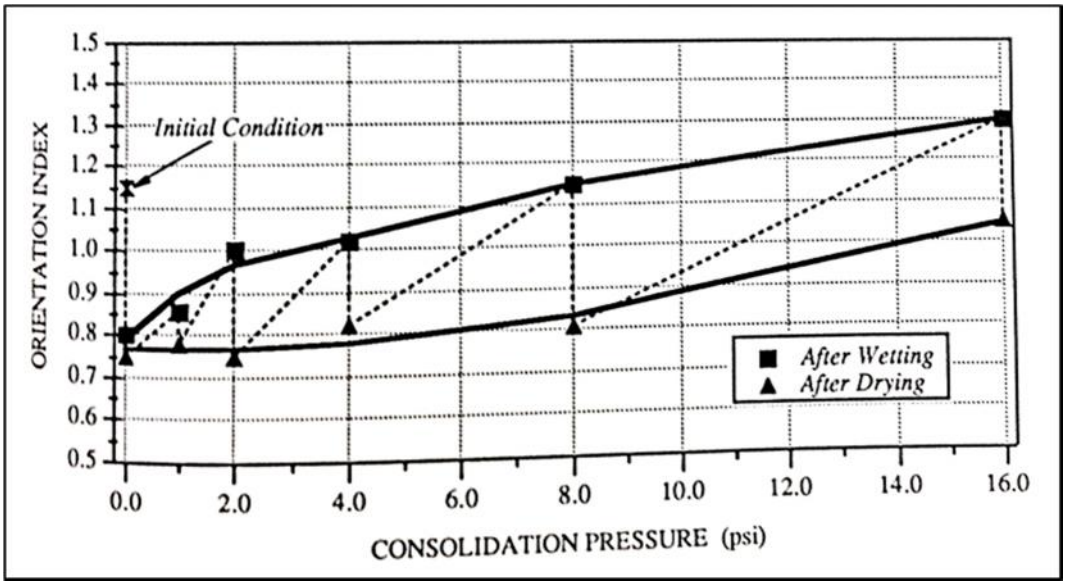


Figure 2.6: Orientation indices at the end of wetting and drying for a Beaumont Clay specimen versus the applied effective consolidation pressure (Kayyal 1991)

### 2.1.2 Shear strength

High-plasticity partially saturated clays often exist in an overconsolidated state, even if preloading is unapparent. Because, the naturally existing high-plasticity clay has probably been exposed to environmental wetting and drying conditions. Although the stress-strain relationship of overconsolidated soil is commonly accepted to follow a strain softening behavior, i.e., peak-residual behavior (Figure 2.7); Skempton (1970) suggested that overconsolidated soil subjected to cycles of wetting and drying follow a shear hardening mechanism. Skempton (1970) suggested that overconsolidated clays subjected to wetting and drying follows a hyperbolic model called the "fully softened condition" (Figure 2.7). The study suggested that the ultimate strength of this fully softened condition is between the peak and residual strengths, and equal to the shear strength of normally consolidated clay. Wright (2005) evaluated the shear strength of overconsolidated clay samples before and after repeated wetting and drying cycles for different confining stresses, and obtained a shear strength envelope from the measured stress-strain curves (Figure 2.8). Wright (2005) results supports Skempton (1970)'s theory.

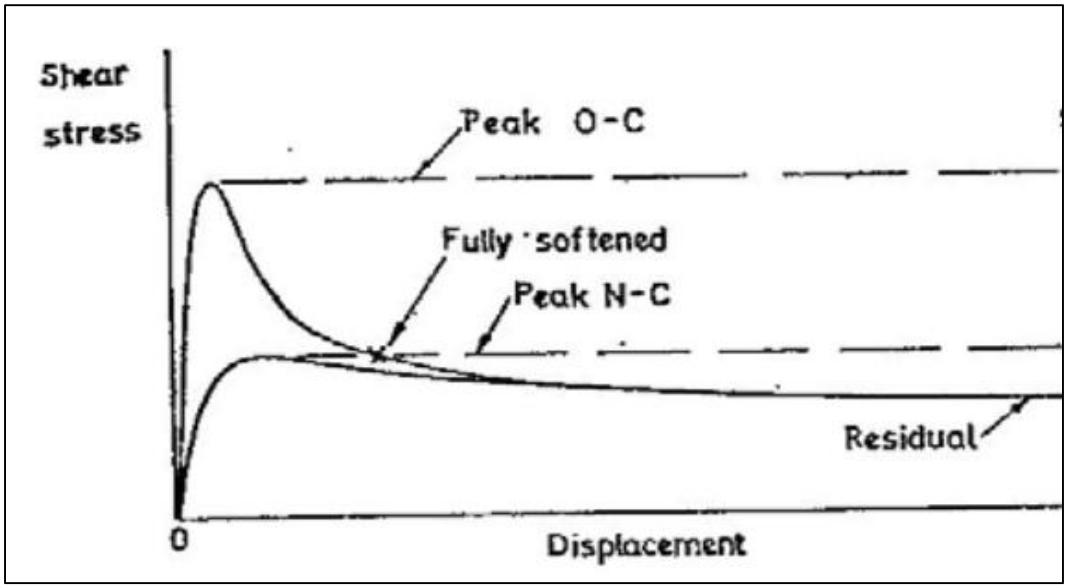


Figure 2.7: Comparison between peak, residual, and fully softened shear strength (Skempton 1970)

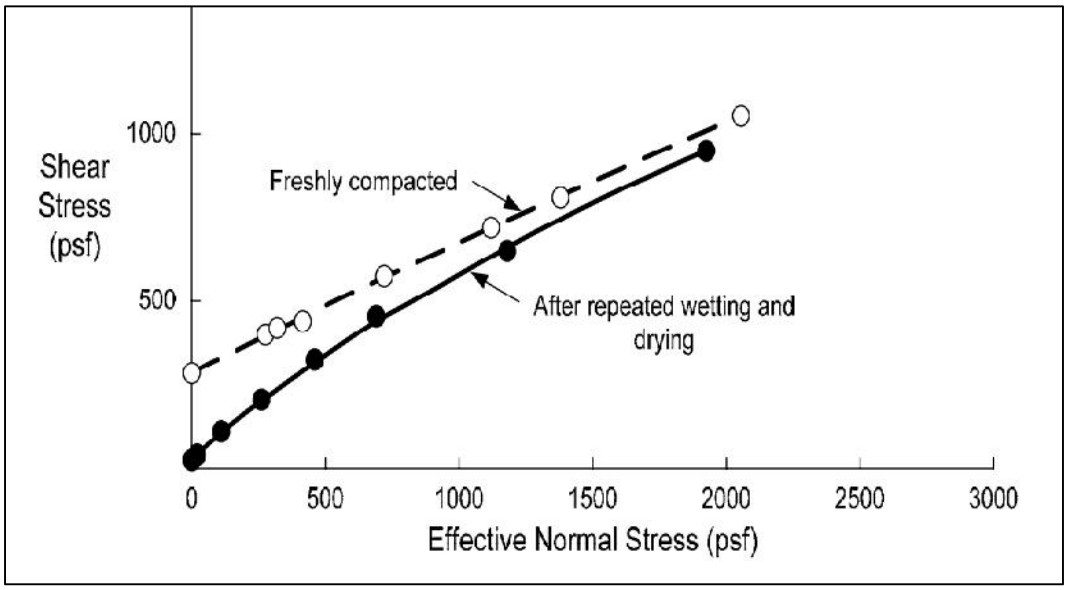


Figure 2.8: Sensitivity of shear strength envelope to cycles of wetting and drying (Wright 2005)

Wright and Duncan (1971) evaluated the sensitivity of the shear strength to the load orientation for clay-rich pepper shale mudrock formation of Waco, Texas. Figure 2.9 presents the compressive strength measurements for specimens loaded in different orientations. The figure shows that the compressive strength is sensitive to the angle between principal loading plan and the bedding planes of the specimen. Results show that the compression strength obtained from an inclined specimen could be three times less than the compression strength of a sample loaded perpendicularly to the bedding plane.

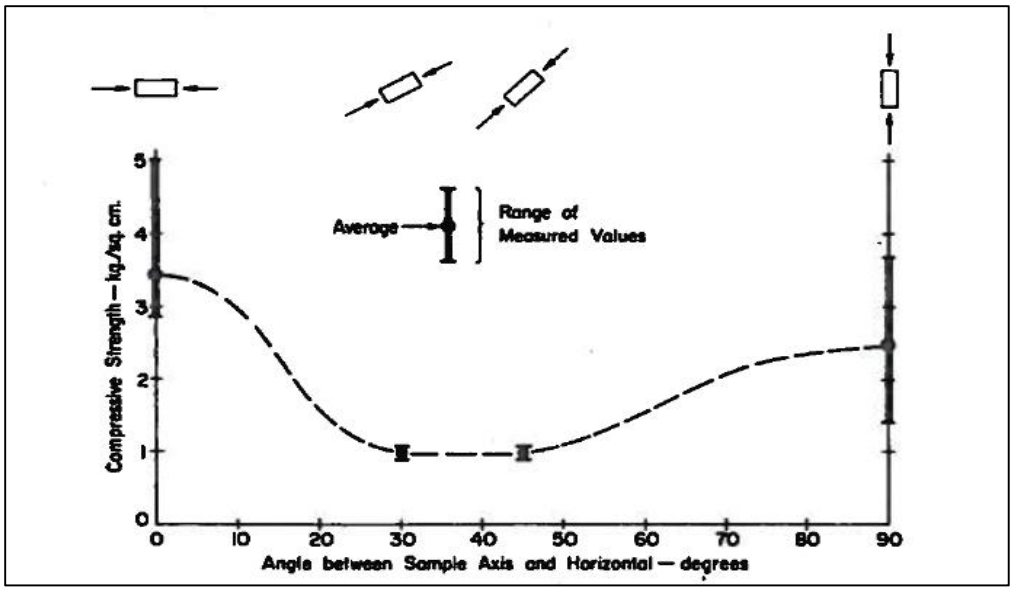


Figure 2.9: Variation in Undrained strength with sample orientation for Pepper Shale (Wright and Duncan 1969)

### 2.1.3 Shear stiffness

Salem (2006) tested the shear wave velocity for 8 specimens of low plasticity clay (CL) in a suction controlled resonant column apparatus. Figure 2.10 shows the degree of saturation of soil samples during compaction and the dry unit weight density reached after compaction. The specimens could be classified into two groups, first, samples that are

compacted with the same compaction effort and variable degree of saturation (samples 1, 2, 3, and 4) (Figure 2.11); second, samples that are compacted at the same degree of saturation with variable compaction efforts (Figure 2.12).

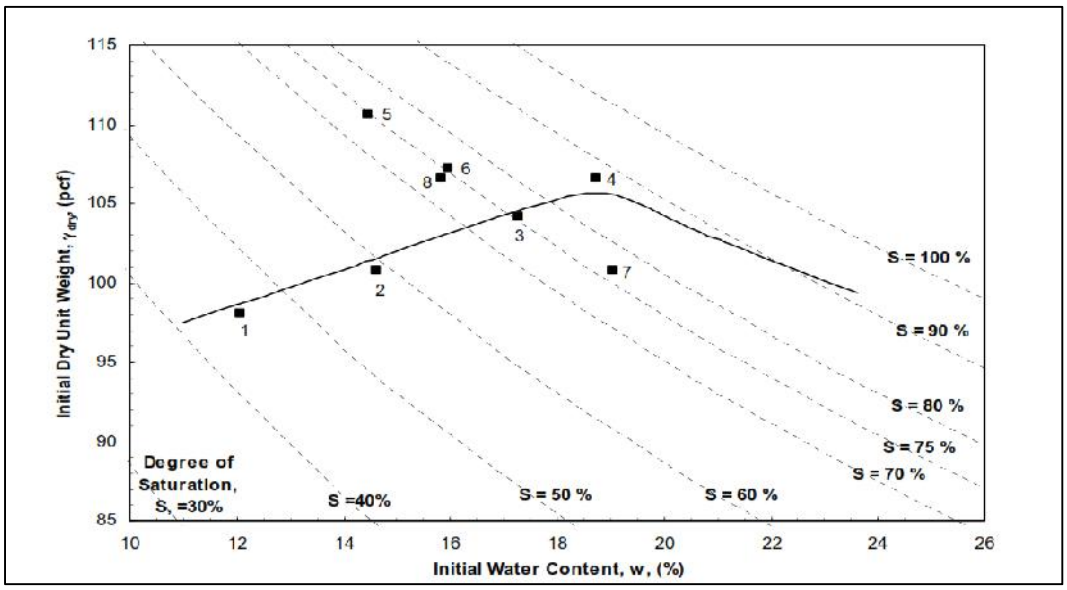


Figure 2.10: Standard Proctor compaction curve with specimens tested in suction-controlled triaxial apparatus (Salem 2006)

Figure 2.11 shows that the soil shear stiffness is sensitive to the compaction degree of saturation such that the higher the compaction degree of saturation the higher the shear stiffness of the soil. Figure 2.12 shows that the maximum shear stiffness is also sensitive to the dry unit weight of soil after compaction (i.e. voids ratio).

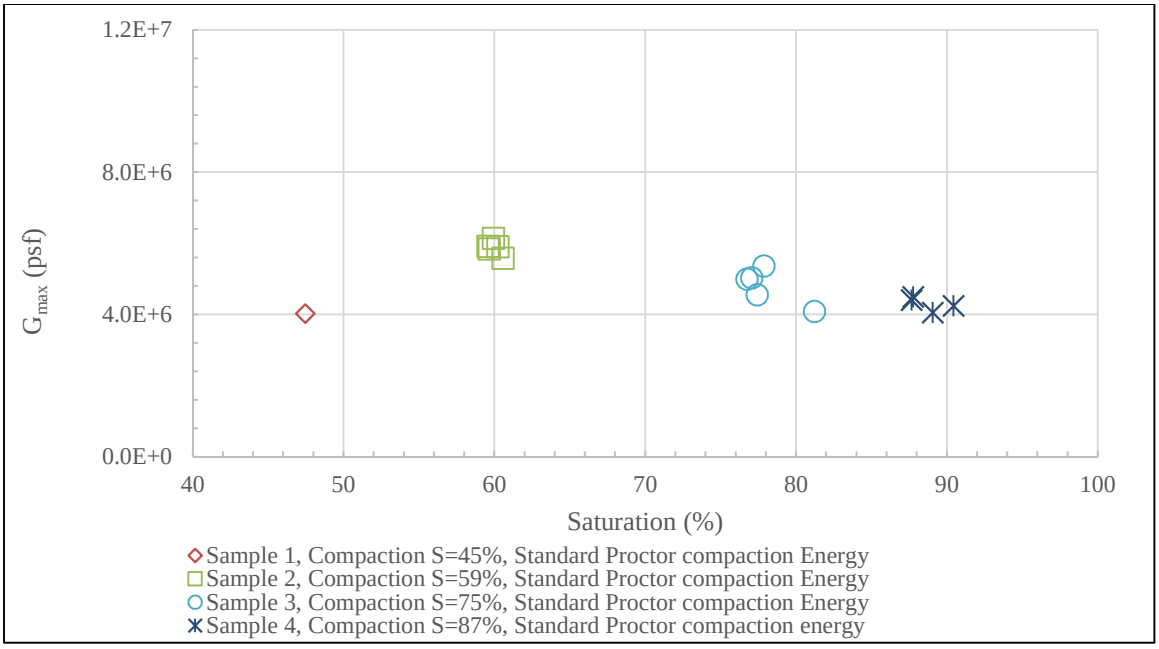


Figure 2.11: Relationship between small strain shear stiffness and degree of saturation for samples compacted with the same compaction energy at different water contents (Salem 2006)

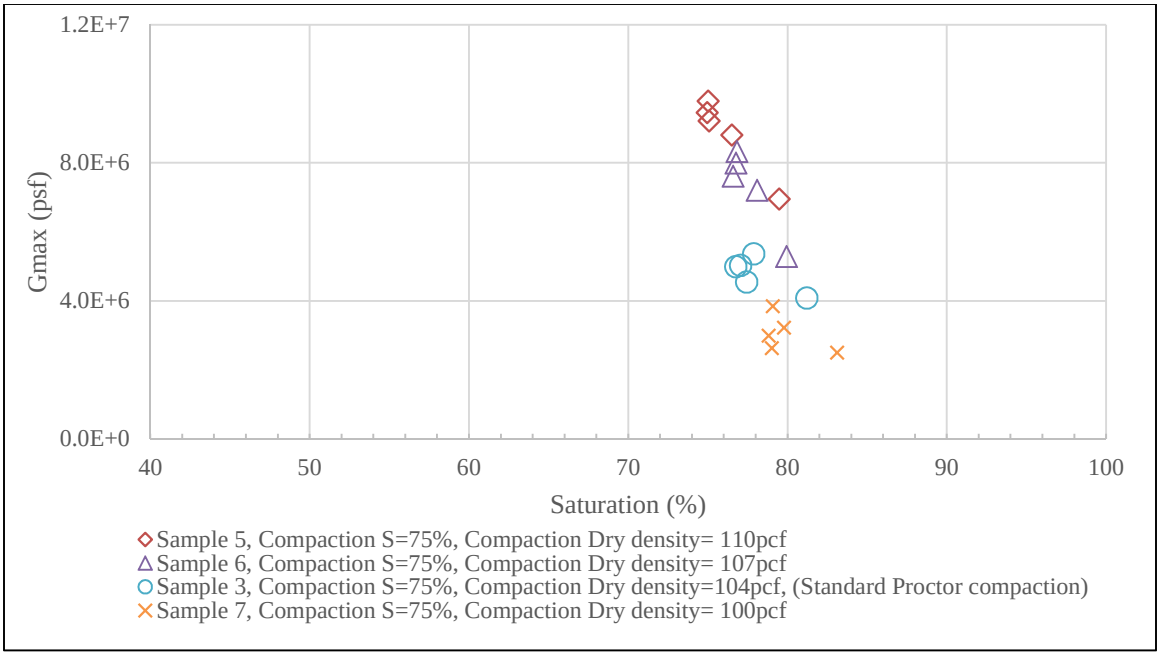


Figure 2.12: Relationship between small strain shear stiffness and degree of saturation for samples compacted with variable efforts but at the same degree of saturation (Salem 2006)

Wonjsarog et al (2004) measured the stiffness of London clay in the vertical and horizontal directions. The London Clay is considered as a useful reference because it has similar geologic formation of the Taylor clay commonly encountered in Texas. Figure 2.13 presents Young's moduli in the vertical and horizontal directions normalized to a reference stress, with respect to the mobilized axial strain. Results show that the stiffnesses of the vertical and horizontal directions are not equal for all strain levels; such that, the specimen tested in the horizontal direction, i.e., loaded parallel to the bedding plane, is stiffer than the sample tested in the vertical direction.

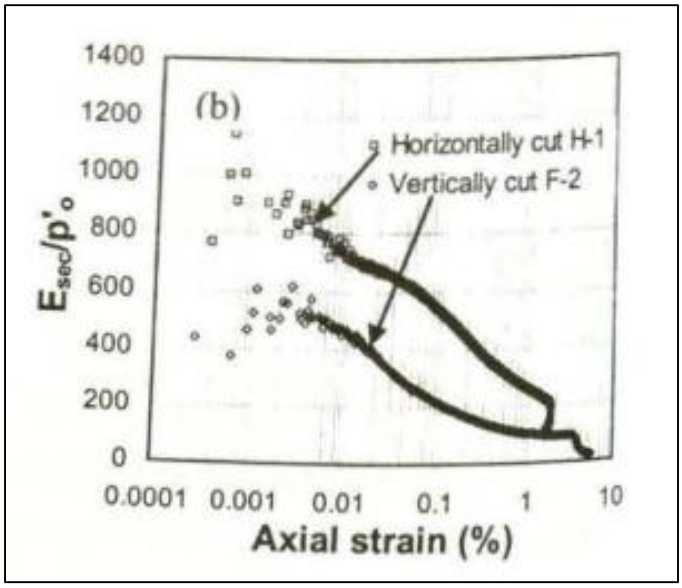


Figure 2.13: Sensitivity of normalized secant axial stiffness to specimen orientation (Wongsaroj et al. 2004)

### 2.1.4 Describing the behavior of partially saturated soils

There are two schools of thought in describing the behavior of partially saturated soils. First, the Fredlund and Morgenstern (1977)'s ideology of describing the partially saturated soil with two independent stress variables. The two independent stress parameters are the total stress over the pore-air pressure, the matric suction, defined as the pore-air pressure over the pore-water pressure, and $\chi$ coefficient. Second, the Lu and Likos (2007)'s that describe the effective stresses in partially saturated soil in terms of the "suction stress" rather than the matric suction and $\chi$ coefficient. The two definitions of effective stresses are discussed in details in chapter 8.

## 2.2 RETAINING WALLS

Walls retaining excavations, often referred to as cut walls, are classified as either temporary or permanent walls. Temporary walls, such as infrastructure lining walls and

basement-excavation walls prior to slab/struts are designed for short term conditions. Permanent walls, such as bridge abutments and underground stations are designed for long term conditions; because, long-term conditions of cut walls are more critical than the short term conditions. Short-term conditions of soil indicate the condition when the steady state of pore-water pressure has not been reached yet and the soil experience negative excess pore-water pressure generated from excavation (i.e. excavation induced pore-water pressure). Long-term condition of soil is generally used to indicate the condition when pore-water pressure reaches a steady state and the excavation induced excess pore-water pressure dissipates. The soil retained by cut walls experience negative excess pore-water pressure, which generally stabilizes structural elements during short-term conditions. During the transition from short-term conditions to long-term conditions, the excess pore-water pressure dissipates until the long-term conditions are reached; this dissipation of negative excess pore-water pressure reduces the stability of structural elements.

Currently there is high level of uncertainty in the lateral earth pressure design loads that represents the additional loads due to soil swelling. Figure 2.14 presents the range of assumptions followed by practitioner. Equivalent fluid pressure ranging between 40pcf and 120pcf are adopted in practice; Hong (2008) even recommended higher lateral earth pressure, and suggested that the lateral earth pressure on the active side is calculated as a lower envelope between the passive earth pressure and the swelling pressure; however, this extreme design load is not adopted by practitioners.

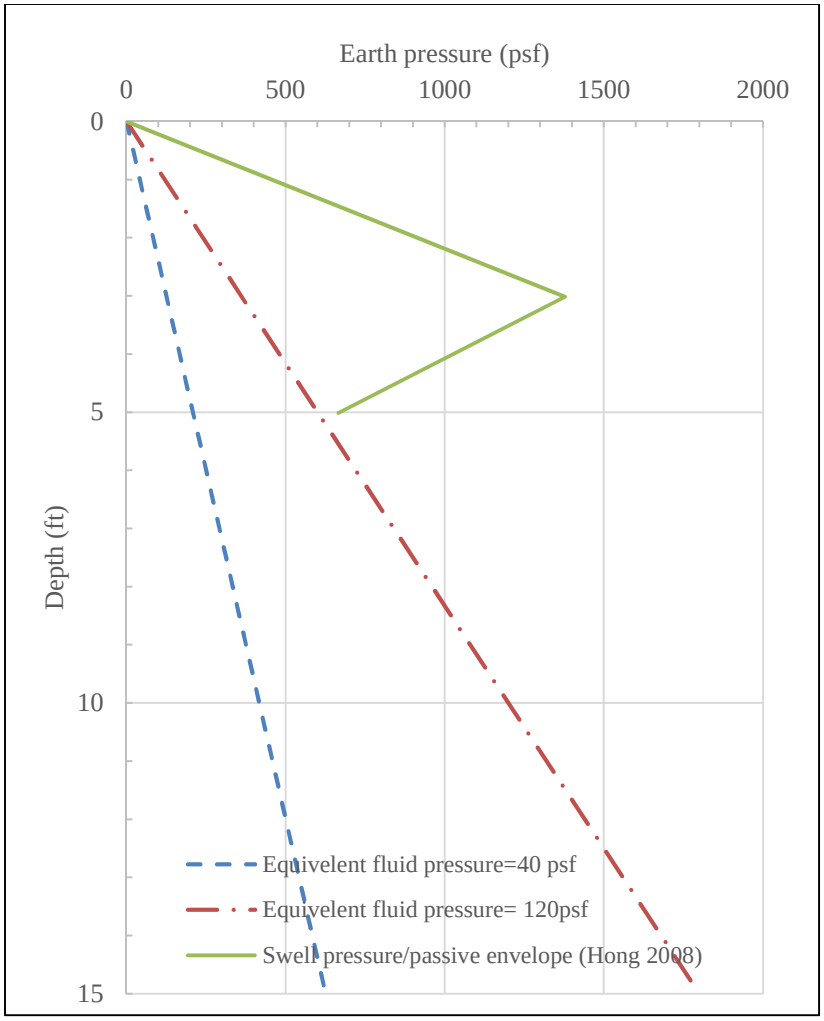


Figure 2.14: Uncertainty in lateral earth pressures distribution during short-term conditions (Brown 2015)

Pufahl et al. (1982) suggested that the lateral earth pressure of swelling clay is sensitive to the level of confinement the soil is subjected to; therefore, designating the design load as a given or an input overlooks the confinement from the wall and the additional loads, hence, overlooking the fact that the behavior of retaining walls in high-plasticity partially saturated soil is a soil-structure interaction problem. Walls design based

on factoring the design loads also overlooks the fact that the soil properties (i.e. soil resistance) changes as the soil saturation changes.

### 2.2.1 Recent Failures in Texas: Short-term conditions

Smith (2009) reported the failure of the President George Bush Turnpike Bridge in Northwest Dallas, Texas (Figure 2.15). The bridge is founded in the Eagle Ford formation; the Eagle Ford formation is a high plasticity clay commonly found in Texas. The bridge was constructed using top-down construction sequence. After the installation of the bridge deck and completion of the first excavation stage down to the drilling platform of the shallowest group of anchors, 4 inches of deflection was observed at the top of the wall, and the bridge deck failed. The author attributed the failure to adopting a low lateral earth pressure coefficient ($k_0$) during the design stage. The $k_0$ value adopted in the design procedure was 0.64; the study reports that dilatometer measurements indicate that the $k_0$ value is 2.6.

Figure 2.15: Wall failure during short-term conditions (Smith 2009)

### 2.2.2 Recent Failures in Texas: Long-term conditions

Adil Haque and Bryant (2011) reported the failure of the Las-Colinas Bridge in Irving, Texas (Figure 2.16). The bridge is founded in the Eagle Ford formation. After the construction was completed, visual inspection concluded failure of a substantial body of soil. The authors attributed the failure to the fact that the wall design did not account for changes in the soil properties that took place due to the excavation works, i.e., soil resistance of the excavated side. The authors added that the behavior of the wall is more sensitive to changes in the soil properties on the excavated side than it is sensitive to the additional pressure due to changes in the degree of saturation. In other words, the deflection of the wall is more sensitive to the loss of confining pressure on the passive side, than it is sensitive to the inundation of soil on the active side.

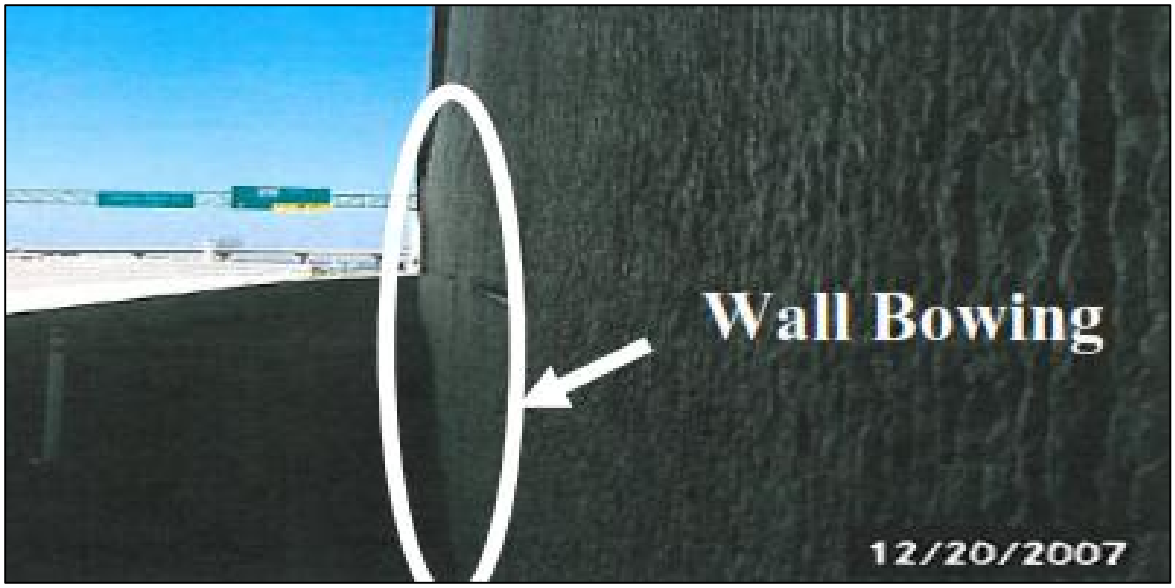


Figure 2.16: Wall failure during long-term conditions (Adil Haque and Bryant 2011)

This chapter presented the difficulties associated with predicting the behavior of partially saturated soils. Better understanding of the behavior wall retaining expansive soils subjected to variation in the degree of saturation could be obtained by monitoring a wall retaining expansive soil and is being subjected to wetting and drying during the monitoring period. Such data are hard to get; because, it requires extended monitoring period of wall behavior as well as monitored variation of the ground saturation conditions. Chapter 3 presents a unique set of data of a full-scale wall that was monitored for four consecutive years.

# CHAPTER 3: The Reese wall: Full-Scale Wall Measurements

The objective of this chapter is to refer to a research wall that was built in an expansive soil stratigraphy. The wall was subjected to sever wetting and drying conditions to acquire insight about the behavior of walls retaining expansive soils subjected to fluctuation in the soil degree of saturation.

A full-scale wall was built according the TxDOT design procedures in a high-plasticity soil to study the behavior of drilled shaft retaining walls constructed in partially saturated high-plasticity soil subjected to wetting and drying. Ellis (2007) presented detailed site investigation and laboratory works. Koutrouvelis (2012) presented the detailed procedures of interpreting the field measurements into deflection and bending moment profiles. Brown (2013) proposed the applicability of predicting the behavior of the wall during short-term and long-term conditions using P-y curves analysis. The comprehensive study conducted to evaluate the current design procedures was discussed in TxDoT report FHWA/TX-13/0-6603-2.

The objective of this study is to develop a framework that could be used in predicting the behavior of walls retaining expansive soils. The measured behavior of the Reese wall is used as a benchmark in developing the framework. This section highlights the main characteristics of the full-scale model of the wall and then a description of the numerical model of the same wall is discussed.

## 3.1 PROJECT DESCRIPTION

In April 2010, a drilled-shaft retaining wall was constructed in Manor, Texas, in honor of Lymon C. Reese. Figure 3.1 shows the location of the Reese wall relative to the geologic map of areas prone to swelling; the wall is located at the western corridor of high swell potential soil. The wall is built on the property of R&L Transfer & Storage Co. North

to the site is Highway 290, South to the site is the old highway 20, and, East to the site is old Kimbro Road (Figure 3.2).

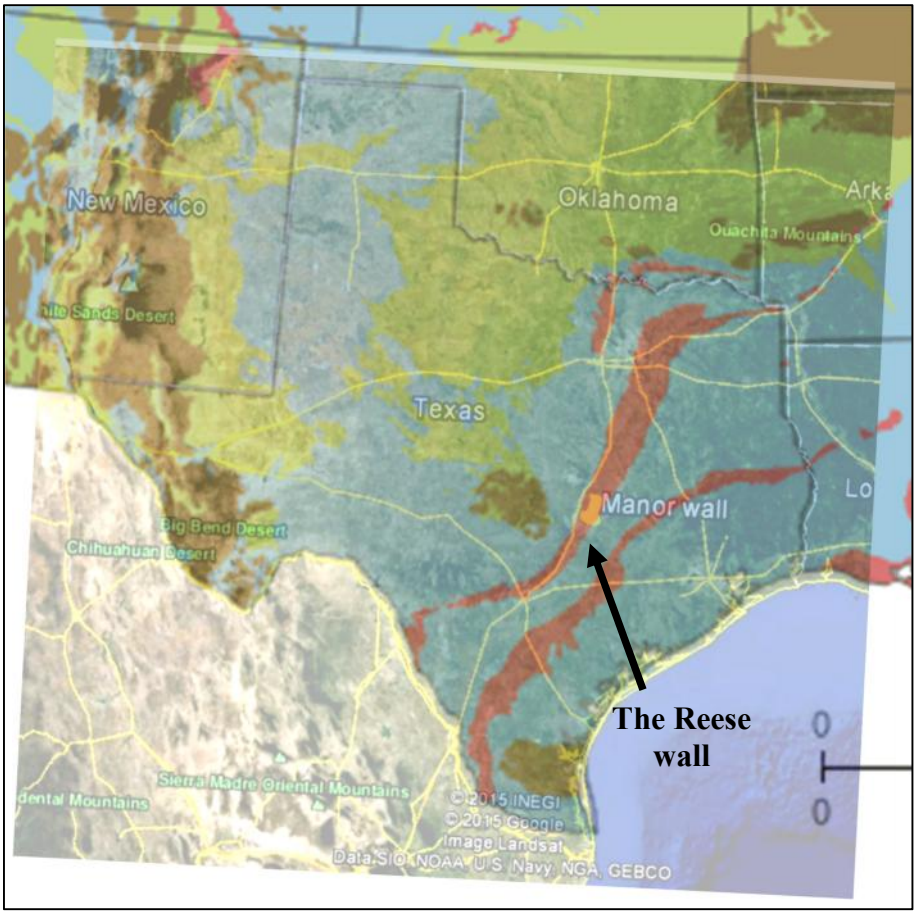


Figure 3.1: Location of the Reese wall in Manor, TX

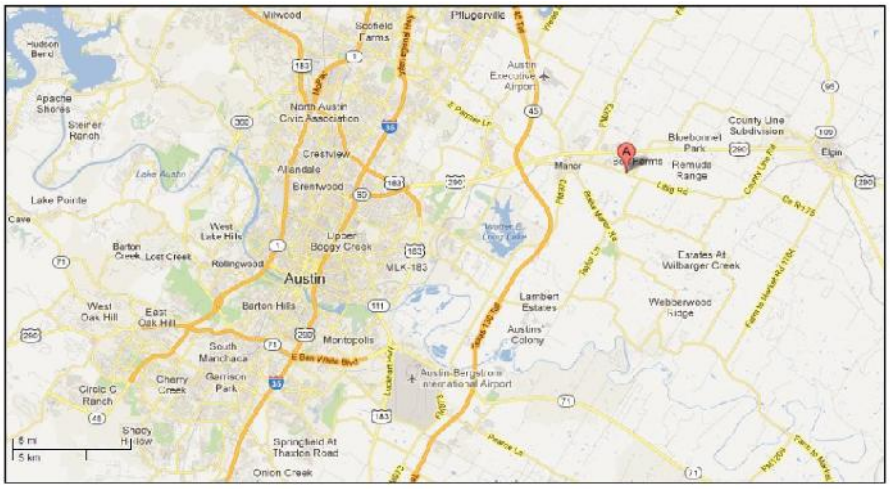


Figure 3.2: Location of the Reese wall relative to neighboring highways Manor, TX

## 3.2 METEOROLOGICAL DATA

The site investigation of the Reese wall project started in December 2009, the excavation works was completed in October 2010. After completion of the excavation works, the state of Texas experienced a groundbreaking drought that lasted for more than two years. Figure 3.3 presents the percentage of area in different drought categories, during the summer of 2011, 86% of the Texas state area experienced “Exceptional Drought” conditions during that period of time.

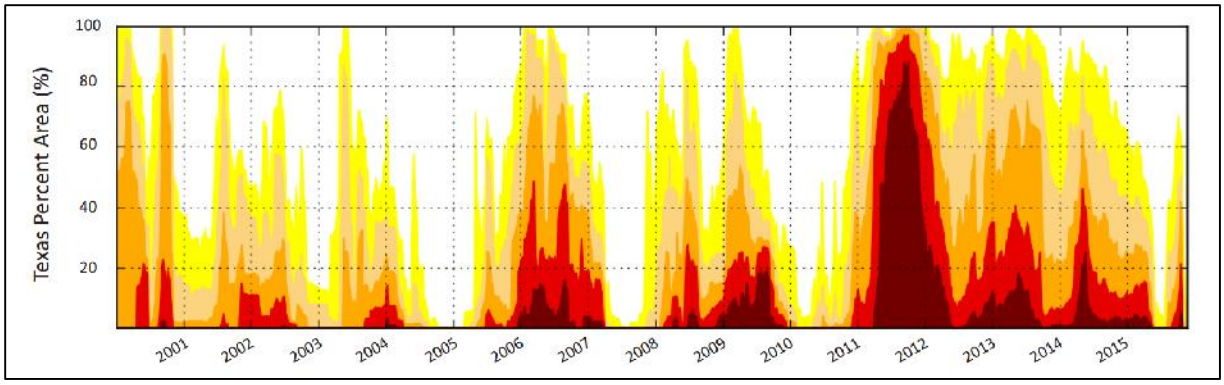


Figure 3.3: Historic records since 2000 of the Percentage of area affected by the drought (stateimpact.npr.org/texas)

The site investigation of the Reese wall was conducted during 2009-2010 winter. Figure 3.4 shows the dates of the borehole drilling, Spectral Acceleration of Surface Waves (SASW), and the start and end dates of the excavation works. For eight months prior to the wall construction (i.e. Dec 09 to July 10) the site experienced average to above average rain fall; after the wall construction the site experienced 2month of below average rainfall (April and May), followed by two months of above average rainfall (June and July).

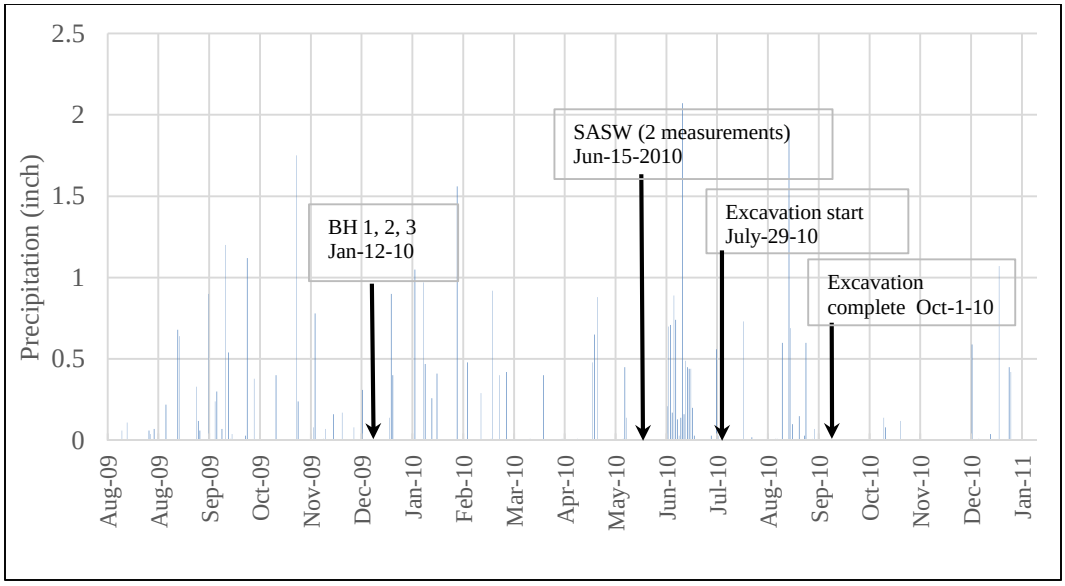


Figure 3.4: Recorded rainfall depths during site investigation and construction works

The Reese wall site experienced above average temperature record during the same period, Figure 3.5 shows the temperature high, low, and average temperature records during the site investigation, wall construction and excavation works. Figure 3.6 presents the high, low, and average temperature records during different wetting and drying cycles of the Reese wall site.

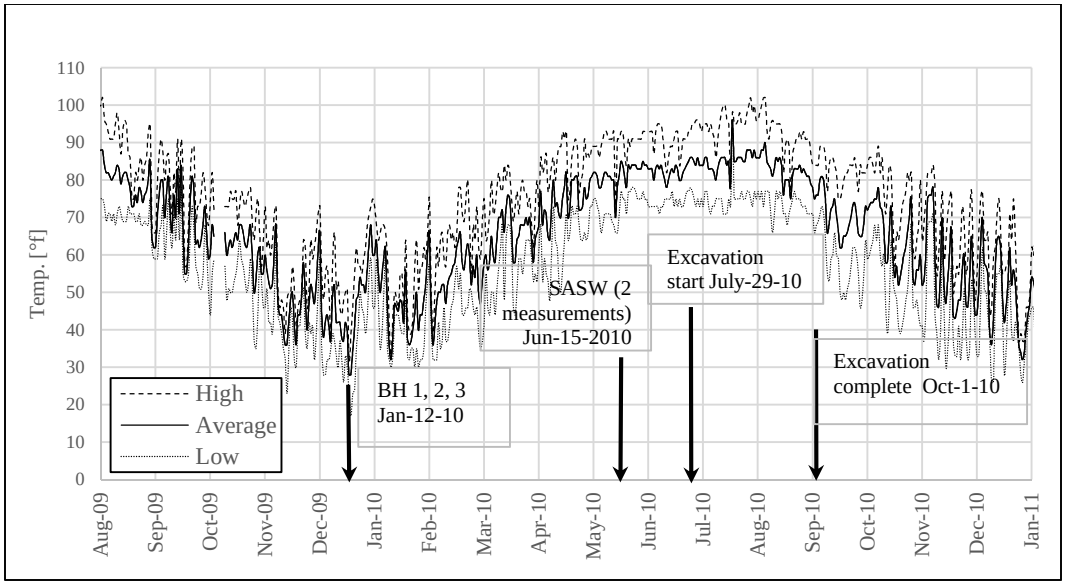


Figure 3.5: Recorded temperatures during site investigation and construction works (www.Wunderground.com)

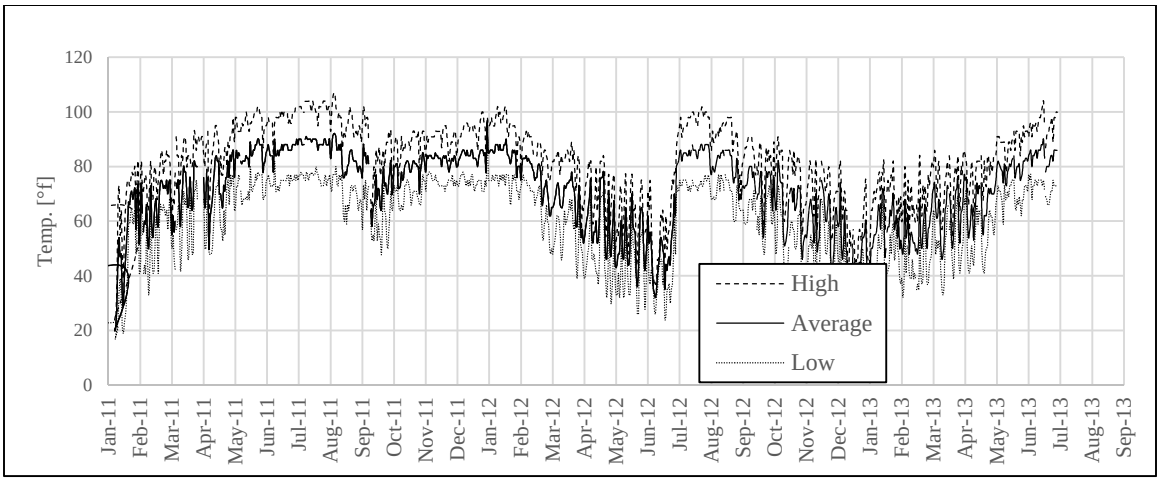


Figure 3.6: Temperature measurements during monitoring period (www.Wunderground.com)

## 3.3 SITE INVESTIGATION

Three geotechnical borings that extended to a depth of 50ft were conducted in January 2010. Borings showed that the test wall is underlain by approximately 50ft of highly expansive Taylor Clay. The Taylor Group was deposited in east-central Texas during the late Cretaceous period with the dominant clay mineral being montmorillonite (Ellis 2011). The clay is blocky, highly fissured, heavily overconsolidated, and full of desiccation cracks (Figure 3.7).

Figure 3.7: Desiccation cracks of the soil during site investigation

### 3.3.1 Atterberg limits

The Reese wall is underlain by 50 feet of the Taylor formation; a high plasticity problematic soil common in Texas. Figure 3.8 shows the Atterberg limits of the subsurface formation and the water content measurement during site investigation phase. The plasticity index of the top 15ft ranges between 35 and 75, and about 75 for soil deeper than

15ft. Natural moisture contents range from 24 to 37 percent which is closer to the plastic limit of the soil.

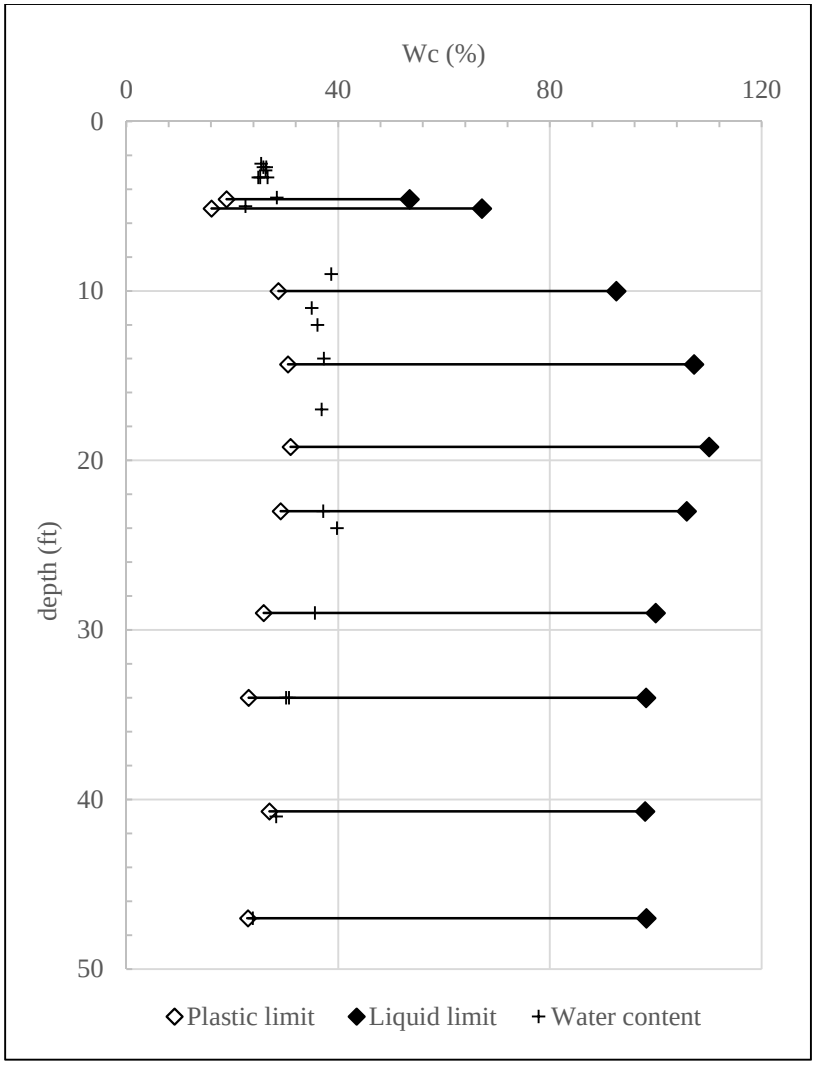


Figure 3.8: Plasticity of the Taylor Clay

Dakshanamurthy and Raman (1973) classified the swell potential of soil according to the plasticity index and liquid limit of the soil (Figure 3.9). Atterberg limits of the Taylor

Clay classifies the soil as high-swelling to extra high swelling. The Atterberg limits of the London Clay is also presented for reference.

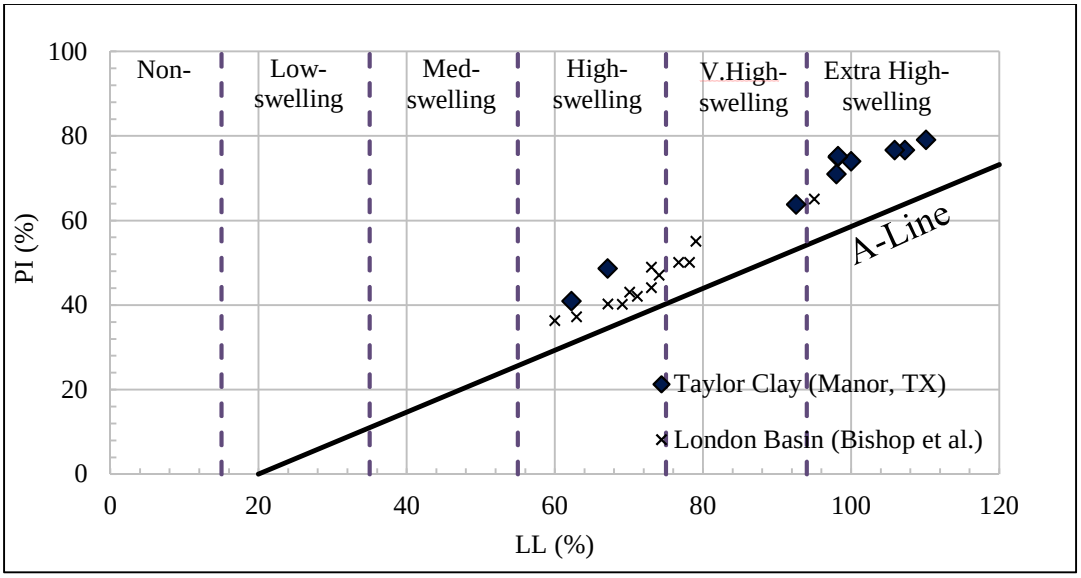


Figure 3.9: Classification of the Taylor Clay swell potential (Dakshanamurthy and Raman 1973)

Figure 3.10 presents the grain size distribution of clay specimens; results show that the percentage of clay finer than 0.002mm ranges between 52 and 80%. Seed et al (1962) classified the swell potential of soil according to the clay activity and percentage of clay passing sieve 0.002mm; the Taylor clay is classified as very high swell potential (Figure 3.11).

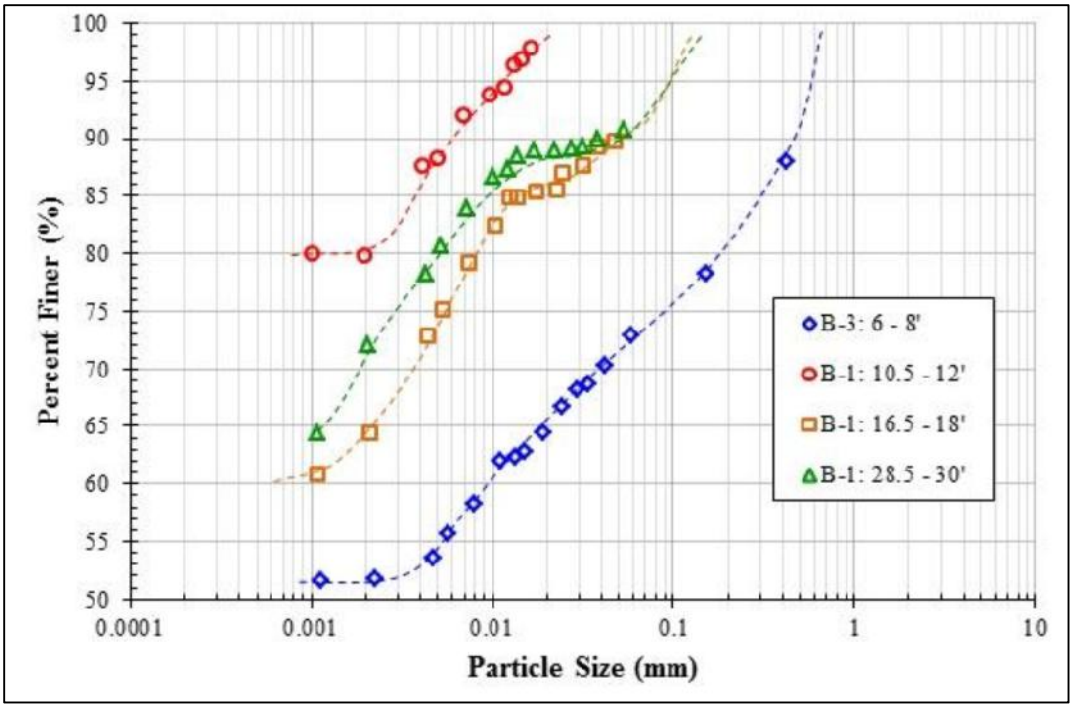


Figure 3.10: Grain size distribution (Ellis 2011)

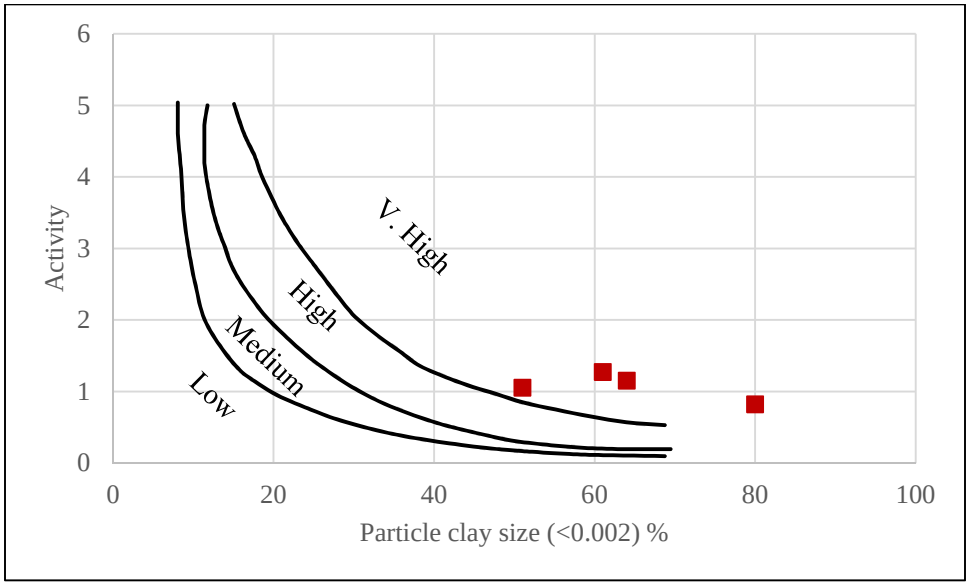


Figure 3.11: Soil swell potential (Seed et al. 1962)

### 3.3.2 Dry unit weight

Figure 3.12 presents the total unit weight measurements obtained from high quality laboratory measurements and second party measurements. The high quality measurements show that the total unit of the top 10ft weathered soil ranges from 120pcf to 125pcf. Results show that the total unit weight of the soil decreases with depth; however such observation is questionable and such observation might be attribute to the difficulties of the trimming process of the highly cracked soil. The total unit profile presented in Table 3.1 is adopted.

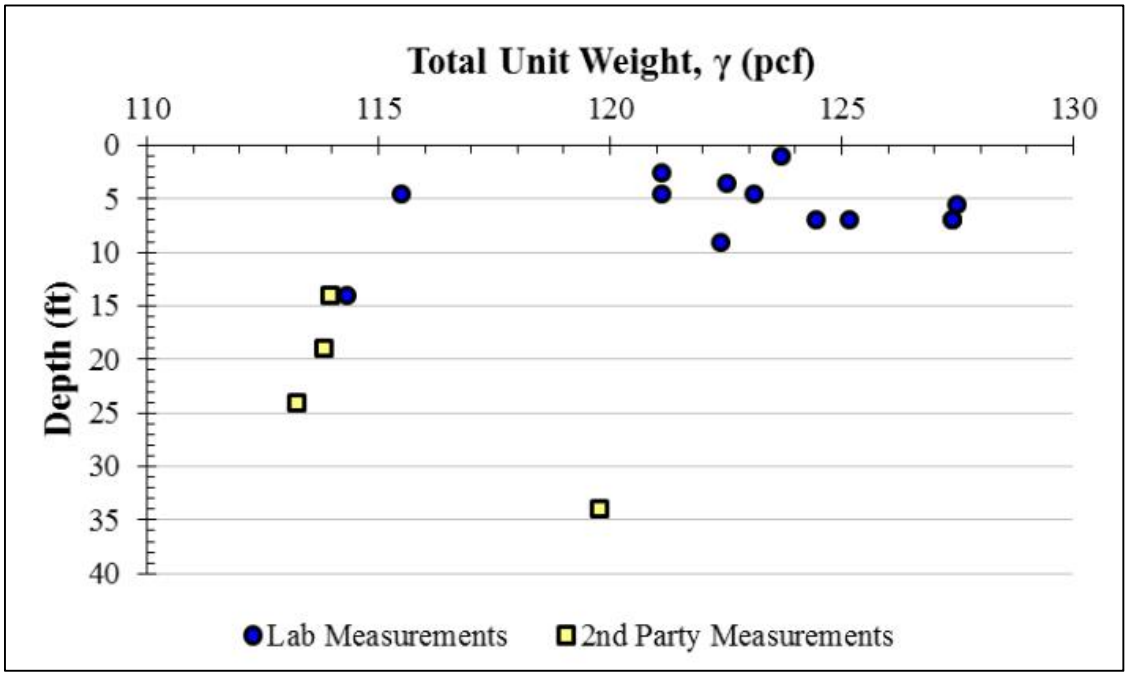


Figure 3.12: Dry density measurements and estimated profile (Ellis 2011)

Table 3.1: Interpreted profile of soil unit weight

| Depth (ft) | Total Unit Weight (pcf) |
|---|---|
| 0-5 | 120 |
| 5-10 | 123 |
| Below 10 | 126 |

### 3.3.3 Shear Strength

Figure 3.13 presents the undrained shear strength measurement at the Reese wall site. The insitu shear strength is estimated from Texas Cone Penetration measurement and pocket penetrometer measurements. The soil shear strength is measured in the laboratory by unconsolidated undrained triaxial tests. The undrained shear strength of the top 20ft is approximately 2000psf; deeper than 20ft, the undrained shear strength of the soil increases almost linearly to a depth of 40ft. The TCP test are not reliable beyond shear strength of 8000psf, i.e., soil deeper than 40ft. Comparison between the pocket penetrometer shear strength estimates and the UU and TCP measurements suggest that the undrained shear strength of the soil is significantly reduced by the fissures in the soil. The pocket penetrometer is usually conducted by the field engineer on intact soil samples, trying to avoid any obvious fissures in the soil; while UU and TCP measure the overall shear strength of the soil.

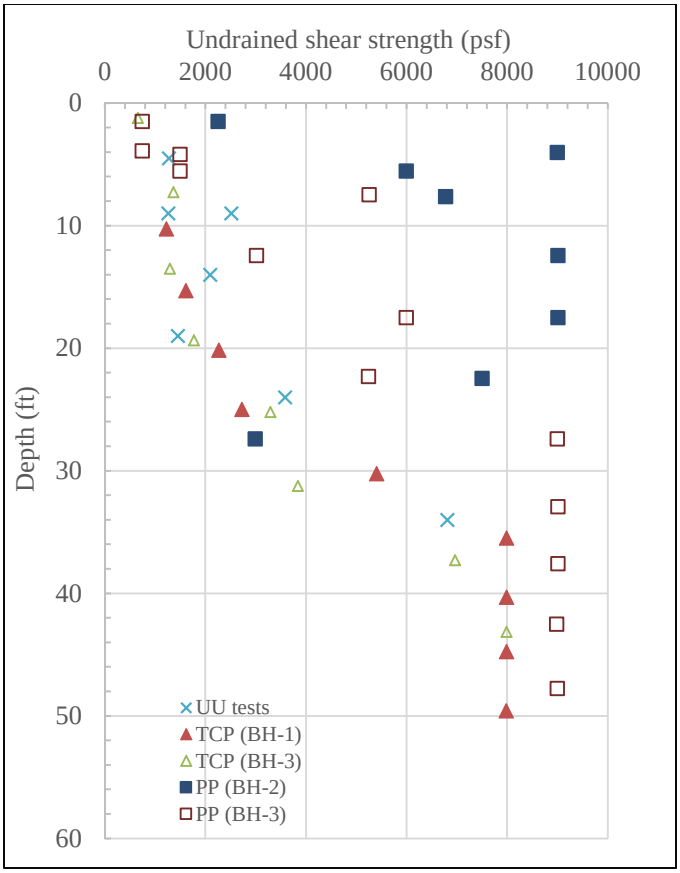


Figure 3.13: Undrained shear strength estimated from (a) Unconsolidated Undrained tests (b) Texas Cone Penetration tests (c) Pocket penetrometer

### 3.3.4 Small-strain stiffness

The soil profile is filled with fissures and dissection cracks that resulted in difficulties in obtaining undisturbed samples. Insitu shear wave velocity measurements were obtained using Spectral Analysis of Surface Waves (SASW) measurements, measurements were obtained on June 15th and July 26th. Small strain shear stiffness is calculated from the shear wave velocity measurements according to Equation 3.1. Figure 3.14 shows the estimated small-strain shear stiffness profiles.

$$G = V_s^2 \frac{\gamma}{g}$$ Equation 3.1

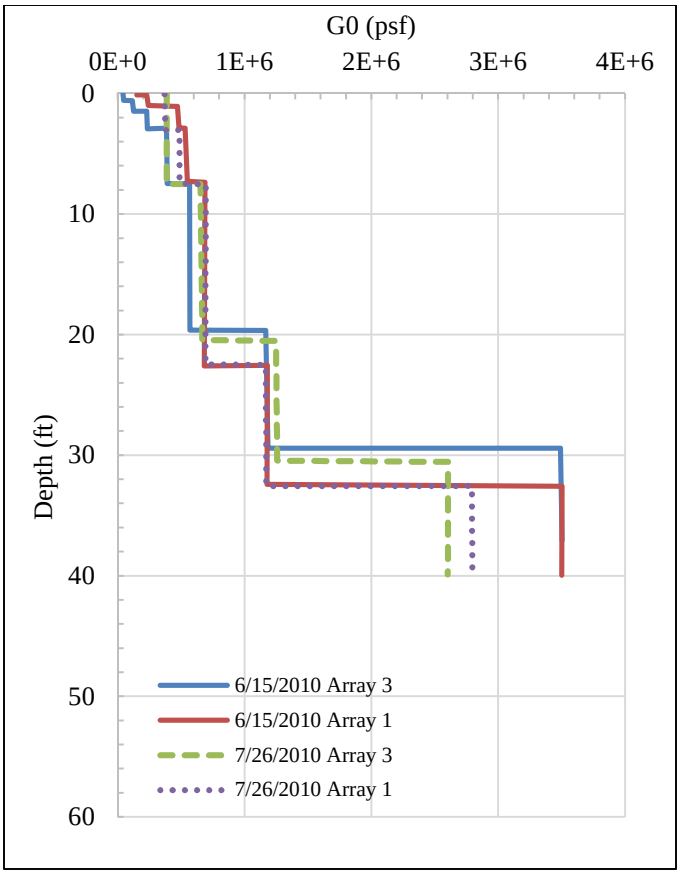


Figure 3.14: Spectral Analysis of Surface Waves (SASW)

### 3.3.5 Large-strain stiffness

Figure 3.15 shows the stress-strain measurements of Taylor clay from unconsolidated-undrained triaxial tests. Triaxial compression tests were run in accordance with ASTM D2850. The UU triaxial tests were run in the University of Texas and the Fugro Consultants, Inc. laboratories. Tests indicate a trend of increasing shear strength with depth; however, the structure of fissures and desiccation cracks facilitated the failure before shear plane developed within the intact soil.

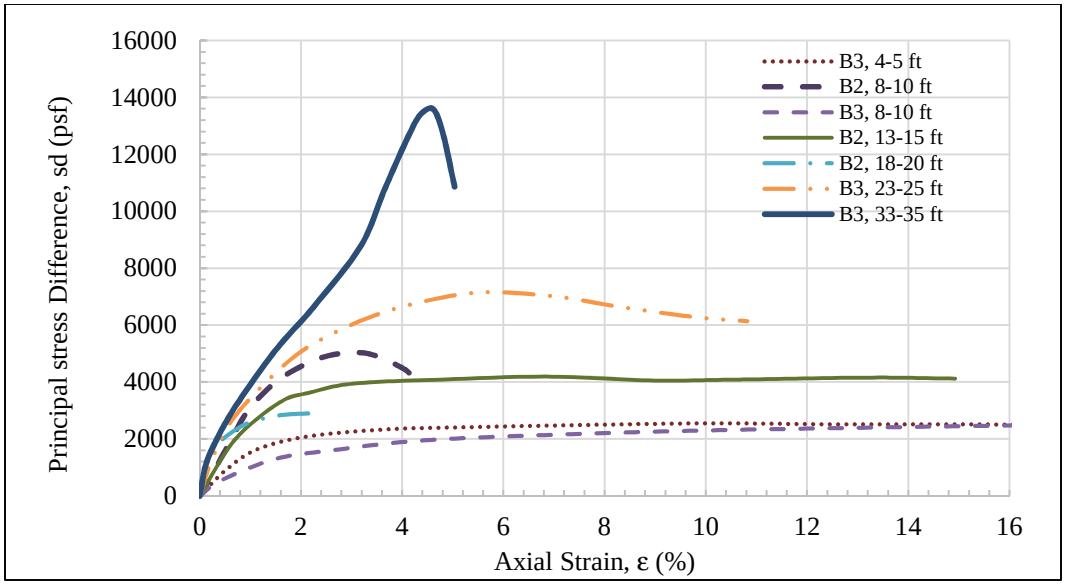


Figure 3.15: Stress-strain measurements from unconsolidated undrained triaxial tests

### 3.4 WALL CHARACTERISTICS

The wall consists of 25 drilled shafts, with 2ft diameter and clear spacing of 6inchs. Shafts embedment varies along the excavation. The maximum wall length, located at the center of excavation, is 35ft and the minimum wall length, located at the sides of the excavation is 20ft (Figure 3.16). After the wall construction 15ft of soil was excavated on the northern side of the wall (i.e. cantilever height equals 15ft). The excavated side of the drilled shafts was later furnished using shotcrete surfacing.

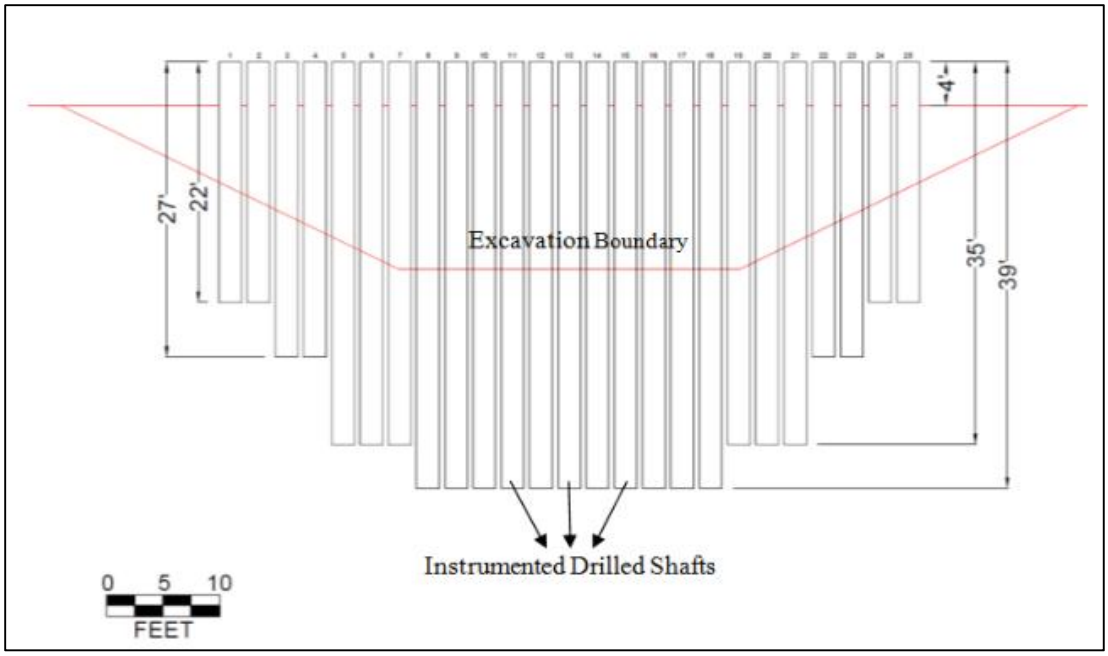


Figure 3.16: Elevation view of drilled shaft wall

In spite of the high level of uncertainty and complexity of drilled shaft retaining walls in swelling soil, the number of cases of failure is relatively limited (Section 2.2). This observation means that the current TxDOT design procedures are conservative; however, it questions whether walls designed according to the procedures are optimal or not. The current TxDOT design procedure estimates the maximum bending moment as 1.5times the bending moment at the excavation level. The earth pressure for stiff clay is calculated based on a friction angle of 30°. The maximum bending moment is factored by 1.7 to estimate the ultimate bending moment on the wall, and the resistance of the excavated side is reduced by 50%. The deflection of the wall top is analyzed using P-y software, additionally the depth of the shafts is increased by a factor of 1.33.

The bending stiffness and retained height of the Reese wall are compared to 17 cantilever walls constructed in London clay and reported by Long (2001); Figure 3.17 shows that the Reese wall is stiffer than most of the recorded cases.

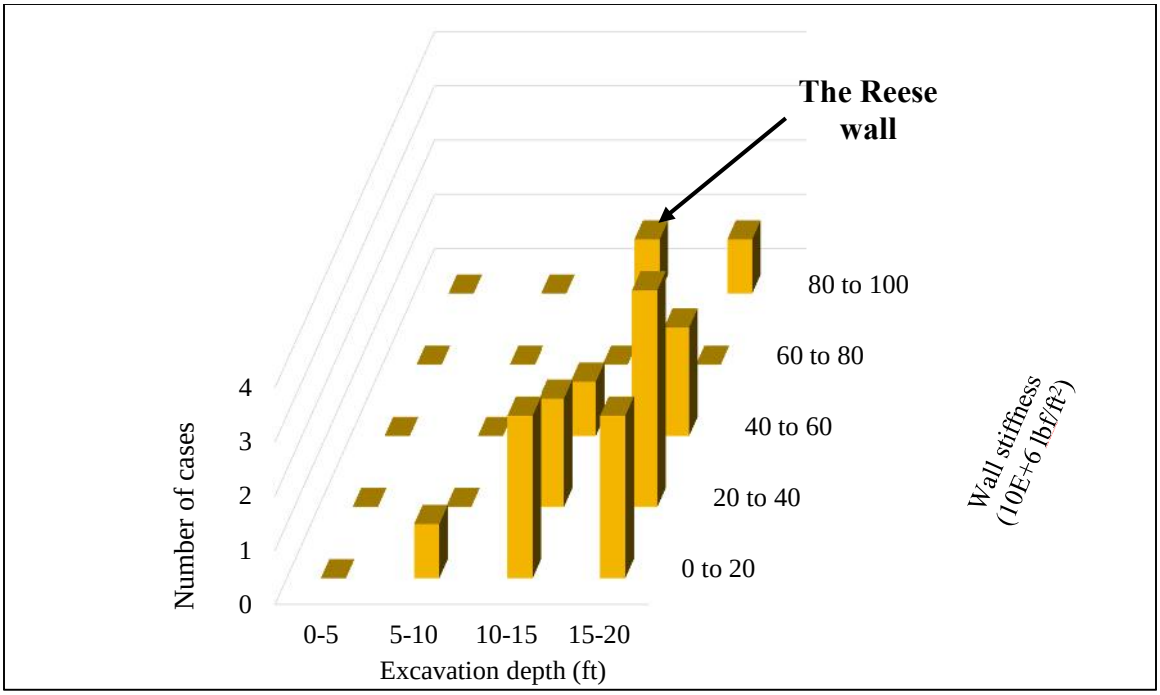


Figure 3.17: Comparison between the stiffness and retained height of the Reese wall and the stiffness and the retained height of cantilever walls constructed London Clay

The bending moment of the wall is calculated as the product of the bending curvature and the bending stiffness of the wall. The maximum bending curvature estimated from inclinometer measurements is 2.5E-4 radians/inch; the cracking bending stiffness of the shafts is calculated from strain compatibility of composite sections (Figure 3.18). Although the maximum bending curvature measured during short-term conditions is less than the cracking bending curvature, the concrete is assumed to be cracked, because, a

combination of concrete curing and expansive soil movements resulted in development of tension cracks and residual stresses throughout the shafts (Brown et al. 2011).

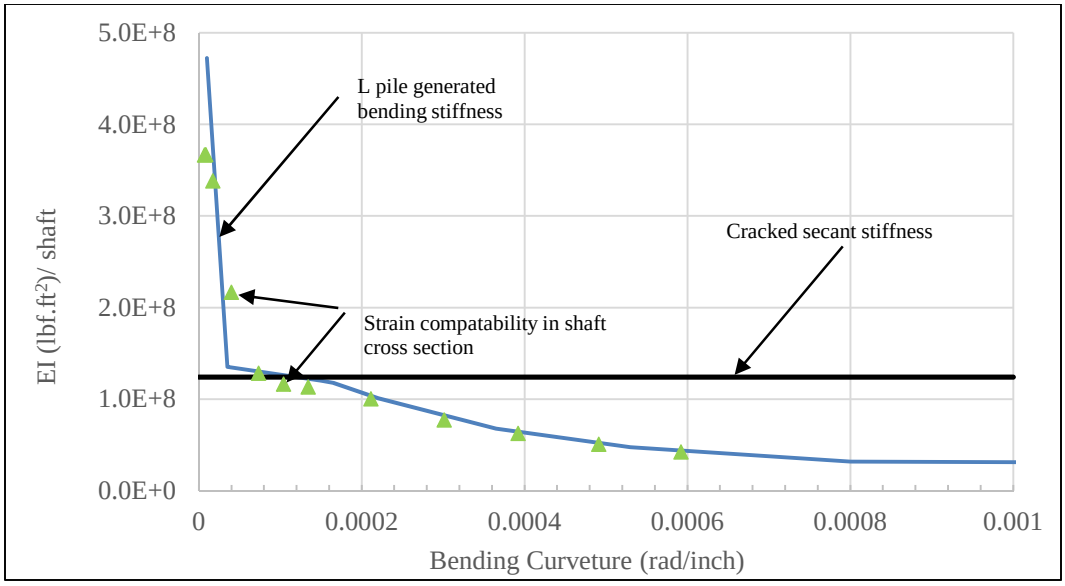


Figure 3.18: Relationship between the bending moment and bending curvature of the Reese wall drilled shafts

### 3.5 Field Measurements

Three shafts at the mid span of the wall were instrumented; field measurements were obtained for a total period of four consecutive years. Each instrumented shaft was instrumented by two rows of optical strain gauges and one inclinometer. The strain gauges were spaced at 18inchs, such that, one row was placed at a compression rebar, i.e., excavation side, and the other row was placed at a tension rebar, i.e., retained side; inclinometers were installed at the neutral axes (i.e. centerline of shafts) (Figure 3.19). Pairs of strain gauges are at 2ft spacing in the vertical direction (Figure 3.20). A potentiometer was used to measure the maximum deflection at the wall top. A 45ft deep

inclinometer was installed 5.5ft behind the wall to monitor the global behavior of wall and surrounding soil.

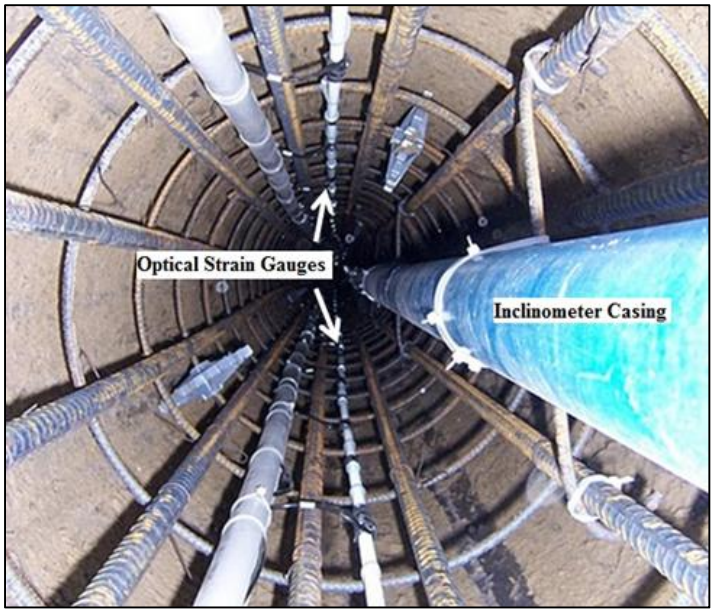


Figure 3.19: Cross section of instrumented shafts

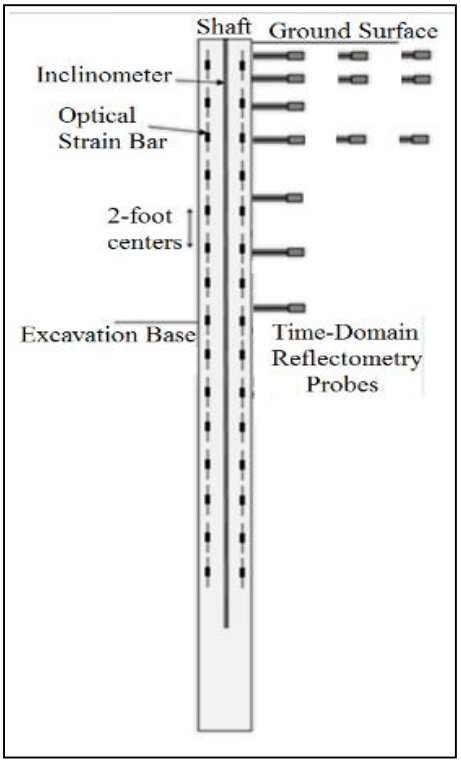


Figure 3.20: Elevation section of instrumented shafts

### 3.5.1 Data interpretation

Inclinometers data was used to compute the deflection profile, and double integrated to estimate the bending moment profile (Koutrouvelis 2012 and Brown 2013). Strain gauges at the tension and compression sides of the same depth were used to calculate the bending moment at this depth and a bending moment profile was interpolated. Wall deflection was monitored for almost four consecutive years during which the state of Texas experienced extreme drought conditions.

Figure 3.21 shows the mathematical relationship between walls behavior (i.e. deflection) and straining actions (i.e. bending moment, shear force, and applied stresses). Inclinometer measurements (i.e. rotation) are integrated to obtain the wall deflection and

differentiated to obtain the wall bending moment. Strain gauge measurements are double integrated to obtain the wall deflection.

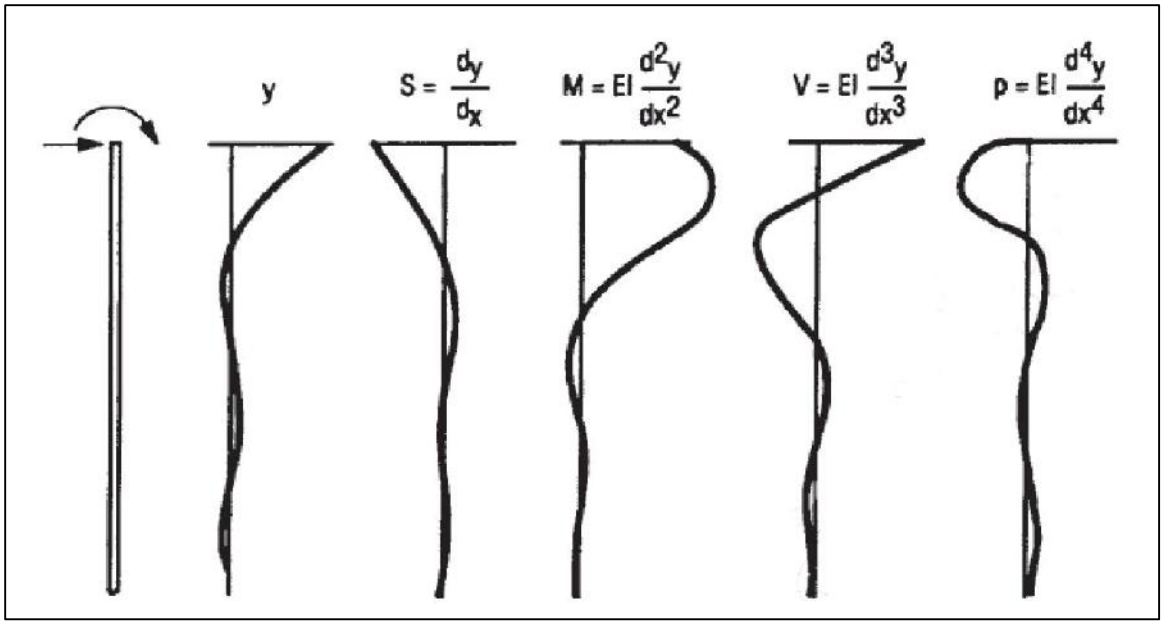


Figure 3.21 Mathematical relationship between deflection (y), slope (S), bending moment (M), shear force (V), and soil reaction force (p) for a laterally loaded pile (after Reese and Van Impe, 2001)

As bending moment developed in the shafts, some pairs of gauges measured strains that are consistent with estimates from inclinometer data; however, the majority of strain gauge measurement could not be directly used to compute bending moments. The strain gauges were affected by a variety of forces beyond pure bending moment during excavation (e.g. tension cracking, residual strains during concrete placement and curing, thermal strains, expansive soil movement, etc.). Figure 3.22 shows measurements from a pair of strain gauges that successfully recorded strains at the tension and the compression

sides; bending moment is calculated from the axial compression and tension strain following Equation 2.2.

$$\text{Bending Moment} = EI \times \frac{\varepsilon_{comp} - \varepsilon_{tension}}{\text{Diameter} - 2\times \text{concrete cover}} \qquad \text{Equation 3.2}$$

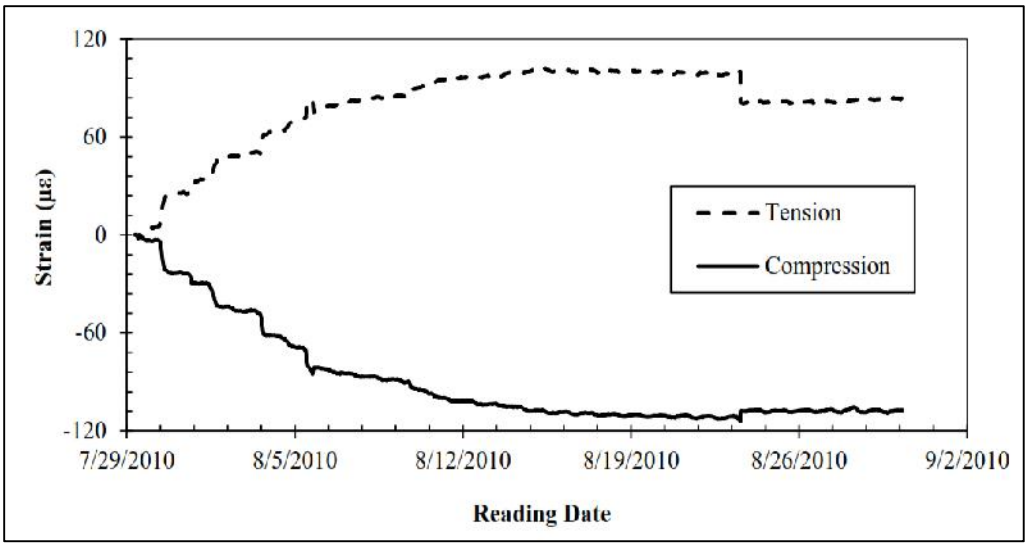


Figure 3.22: Sample of strain gauge measurements

### 3.5.2 Project stages

The main objective of this study is to understand the behavior of high-plasticity clays during the variation in the soil degree of saturation. Figure 3.23 presents the start and end dates of the excavation, wetting, and drying stages of the Reese wall project. First, the site experienced a drying stage according to the natural moisture fluctuation between Oct 1st, 2010 and May 3rd, 2012. Second, the inundation pond was filled for two months until July 2nd, 2012. Third the site experienced the second drying stage according to the natural moisture fluctuation between July 2nd, 2012 and February 1st, 2013. Fourth the inundation pond was filled for four months until June 1st.

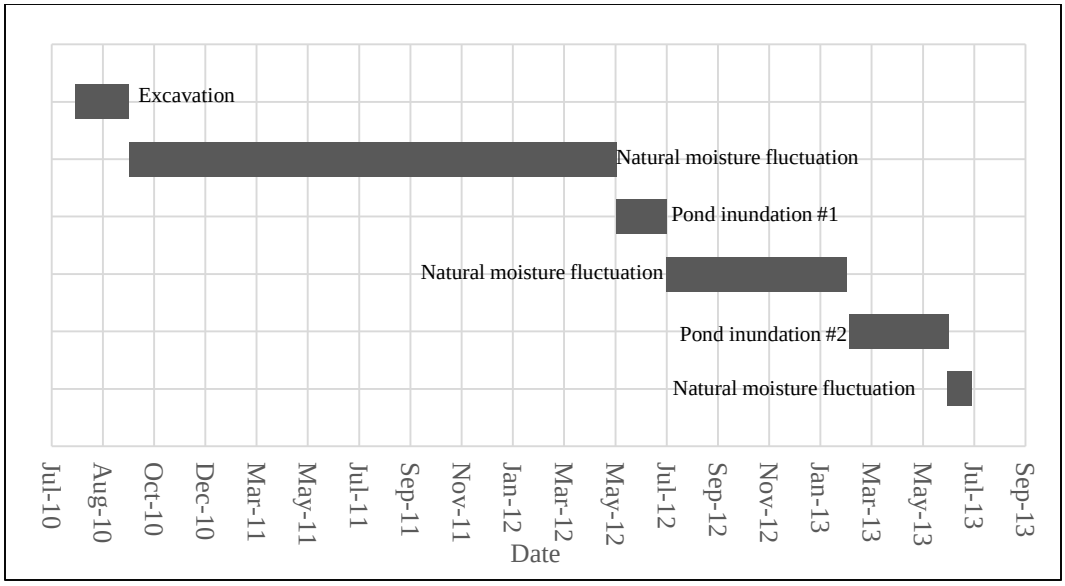


Figure 3.23: Construction activities timeline

Drying condition was imposed by leaving the site to dry due to the natural moisture fluctuation, which luckily was an exceptional drought condition (because that means that the research wall encountered sever conditions). Wetting conditions was imposed by inundating a 20ft by 40ft inundation pond on the retained side of the wall (Figure 3.24). The shoulder lining of the inundation pond consists of 2ft deep compacted clay (Figure 3.25), built to direct the infiltration of the water into the soil and prevent radial loss of water.


Figure 3.24: Inundation pond during wet conditions

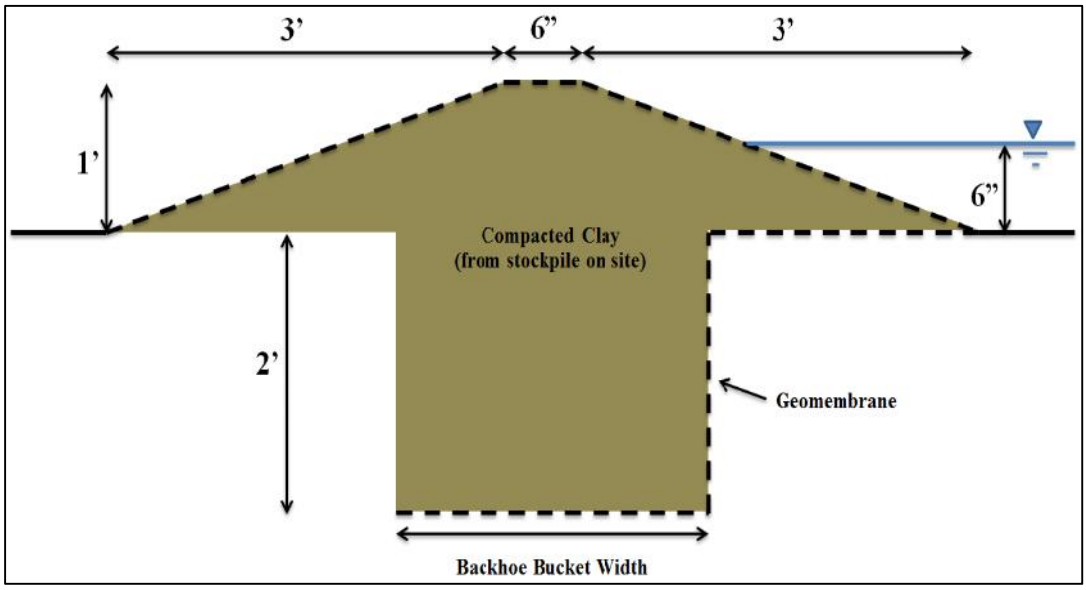


Figure 3.25: Cross section of inundation pond lining (Brown 2013)

The inundation of the soil with an inundation pond could be considered as severe conditions, because of two reasons. First, the pond is inundated for extended periods of

time; second, movement of the inundation water is controlled, i.e., runoff is controlled. Neither of these two conditions are expected in actual insitu conditions; however, these conditions are adopted to subject the wall to severe conditions and better understand the behavior of partially saturated soils.

### 3.5.3 Measured wall response

***Short-term conditions: Deflection***

Excavation works began on July 29th, 2010 and took place over a period of approximately four weeks. First 9ft deep, 5ft wide, trench was excavated on July 31$^{st}$. Then, the side of the trench was graded to approximately 0.5:1 slope on August 23$^{rd}$. Then more soil was excavated to reach a depth of 15ft, while maintaining the side slope at approximately 0.5:1. Then the slope of the side slope was graded to approximately 3:2 slope on October 1st. Finally the excavated side of the wall was furnished with shotcrete facing.

The top of the Reese wall deflected by 0.95inch due to excavation works Figure 3.26 shows the measured deflection profile estimated from the inclinometer data. The profile shows that the wall does not experience a point of fixity (i.e. pivotal point), in other words the entire wall experiences movement toward the excavated side. Soil movements 5.5ft behind the wall also shows that the wall experiences a global movement, that extends deeper than the toe of the wall, rather than a rotational movement around a point of fixity (Figure 3.27).

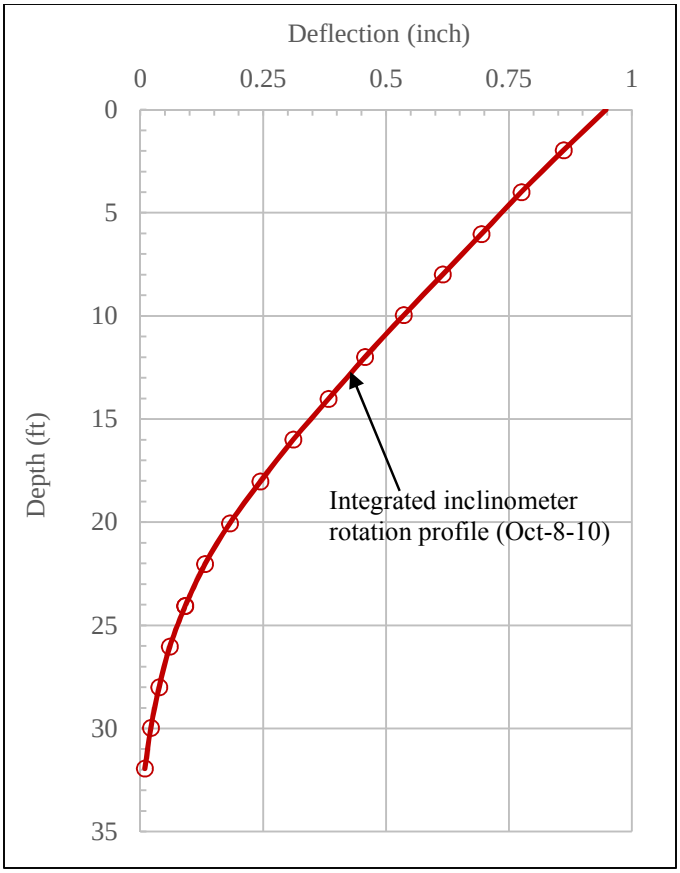


Figure 3.26: Wall deflection profile (inclinometer measurements) (Brown 2013)

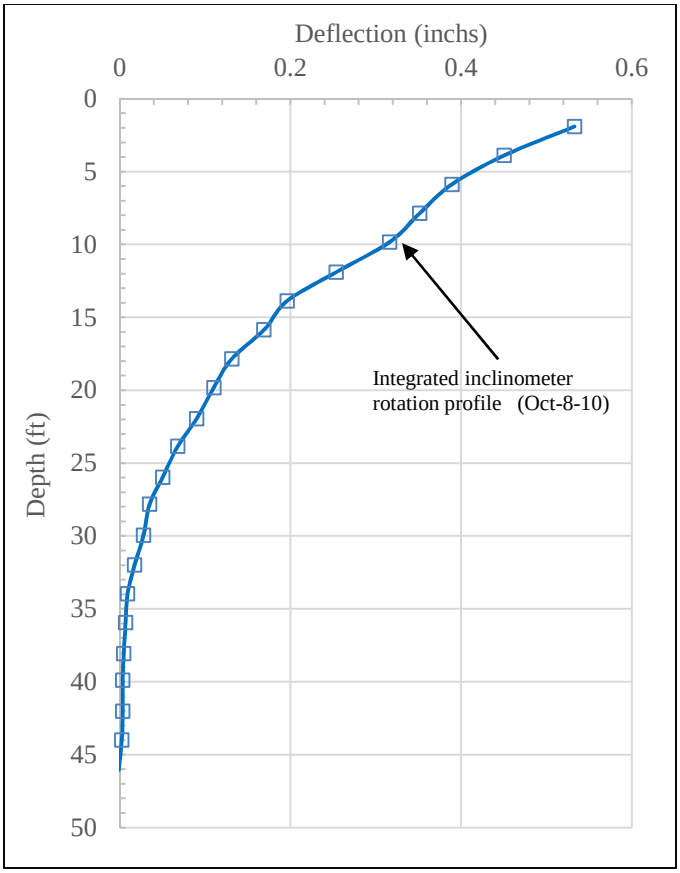


Figure 3.27: Deflection profile 5.5ft behind wall (inclinometer measurements) (Brown 2013)

Figure 3.28 shows a comparison between the maximum deflections of the east, central, and west shafts development with time. During excavation, the wall responded immediately to the relief of stress with roughly 0.4inchs, as the slopes were introduced the maximum deflection continued to increase reaching 0.8inch, and the final leveling of slopes to 2:1 gradient resulted in maximum deflection of 0.95inch. Comparison between the maximum deflection measurements of the East and West shafts shows some difference between the shafts. This observation suggests that the wall does not resemble perfect plane strain conditions.

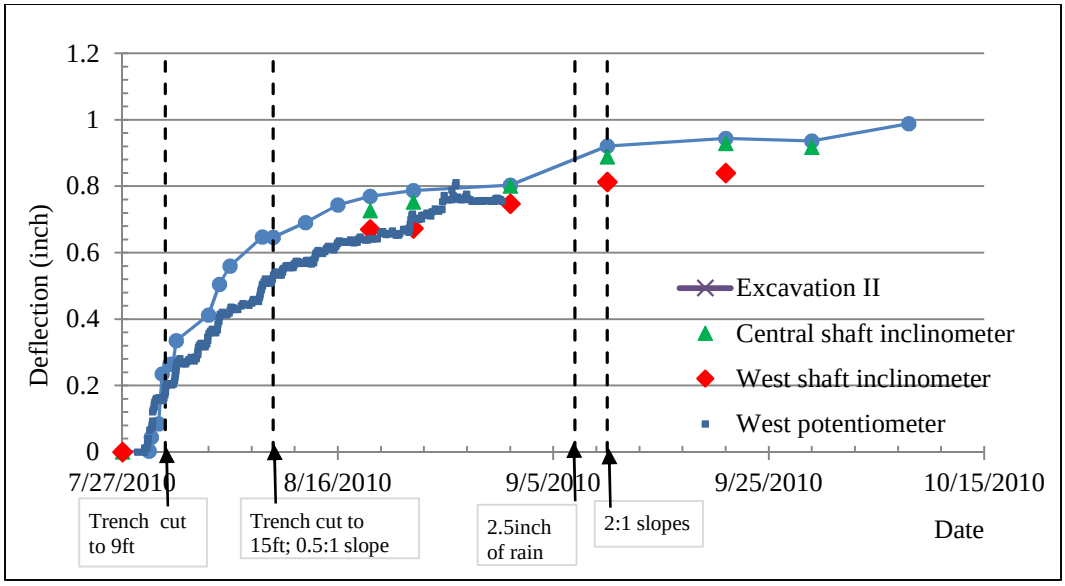


Figure 3.28: Maximum wall deflection propagation with excavation stages (Brown 2013)

***Short-term conditions: Bending moment***

Figure 3.29 presents the bending curvature profile obtained from strain gauge measurements and inclinometer measurements. Comparison between strain gauge and inclinometer measurements show that the reliability of the strain gauge measurements is questionable because of the difficulty in interpreting a uniform bending curvature profile from the strain gauge measurements. Zero Curvature is observed at the top 10ft of the wall (i.e. 70% of the cantilever height) which suggest that the wall movement is more of a global movement. The maximum bending curvature is observed 5ft below the excavation level (i.e. 30% below the excavated height).

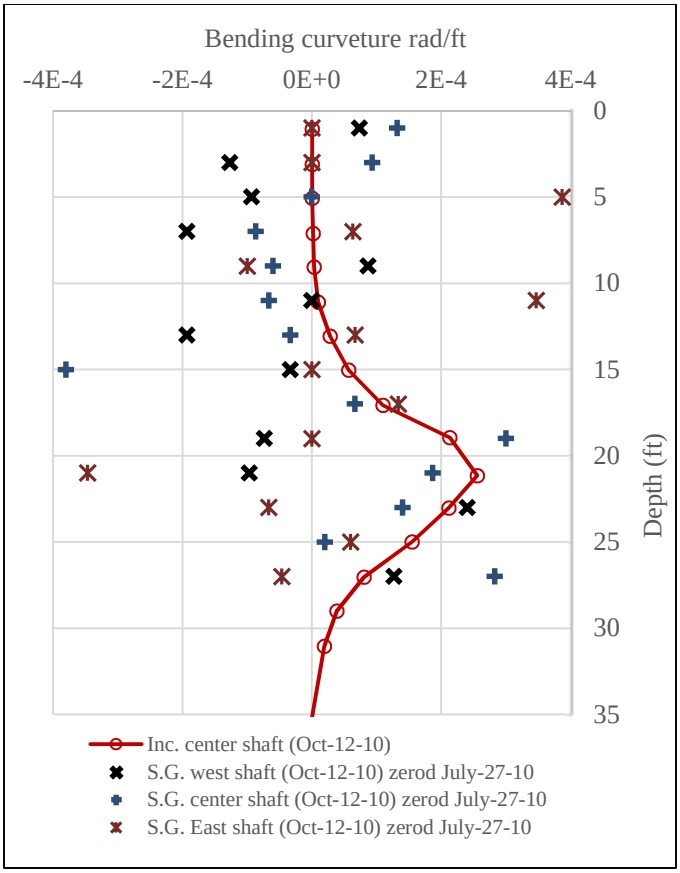


Figure 3.29: Measured bending curvature profile of the wall

Figure 3.30 and Figure 3.31 present the estimated bending moment profiles assuming uncracked and cracked bending stiffness values, respectively. The maximum bending moment assuming uncracked stiffness is 80,000 lb.ft; while, the maximum bending moment assuming cracked stiffness is 36,000 lb.ft.

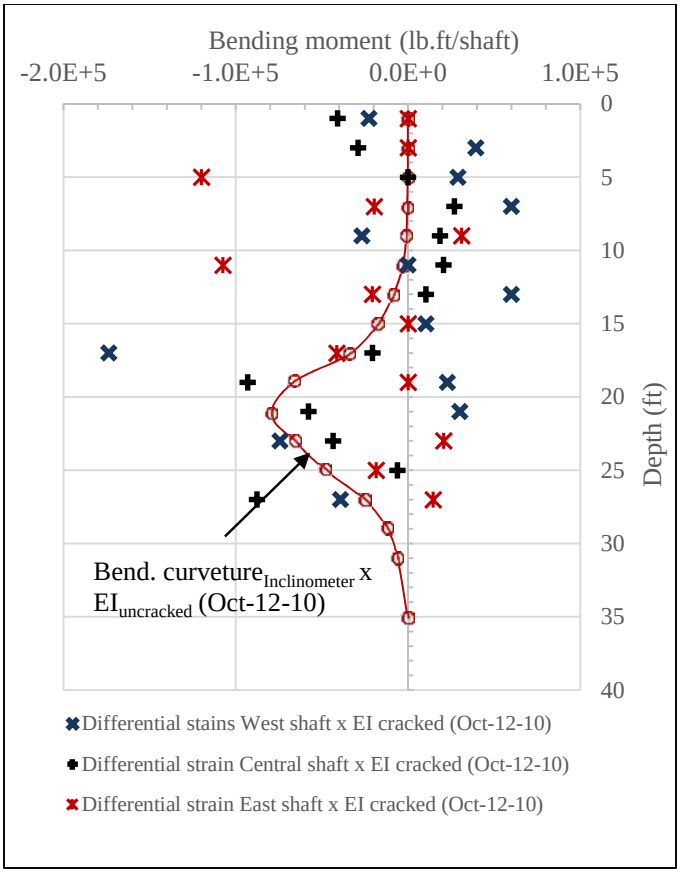


Figure 3.30: Calculated bending moment profile assuming uncracked bending stiffness

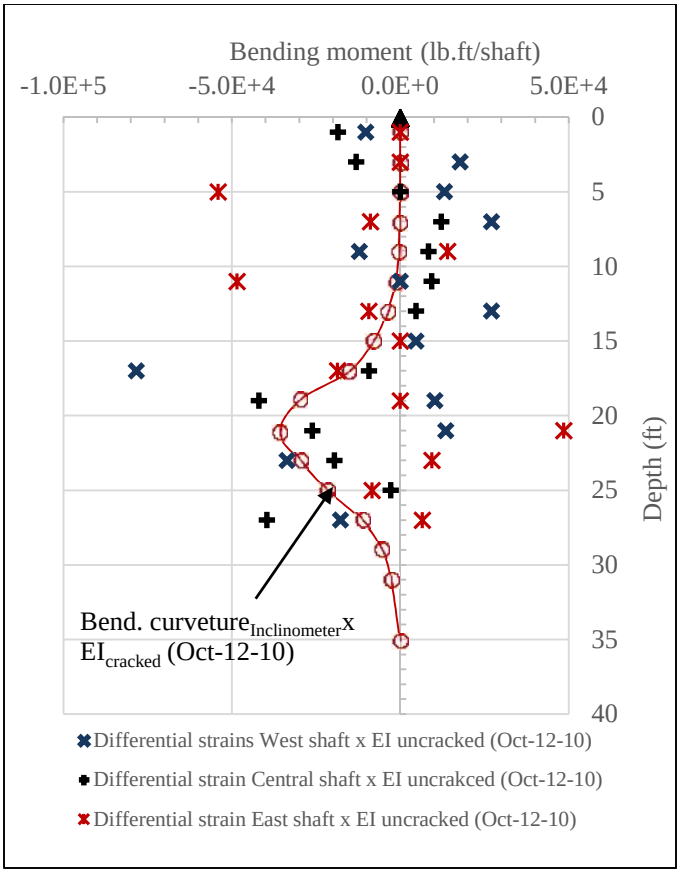


Figure 3.31: Calculated bending moment profile assuming cracked bending stiffness

***Long-term conditions: Deflection***

Figure 3.32 presents the measured deflection profiles after: excavation, wetting, and drying stages. The immediate deflection of the Reese wall measured at the end of excavation works (October 8$^{th}$, 2010) is 0.95inch. During the natural moisture fluctuation cycle following the excavation works, the Reese wall retracted toward the retained side, the minimum deflection measured during the first natural moisture fluctuation (November 16$^{th}$, 2011) is 0.6inch. Backward movement of the Reese wall does not mean that the soil pulls the wall backward, it means that the self-retained on the active side deepened, and a thicker layer does not rely on the wall for support. Following the natural moisture

fluctuation, the inundation pond was filled. The maximum wall deflection measured at the end of the first inundation cycle (July 2nd, 2012) is 3.7inches. The wall deflection measured at the end of the second natural moisture fluctuation cycle (February 4th, 2013) is 4inches; unlike the first natural moisture fluctuation cycle, the Reese wall did not experience backward movement during the second natural moisture fluctuation cycle. The maximum wall deflection measured at the end of the second inundation period (July 3rd, 2013) is 4.7inches. Figure 3.33 presents the time trail of the maximum wall deflection.

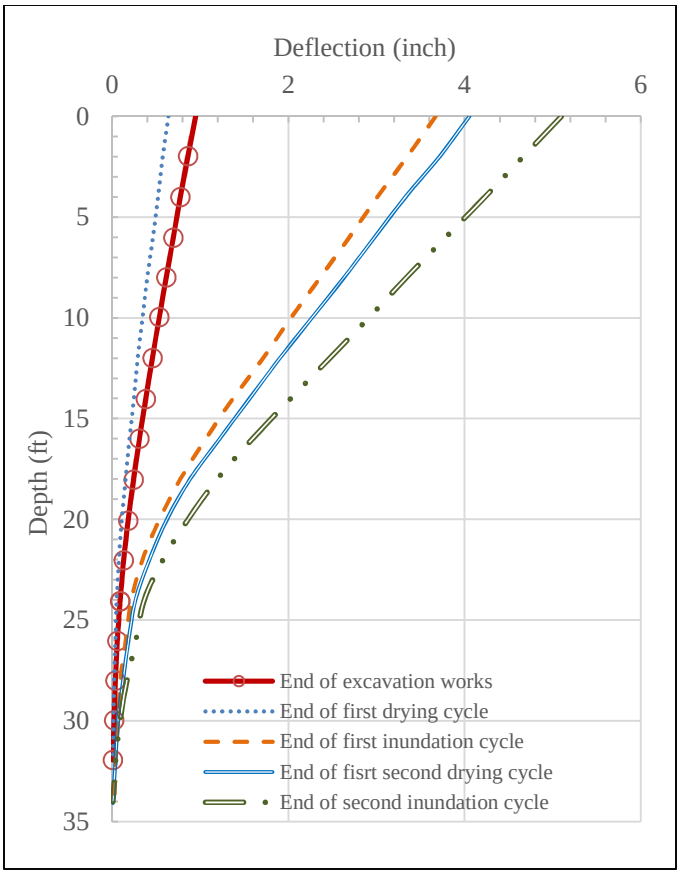


Figure 3.32: Measured wall deflection profile during (i) Natural fluctuation period 1 (ii) Inundation period 1 (iii) natural fluctuation period 2 (iv) Inundation period 2

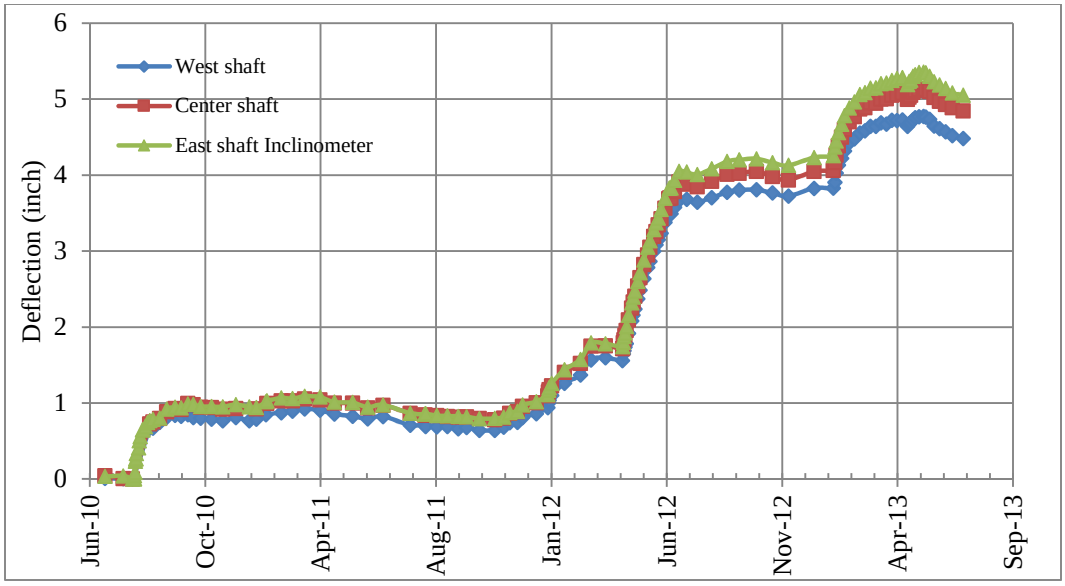


Figure 3.33: Maximum wall deflection propagation during cycles of wetting and drying (Brown 2013)

***Long-term conditions: Bending moment***

Figure 3.34 presents the measured bending moment profiles after: excavation, wetting, and drying stages. The immediate bending moment of the Reese wall measured at the end of excavation works (October 8th, 2010) is 32,000lb.ft/shaft. The bending moment decreased slightly during the natural moisture fluctuation cycle, the bending moment measured during driest conditions of the first natural moisture content (November 16th, 2011) is 25,000lb.ft/shaft. The maximum bending moment measured at the end of the first inundation cycle (July 2nd, 2012) is 160,000lb.ft/shaft. The bending moment measured at the end of the second natural moisture fluctuation cycle (February 4th, 2013) is 170,000lb.ft/shaft. The maximum bending moment measured at the end of the second inundation period (July 3rd, 2013) is 210,000lb.ft/shaft. The bending moment at the top 10ft of the soil is negligible throughout all the stages. The maximum bending moment is 21ft deep, i.e., 6ft deeper than the excavation bed.

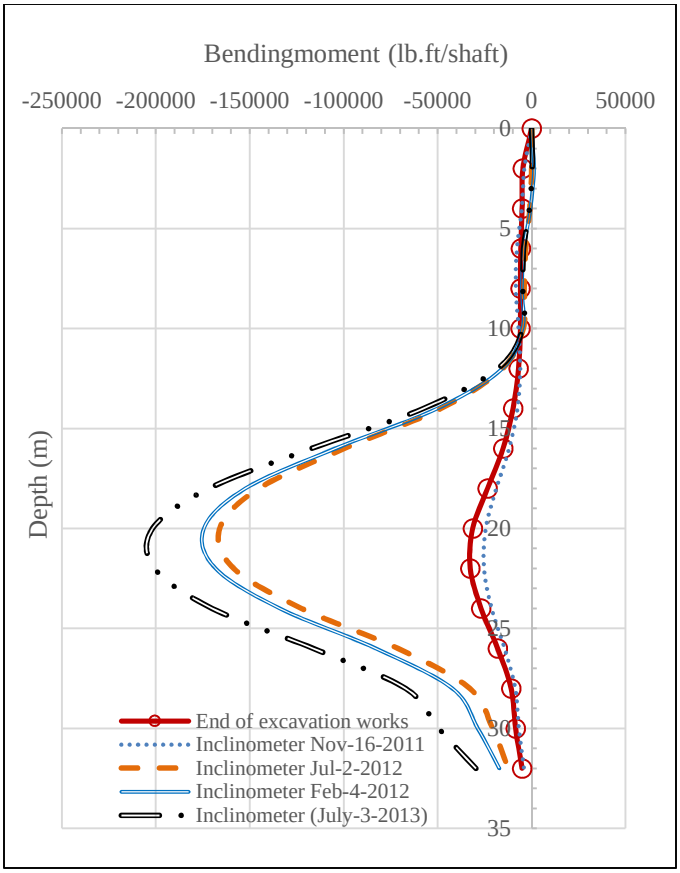


Figure 3.34: Measured wall bending moment profile during: (a) First drying cycle (b) First inundation cycle (c) Second drying cycle (d) Second inundation cycle (Brown 2013)

This chapter presented a unique set of data of a drilled shaft retaining wall constructed in expansive soil stratigraphy. The chapter presented site investigation plan, the wall properties and the deflection and bending moment profiles during cycles of wetting and drying. Chapter 4 presents predictions of the Reese wall deflections and bending moment. The predicted behavior is then compared the measured behavior, and the accuracy of analytical predictions are discussed.

# CHAPTER 4: THE REESE WALL: ANALYTICAL PREDICTIONS

The objective of this chapter is to evaluate the accuracy of an analytical method used to predict the deflection and bending moments. The deflection and bending moment profiles are predicted using the analytical method; then, the predicted profiles are compared to the actual field measurements; the comparison is done for short-term and long-term conditions.

## 4.1 SHORT-TERM BEHAVIOR

Previous studies estimated walls deflection during short-term conditions using various methods. Mana and Clough (1981) predicted upper and lower bounds for the wall deflection as a function of the factor of safety against basal heave from case history measurements. Clough et al. (1989) correlated the expected wall movement as a function of the factor of safety against basal heave and system stiffness from case history data of propped walls. Methods that rely on correlating the wall movement to factor of safety against basal heave could be misleading; because, walls constructed in soil with very high shear strength are not generally close to failure condition.

Osman and Bolton presented the Mobilized Strength Design (MSD) method to predict the maximum wall deflection for cantilever walls. The MSD method correlates the mobilized shear/ultimate shear strength ratio to the retained height/depth of fixity ratio. Beam-spring analysis, i.e. P-y relationship of soil springs, is a more descriptive analytical method that predicts the deflection profiles rather than the maximum deflection value only. However, predicting the behavior of retaining walls using P-y analyses overlooks the global movement of walls and the surrounding soil, this phenomenon could only be captured using Finite Element analyses. The following sections presents analytical

predictions of the Reese wall behavior using MSD method and back calculated P-y curves for the Reese wall.

### 4.1.1 Mobilized Strength Design method

The MSD method assumes that the wall is rotating about some point near its toe, and an idealized stress profile is assumed in terms of two unknowns, namely, the mobilized shear stress ($c_{mob}$) and the distance between the point of fixity and the wall toe (r) (Figure 4.1). Equilibrium of lateral forces and equilibrium of moments are solved for the two unknowns. Osman and Bolton (2004) solved the two equations in two unknowns for different cases of excavation height ratios and obtained two design charts; namely, the relationship between the mobilized shear strength/(unit weight x wall length) ($c_{mob}/\gamma D$) and excavation height ratio (h/D) (Figure 4.2); and, the relationship between the depth of the point of fixity/wall length (r/D) and the wall excavation height ratio (H/D) (Figure 4.3). Such that D is defined as the total wall length.

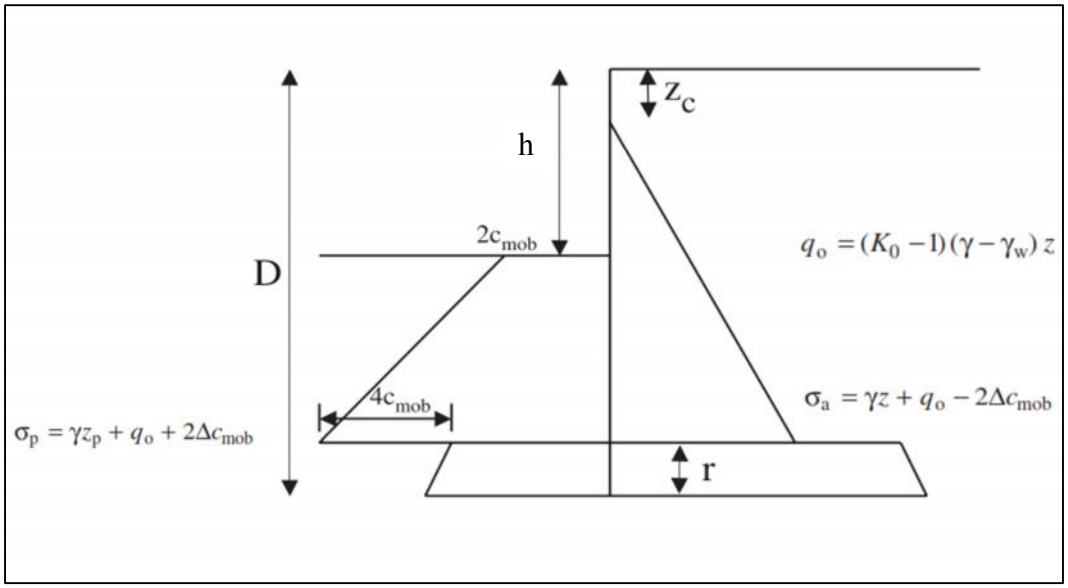


Figure 4.1: Lateral earth pressures distribution during short-term conditions

***Deflection***

The excavation height ratio of the Reese wall at the mid-span is the ratio between the cantilever height (15ft) and the total wall length (35ft), i.e., the excavation height ratio equals 3/7. The $c_{mob}/\gamma D$ ratio of the Reese wall during short conditions ranges from 0.12 and 0.14 for $k_0$ values of 1 and 2 (Figure 4.2). The mobilized shear strain is then estimated according to a normalized-stress strain relationship (Figure 4.4). The average of the ultimate shear strength of the soil profile is 2275 psf; therefore, according to Figure 4.4 the mobilized shear strain during short-term conditions for $k_0$ values of 1 and 2 are 0.0035 and 0.0048, respectively.

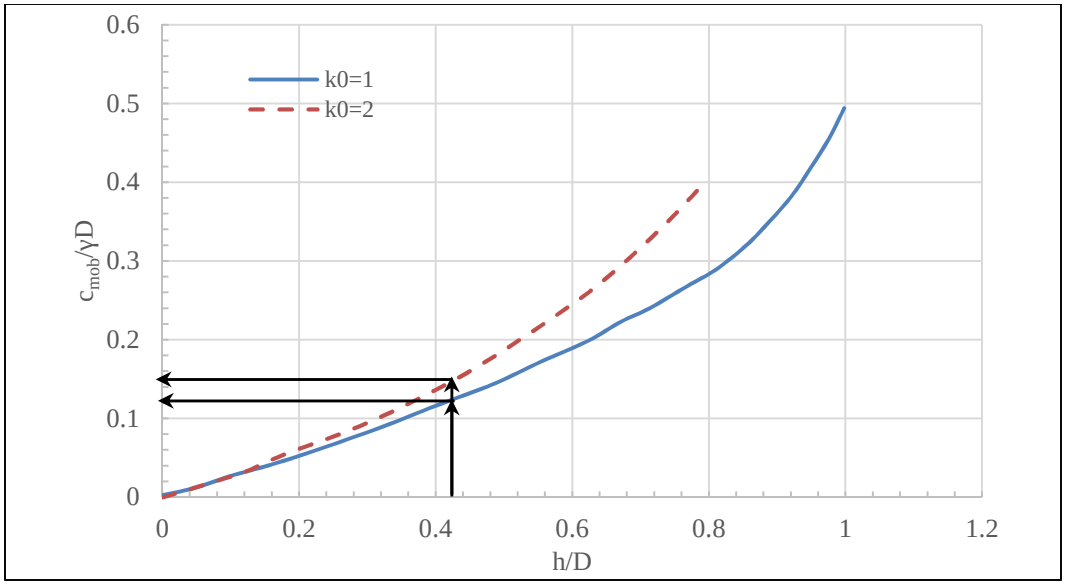


Figure 4.2: Normalized mobilized shear strength as a function of excavation height ratio (Osman and Bolton 2004)

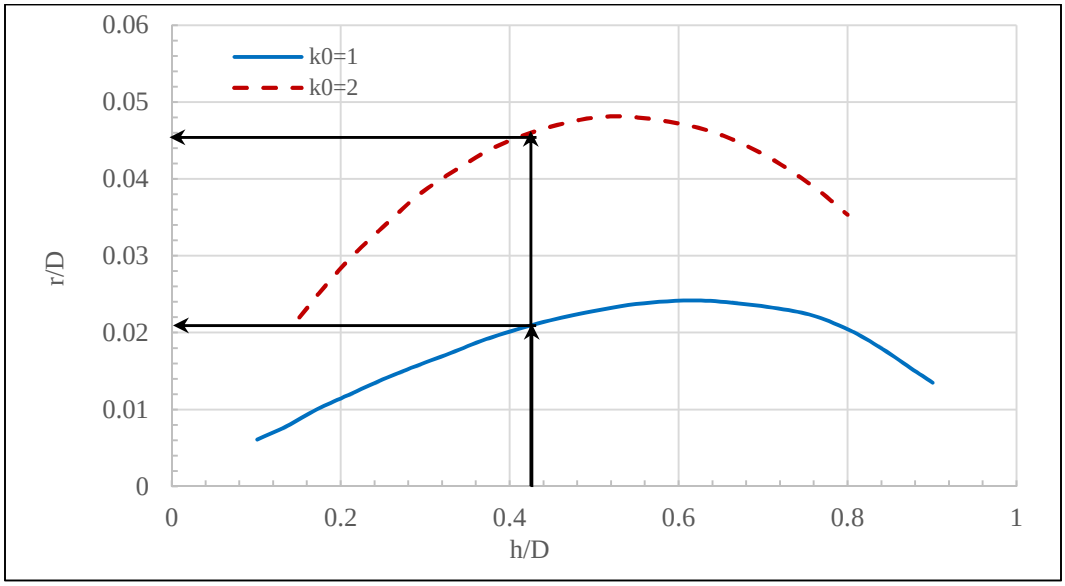


Figure 4.3: Depth of the point of fixity as a function of excavation height ratio (Osman and Bolton 2004)

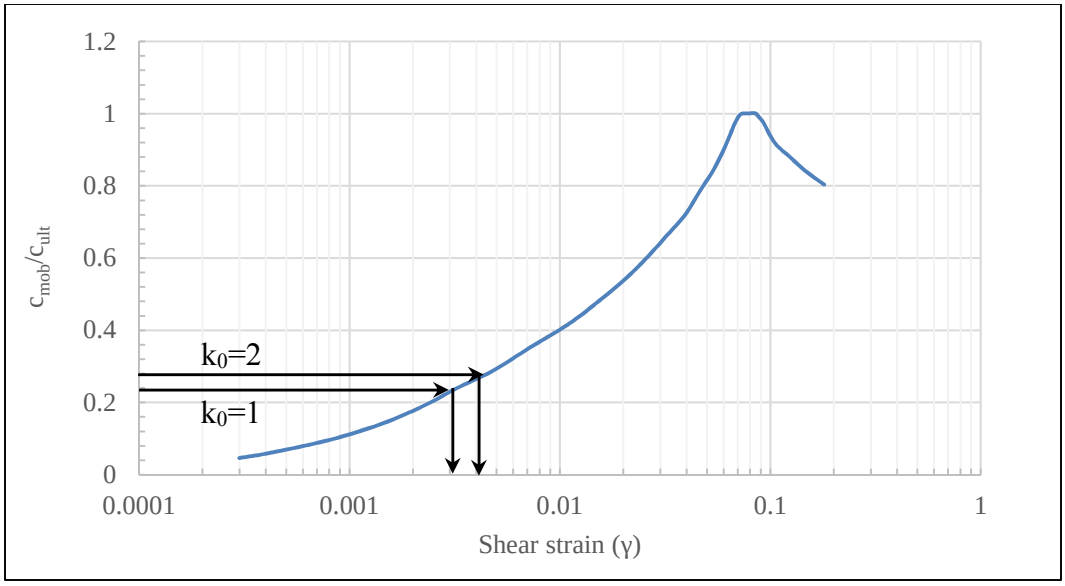


Figure 4.4: Mobilized shear strength as a function of shear strain for London Clay (Jardine et al. 1984)

Osman and Bolton (2004) simplified the kinematics of the undrained behavior as distortion of a triangular wedge (Figure 4.5), where δθ is the incremental angle of rotation. The distortion of the triangular wedge is described by limiting the volumetric strain to zero, according to Equation 4.1

$$\delta\varepsilon_{vol} = \delta\varepsilon_h + \delta\varepsilon_v = 0 \qquad \text{Equation 4.1}$$

Where the $\delta\varepsilon_{vol}$ is the incremental volumetric strain, and $\delta\varepsilon_h$ and $\delta\varepsilon_v$ are the incremental horizontal and vertical strains. The horizontal strain is calculated as the ratio of the horizontal deflection to the width of the wedge (Equation 4.2); and the vertical strain is calculated from relationship between vertical and horizontal strains (Equation 4.1). The incremental shear strain is calculated according to Equation 4.3. The Reese wall maximum deflection during short-term conditions is 0.95 inches; the predicted wall deflection using the MSD method is 0.7 and 1 inches assuming $k_0$ values of 1 and 2, respectively. Interpolating the deflection assuming $k_0$ of 1 and 2 to match the measured deflection of the

Reese wall, a $k_0$ of 1.65 is evaluated as a reasonable lateral earth pressure coefficient of the Reese wall.

$$\delta\varepsilon_h = -\frac{H-r \times \delta\theta}{H-r} = -\delta\theta \qquad \text{Equation 4.2}$$

$$\delta\varepsilon_s = \delta\varepsilon_v + \delta\varepsilon_h \qquad \text{Equation 4.3}$$

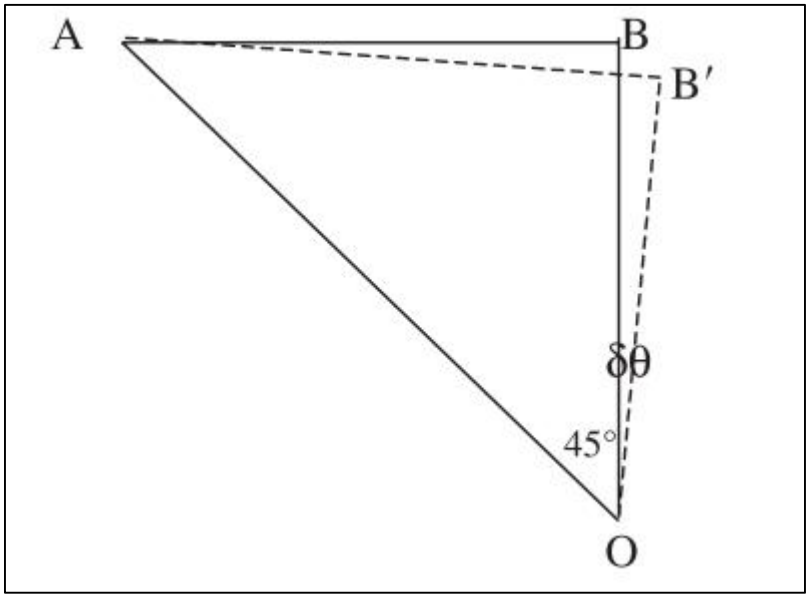


Figure 4.5: Kinematics for undrained conditions

Figure 4.6 shows the UU test results, the average profile of the undrained shear strength, and the shear strength profiles according to the upper and lower bounds of the shear strength measurements. The upper and lower bounds are approximately +/- 40% of the average shear strength profile.

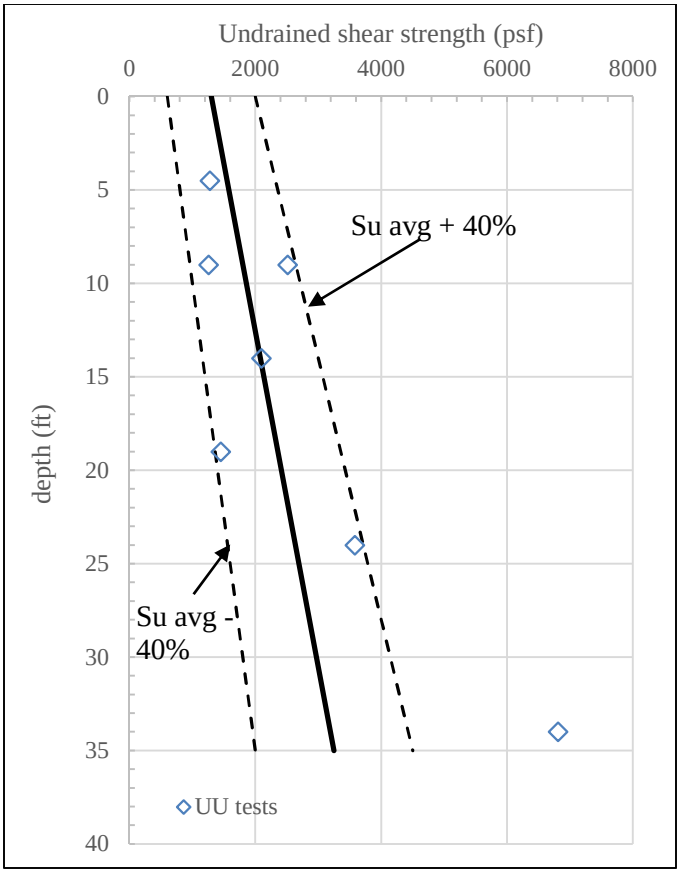


Figure 4.6: Undrained shear strength profiles adopted in the MSD method

Figure 4.7 and Figure 4.8 present the maximum deflections and bending moments predicted using the MSD method assuming different shear strength profiles and $k_0$ values of 1 and 2, respectively. The deflection is predicted for different excavation height ratios (h/D). Results show that the predicted deflection using the MSD method is sensitive to the ultimate shear strength input value. Deflection predictions assuming the average and the lower-bound shear strength profiles are not very sensitive to the excavation height ratio; however, deflection predictions assuming the upper-bound shear strength profile are more sensitive to the excavation height ratio. Adopting the lower bound profile and the average profile estimated maximum deflections that are close to the Reese wall measurements;

however, adopting the upper bound shear strength profile overestimated the maximum deflections of the Reese wall conditions.

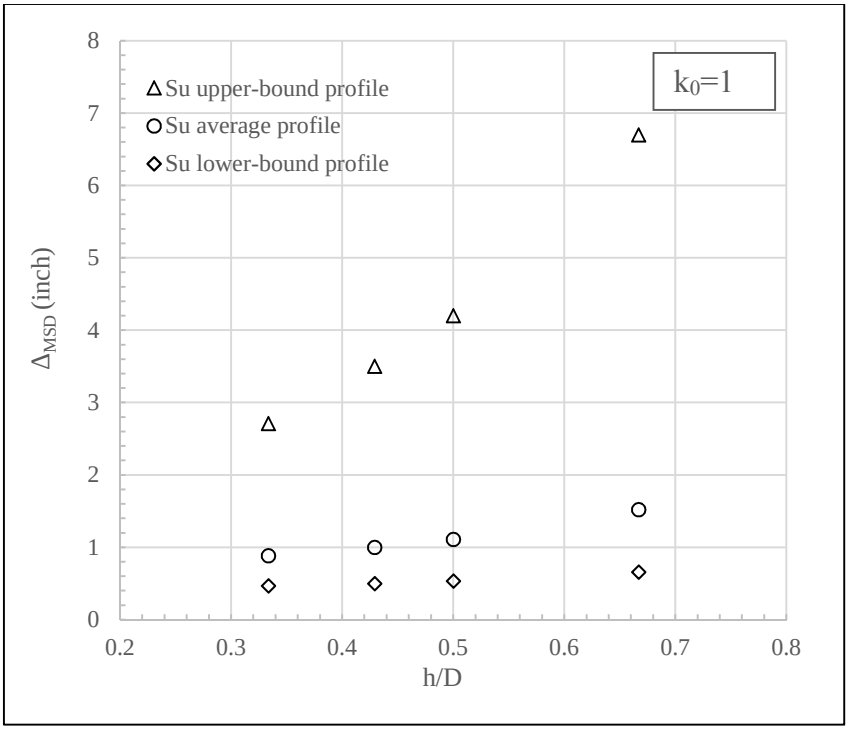


Figure 4.7: Sensitivity of the MSD maximum deflection prediction to shear strength input value ($k_0$=1)

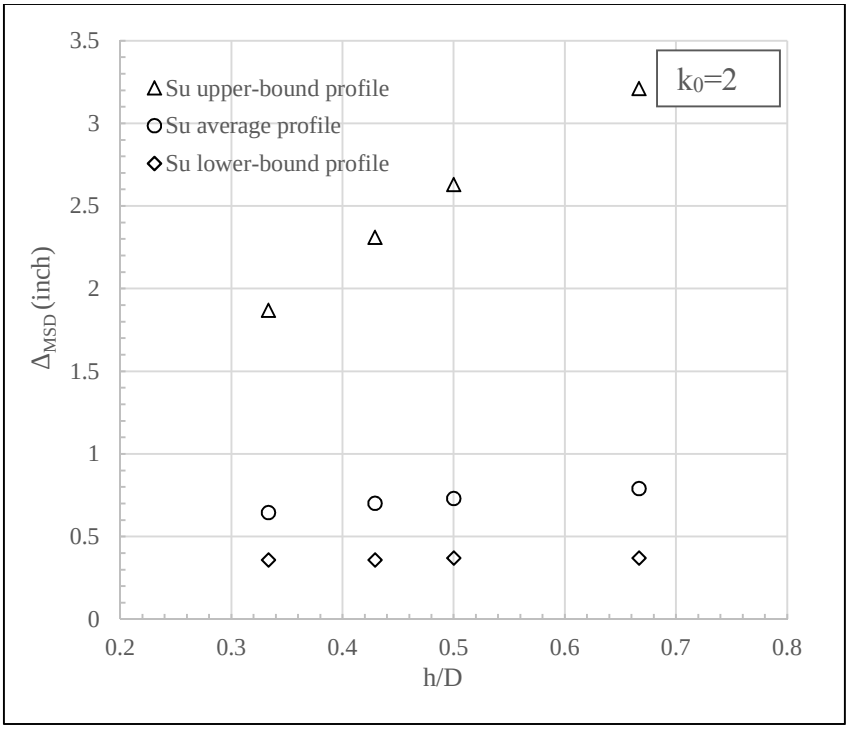


Figure 4.8: Sensitivity of the MSD maximum deflection prediction to shear strength input value ($k_0$=2)

***Bending moment***

Figure 4.9 presents a comparison between the measured bending moment profile and the bending moment profile predicted using the MSD method. The predicted bending moment profile is estimated according to the stress distribution presented in Figure 4.1. The MSD method overestimated the maximum bending moment of the Reese wall by a roughly a factor of 2. Adding to that, the MSD method estimated that the location of the maximum bending moment is about 30ft deep; while the maximum bending moment of the Reese wall is 20ft deep. Errors in estimating the location and magnitude of the maximum bending moment is because the MSD method describes the behavior of the Reese wall as rotational movement around the point of fixity; while the actual movement of the Reese wall is more of a global movement as discussed earlier in section 3.5.

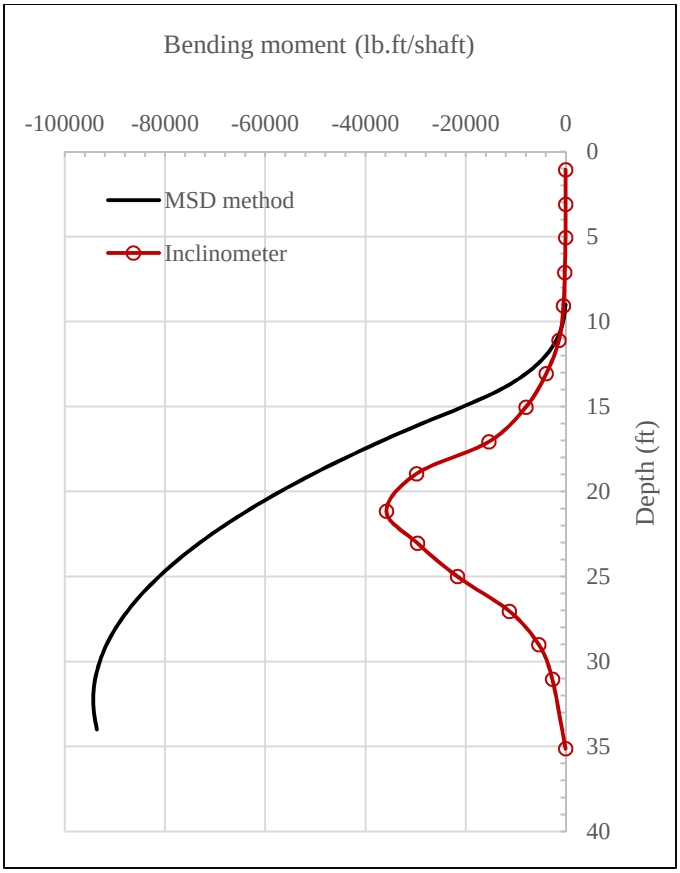


Figure 4.9: Comparison between measured bending moment profile and predicted bending moment profile

### 4.1.2 P-y curves analyses

The lateral earth pressure profile is defined as the fourth derivative of the deflection with depth (Figure 3.37). Brown (2013) back-calculated the P-y curves for the Reese wall during short-term conditions. The curves are developed by calculating the lateral earth pressure during different excavation stages of excavation and plotting these values against the corresponding measured deflections. Brown (2013) compared the-back calculated P-y curves to P-y curves that practitioners use to describe the behavior of soil during undrained conditions. Equations describing different P-y relationship are discussed in details in the

L-pile software Technical Manual. The P-y curves proposed for soil behavior during short-term conditions are:

1- Stiff Clay without free water (Reese and Welch 1972)
2- Stiff Clay with free water (Reese et al. 1975)
3- Drained P-y curves for cohesionless soil (fully softened friction angle) (Reese 1974)
4- Drained P-y curves for cohesionless soil (peak friction angle) (Reese 1974)

Figure 4.10 and Figure 4.11 present the relationship between the soil resistance and the horizontal deflection of the Reese at 16ft and 22ft depths, respectively. The Figures compare the proposed P-y curves to the back-calculated P-y curve obtained from field measurements. Brown concluded that the drained P-y curves for cohesionless soil which assumes a fully softened friction angle provides a reasonable approximation of the wall soil response.

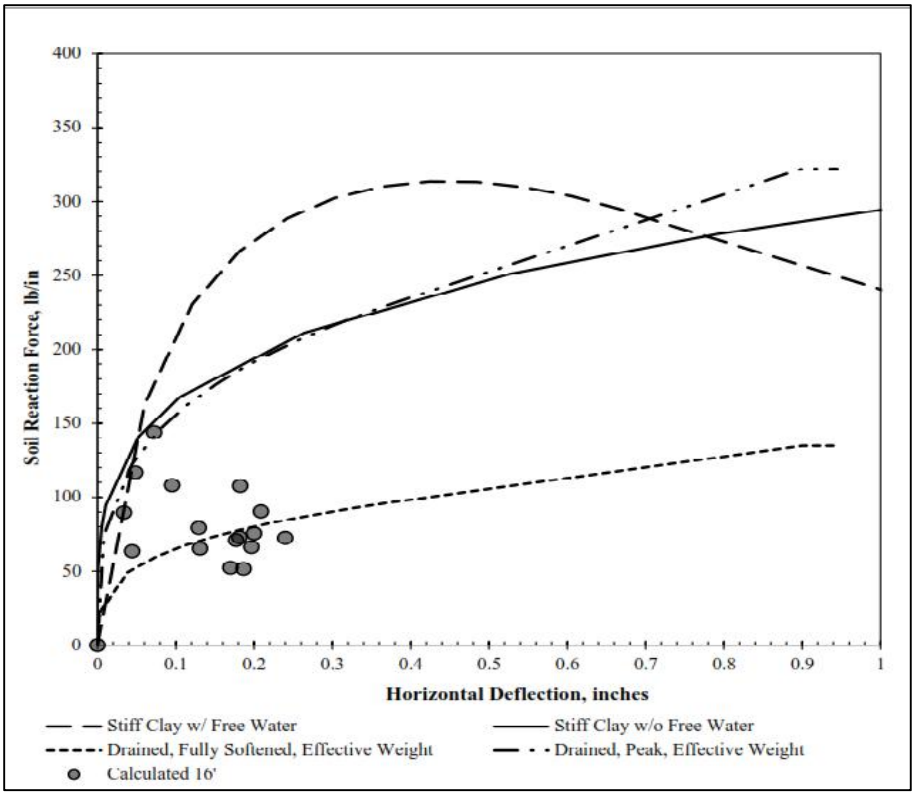


Figure 4.10: Comparison of back-calculated p-y curves during excavation with proposed P-y curves at a depth of 16ft below ground surface (Brown 2013)

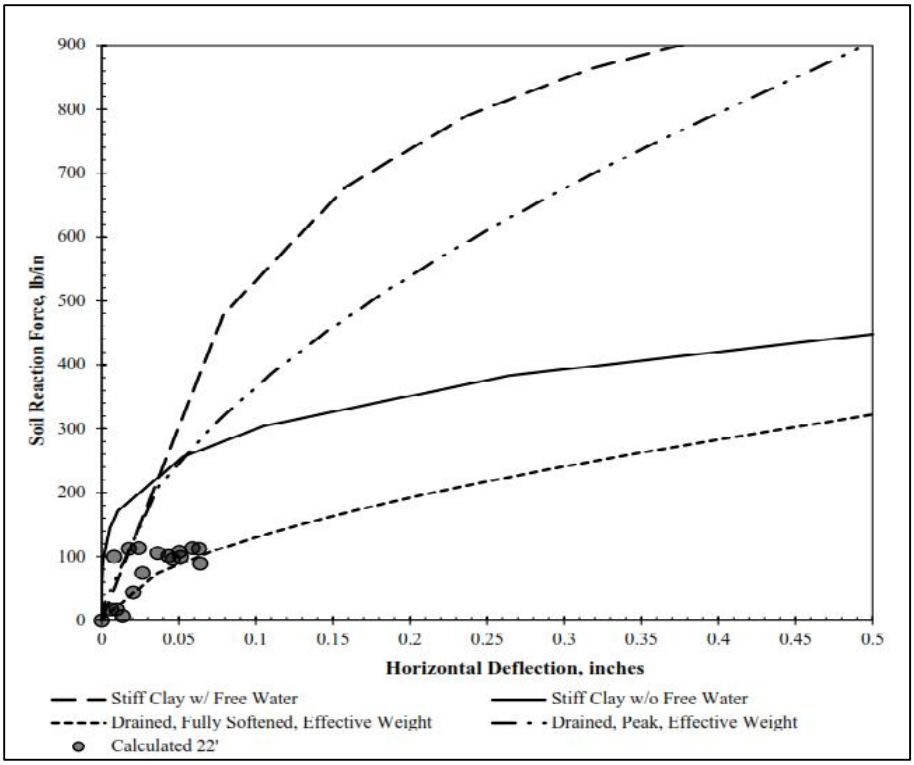


Figure 4.11: Comparison between back-calculated p-y curves during excavation and proposed P-y curves at a depth of 22ft below ground surface (Brown 2013)

The fully softened friction angle of clay (introduced in Figure 2.7) is estimated by measuring the drained shear strength of remolded clay. The clay is remolded at a water content equal to liquid limit of the soil minus ten percent, i.e., $w_{c\ (remolding)} = LL-10\%$. Figure 4.12 presents the drained shear strength measurements of the Taylor clay; results shows that the average fully softened friction angle of the soil is approximately 24°. The secant fully softened friction angle ranges between 21° and 26°.

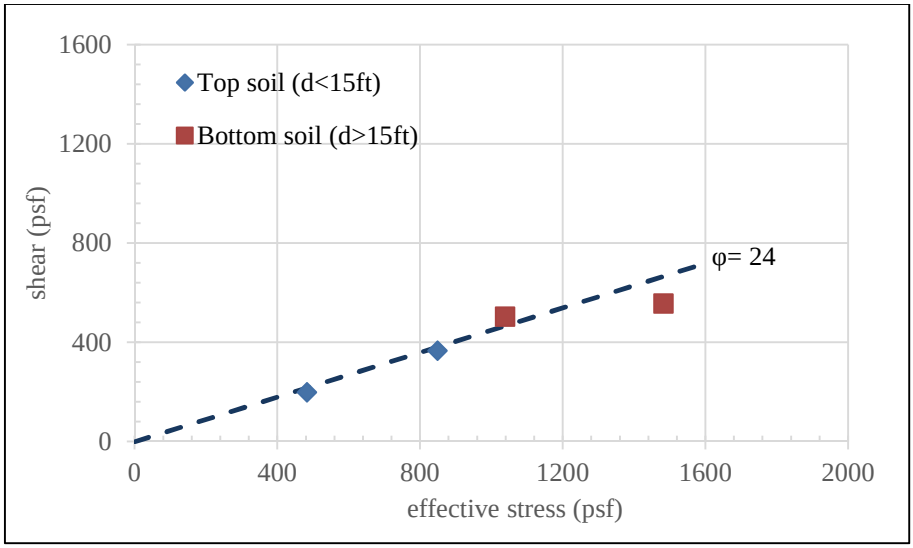


Figure 4.12: Fully softened shear friction angle measurements

Stark and Eid (1997) correlated a relationship between the secant fully softened friction angle, the Liquid limit, and the effective normal stress. Fully softened friction angle measurements are compared to Stark and Eid (1997)'s correlation in Figure 4.13. The secant fully softened friction angle estimated from Stark and Eid (1997)'s correlation is consistent with the fully softened shear strength measurements, such that the correlated friction angle ranges from 21° to 26°.

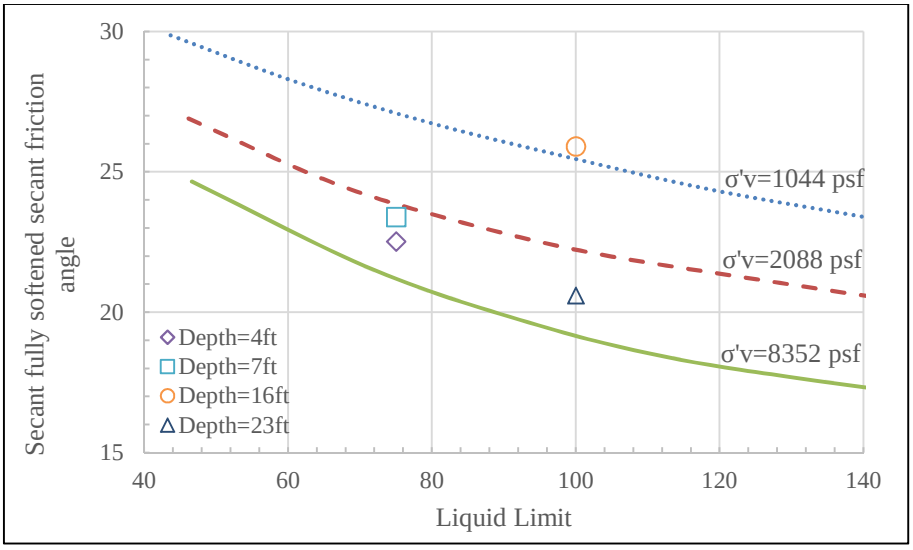


Figure 4.13: Correlation between Liquid Limit, fully softened friction angle and effective normal stress (Stark and Eid 1997)

Section 4.1 presented the MSD analytical prediction of the Reese wall behavior, and presented the back calculated P-y curves of the Reese wall, during short-term conditions. The MSD method assumes that the wall rotates around a point of fixity near the toe (Figure 4.1). Field measurements indicated that the kinematics of the Reese wall during short conditions is more of a global transition of the wall and retained soil towards the excavated side. Therefore, the earth pressure distribution profile adopted in the MSD method does not accurately represent the kinematics of the Reese wall during short-term conditions.

The MSD method assumes a triangular lateral earth pressure on the active side, which results in bending moments in the top 10ft of the wall (Figure 4.9). Field measurements did not indicate bending moments in the top 10ft of the wall. The difference between the measured and the analytically predicted bending moment profiles could be attributed to the fact that the analytical predictions (i.e. MSD method, and P-y analyses)

overlook the global movement of the wall and surrounding soil. This global movement could be predicted using finite element modelling of the problem.

P-y analysis requires knowledge of the retained lateral loads; in other words, the retained active stresses along the retained height of the wall is an input to the analysis. There are no consensus about the lateral earth pressure during short-term conditions because these stresses are function of the wall stiffness, wall geometry, and lateral earth pressure coefficient. Modelling the Reese wall using the Finite Element method bypass the designer from estimating the stresses applied on retaining walls; because stresses are estimated according to the strain compatibility and constitutive model of the wall and soil.

Practitioners account for the sensitivity of the soil stiffness to the mobilized strain by factoring the soil stiffness. Modelling the short-term behavior of walls adopting a constitutive model that automatically relates the stiffness of the soil to the mobilized shear strains would bypass practitioners from manually factoring the soil stiffness according to their own judgment.

## 4.2 LONG-TERM BEHAVIOR

### 4.2.1 Mobilized Strength Design method

Bolton et al (1990) developed MSD for long-term conditions. The MSD method assumes that the water pressure follows hydrostatic pressure, and, the wall is rotating about some point near its toe, and an idealized stress profile is assumed in terms of two unknowns, namely, the mobilized friction angle which defines the active and passive earth pressure coefficients ($k_a$ and $k_p$, respectively) and the distance between the point of fixity and the wall toe (r) (Figure 4.14). Equilibrium of lateral forces and equilibrium of moments are solved for the two unknowns. Bolton et al (1990) solved the two equations in two

unknowns for different cases of wall excavation height ratios and obtained two design charts; namely, the relationship between the mobilized friction angle ($\varphi_{mob}$) and the embedment ratio (d/h) (Figure 4.15); and, the relationship between the rotating depth/wall length ($h+z_p$)/D and the embedment ratio (d/h) (Figure 4.16).

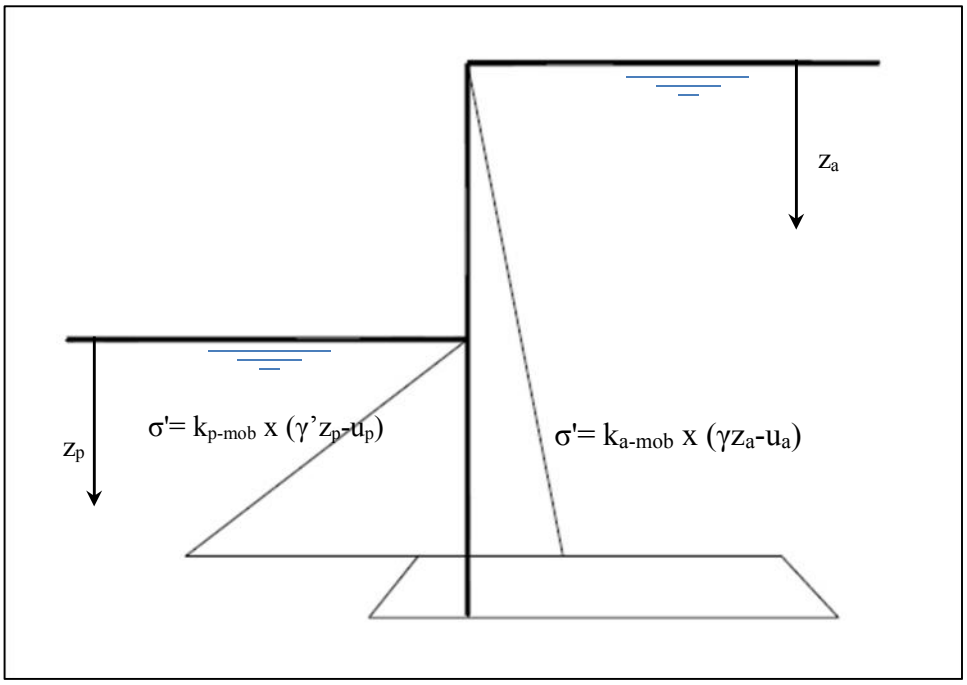


Figure 4.14: Effective stress distribution during long-term conditions (Bolton et al. 1990)

***Deflection***

Figure 4.15 presents the mobilized friction angle versus embedment ratio relationships for 4 cases. The δ'/φ' ratio presents the ratio between the interface coefficient, where δ' is the wall interface friction angle, such that δ'/φ'=0 represents a perfectly smooth wall surface and δ'/φ'=1 represents a rough wall surface. The a/h ratio presents phreatic surface ratio on the retained side, where (a) is the depth of the piezometric line on the

retained side, such that a/h=0 represents a case where the piezometric line on the retained side coincide with the ground surface, while, a/h=1 represents a case where the piezometric line is equal to the excavation depth.

The embedment ratio (d/h) of the Reese wall is 1.33; according to Bolton et al. (1990) if the piezometric line of the Reese wall during inundation stages is assumed to be at the ground surface, i.e., a/h= 0; and, the wall is assumed to be rough, i.e., δ'/φ'=1, the mobilized friction angle of the Reese wall during long term conditions is 32°.

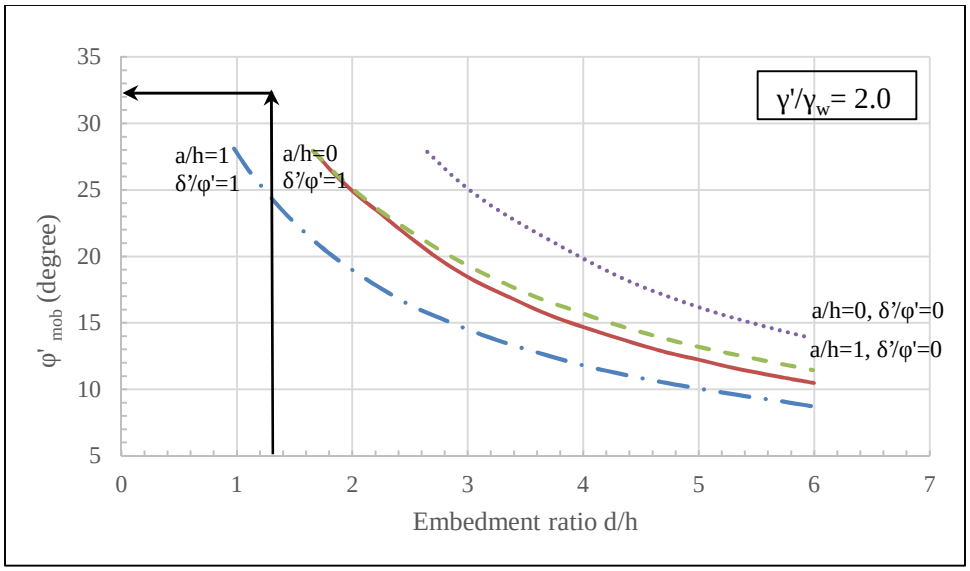


Figure 4.15: Mobilized angle of shear strength as a function of embedment ratio

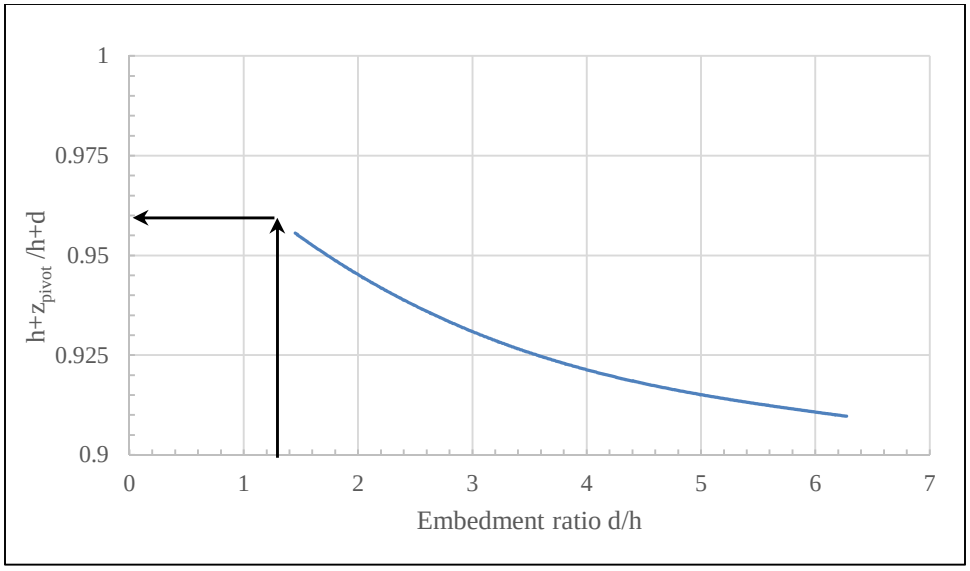


Figure 4.16: Depth of the point of fixity as a function of embedment ratio

According to Figure 4.15 the mobilized friction angle exceeds the ultimate friction angle of London Clay. To facilitate the MSD and estimate a ballpark deflection to evaluate the accuracy of the method, the ultimate friction angle of the London clay is adopted as the mobilized friction angle. Figure 4.17 presents the mobilized friction angle versus shear strain relationship (Jardine et al. 1984); the mobilized friction angle is assumed to be 26°, and the corresponding shear strain is 0.04.

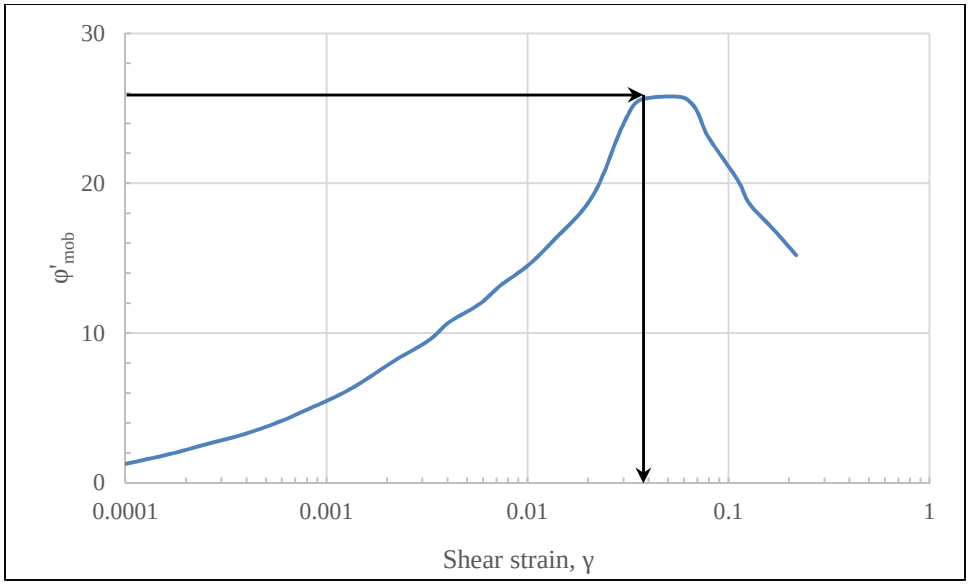


Figure 4.17: Mobilized angle of shearing resistance φmob as a function of shear strain γ for a sample of London clay (Jardine et al. 1984)

The kinematics of walls movement during short-term conditions is based on the fact that the volume of deforming soil is constant. Although the constant volume deformation mechanism is only applicable to short-term conditions, Bolton et al. (1990) extended the same concept to the long-term conditions, and suggested that "reasonable predictions" could be obtained following the same kinematics of the short-term conditions. Thus, the predicted wall movement during long-term conditions following the MSD method is 1.4ft. The maximum measured wall deflection of the Reese wall is 5inches; therefore, the MSD method overestimates the wall deflection during long-term conditions.

***Bending moment***

Figure 4.16 presented the relationship between fixity ratio and the wall embedment depth, estimated by Bolton et al. (1990) for the long-term conditions. The fixity ratio is defined as the depth of the point of fixity measured from the ground level on the active side

($h+z_{pivot}$), to, the total length of the wall (h+d) ratio. The fixity ratio corresponding to the embedment ratio of the Reese wall is 0.96. Deflection profile measured during the long-term conditions of the Reese wall does not indicate a point of fixity at the wall toe.

Figure 4.18 presents a comparison between the measured bending moment profile and the bending moment profile predicted using the MSD method. The predicted bending moment profile is estimated according to the stress distribution presented in Figure 4.14. The MSD method underestimates the maximum bending moment of the Reese wall by a roughly a factor of 2. Adding to that, the MSD method estimates that the location of the maximum bending moment is about 25ft deep; while, the maximum bending moment of the Reese wall is 20ft deep. Errors in estimating the location and magnitude of the maximum bending moment is could be attributed to the assumptions that the MSD method adopts for long-term conditions. The MSD method adopts the assumption that the deformed soil experiences zero volumetric change even during long-term conditions, and considers the wall movement to be a rotational movement around a point of fixity close to the wall toe.

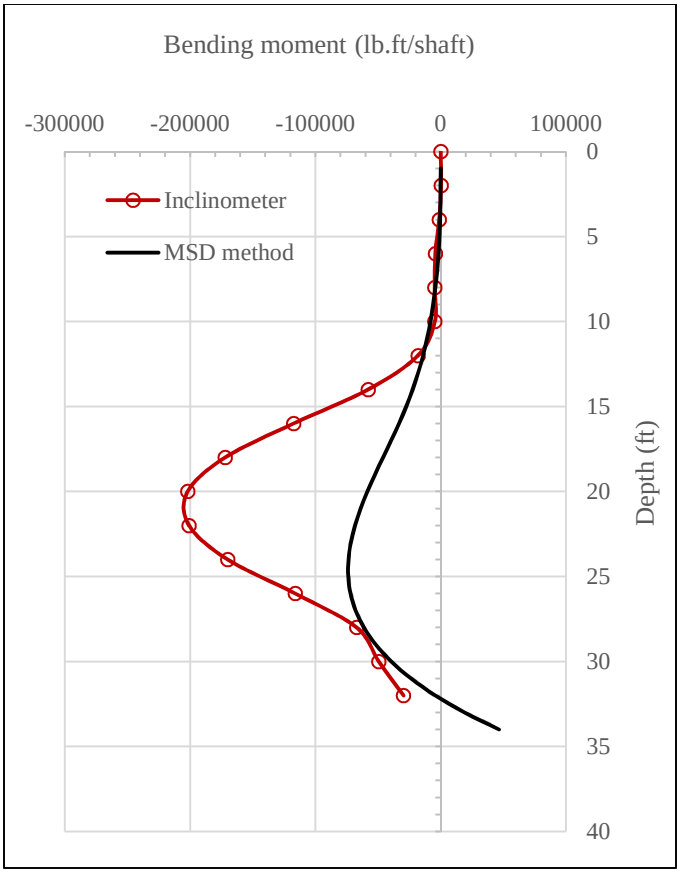


Figure 4:18: Comparison between measured bending moment profile and predicted bending moment profile

### 4.2.2 P-y curves analyses

Brown (2013) back-calculated the P-y curves for the Reese wall during long-term conditions. The curves are developed by back-calculating the lateral earth pressure during the wetting and drying cycles and plotting these values against the corresponding measured deflections. Figure 4.19 presents a comparison between the back-calculated stress profile and stress profiles adopted in practice. The figure shows that the stress profiles adopted in practice overestimates the stress experienced by the Reese wall. The figure also shows that

the stress profile that suggests using the lower envelope of swell and passive pressures is significantly overestimating the stresses on the Reese wall.

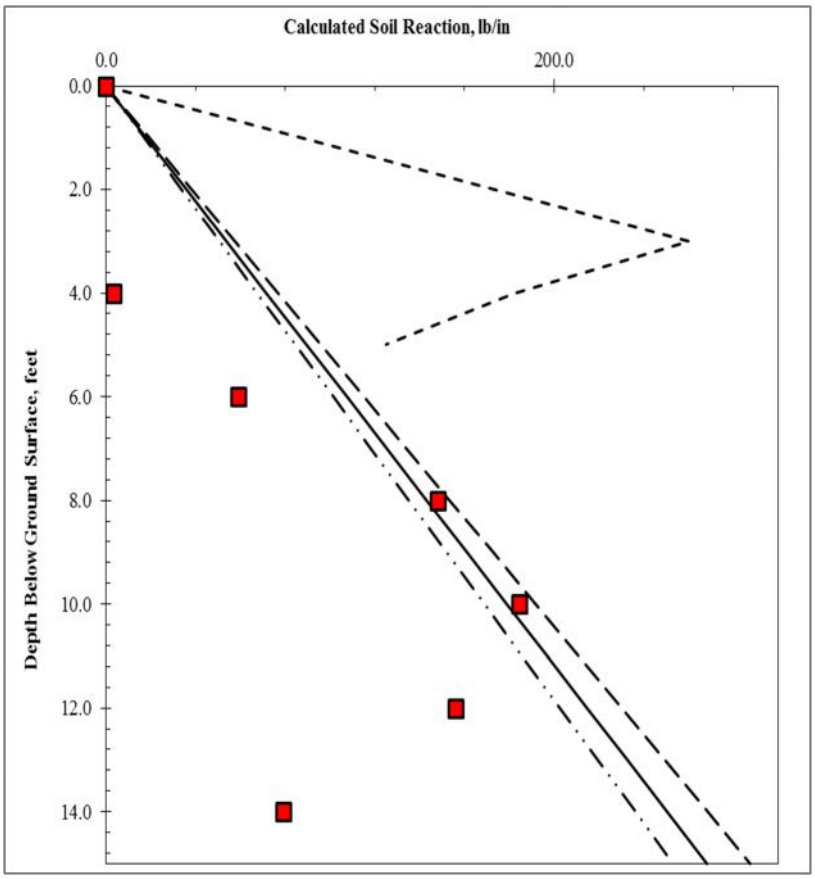


Figure 4.19: Back calculated lateral earth pressure during long-term conditions (Brown 2013)

Brown (2013) compared the-back calculated P-y curves to P-y curves that practitioners use to describe the behavior of soil during drained conditions. Equations describing different P-y relationship are discussed in details in the L-pile software Technical Manual. The P-y curves proposed for soil behavior during long-term conditions are:

1- Stiff Clay without free water (Reese and Welch 1972)

2- Stiff Clay with free water (Reese et al. 1975)

3- Drained P-y curves for cohesionless soil (fully softened friction angle) (Reese 1974)

4- Drained P-y curves for cohesionless soil (peak friction angle) (Reese 1974)

Figure 4.20 and Figure 4.21 present the relationship between the soil resistance and the horizontal deflection of the Reese at 16ft and 24ft depths, respectively. Figures compare proposed P-y curves to the back-calculated P-y curve obtained from field measurements. Brown (2013) concluded that the drained P-y curves for cohesionless soil which assumes a fully softened friction angle provides a reasonable approximation of the wall soil response.

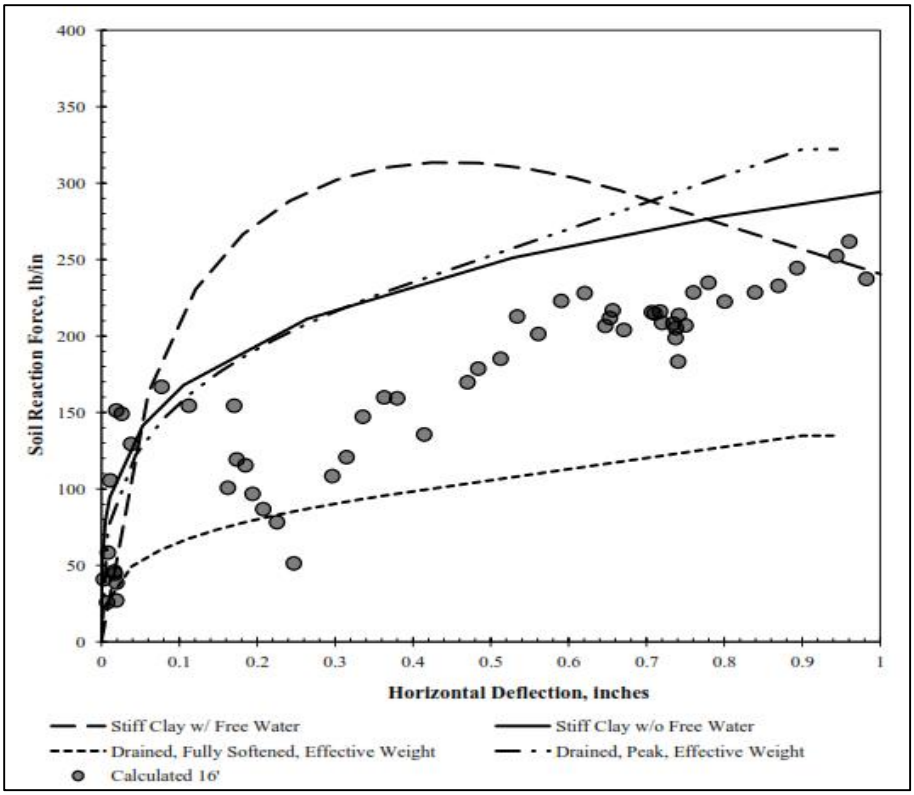


Figure 4.20: Comparison of back-calculated p-y curves during inundation testing with proposed P-y curves at a depth of 16ft below ground surface (Brown 2013)

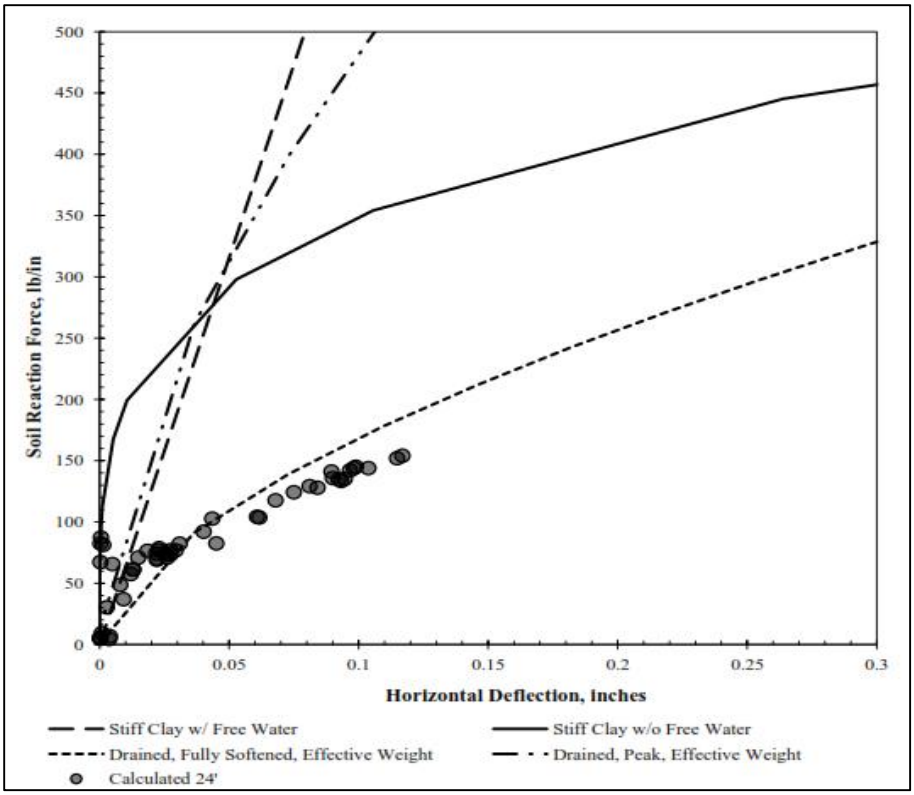


Figure 4.21: Comparison of back-calculated p-y curves during inundation testing with proposed p-y curves at a depth of 24ft below ground surface (Brown 2013)

Section 4.2 presented the MSD analytical prediction of the Reese wall behavior, and presented the back calculated P-y curves of the Reese wall, during long-term conditions. The MSD analytical method adopts two assumptions to describe the behavior of walls during long-term conditions. First the kinematics of wall movement is assumed to be rotating about a certain point of fixity, and that the volumetric strain of the active soil wedge is negligible. Second, the induced stress is solely a function of the mobilized shear strains. The monitored Reese wall behavior, during long-term conditions, did not exhibit a point of fixity; and, generally the volumetric strains for highly expansive soils are far from being negligible.

This chapter predicted the behavior of the Reese wall during short-term and long-term conditions. The behavior was predicted using the analytical MSD method. Comparison between the MSD results and the actual measurements show that the MSD could lead to misleading estimates of the deflection and bending moments, during both short-term and long-term conditions. The chapter also presented a sample of the P-y curves back-calculated by Brown (2013) for the Reese wall. Discrepancy in the predicted deflection and bending moment profile indicate the necessity of using a more robust analysis of the problem. Chapter 5 introduces a Finite Element model of the Reese wall.

# CHAPTER 5: THE REESE WALL: FINITIE ELEMENT MODEL

The objective of this chapter is to present a numerical simulation of the Reese wall. The properties of the numerical model are presented in this chapter. Properties include: properties of the soil mesh, boundary conditions, stratification of the soil profile, constitutive model, and, description about the Finite Element software.

A numerical model is simulated for the Reese wall, the model is simulated in plane strain conditions using the Finite Element method; PLAXIS 2D software. PLAXIS software is a geotechnical purpose software used to model the soil-structure problems. Predicted deflection and bending moment profiles are then compared to the field measurements, to evaluate the accuracy of the numerical model. Measured and predicted deflection and bending moment profiles are compared for different wall conditions namely, short-term conditions and long-term conditions. Once the simulated deflection and bending moment profiles from the numerical model match the measured deflection and bending moment profiles the conditions of the wall are extrapolated and the parametric analyses of the wall are simulated.

## 5.1 SOIL MESH AND BOUNDARY CONDITIONS

The subsurface soil is simulated with 3945 (15-nodes) triangular elements and the drilled shaft retaining walls is simulated as a plate element with 105 nodes. Soil elements have vertical and horizontal displacement degrees of freedom while wall elements have vertical displacement, horizontal displacements, and rotational degrees of freedom. The model total width and total height are 6 times and 3 times the wall length, respectively (Figure 5.1). The soil mesh is densified for layers shallower than 35ft (i.e. the wall length), and is even denser in the active and passive wedges of the wall. The average size of the soil elements in the active and passive wedges is 1ft.

Horizontal Displacements at the sides and vertical displacements at the base are restrained (Figure 5.1). The top 20ft of soil is incremented into 2.5ft layers, stiffness properties of these layers are determined according to a framework discussed in chapter 9. Stress-strain relationship of soil layers and the wall are discussed in the following chapters.

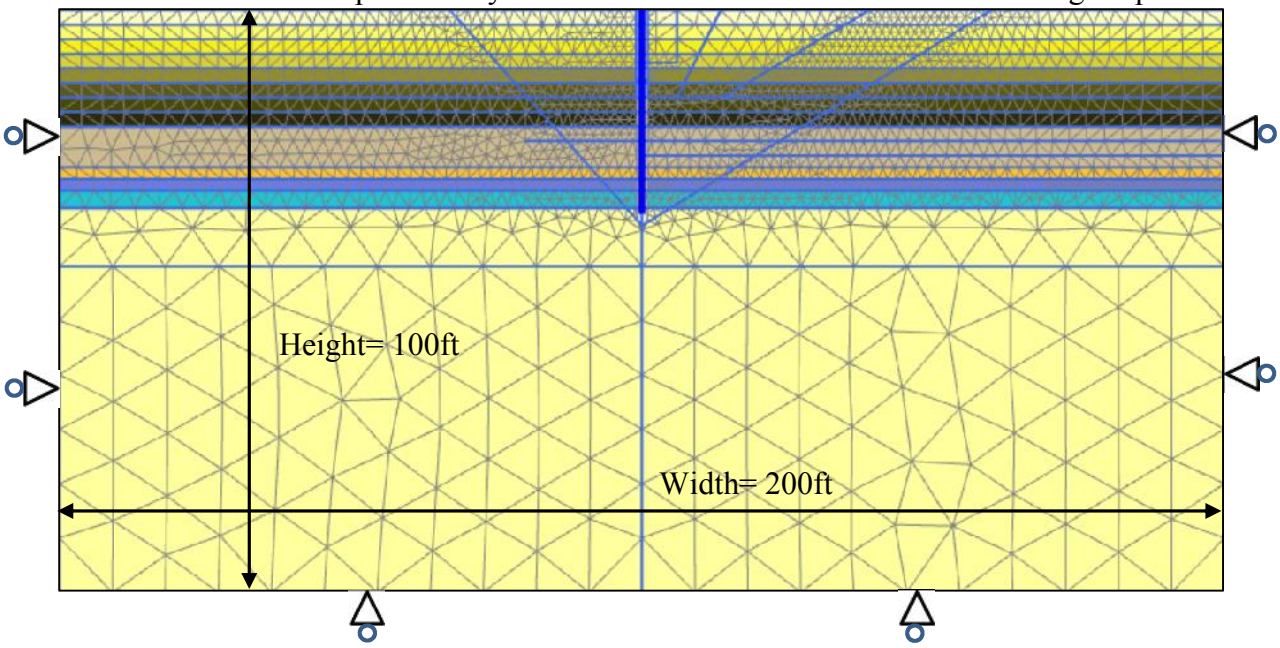


Figure 5.1: Finite Element model mesh

## 5.2 Soil Stratification

During the wetting and drying cycles of the Reese wall, the degree of saturation varies, and the variation is function of the depth of the soil. The shallower the soil the more severe the variation is in the degree of saturation. The top 20ft of soil on the active side of the wall is incremented into 2.5ft thick layers, to assign changes in the soil properties according to a resolution of 2.5ft layers. Instrumentation of the soil profile is limited to the top 20ft because the active zone of the soil is roughly about 15ft. The active zone of the soil is the depth of the soil subjected to significant changes of the water content. Incrementing the active zone of the soil into 2.5ft thick layers enables control of the soil

properties; properties are calculated individually for each layer according to the variation in moisture content of each layer.

On the passive side of the wall, the top 28ft of soil is incremented, i.e., deeper soil stratigraphy is incremented because the soil properties on the passive side is influenced by the loss of overburden stress, in addition to the variation in the water content, and the depth of the soil affected by the excavation works depends on the geometry of excavation.

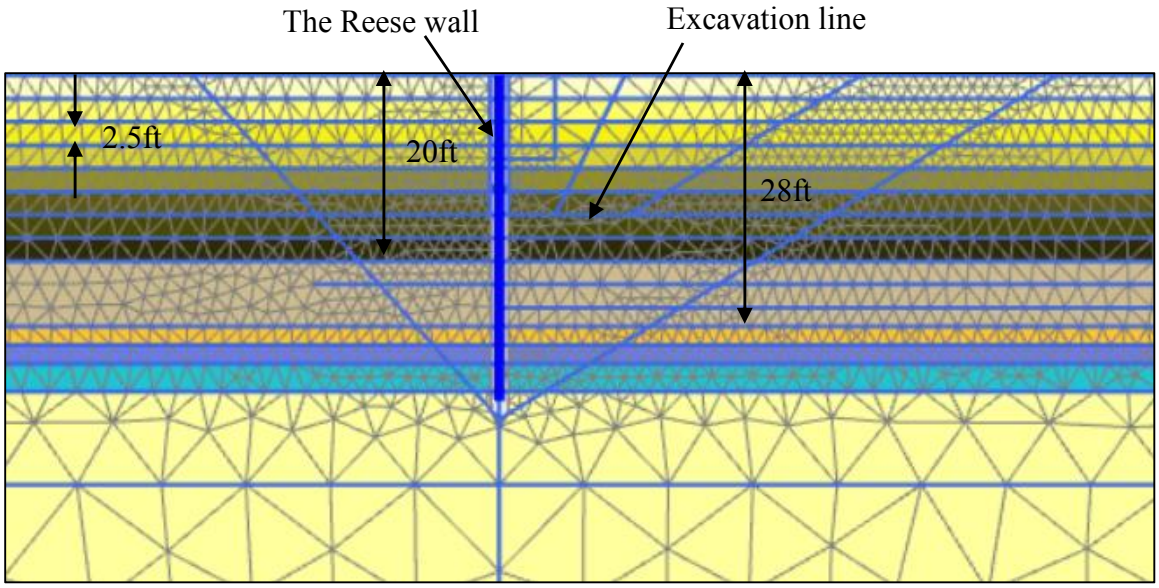


Figure 5.2: Numerical model soil stratification on the active and passive sides

### 5.3 Soil Properties Input Method

PLAXIS offers three input methods for the HSS model, namely: Drained, Undrained A, Undrained B. Each input method requires strength and stiffness input parameters of different drainage conditions. Table 5.1 presents the drainage conditions of strength and stiffness parameters for each method. The soil property input method does not govern the drainage condition of the analysis, i.e. drained or undrained analysis. The

drainage condition of the analyzed stage is determined in PLAXIS according to the "Calculation type" of each stage of construction, the "Time Interval" of the stage and the "Flow Parameters" adopted in the soil properties.

Table 5.1: Drainage conditions of strength and stiffness parameters for PLAXIS input methods of soil properties

| Input method | Strength parameters | Stiffness parameters |
|---|---|---|
| Drained | Effective | Effective |
| Undrained A | Effective | Effective |
| Undrained B | Total | Effective |

## 5.4 CONSTITUTIVE MODEL

The Hardening Small Strain (HSS) constitutive model, available in PLAXIS software, is adopted in the Reese wall numerical model. The basis of the HSS model were presented by Schanz et al (1999) study, the study developed the Hardening model based on laboratory measurements of loose sand. PLAXIS provides the HSS model which accounts for the stiffness nonlinearity of soil at small strains, and reduces to the Hardening model at large-strains.HSS model is described as "Hardening" because it accounts for the hardening of the soil stiffness with the increase in the confining stress, i.e. isotropic hardening; the capability of the HSS model to describe the isotropic hardening properties depends on the soil input method.

The HSS model adopts Equation 5.1 for describing the stiffness-stress relationship, where ($G_{max}^{ref}$) is the maximum shear stiffness at a reference effective confining stress ($\sigma'_{3\,ref}$), ($\varphi$) is the soil friction angle, and (m') is a power correlation coefficient. "Undrained B" input method is adopted in the Reese wall numerical model for two reasons. First, the soil strength of the Reese wall site was evaluated in term of total stress measurements, namely,

UU laboratory tests and TCP insitu tests. Second, the "Undrained B" input method is adopted to suppress the default hardening equation adopted in PLAXIS and the user-defined stiffness input values could be directly adopted in the stiffness matrix of the soil continuum. Suppressing the default isotropic hardening equation means that soil depths with equal strength and stiffness properties should be stratified as one layer, and the number of layers would depend on the variability of the soil strength and stiffness. Section 5.2 presented that the soil profile is incremented into 2.5ft layers.

$$G_{max} = G_{max}^{ref} \cdot \frac{S_u \cos\varphi - \sigma'_3 \sin\varphi}{S_u \cos\varphi - \sigma'_{3\,ref} \sin\varphi}^{m'} \qquad \text{Equation 5.1}$$

The stiffness nonlinearity is described in the numerical model according to Equation 5.2; where $\gamma$ is the shear strain, $\gamma_{70}$ is the shear strain at 70% of the maximum shear stiffness, and, the a coefficient is a hardening coefficient with recommended value of 0.385 (Santos and Correia 2001). Although the $\gamma_{70}$ parameter which describes the relationship of the small strain stiffness non-linearity is sensitive to the effective stress. A constant $\gamma_{70}$ is adopted in this study.

$$\frac{G_{secant}}{G_{max}} = \frac{1}{1+a\frac{\gamma}{\gamma_{0.7}}} \qquad \text{Equation 5.2}$$

After a certain strain (i.e. cutoff strain), the soil stiffness is described according to different stress-strain relationship. The cutoff strain is defined in the numerical model according to Equation 5.3, where $G_{ur}$ is the shear stiffness of soil in unloading-reloading conditions.

$$\gamma_{cutoff} = \frac{1}{0.385} \times \left(\frac{G_{max}}{G_{ur}} - 1\right) \times \gamma_{0.7} \qquad \text{Equation 5.3}$$

If zero dilation angle is adopted, the stress-strain relationship at large-strains is described by a hyperbolic equation (Equation 5.4); where q is the deviatoric stress/2; $q_a$ is the asymptotic value of the shear strength, such that $q_a$ equals the ultimate shear strength x a reduction value ($R_f$=0.9); $E_i$ is the initial stiffness of the soil, the initial stiffness is related to the stiffness at 50% of the ultimate shear strength ($E_{50}$) according to Equation 5.5; where $E_i$ and $E_{50}$ are effective stiffness parameters.

$$\varepsilon_a = \frac{1}{E_i} \times \frac{q}{1-\frac{q}{q_a}} \qquad \text{Equation 5.4}$$

$$E_i = \frac{2E_{50}}{2-R_f} \qquad \text{Equation 5.5}$$

### 5.5 DRAINAGE CONDITIONS

The Undrained B method requires effective stiffness parameters. However, only UU stress-strain measurements are available at large-strains. Equations 4.6 through 4.10 present the procedures adopted in the PLAXIS software to calculate the total stress-strain relationship from the effective stress parameters.

Equation 5.6 describes the effective shear stiffness at 50% of the ultimate shear strength ($G_{50}$) in terms of $E_{50}$ and the drained Poisson ratio ($\nu$). Since pore-water cannot affect the shear stresses the effective shear stiffness is equal to the total shear stiffness. Equation 5.6 describes the total axial stiffness at 50% of the ultimate shear strength ($E_{50}$) in terms of $G_{50}$ and the undrained Poisson ratio ($\nu_u$).

$$E_{50} = 2G_{50}(1 + \nu) \qquad \text{Equation 5.6}$$

Equation 5.7 describes the undrained Poisson ratio in terms of the *v*, soil porosity (n), and, soil skeleton and water bulk moduli (K' and $K_w$), respectively. Equation 5.8 describes the soil skeleton bulk modulus in terms of the effective axial stiffness and drained Poisson ratio.

$$v_u = \frac{v+\frac{K_w}{3nK'}(1+v)}{1+\frac{2K_w}{3nK'}(1+v)} \qquad \text{Equation 5.7}$$

$$K' = \frac{E'}{3(1-2v')} \qquad \text{Equation 5.8}$$

This chapter presented a description of the numerical model of the Reese wall. The remaining part of the dissertation is divided into two sections. Section I presents the numerical model results and sensitivity analyses of the Reese wall during short-term conditions. Section II presents the numerical model results and sensitivity analyses of the Reese wall during long-term conditions.

# SECTION I: SHORT-TERM BEHAVIOR OF WALLS

# CHAPTER 6: SHORT-TERM BEHAVIOR: THE REESE WALL (FINITE ELEMENT MODEL)

The objective of this chapter is to compare the actual behavior of the Reese wall with the predicted behavior. The chapter start with presenting the soil input properties of the numerical model and the adopted construction stages.

## 6.1 SOIL INPUT PARAMETERS

### 6.1.1 At-rest lateral earth pressure coefficient ($k_0$)

Initial stress are generated in the numerical model according to the soil unit weight and the lateral at-rest earth pressure coefficient ($k_0$). The $k_0$ input parameter for the Reese wall site is estimated according to three correlations. Brooker and Ireland (1965) correlated the $k_0$ to the soil plasticity index (PI) and the overconsolidation ratio (OCR) (Figure 6.1). Mayne et al (1987) correlated the $k_0$ from a self-boring pressure meter test (SBPMT) to the OCR ratio (Figure 6.2) and relied on specimens that consisted of 41 intact clays and 12 fissured clays. Kulhawy et al (1990) correlated the $k_0$ measurements from Dilatometer, SBPMT and pressuremeter tests to the corrected standard penetration blow counts ($N_1$) (Figure 6.3).

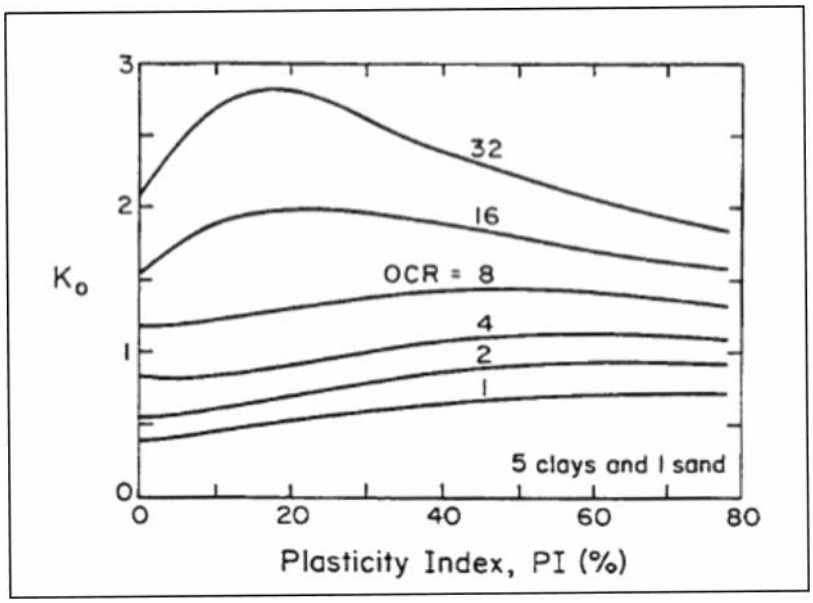


Figure 6.1: $k_0$ correlation with plasticity index and overconsolidation ratio (Brooker and Ireland 1965)

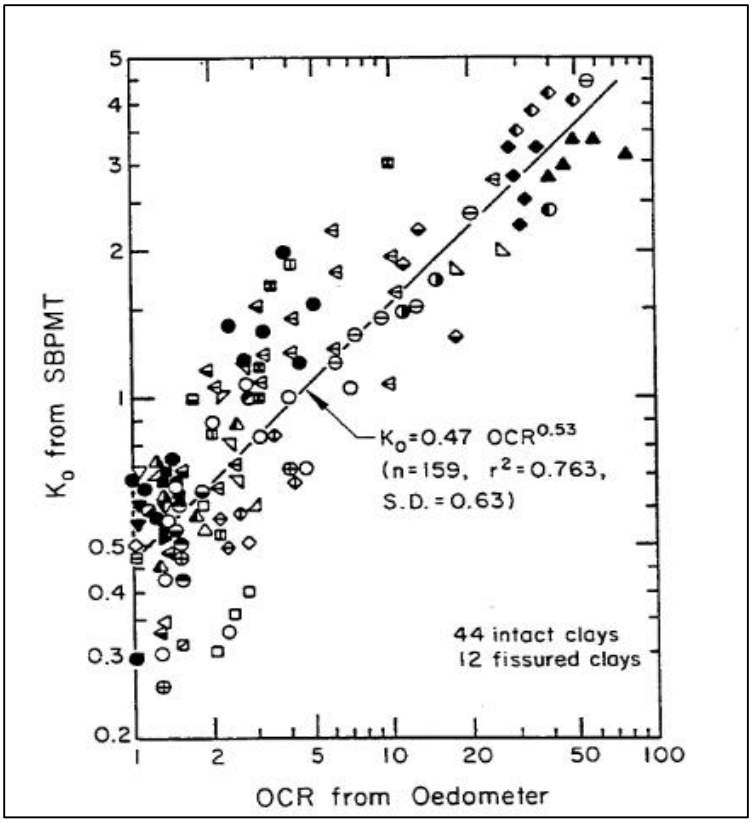


Figure 6.2: $k_0$ correlation with overconsolidation ratio (Mayne et al. 1987)

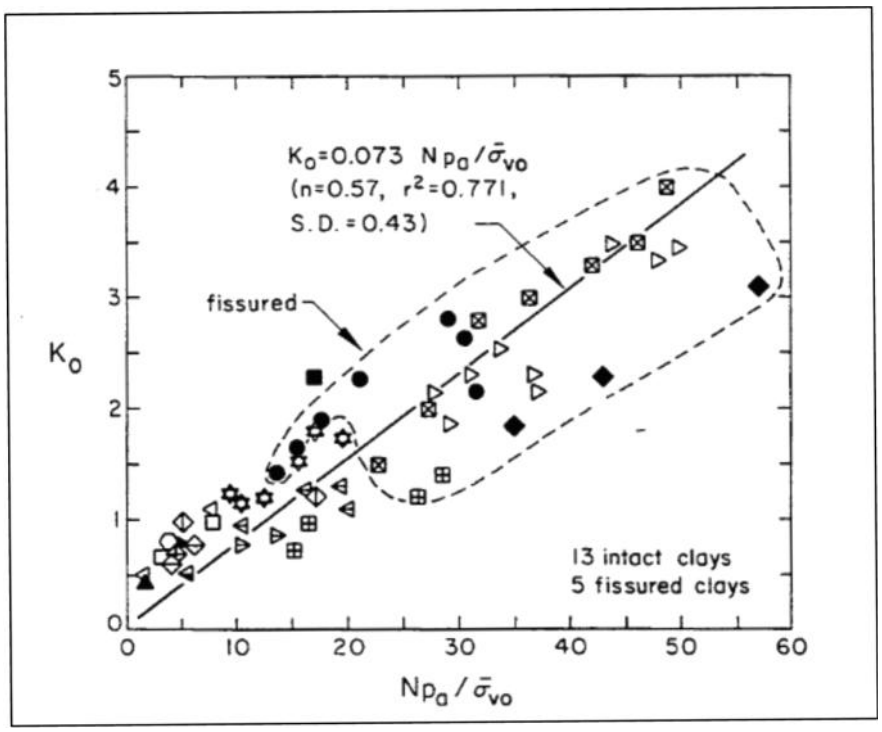


Figure 6.3: $k_0$ correlation with corrected Standard Penetration blow counts N1 (Kulhawy et al. 1990)

The OCR of the Reese wall site was estimated from 3 one-dimensional Oedometer tests; results showed that the OCR of the top 5ft ranges between 12 and 14, while the OCR at a depth of 14ft is 9. Figure 6.4 presents the estimated $k_0$ values and the $k_0$ input profile adopted in finite element model.

Bolton et al (1990) suggested that $k_0$ values greater than 2 could be found in ancient clay overconsolidated by the removal of load. Bolton et al. (1990) also suggested that excavation of diaphragm walls using drilling fluid is likely to reduce $k_0$ values to the hydrostatic pressure of bentonite. Bolton (1990) suggested that the $k_0$ value is reduced by shafts drilling process, drilling sequence, and whether casing is used to support the ground before concrete placement. Drilling fluid was not used during the construction of the Reese

wall, and the shafts were drilled in open cut conditions. The $k_0$ value of unity is adopted at the top 5ft of the wall assuming the earth pressure is limited to the hydrostatic pressure of the concrete slump.

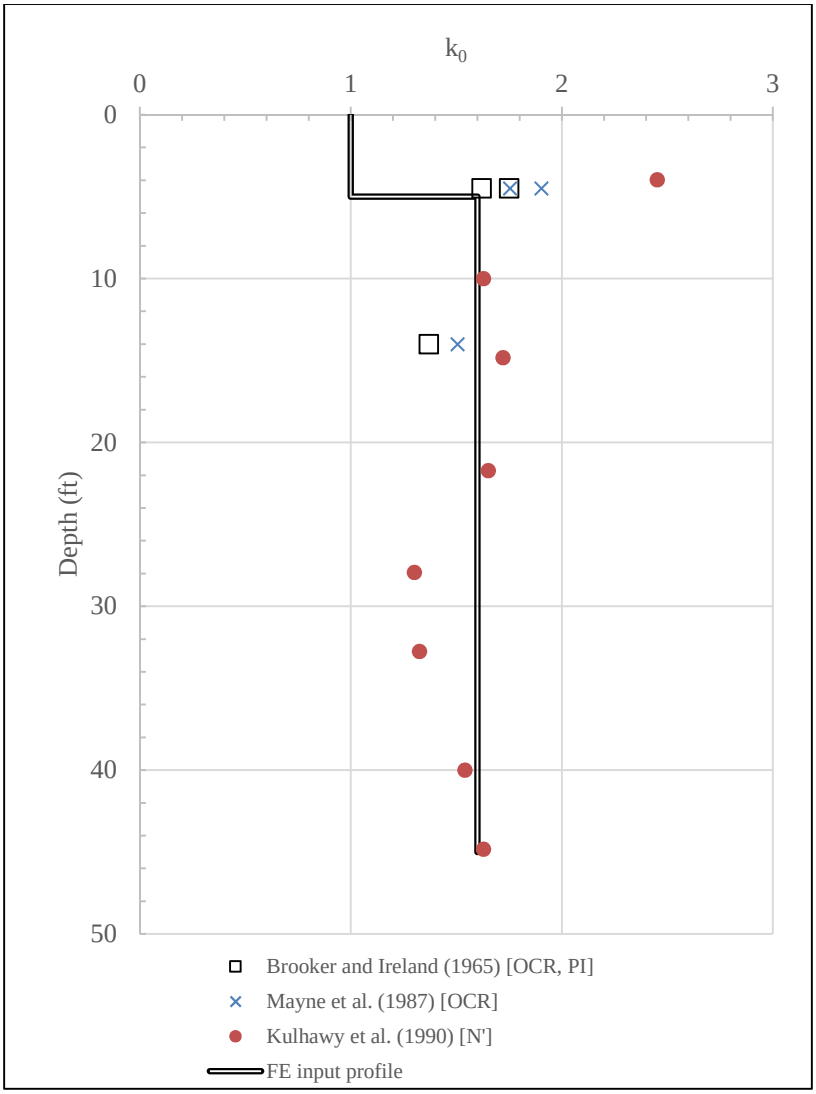


Figure 6.4: Estimated $k_0$ values and input profile

### 6.1.2 Small-Strain Stiffness

Measuring the undisturbed small-strain stiffness of the highly fissured Taylor clay is challenging; therefore, insitu shear wave velocity at small strain measurements was conducted. Insitu shear wave velocity was measured by installing accelerometers into the ground surface and a shear wave is introduced (Figure 6.5). The shear stiffness at small strains are estimated using the Spectral Analysis of Surface Waves (SASW). Four arrays of SASW estimates were conducted, two on the retained side, and two on the excavation side prior to excavation works. Figure 6.6 presents the results of the estimated small strain shear stiffness and the stiffness profile adopted in the numerical model.


Figure 6.5: Spectral analysis of Surface Waves measurement setup

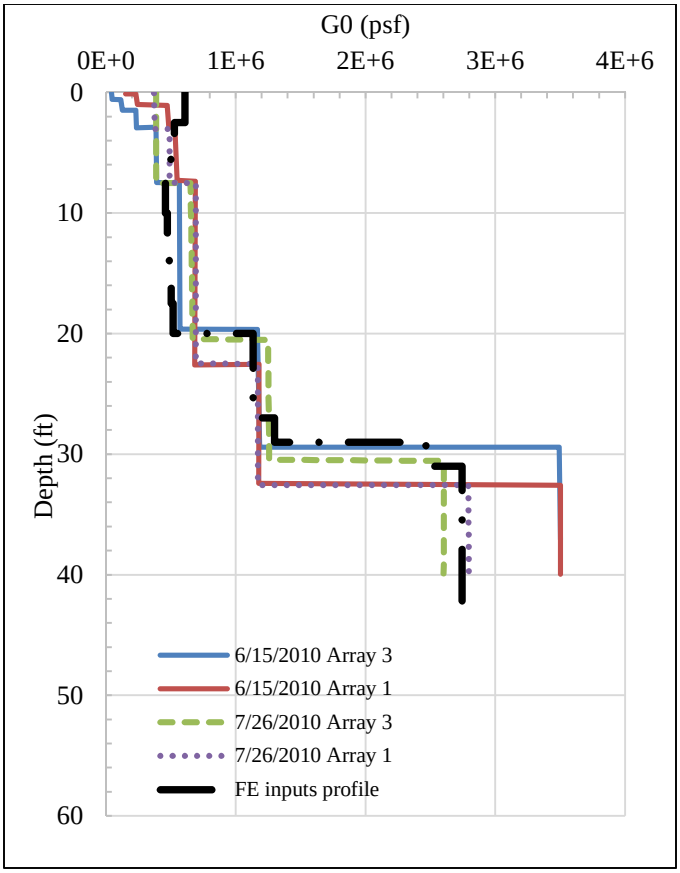


Figure 6.6: Comparison between measured SASW profile and G0 input profile

Small-strain stiffness is not commonly measured in retaining wall projects; however, it was intentionally measured in this research project to illustrate its significance in describing the behavior. Section 7.3 presents a sensitivity of the predicted behavior to adopting a constitutive model that accounts for stiffness nonlinearity at small strains.

Standard Penetration Test (SPT) is commonly conducted in retaining wall projects. Imai (1977), Wroth (1979), Lee (1990), Jafari et al. (2002) and Pitilakis (1999) correlated the shear wave velocity standard penetration blow counts (Figure 6.7). SPT-$V_s$ measurement of the Reese wall site are compared to the correlations found in literature

(Figure 6.7). Comparison shows that the SPT-$V_s$ correlations consistently overestimates the shear wave velocity of the Reese wall site.

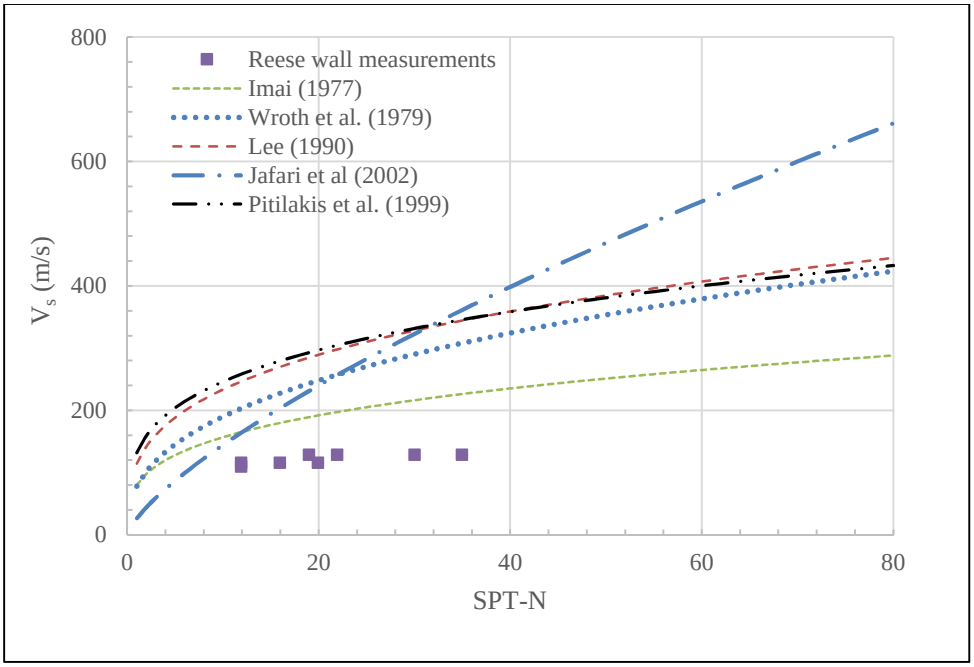


Figure 6.7: Comparison between (Vs, SPT) measured and empirical correlations

The shear stiffness-shear strain relationship (i.e. stiffness nonlinearity) for the Reese wall site is assumed to resemble the resonant column measurements of London Clay reported by Vardanega et al. (2013) (Figure 6.8). London clay measurements are adopted because it has similar characteristics to the Taylor clay. Figure 6.8 presents a comparison between the shear stiffness-shear strain measurements and the relationship adopted in the numerical model.

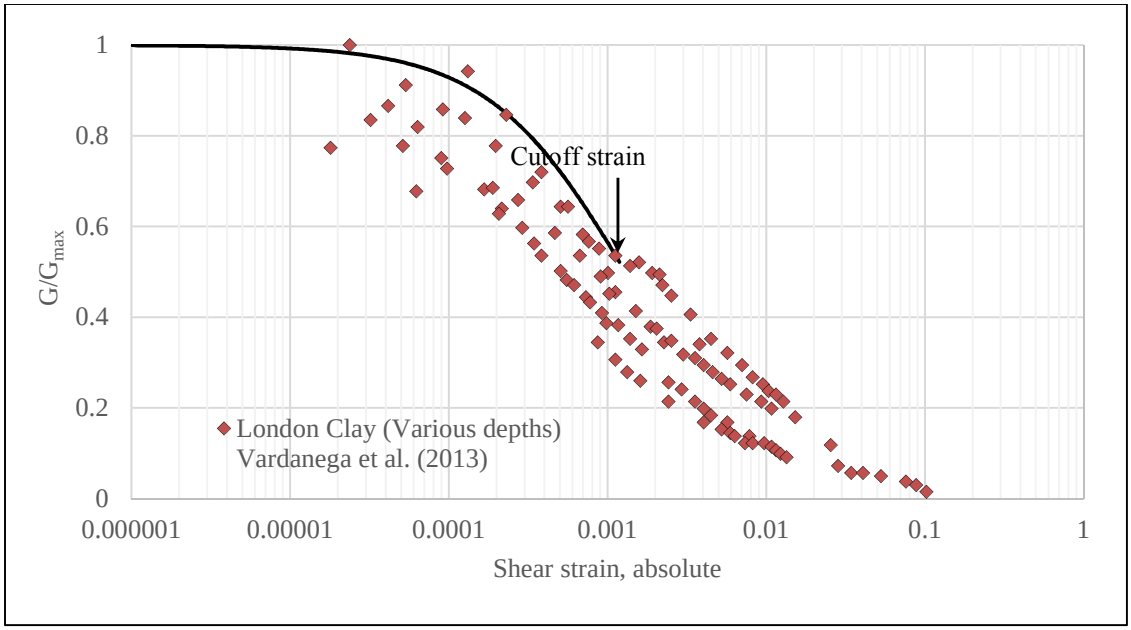


Figure 6.8: Comparison between small strain shear stiffness-shear strain measurements (Vardanega et al. 2013) and shear stiffness-shear strain relationship adopted in the numerical model

### 6.1.3 Large-strain stiffness

Stiffness parameter of different soil layers are obtained by calibrating the computed UU stress-strain curves with the actual measurements. Figure 6.6 compares between deviatoric stress ($\sigma_d$) to axial strains ($\varepsilon_a$) measurements from different depths, with, the calibrated stress-stress curves.

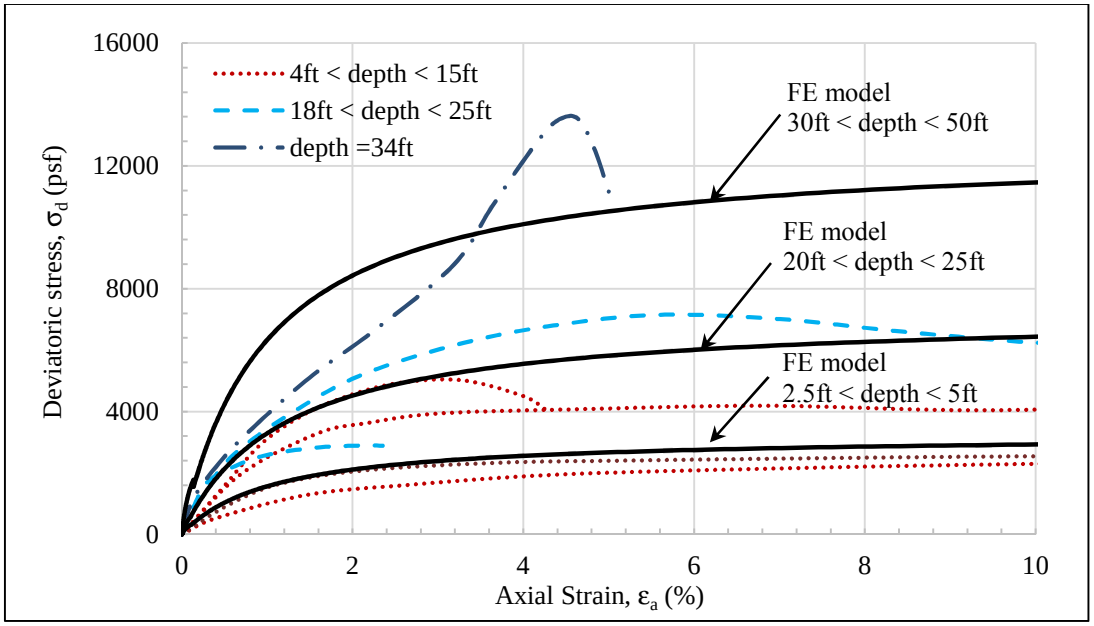


Figure 6.9: Comparison between measured stress-strain relationship at large strains and stress-strain relationship adopted in the numerical model

Figure 6.10 presents the shear stiffness-shear strain relationship adopted in the numerical model for absolute shear strain values ranging from 0 to 1. The figure shows that the shear stiffness-shear strain relationship is discontinues at the cutoff strain. The discontinuity in the stress-strain relationship could compromise the accuracy of the predicted deformations if the magnitude of mobilized shear strain is close to the cutoff strain level. However deformation mobilizing shear strains different from the cutoff strains are probably less sensitive to this continuity.

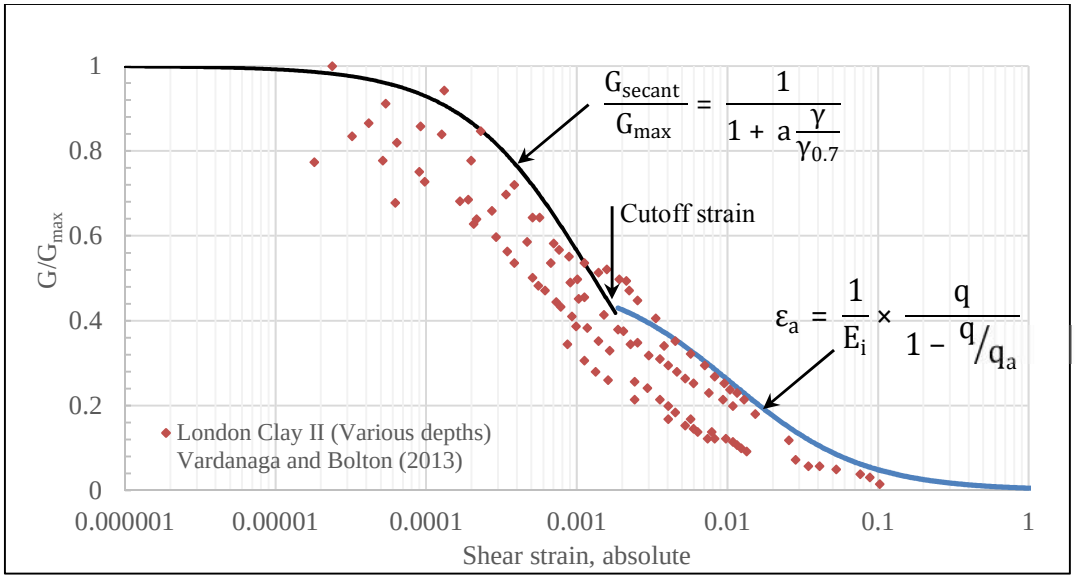


Figure 6.10: Stress-strain relationship at different strain levels

## 6.2 CONSTRUCTION STAGES

### 6.2.1 Actual stages of full-scale wall

Excavation works began on July 29th, 2010 and took place over a period of approximately four weeks. First, 9ft deep, 5ft wide, trench was excavated (Figure 6.11), then 0.5:1 slopes were introduced to the middle of the excavated side (Figure 6.12), then excavation reached the targeted excavation depth (15ft) maintaining 0.5:1 slopes (Figure 6.13), then the excavation slopes were reduced to 3:2 slopes (Figure 6.14), and finally the excavated side of the wall was furnished with shotcrete facing (Figure 6.15).


Figure 6.11: Excavation of 9ft deep trench (7/29/2010)


Figure 6.12: 1:1 Slope excavation to the depth of 9ft (8/1/2010)


Figure 6.13: 1:1 Slope excavation to the depth of 15ft (8/23/2010)


Figure 6.14: 3:2 Slope excavation to the depth of 15ft (10/1/2010)


Figure 6.15: Shotcrete finishing of passive side (10/10/2010)

Figure 6.16 presents the excavation elevation cross section at different excavation dates. The full cantilever depth of 15ft was reached on August 13th, and the preliminary slopes were completed on August 19th. The slopes were improved on September 30th, and facing was installed on October 10th.

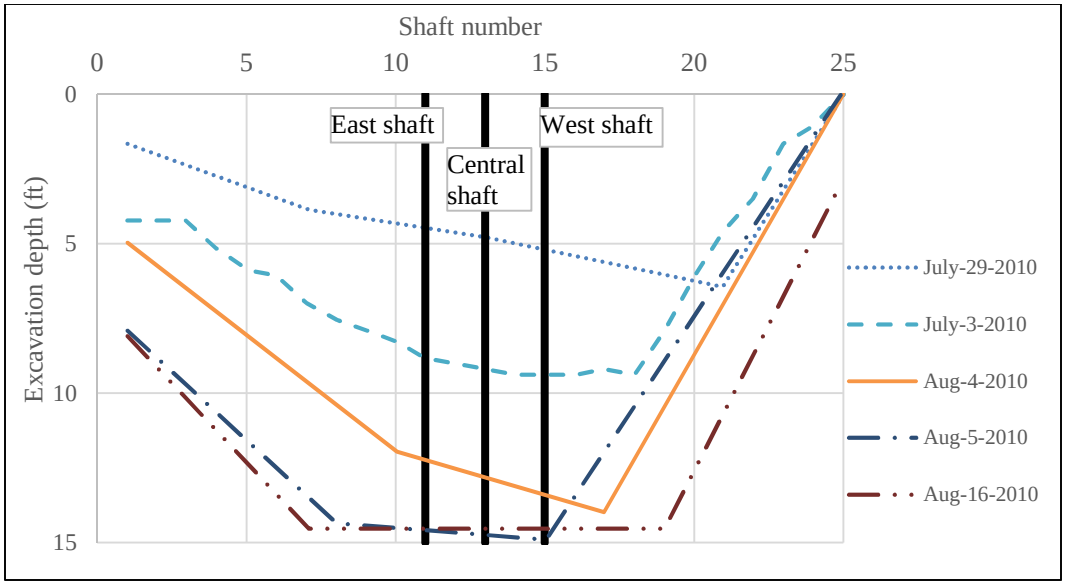


Figure 6.16: Elevation cross section of shaft depths and excavation works

### 6.2.2 Simulated stages of numerical model

Excavation stages are simulated in the numerical model in three stages of excavation. Figure 6.17 presents first stage of excavation where 9ft of soil is excavated on one side of the wall to simulate the behavior of the wall on July 29$^{th}$ (Figure 6.11). Figure 6.18 presents the second stage of excavation where 15ft of soil is excavated with side slope of 0.5:1 to simulate the behavior of the wall on August 23$^{rd}$ (Figure 6.13). Figure 6.19 presents the last stage of excavation where the side slope is leveled to 3:2 slope to simulate the behavior of the wall on October 1$^{st}$ (Figure 6.14).

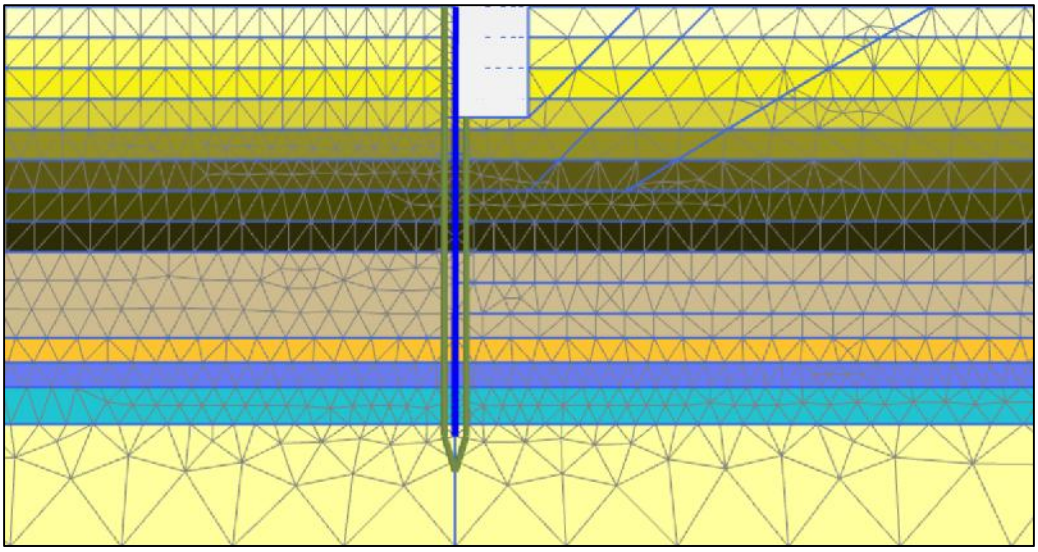

Figure 6.17: FE model stage (1) (9ft deep trench excavation)

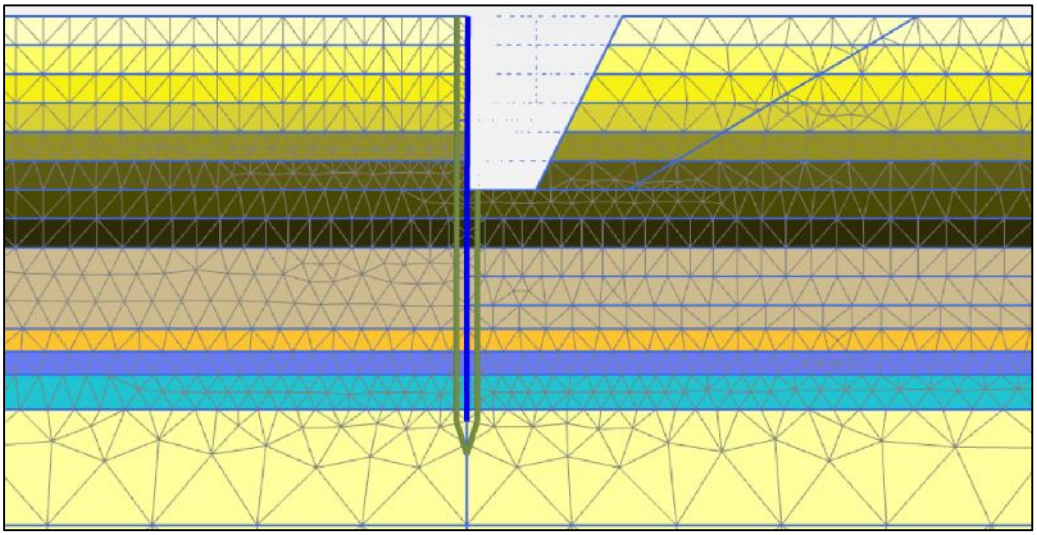

Figure 6.18: FE model stage (2): 9ft deep excavation with 0.5:1 slope

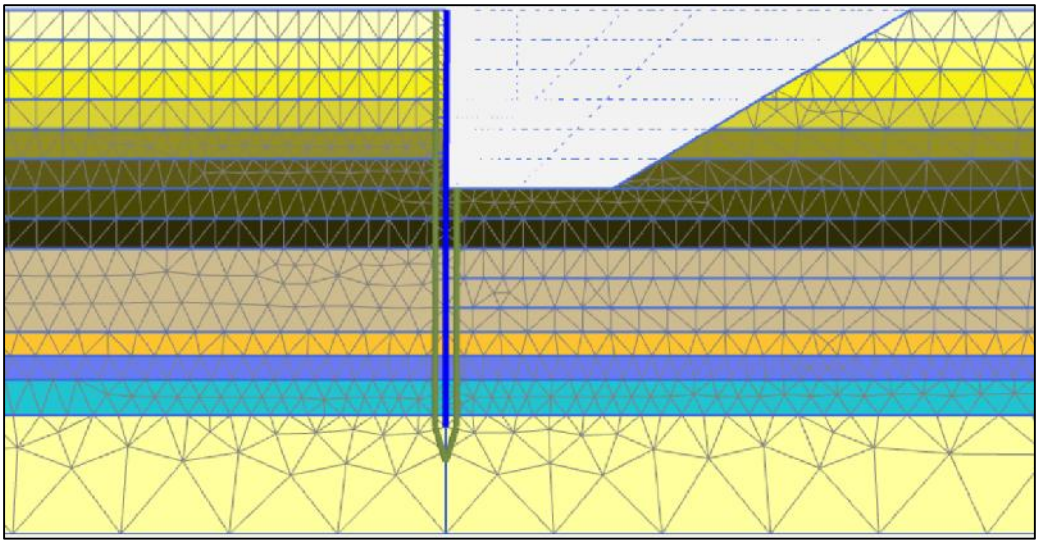

Figure 6.19: Stage (3): 15ft deep excavation with 3:2 slope

### 6.3 PREDICTED WALL RESPONSE

Numerical model deflection predictions are compared to the field measurements during different excavation stages (Figure 6.20). The figure presented field measurements from three inclinometers (East, Central, and west) and a linear potentiometer measuring the deflection at the top of the west shaft. The predicted wall deflection shows reasonable agreement with field measurements during the first and the last stages of excavation. The field measurement indicate that the wall maximum deflection during the first and last stages of excavation are 0.2 and 0.95 inches, respectively; while the predicted maximum wall deflection are 0.17 and 1.1inches, respectively.

The field measurements indicate that the wall maximum deflection during the second stage of excavation ranges from 0.55 inches to 0.65 inches; while, the predicted wall deflection is 0.9inches. Figure 6.16 presented the elevation cross section of the excavating levels during different stages of construction. The close proximity of the excavation slopes (slopes in the elevation view) to the instrumented piles suggests that field

conditions might not perfectly resemble plane-strain conditions. The delayed excavation of the berm close to the west shaft could have reduced the deflection of the walls, such that the west shaft is the most affected by the presence of the berm and the East shaft is the least affected, this observation complies with the difference between the three instrumented shafts presented in Figure 6.20.

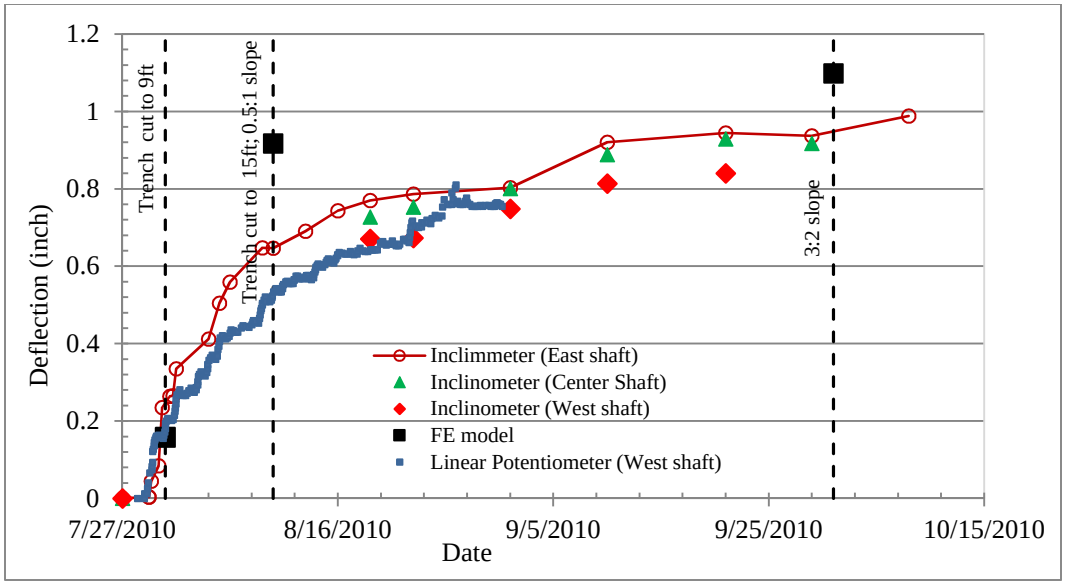


Figure 6.20: Comparison between measured and predicted maximum wall deflections during different excavation stages

Figure 6.21 presents a comparison between the measured deflection profile and the predicted deflection profile. The predicted wall deflection profile shows reasonable agreement with the measured wall deflection. The measured maximum wall deflection is 0.95, while the predicted maximum wall deflection is 1.1 inches. Measured and predicted deflection profiles indicate that the wall toe moves toward the excavated side, this observation indicates that the wall experiences a global movement toward the excavated side, rather than a rotational movement about a point of fixity.

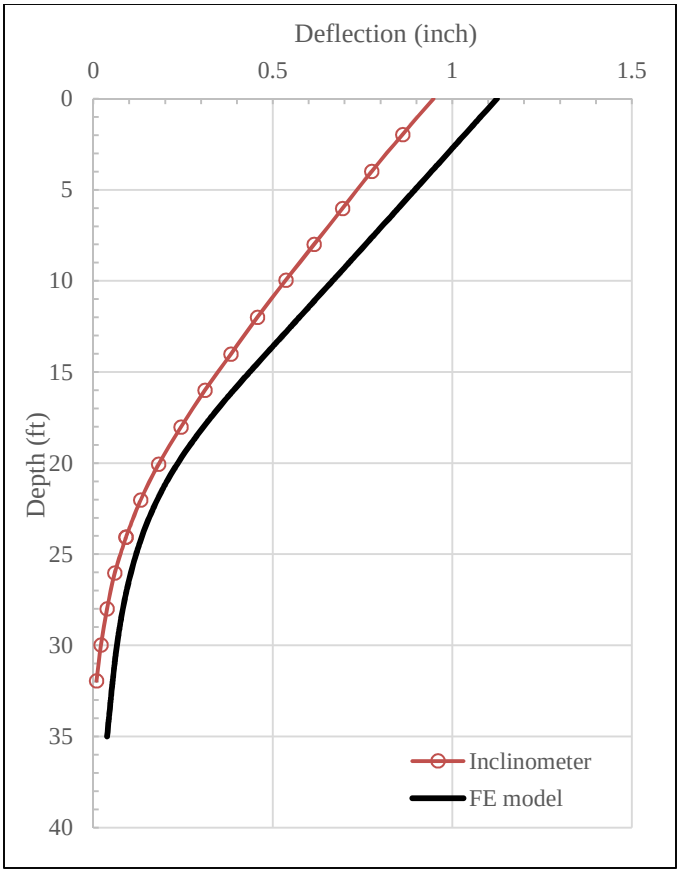


Figure 6.21: Comparison between measured deflection profile and predicted deflection profile

During short-term conditions excavation induced negative pore-water pressure are generated. The excavation induced pore-water pressure results in predicting negative bending moment in the retaining wall (i.e. tension on excavated side). To overcome this anomalous prediction, the pore-water pressure degree of freedom of the soil within 0.5ft proximity of the wall is suppressed, by assigning dry soil (Figure 6.22). In other word, the pore-water pressure boundary conditions of the soil in proximity of the wall is assigned as zero. This measure is adopted for the soil that experiences excavation induced negative pore-water pressure; therefore, this measure is adopted only in the top 15ft of soil.


Figure 6.22: Boundary condition of soil in proximity to the wall

Figure 6.23 presents a comparison between the measured and predicted deflection profiles 5.5ft behind the wall. Although the difference between the maximum predicted and maximum measured deflections is less than 0.1inch, the trend of the two profiles do not match for depths shallower than 10ft. Such that, the maximum measured deflection profile is at the top of the wall while the maximum predicted deflection is at a depth of 10ft, and the deflection decreases at depths shallower than 10 ft. This could be attributed to the presence of fissures and desiccation cracks insitu that causes the top soil to behave as a granular material rather than a cohesive material, or, the presence of excavation induced pore-water pressure in the numerical model that are minimized insitu due to the presence of fissures and desiccation cracks.

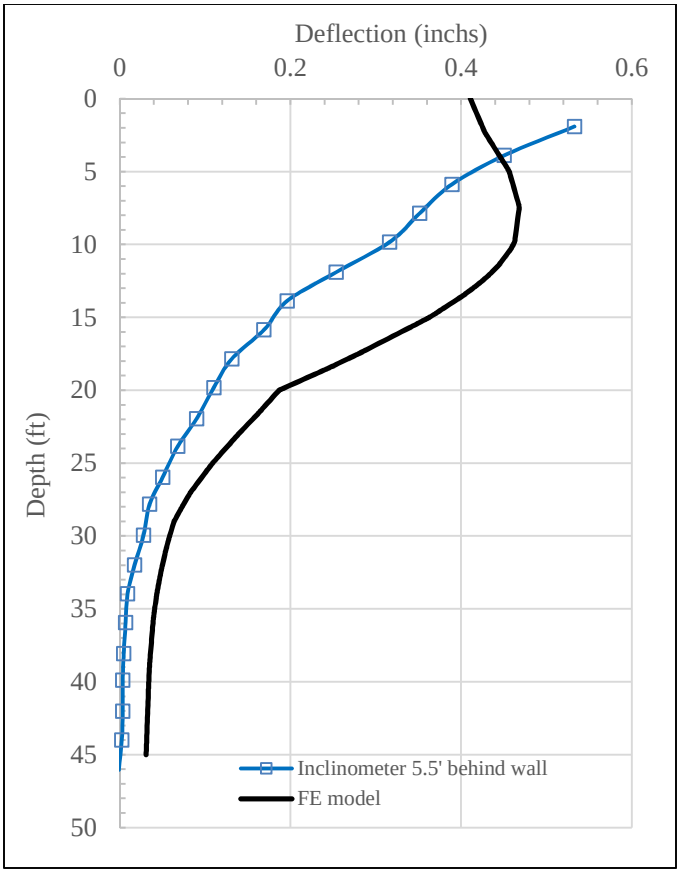


Figure 6.23: Comparison between measured and predicted deflection profiles of soil 5.5ft behind the wall on the retained side

Figure 6.24 presents a comparison between the measured and the predicted bending moment profiles, where two sets of bending moment measurement are presented (strain gauges and inclinometer). The measured bending moments are calculated based on the measured curvature and cracked bending stiffness value. The predicted bending moment profile shows reasonable agreement with the measured profile. The maximum predicted and measured bending moment values are experienced at a depth of 20ft. Both, predicted and measured bending moment profiles shows negligible bending moment at the top 10ft of soil, emphasizing the conclusion that the behavior of the Reese wall during short-term

conditions was due to global straining rather than earth pressure of the retained soil. The maximum measured bending moment is 36,000lb.ft/shaft; while, the maximum predicted bending moment is 46,000lb.ft/shaft.

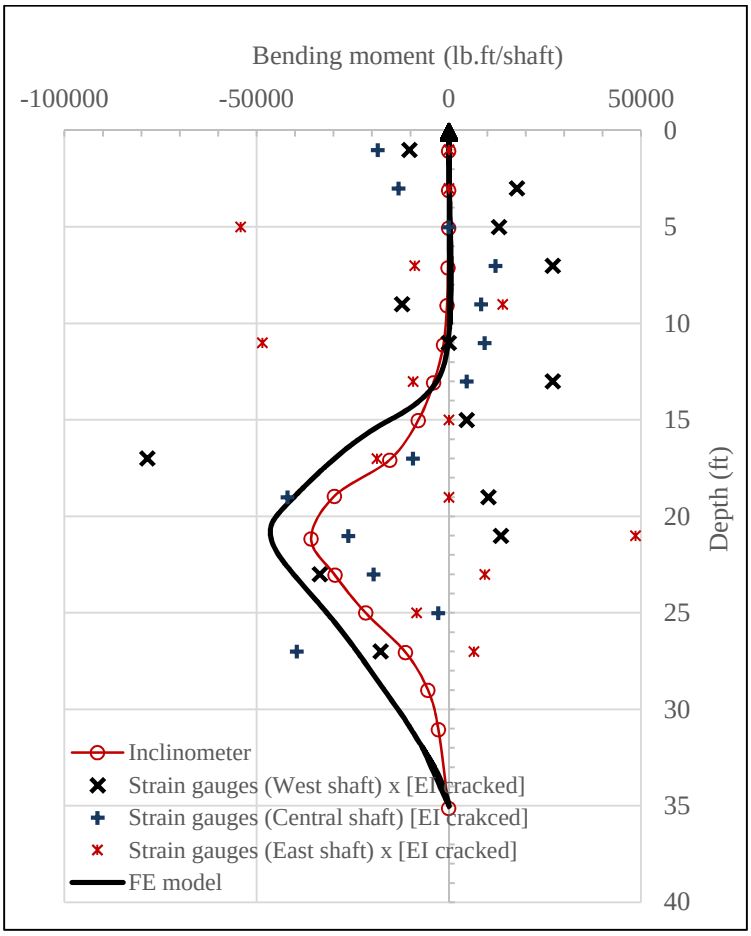


Figure 6.24: Comparison between measured bending moment profile assuming cracked wall and predicted bending moment profiles

One of the advantages of using Finite Element modelling of the short-term behavior of the Reese wall is to bypass practitioners from factoring the stiffness of the soil according to their own judgment that theoretically ought to be correlated to the mobilized shear strains. Figure 6.25 and Figure 6.26 presents the predicted mobilized shear strain profiles

at 1ft and 5.5ft behind the Reese wall, respectively; along the mobilized shear strain profiles, secant stiffness ratios corresponding to different shear strains are marked (according to Figure 6.10). The stiffness of the top 5ft of soil ranges from 60 to 80% of the maximum shear stiffness. The stiffness of the soil between 5ft and 20ft deep ranges from 35 to 60%. The stiffness of the soil deeper than 20ft is generally more than 70% of the maximum shear stiffness. The stiffness of the soil depends on the depth of the soil and the distance from the wall; therefore the use of a Finite Element model that calculates the soil stiffness of the soil for each soil element is important. Another form of presenting the mobilized shear strains and the corresponding shear stiffness is presented in Figure 6.27. The figure presents the mobilized shear strains with respect to the strain-stiffness nonlinearity curve.

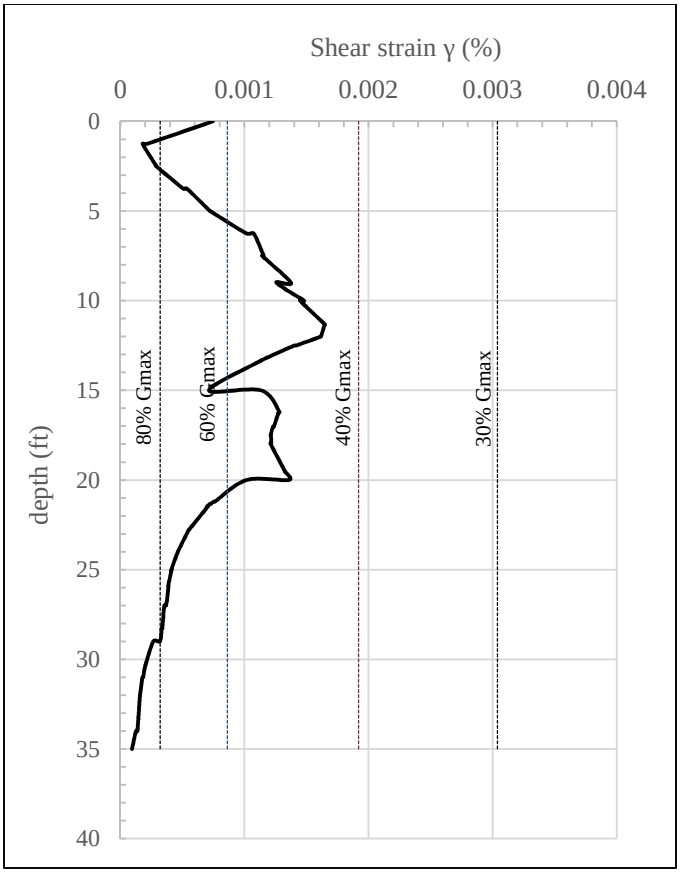


Figure 6.25: Predicted mobilized shear strain profile 1ft behind wall due to excavation works; and corresponding stiffness reduction factors according to the FE stiffness non-linearity model

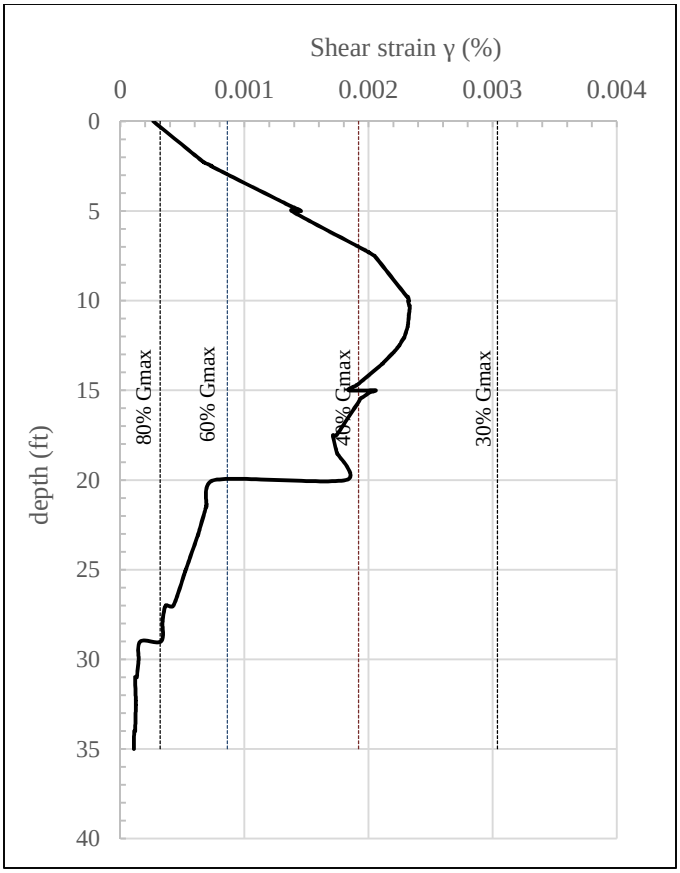


Figure 6.26: Predicted mobilized shear strain profile 5.5ft behind the wall due to excavation works; and corresponding stiffness reduction factors according to the FE stiffness non-linearity model

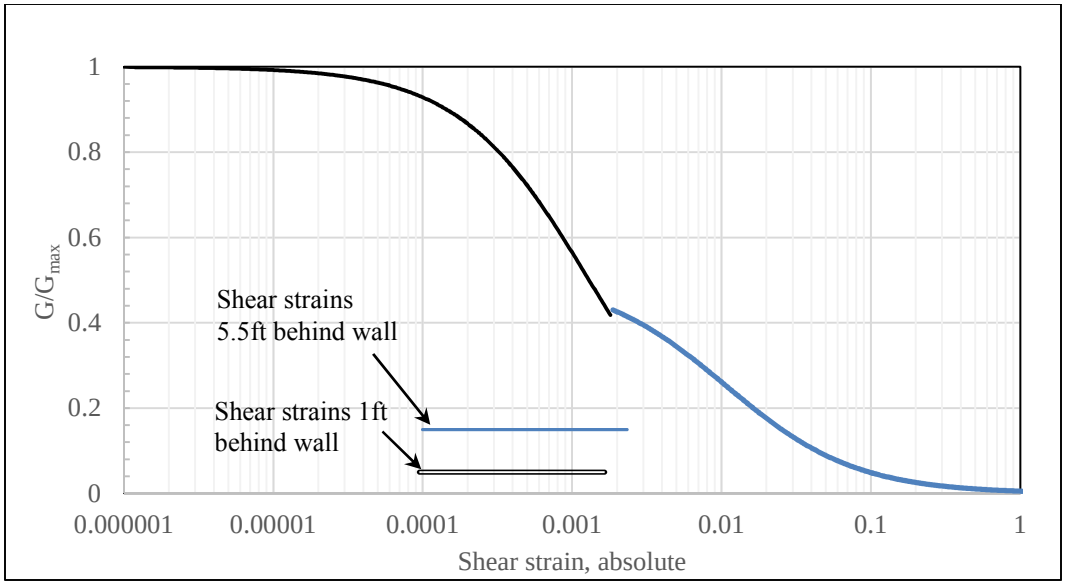


Figure 6.27: Comparison between mobilized shear strain and stiffness strain relationship at small strain conditions

Figure 6.28 presents the maximum mobilized shear strain in the soil with respect to the UU stress strain measurements. The figure shows that shear strains mobilized during short-term conditions of the Reese wall are roughly an order of magnitude less than the failure shear strain. This strain is equivalent to deviatoric stresses that are also roughly an order of magnitude less than the deviatoric stress at failure. This observation suggests that common UU stress strain measurements are not representative of the soil stiffness during short-term conditions. A more affirmative conclusion would be that stiffness measurement that correlate to a failure condition of soil such as Standard Penetration Test is not representative of the soil conditions during short-term conditions.

The following section presents predicted wall deflection adopting different soil constitutive models to show the necessity of measuring the small strain stiffness measurements in describing the Reese wall behavior during short-term conditions.

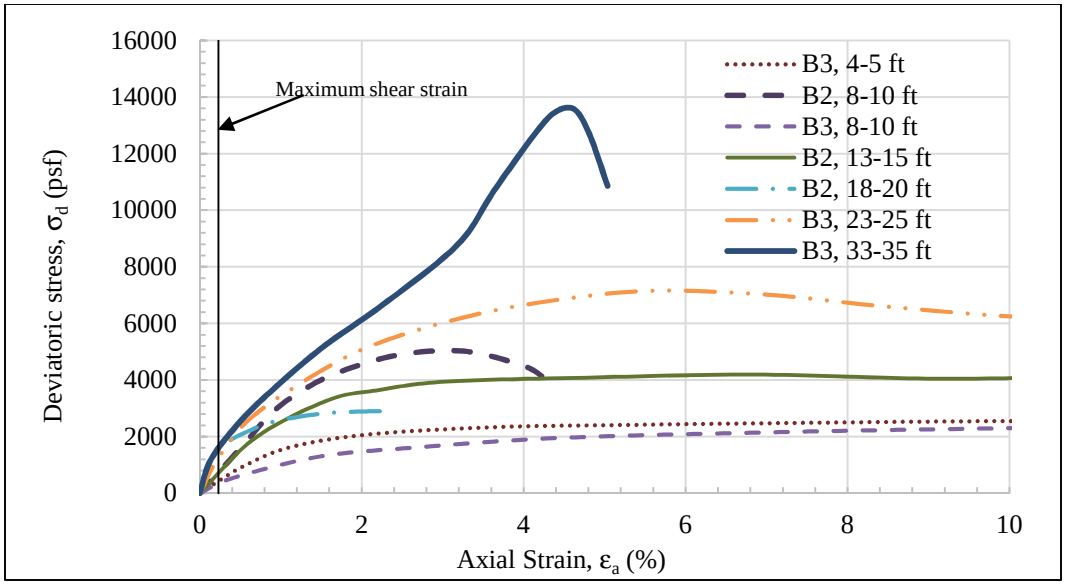


Figure 6.28: Comparison between mobilized shear strain and stiffness strain relationship at large strain conditions

This chapter presented the soil input properties governing the analysis of the short-term conditions, such as at rest lateral earth pressure coefficient $k_0$, and, the small strain stiffness profile of the soil during the excavation stage. A $k_0$ value of 1.6 was estimated according to correlation with the OCR and PI; the predicted deflection and bending moment profiles showed good agreement with the measured profiles. The stiffness reduction factor ranged between 50% and 80%. The following chapter extrapolates the conditions of the Reese wall site to different condition, the sensitivity of the wall behavior is tested to changing the depth of the wall embedment, the wall stiffness and the constitutive model adopted for the analysis.

# CHAPTER 7: SENSITIVITY ANALYSES OF WALL BEHAVIOR DURING SHORT-TERM CONDITIONS

This chapter extrapolate the numerical model of the Reese wall to cases different than the actual field conditions. The objective of this chapter is study the sensitivity of the short-term behavior of walls to several factors, such as, wall design parameters and soil properties.

Wall deflection design requirements are often described in terms of the maximum wall deflection normalized to the retained height ($\Delta/h$). In this chapter, the sensitivity of wall deflection are presented in terms of the normalized deflection $\Delta/h$ ratio; and, the sensitivity of bending moment are presented in terms of the maximum bending moment ($M_{max}$) normalized to the bending moment from a linear earth pressure distribution with lateral earth pressure coefficient $k_0$, i.e., $M_{max}/\gamma k_0 h^3/6$; where $\gamma$ is the bulk density, and h is the retained height.

## 7.1 SENSITIVITY OF WALL BEHAVIOR TO WALL DESIGN PARAMETERS

The Reese wall numerical mode is extrapolated to different cases in parametric analyses to study the sensitivity of the wall embedment depth and wall stiffness on the deflection and bending moment profiles. This section presents results of the parametric analyses conducted to study the sensitivity of walls behavior to the wall design parameters, namely the wall embedment ratio and the wall stiffness.

### 7.1.1 Embedment ratio

The embedment ratio (d/h) is defined as the ratio between the embedded depth of the wall below the excavation level (d) and the retained height (h) of the wall, thus, the embedment ratio of the Reese wall is 1.33.

The integrity of temporary walls, i.e. walls in short-term conditions, could be jeopardized if the wall site experiences rainfall. Rainfall could instantaneously induce additional stresses on the wall, if drainage layers are not assembled on the retained side of walls. Two cases of short-term conditions are investigated in this section, first, a short-term condition assuming no hydrostatic pressure, this condition is referred to as dry cracks conditions. Second, a short-term condition assuming that the ground water table rises to the ground level due to meteorological reasons, this condition is referred to as water filled cracks.

***Dry cracks***

Figure 7.1 presents deflection profiles predicted for walls with embedment ratios ranging between 0.5 and 2 and dry cracks condition. Beyond an embedment ratio of d/h=1, the short-term deflection of walls is not sensitive to the wall embedment ratio, such that, the predicted deflection profiles for d/h ratios higher than d/h=1 coincide. The maximum deflection of the Reese wall is 1.1inches at the wall top; decreasing the wall embedment (d) to 7.5ft rather than 15ft (as for the case of the Reese wall), results in increasing the maximum deflection to 1.3inches.

Deflection profiles do not show a point of fixity, neither for the maximum nor minimum embedment ratios. This observation emphasizes that the behavior of walls during short-term conditions is more of a global movement towards the excavated side, as previously suggested in section 3.5 and section 4.5.

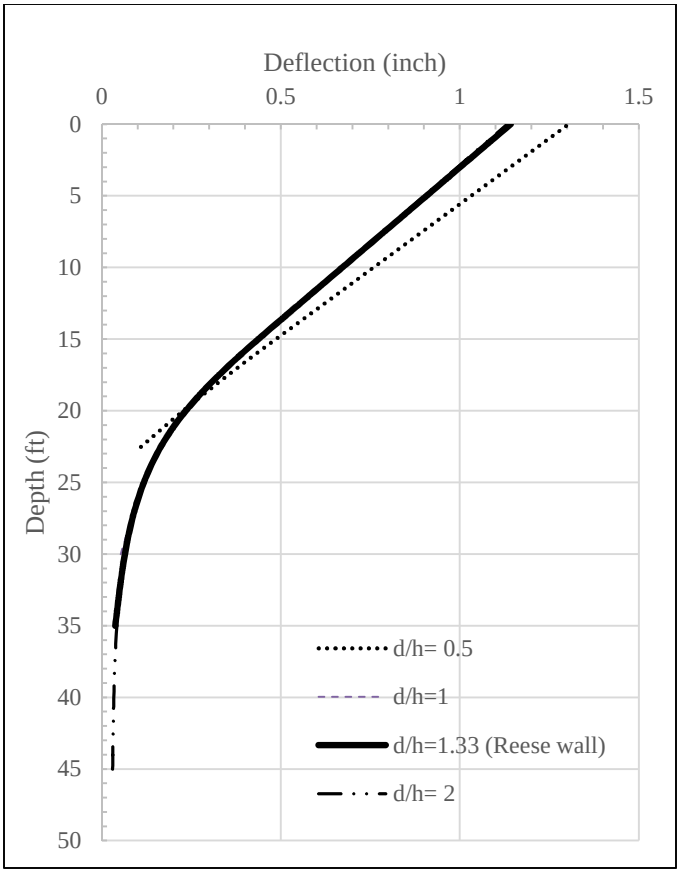


Figure 7.1: Predicted deflection profiles using the Finite Element method of walls with different embedment ratios assuming dry cracks

Figure 7.2 presents bending moment profiles predicted for walls with embedment ratios ranging between 0.5 and 2. The location of the maximum bending moment is almost constant and is located 5ft below the excavation bed. Beyond an embedment ratio of d/h=1, the short-term maximum bending moment of walls is not sensitive to the wall embedment ratio, such that, the predicted maximum bending moment for d/h ratios higher than d/h=1 coincide. The maximum bending moment of the Reese wall is 45,000lb.ft/shaft; decreasing the wall embedment (d) to 7.5ft rather than 15ft (as for the case of the Reese wall), results in decreasing the maximum bending moment on the wall to 15,000lb.ft/shaft.

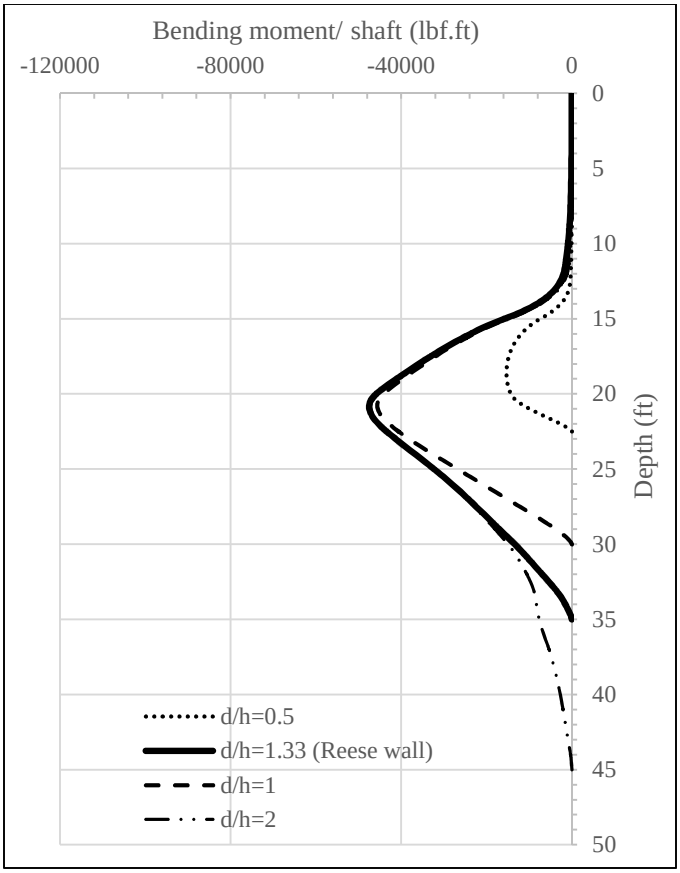


Figure 7.2: Predicted bending moment profiles using the Finite Element method of walls with different embedment ratios assuming Dry cracks

Results presented in Figure 7.1 and Figure 7.2 shows that building deeper walls: 1-does not reduce the maximum wall deflection significantly, 2-requires stiffer walls to endure higher bending moments. It is the responsibility of the design engineer to compromise between the cost of building deeper walls that should sustain higher bending moments and walls deflections.

***Water filled cracks***

Figure 7.3 presents deflection profiles predicted for walls with embedment ratios ranging between 0.5 and 2 and water filled cracks conditions. Beyond an embedment ratio of d/h=1, the short-term deflection of walls is not sensitive to the wall embedment ratio, such that, the predicted deflection profiles for d/h ratios higher than d/h=1 coincide. The predicted maximum deflection of the Reese wall during short-term conditions and water filled cracks is 2.8inches, on a side note, the maximum measured deflection of the Reese wall is 5inches. Decreasing the wall embedment (d) to 7.5ft rather than 15ft (as for the case of the Reese wall), results in increasing the maximum deflection from 2.8inches to 4.5inches.

Similar to the deflection profiles for dry cracks, the deflection profiles for water filled cracks do not show a point of fixity, neither for the maximum nor minimum embedment ratios. This observation suggests that the behavior of walls during short-term conditions is more of a global movement towards the excavated side.

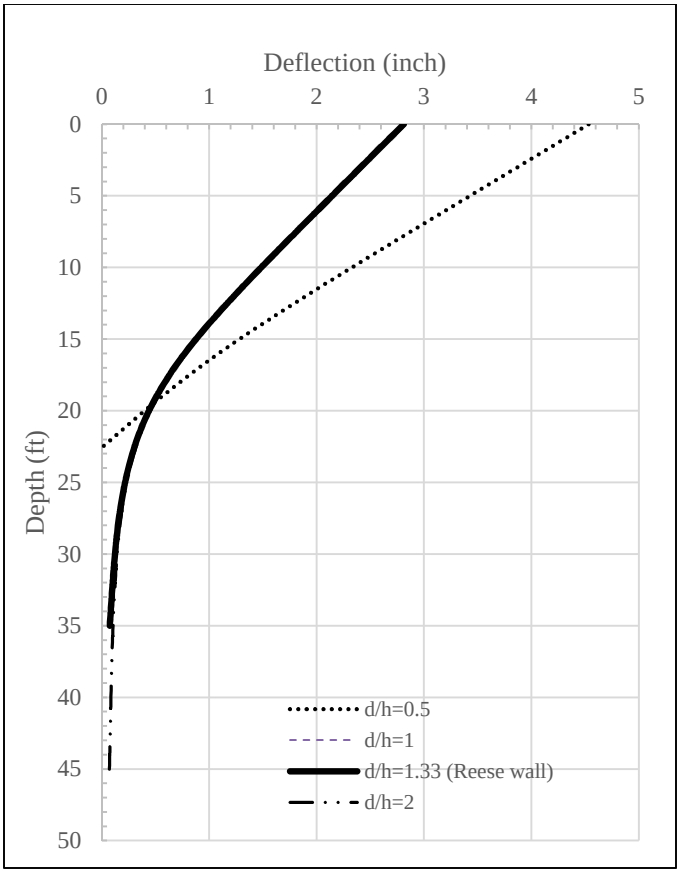


Figure 7.3: Predicted deflection profiles using the Finite Element method of walls with different embedment ratios assuming water-filled cracks conditions

Figure 7.4 presents a comparison between normalized deflection versus embedment ratio relationship for the two conditions, namely, dry cracks and water filled cracks. Results show that the normalized deflection for both cases is asymptotic at an embedment ratio of d/h=1. Building walls with embedment ratio more than d/h=1, does not reduce the maximum deflection at the wall top. However, caution is advised generalizing this conclusion to other walls; because, the Reese wall is stiffer than typical temporary walls since it is intended to be a permanent wall.

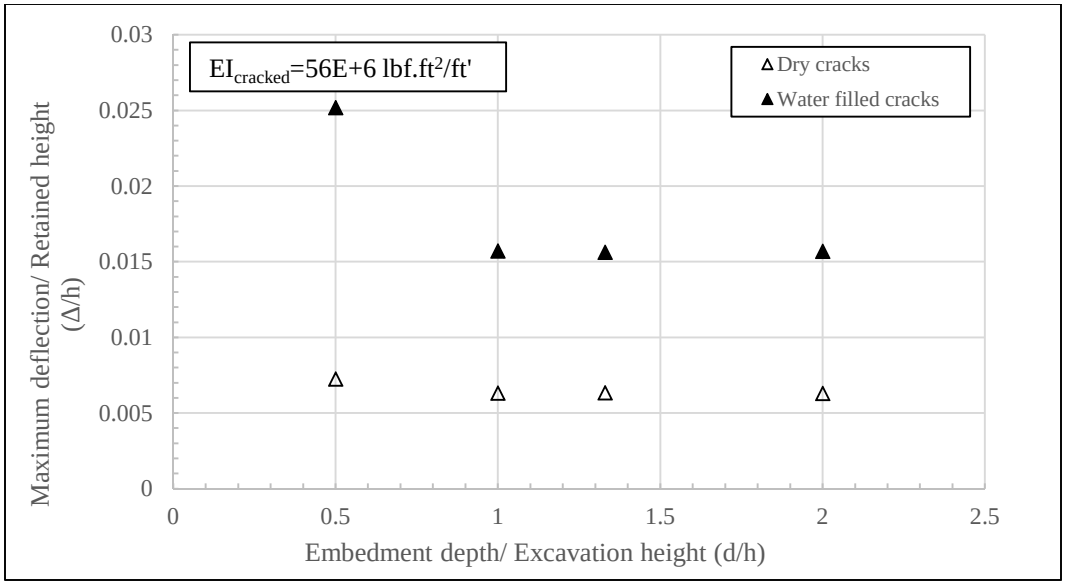


Figure 7.4: Normalized predicted maximum wall deflection of walls with different embedment ratios assuming dry and water filled cracks conditions

Figure 7.5 presents bending moment profiles predicted for walls with embedment ratios ranging between 0.5 and 2 and water filled cracks conditions. Beyond an embedment ratio of d/h=1, the short-term bending moment of walls is not sensitive to the wall embedment ratio, such that, the predicted bending moment profiles for d/h ratios higher than d/h=1 coincide. The predicted maximum bending moment of the Reese wall during short-term conditions and water filled cracks is 115,000lb.ft/shaft, on a side note, the maximum measured bending moment of the Reese wall is 210,000lb.ft/shaft.

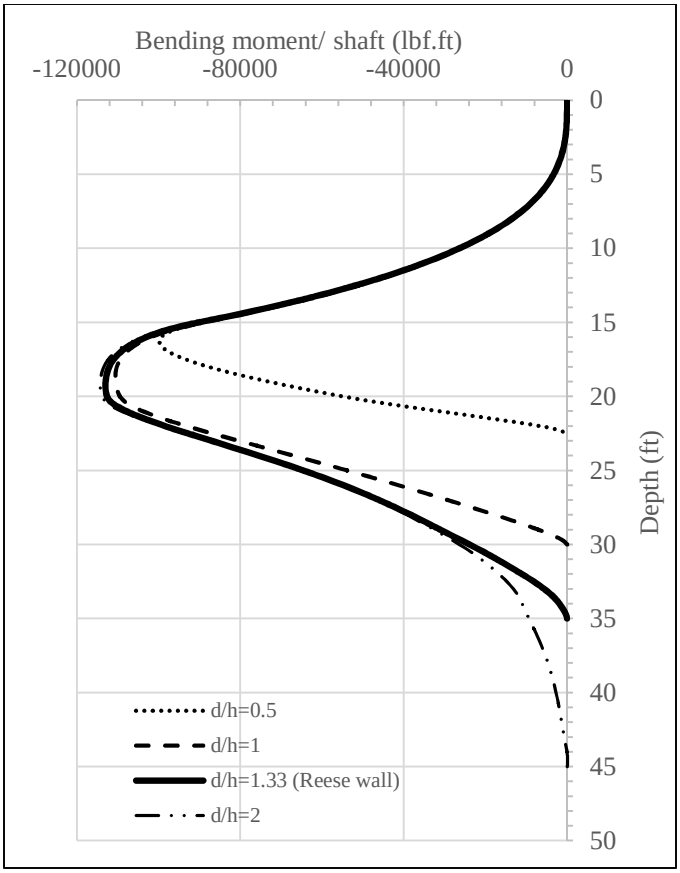


Figure 7.5: Predicted bending moment profiles of walls with different embedment ratios assuming Water-filled cracks conditions

Figure 7.6 presents a comparison between normalized bending moment versus embedment ratio relationship for the two conditions, namely, dry cracks and water filled cracks. Results show that the normalized bending moment for both cases is asymptotic at an embedment ratio of d/h=1.

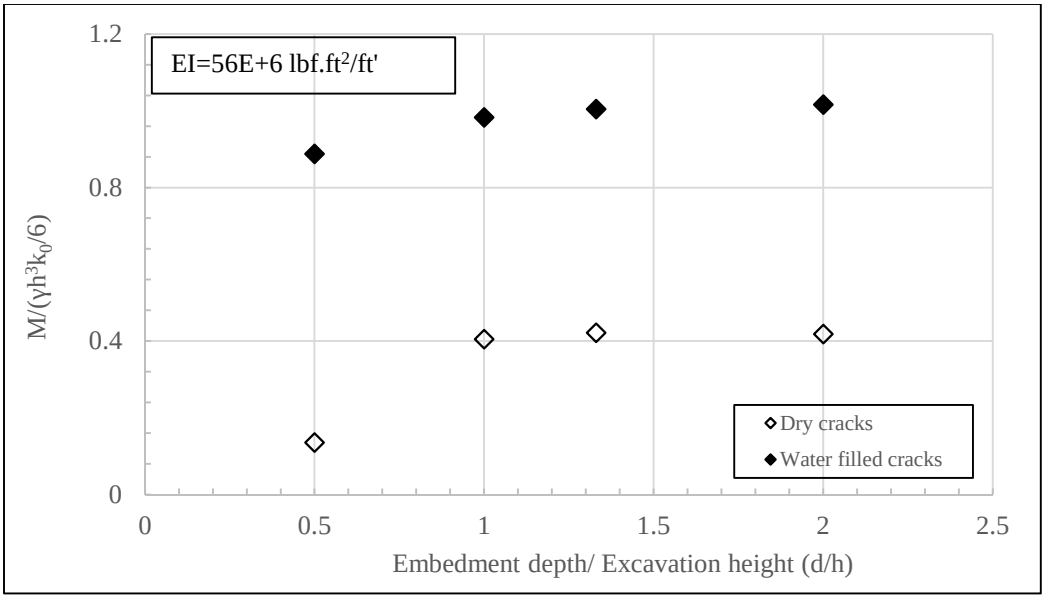


Figure 7.6: Predicted Maximum bending moment normalized to bending moment from linear stress conditions as a function of the wall embedment ratio for: (a) Dry cracks (b) Water-filled cracks conditions

### 6.1.2 Wall stiffness

This section discusses the sensitivity of walls behavior to the bending stiffness (EI) during short-term conditions. As previously discussed in section 3.4, the cracked bending stiffness is adopted for the Reese, i.e., the cracked bending stiffness adopted in the numerical model is EI=56,000,000lb.ft$^2$/ft'. The bending stiffness units is presented per foot run in the out of plane direction; because the model is developed in 2D plane strain conditions. The bending stiffness values adopted in the parametric analysis are calculated for walls with the same reinforcement ratio as the Reese wall (Area steel=1.6%) and variable wall diameters.

Figure 7.7 presents deflection profiles predicted for walls with bending stiffness values ranging between 0, i.e., unrestrained open cut, and 280,000,000lb.ft$^2$/ft' for the dry cracks conditions. The lateral soil movement profile predicted for an open cut condition

shows that the desired soil movement due to excavation is bulging of soil around the excavation level, and the soil below the excavation level tends to move towards the excavated side. The soil movement at the ground surface is 0.5inch, which is less than the soil movement at the bulged depth (0.65inch at depth of 10ft). The presence of a retaining wall tends to linearize the deflection profile, this observation explains the negligible bending moment at the top 10ft of the Reese wall (Figure 6.24).

Figure 7.7 shows that even walls stiffer than the Reese wall do not experience a point of fixity near the wall toe, which emphasizes that the kinematics of the short-term behavior involves global movement in addition to rotational movement.

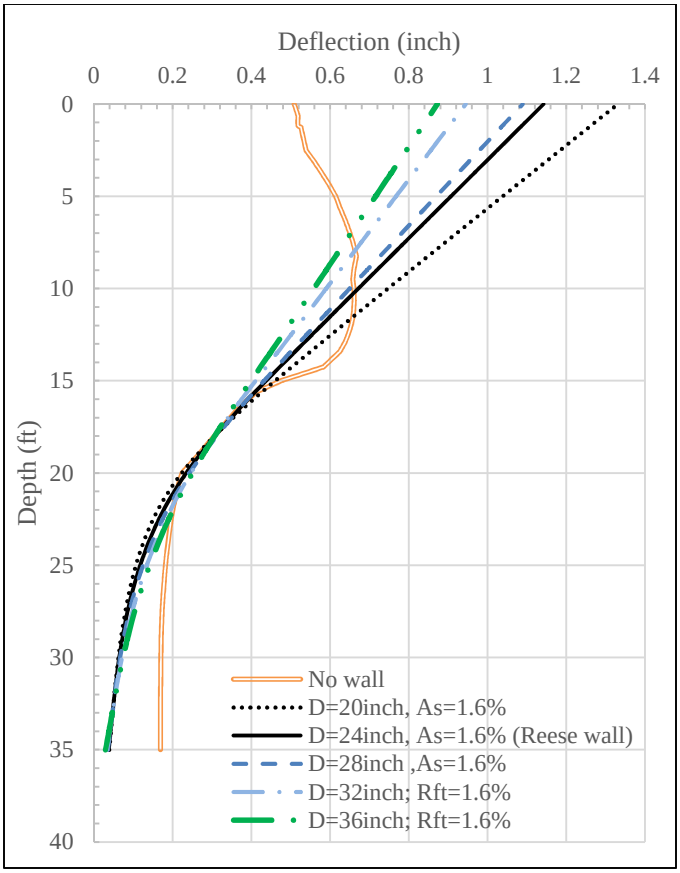


Figure 7.7: Predicted deflection profiles of walls with different stiffness values

Figure 7.8 presents the normalized deflection versus wall bending stiffness. Results show that the wall deflection is slightly sensitive to the wall bending stiffness, for example, increasing the Reese wall stiffness by six folds reduces the maximum deflection from 1.1inch to 0.85inch, i.e., 25% reduction. The normalized wall deflection for an open cut condition is less than the normalized wall deflection of a wall that is six times stiffer than the Reese wall, such that, the normalized deflection for the Reese wall and a wall six folds stiffer are 0.00225 and 0.00175, respectively.

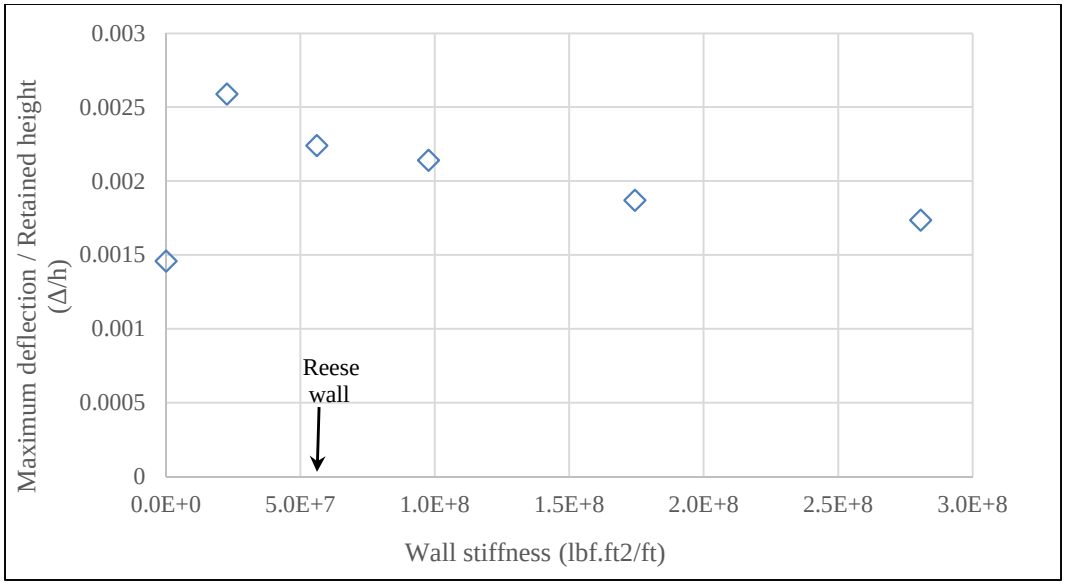


Figure 7.8: Normalized predicted maximum wall deflection of walls with different stiffness values

Figure 7.9 presents bending moment profiles predicted for walls with bending stiffness values ranging between 22,000,000lb.ft/ft' and 280,000,000lb.ft2/ft' for the dry cracks conditions. The figure shows that the location of the maximum bending moment does not vary with variation in the wall stiffness. Given that the wall deflection is not sensitive to the wall bending stiffness, increasing the bending stiffness by definition results in higher bending moment in walls. Figure 7.10 presents the normalized bending moment versus wall bending stiffness. Results show that the wall bending moment is sensitive to the wall bending stiffness

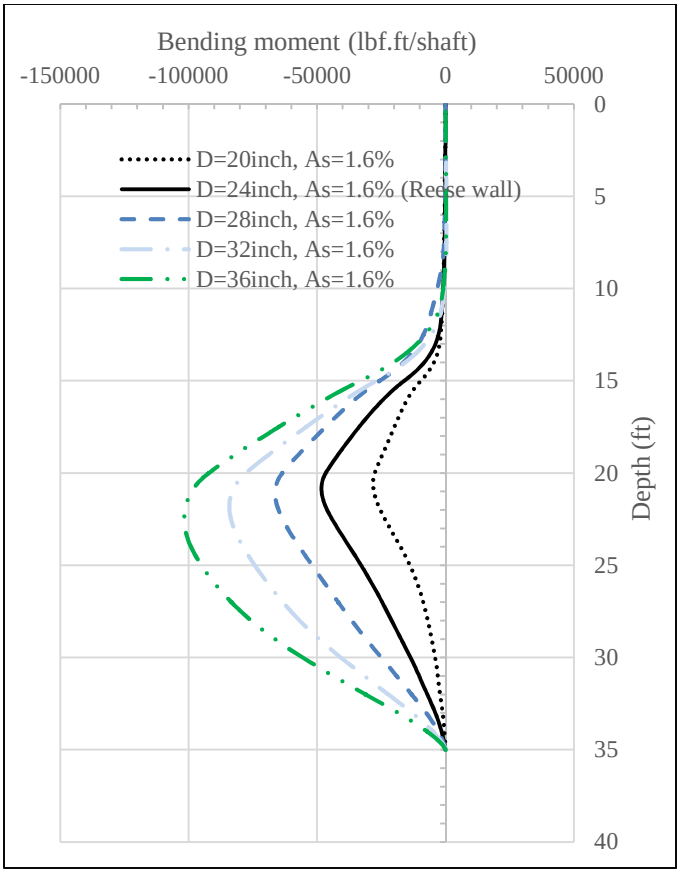


Figure 7.9: Predicted bending moment profiles of walls with different stiffness values

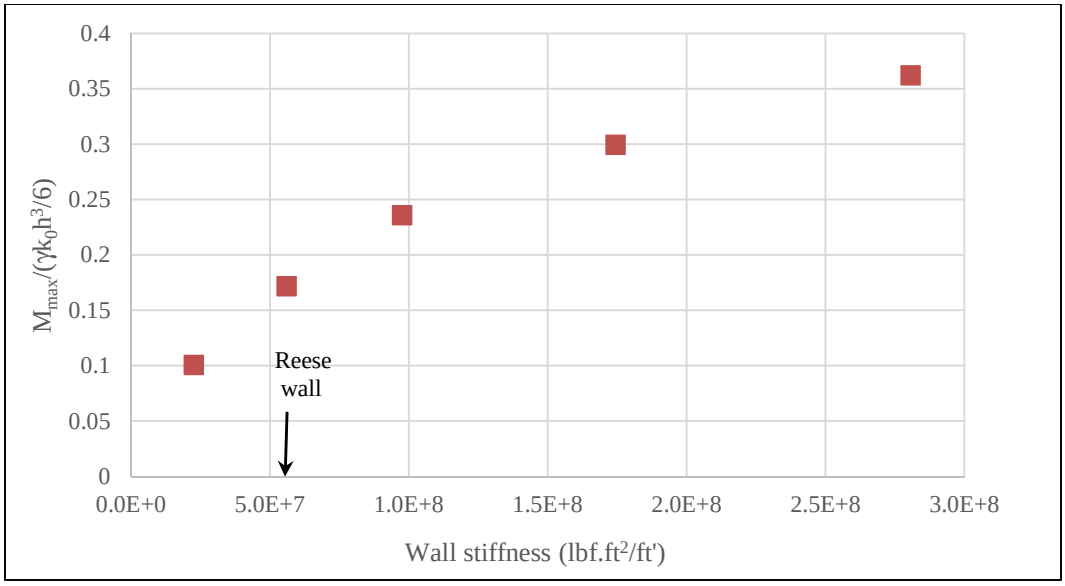


Figure 7.10: Normalized predicted maximum wall bending moment of walls with different stiffness values

## 7.2 Sensitivity of Wall Behavior to Lateral Earth Pressure Coefficient

The Reese wall numerical mode is extrapolated to different cases in parametric analyses to study the sensitivity of the wall embedment depth and wall stiffness on the deflection and bending moment profiles. This section presents results of the parametric analyses conducted to study the sensitivity of walls behavior to the wall design parameters, namely the wall embedment ratio and the wall stiffness.

Smith (2009) attributed the failure of the President George Bush Turnpike Bridge in Northwest Dallas, Texas (Figure 2.16) to underestimating the lateral earth pressure coefficient ($k_0$). Bolton (1990) suggested that the $k_0$ value is less than the insitu undisturbed conditions due to shaft drilling process, drilling sequence, and whether casing is used to support the ground before concrete placement, and suggested that the initial lateral earth pressure on shafts could be limited to the hydrostatic pressure of concrete slump, i.e., $k_0$=1.

This section discusses the sensitivity of walls short-term deflection and bending moment to the initial lateral earth pressure coefficient ($k_0$).

Figure 7.11 presents the deflection profiles predicted for walls retaining soils with lateral earth pressure coefficient ranging between 1 and 3; and, the measured deflection profile of the Reese wall. The figure shows that walls deflection is sensitive to the initial lateral earth pressure coefficient, such that, the maximum wall deflection for $k_0$ values of 1 and 3 are 0.5inch and 3inches, respectively. The figure shows that reducing the $k_0$ value of the top 5ft of soil better matches the predicted and measured deflection profiles than adopting a constant $k_0$ value of 1.6. Figure 7.12 presents the relationship between the normalized maximum wall deflection and the lateral earth pressure coefficient.

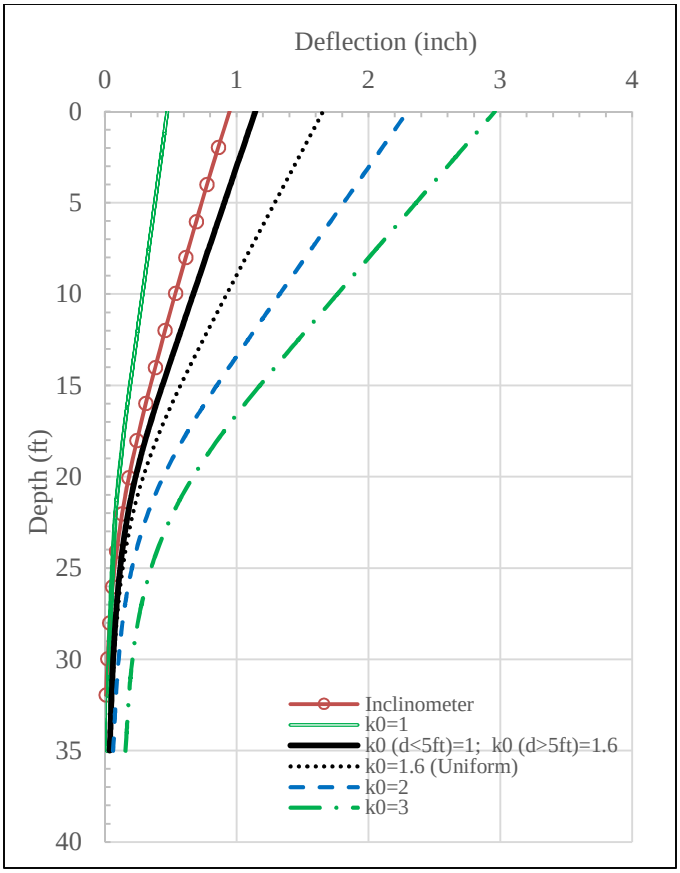


Figure 7.11: Predicted deflection profiles of walls constructed in soil with different initial lateral earth pressure coefficients

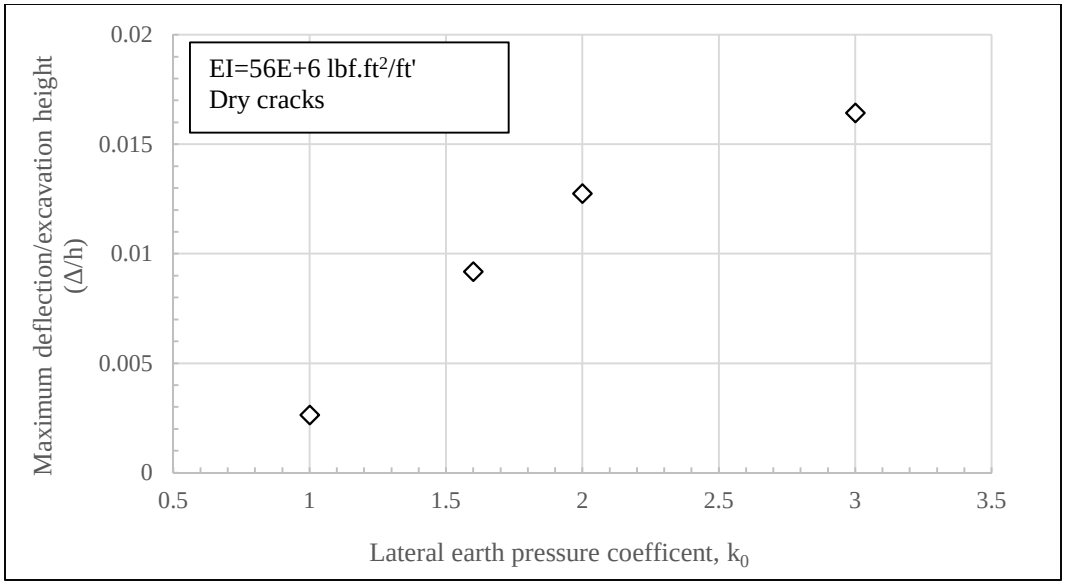


Figure 7.12: Normalized predicted maximum wall deflection of walls subjected to different initial lateral earth pressure coefficient ($k_0$)

Figure 7.13 presents the bending moment profiles predicted for walls retaining soils with lateral earth pressure coefficient ranging between 1 and 3; and, the measured bending moment profile of the Reese wall. The figure shows that walls bending moment profile is sensitive to the initial lateral earth pressure coefficient, such that, the maximum bending moment for $k_0$ values of 1 and 3 are 20,000lb.ft/shaft and 100,000lb.ft/shaft, respectively. Figure 7.14 presents the relationship between the normalized maximum wall deflection and the lateral earth pressure coefficient.

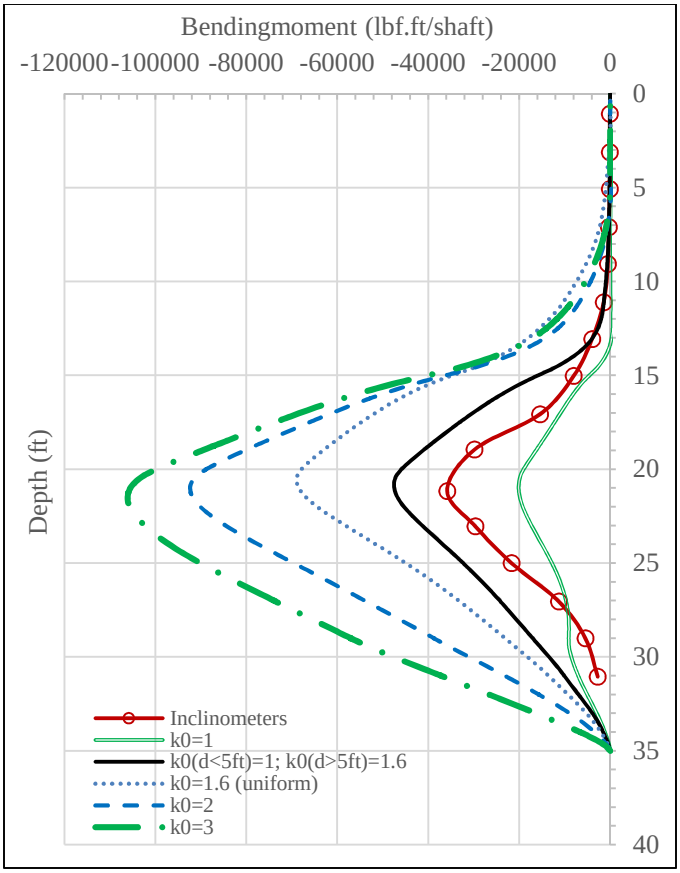


Figure 7.13: Predicted bending moment profiles of walls constructed in soil with different initial lateral earth pressure coefficients

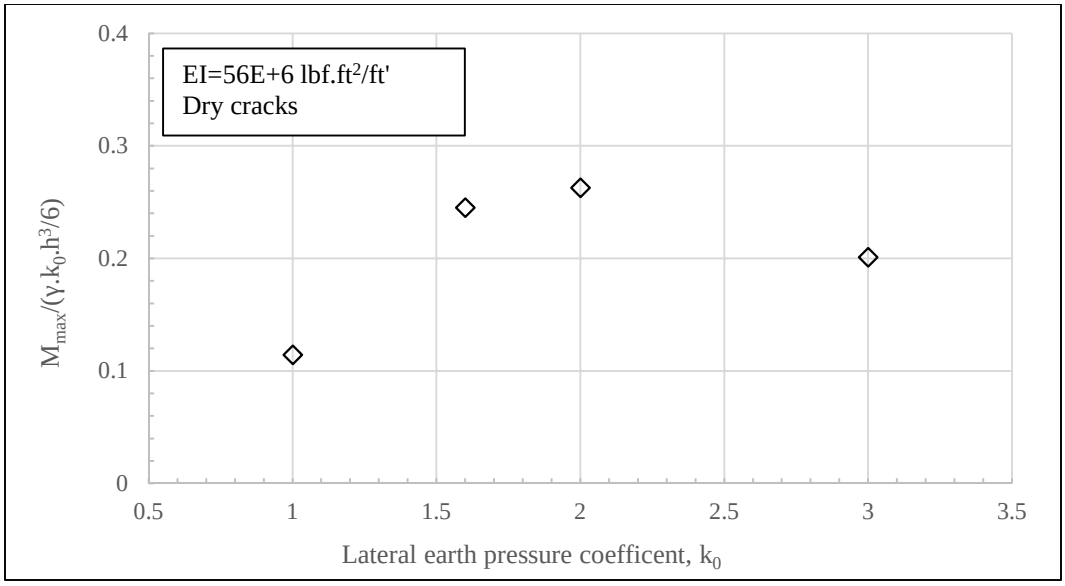


Figure 7.14: Normalized predicted maximum bending moment predictions of walls subjected to different initial lateral earth pressure coefficient ($k_0$)

### 7.3 Sensitivity of the Predicted Behavior to the Soil Constitutive Model

Small-strain stiffness measurement are not common in retaining wall project, more common methods used by practitioner to estimate the soil stiffness are: (i) insitu Pressure Meter Test (PMT) measurement (ii) following a correlation between soil stiffness and undrained shear strength.

PMT was not conducted in the Reese wall site; therefore, a correlation between the SPT measurement and the soil stiffness is adopted to estimate the stiffness that would have been concluded from the PMT test (Figure 7.15). Two correlations are adopted, namely, Ohya et al. (1982) and Bozbey and Togrol (2010). The soil stiffness estimated according to the correlations is adopted in the numerical model, assuming linear elastic constitutive model. Deflection profiles predicted with and without consideration of the small strain stiffness non-linearity are presented in Figure 7.17.

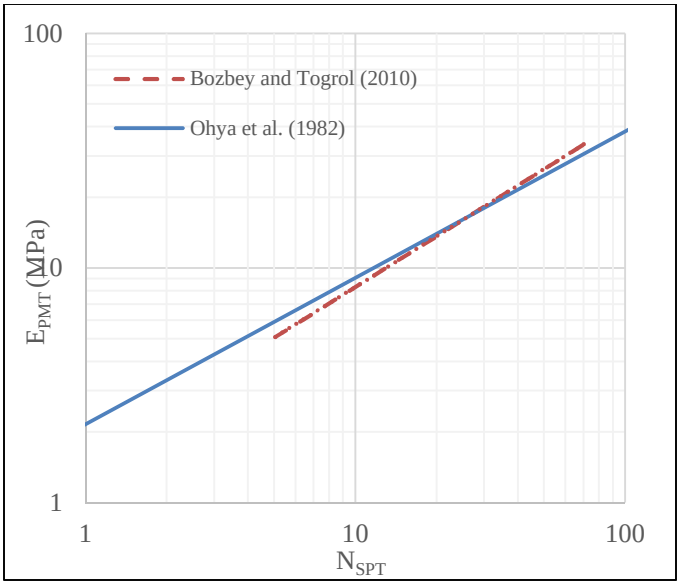


Figure 7.15: Correlation between linear elastic modulus and standard penetration test blow counts (Ohya et al. 1982; Bozbey and Togrol 2010)

Poulos and Davis (1980) correlated the undrained soil stiffness to the undrained shear strength measurements for London Clay (Figure 7.16). The soil stiffness estimated according to the Poulos and Davis correlation is adopted in the numerical model assuming linear elastic constitutive model and the deflection profile is presented in Figure 7.17.

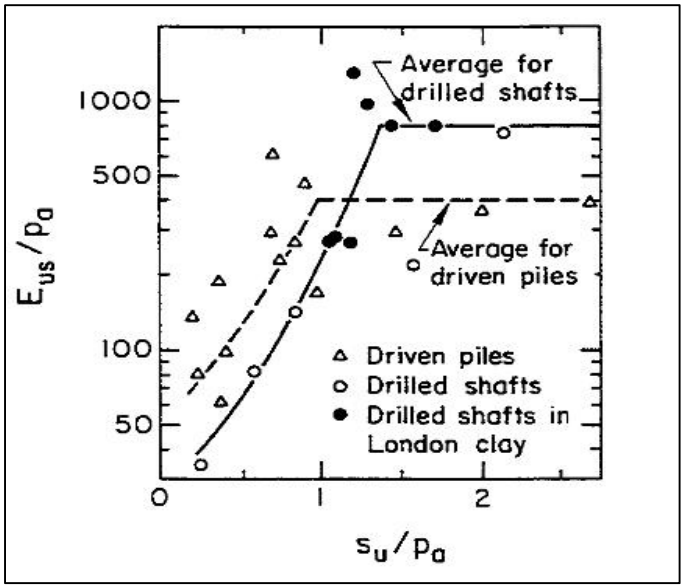


Figure 7.16: Correlation between linear elastic modulus and of undrained shear strength for London Clay (Poulos and Davis 1980)

Figure 7.17 presents a comparison between measured deflection and predicted deflection profiles. Predicted deflection profiles are predicted adopting two constitutive models. First, a constitutive model that accounts for small-strain stiffness non-linearity (Haredning Small Strain model); second, a constitutive model that adopts linear elastic perfectly plastic stress-strain behavior. Linear elastic stiffness are estimated according correlations presented in Figures 7.15 and 7.16. Comparison between predicted deflection profiles show that the deflection profile predicted adopting the Hardening Small Strain model results in the most reasonable agreement with the measured deflection. Deflection profiles that are predicted adopting the Linear Elastic Perfectly Plastic model overestimates the wall deflection.

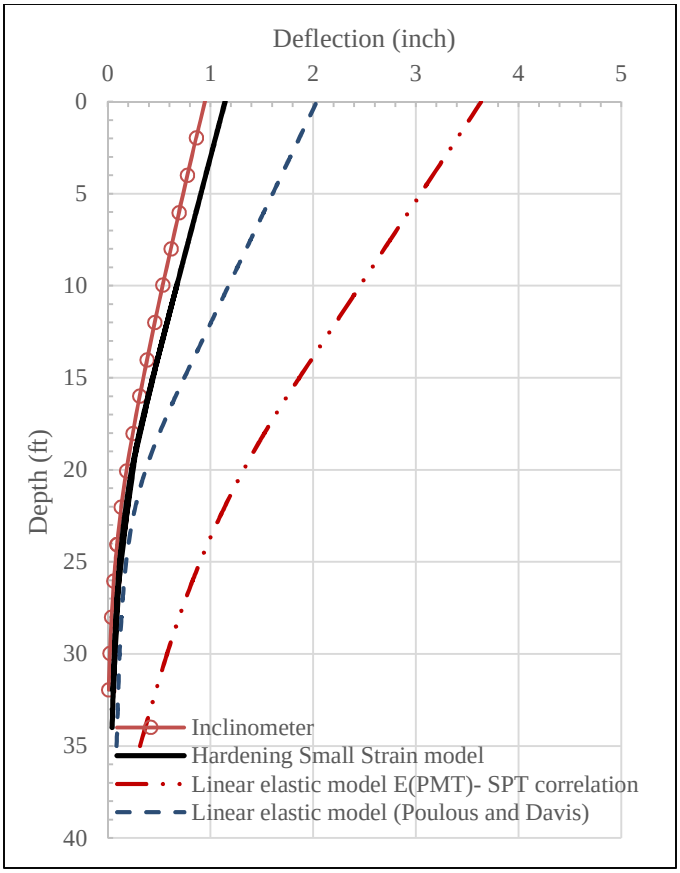


Figure 7.17: Comparison between (i) measured deflection profile (ii) predicted deflection profile adopting HSS model (iii) predicted deflection profile adopting linear elastic modulus from pressure meter estimates (iv) predicted deflection profile adopting linear elastic modulus from Poulos and Davis 1980 reduction factor

Figure 7.18 presents a comparison between measured bending moment and predicted bending moment profiles. Comparison between predicted bending moment profiles show that the profile predicted adopting the Hardening Small Strain model results in the most reasonable agreement with the measured profile. Deflection profiles predicted adopting Linear Elastic Perfectly Plastic model overestimates the wall deflection.

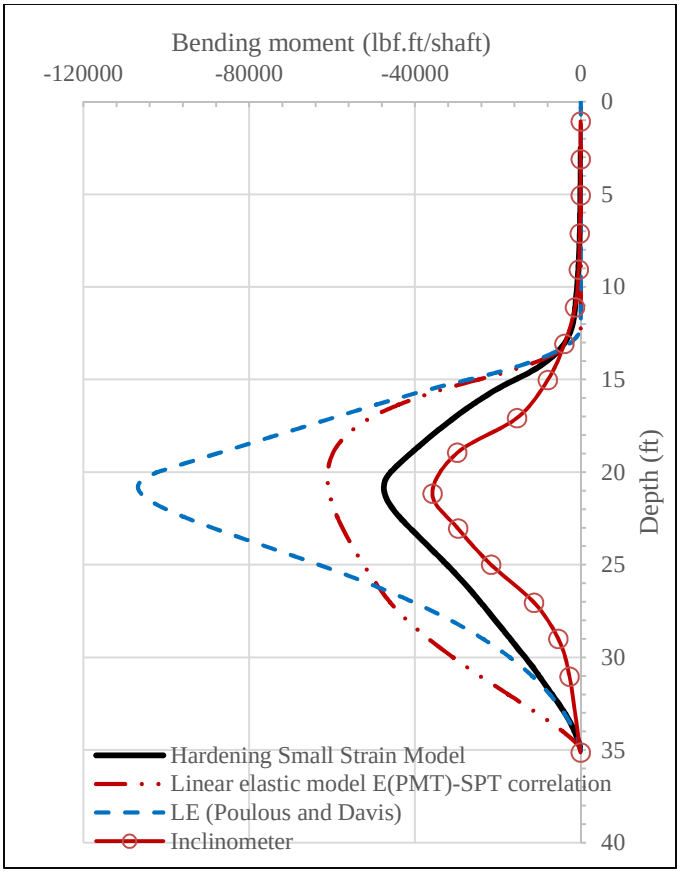


Figure 7.18: Comparison between (i) measured bending moment profile (ii) predicted bending moment profile using HSS model (iii) predicted bending moment profile using linear elastic modulus from pressure meter estimates (iv) predicted bending moment profile using linear elastic modulus from Poulos and Davis 1980 reduction factor

Agreement of the measured deflection and bending moment profile with profiles predicted adopting the HSS model suggests that small-strain stiffness measurement is important in describing the behavior of walls during short-term conditions. Neglecting the small-strain stiffness nonlinearity results in overestimation of the deflection and bending moment.

This chapter studied the sensitivity of walls behavior to wall design parameters such as wall embedment and wall stiffness, and, soil constitutive model. First, the parametric analysis studying the sensitivity of walls behavior to wall embedment showed that walls behavior is not very sensitive to the wall embedment for walls with embedment ratios deeper than 1. Second, the parametric analysis studying the sensitivity of walls behavior to wall stiffness showed that the increasing the wall stiffness decreases the wall deflection; however, the deflection reduction might not be very significant. Second, the sensitivity of the wall behavior to the lateral earth pressure coefficient is presented, and the parametric analysis showed that the $k_0$ value of 1.6, computed from literature correlations, is considered acceptable. Third, the sensitivity of the predicted wall behavior to the adopted constitutive model showed that adopting a model that does not account for the stiffness non-linearity of the soil would overestimate the predicted wall deflection.

The following section of this study (Section II) presents the numerical model results and sensitivity analyses of the Reese wall during long-term conditions. Describing the behavior of the long-term conditions is more challenging than the short-term conditions; because, it involves the response of walls due to variation in the soil degree of saturation. Section II starts by presenting a framework that will be used throughout the rest of the study to describe the behavior of partially saturated soils subjected to changes in the degree of saturation (Chapter 8). Then, the developed framework is adopted for the Reese wall project, and the predicted behavior is compared to the measured behavior in order to assess the applicability of the developed framework (Chapter 9). Later, the sensitivity of the predicted behavior to key parameters encountered in the framework are tested; the parametric analyses also include sensitivity of walls behavior to wall design parameters such as wall embedment and wall stiffness.

# SECTION II: LONG-TERM BEHAVIOR OF WALLS

# CHAPTER 8: DEVELOPING A FRAMEWORK TO DESCRIBE THE BEHAVIOR OF PARTIALLY SATURATED SOILS SUBJECTED TO VARIATION IN THE DEGREE OF SATURATION

This chapter presents a developed framework that proposedly could be used to describe the swelling strains and behavior of partially saturated soils subjected to variation in the degree of saturation. After the bases of the framework are presented, the measured swelling strains of one-dimensional oedometer tests are compared with predicted swelling strains.

Partially saturated soil that is subjected to variation in the degree of saturation exhibit changes in the total soil volume. Soil swell potential is evaluated in the laboratory by one of two methods; either, in a strain controlled test where the partially saturated soil is inundated and the corresponding swell pressure is measured (ASTM D4546-14 Method A), or, in a stress controlled test where the partially saturated soil is inundated the swell strain is measured (ASTM D-4546, Method B). As partially saturated soil is inundated more water fills the soil voids which changes the pore-air pressure and the pore-water pressure, and consequently changes the effective stresses in the soil skeleton.

The effective stress in partially saturated soil is generally described following, Bishop (1959) schools of thought. A more recent study by Lu and Likos (2006) suggested that the effective stress in partially saturated soil could be described according to total stress and the soil degree of saturation. This chapter discusses different ideologies in describing the effective stress definition. The objective of this chapter is to develop a framework that could be used to describe the swell potential of partially saturated soil. The framework adopts the relatively new definition of effective stresses, proposed by Lu and Likos (2006),

to explain the swelling of partially saturated soils phenomenon, such that the soil swelling is attributed to the loss of effective stresses associated with soil inundation.

## 8.1 History of the Effective Stress Definition

Terzaghi (1923) introduced the effective stress expression and modelled the behavior of the soil with the spring analogy. The soil skeleton is modelled as a spring, and the pore-water is modelled as the water around the spring trapped with an orifice. Terzaghi (1923) described the effective stress according to Equation 8.1, where σ is the total stress in soil and water, σ' is the stress in the soil skeleton, and $u_w$ is the pore-water pressure.

$$\sigma' = \sigma - u_w \qquad \text{Equation 8.1}$$

Terzaghi's analogy assumes that the soil is a two-phased material consisting of soil skeleton and pore-water. Aitchison and Donald (1956) showed that, provided that the soil remains fully saturated, Terzaghi's effective stress definition remains adequate, even if the pore-water pressure is in suction, the suction contributes directly to the effective stress. Jennings and Burland (1962) suggested that the effective stress approach is adequate if the level of saturation is higher than a critical degree of saturation; their study suggested that the critical degrees of saturation are 50% and as high as 90% for sand and clay soils, respectively.

During different circumstances such as changes in the ground water table, evapotranspiration, etc. air enters the pore spaces and the soil becomes a three-phased material consisting of soil skeleton, pore-water and pore-air. Once the soil material becomes three-phased material the soil skeleton is in contact with pore-water and pore-air. Jennings (1957), Corney et al (1958), Bishop (1959), and Aitchison (1960) modified Terzaghi (1923)'s definition of the effective stress for partially saturated soils to account for macroscopic pore-water and pore-air pressures. Bishop (1959) introduced an effective

stress expression for partially saturated soil (Equation 8.2), Bishop's expression gained more attention that others because it includes a term for the pressure in the gas phase.

$$\sigma' = \sigma - u_a + \chi(u_a - u_w) \qquad \text{Equation 8.2}$$

Bishop (1959) conceptually related the coefficient $\chi$ to the degree of saturation (S) without defining a mathematical correlation between the two parameters. Bolt (1956), Lamb (1960), and Skempton (1960) showed that the microscopic Van der Waals attraction and electrical double layer repulsion affect the effective stress. Researchers lumped the causes of particle to particle stresses and attempted to correlate the coefficient $\chi$ to various state parameters. For example, Khalili and Khabbaz (1994) and (2004) correlated the coefficient $\chi$ to matric suction normalized by air entry suction; Bishop (1959), Houlsby (1997), Borja (2004), Karube (1986) and Vanapalli et al. (1996) correlated the coefficient $\chi$ to the degree of saturation; Karube (1986), Vanapalli et al. (1996) and Lu and Likos (2004) correlated the coefficient $\chi$ to the effective degree of saturation.

Alonso et al. (1992) developed the "Basic Barcelona Model" which adopt Bishop (1959)'s definition of effective stress and Fredlund and Morgenstern (1977)'s ideology of describing the partially saturated soil with two independent stress variables. The model requires two sets of soil parameters to describe the soil model: first, parameters related to the total stress over air pressure ($\sigma$-$u_a$), second, parameters related to the matric suction ($u_a$-$u_w$).

## 8.2 Difficulties of Implementing Two Stress Variables

### 8.2.1 Matric suction measurement

Several tests are available to measure the matric suction of soil; however, the accuracy of each of these tests are compromised beyond a certain range of matric suction.

Suctions stresses could reach several atmospheres negative on the absolute pressure scale (Bocking and Fredlund 1980); which, causes difficulties measuring matric suction for wide range of suction stresses, both in the laboratory and insitu. The following present different sources of difficulties encountered in measuring matric suction of partially saturated soil.

***Cavitation***

Cavitation is the phenomenon of changing of water from the liquid state to the gaseous state due to drop in pressure, the cavitation of water takes place at approximately a pressure of -1atm. Cavitation is problematic in measuring the matric suction because once water vapor bubbles reaches pressure transducers it results in anomalous matric suction measurements.

Hilf (1956) developed the "axis-translation" technique to overcome problems associated with cavitation. Axis-translation technique basically raises both of the air pressure and water pressure with the same pressure while keeping the difference (i.e. the matric suction) constant. Axis-translation technique is only applicable in the laboratory where engineers have control over the confining pressure of the partially saturated soil e.g. the pressure plate test. The confining pressure in the pressure plate test is applied with chamber air-pressure and the water pressure is applied with controlling matric suction stress of high air-entry ceramic desk (Figure 8.1). Two conditions have to be satisfied for the axis-translation technique to be applicable; first, the confining pressure in the air chamber should be equal to the pore-air pressure within the specimen, second, the high air-entry ceramic desk should be fully saturated. Olson and Langfelder (1965) suggested that for the chamber air pressure to be equal to the pore-air pressure, the pore-air pressure within the soil has to be continuous. Corey (1957), Ladd (1960), Olson (1963), and Langfelder et al. (1968) showed that discontinuity of air occurred around the optimum water content.

Bocking and Fredlund (1980) estimated that applying the axis translation technique for soils with occluded air bubbles (i.e. discontinuous air) might result in overestimating the measured matric suction by up to 100 percent or more. Difficulties ensuring the second condition required for applying the axis-translation technique is discussed in the following subtitle.

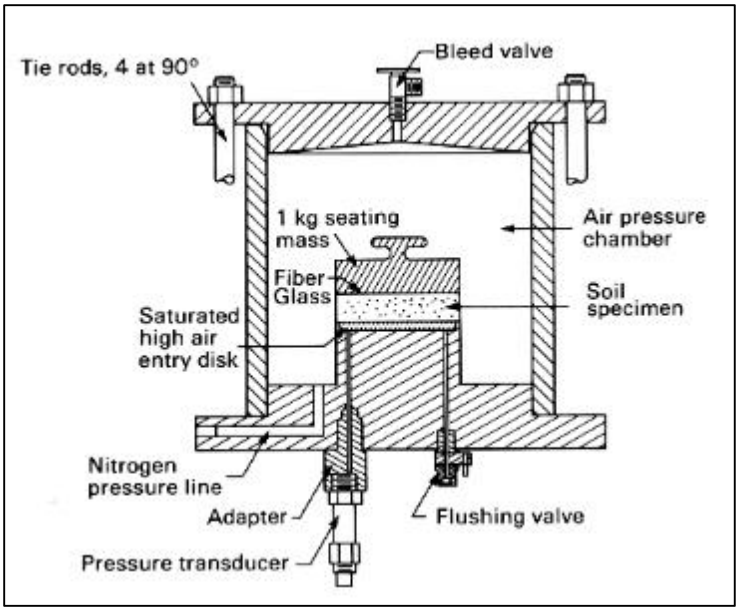


Figure 8.1: Schematic diagram of pressure plate apparatus (Olson and Langfelder 1965)

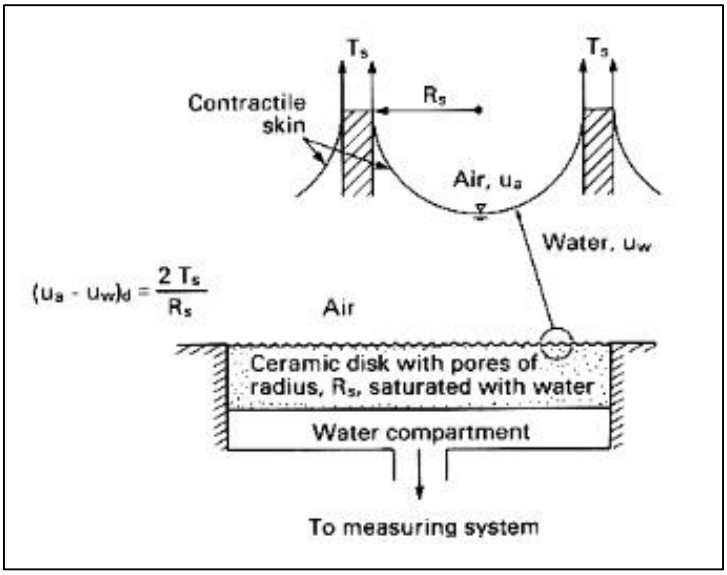


Figure 8.2: Operating principle of a high air-entry porous stone as described by Kelvin's capillary model (Fredlund and Rahardjo, 1993).

***Air diffusion***

Air diffusion is defined as the movement of air from the region with higher air concentration to the region with lower air concentration (Fredlund and Rahardjo, 1993). Matric suction measurement methods such as pressure plate method or filter paper method rely on measuring the water pressure in a fully saturated medium such as ceramic desk in the pressure plate test, and filter paper in filter paper test. The accuracy of matric suction measurement could be compromised if the air present in the unsaturated soil specimen diffuses through the fully saturated medium. Presence of air within the high air-entry porous medium and within the de-aired water connected to pressure transducer result in anomalous measurements of the matric suction.

***Indirect measurement (Electrical conductivity of soil)***

Indirect methods could be used to estimate the soil matric suction, by measuring a soil state parameter that is related to the soil matric suction, such as, gravimetric water

content, or volumetric water content. However, these indirect methods require prior knowledge of the Soil Water Retention Curve (SWRC) i.e., the relationship between the water content and the matric suction. Time Domain Reflectometry (TDR) probes were installed in the Reese wall site. TDR probes measure the electrical conductivity of the partially saturated soil and estimate the gravimetric water content, which could be used to estimate the soil matric suction.

Dellinger (2011) showed that difficulties can be expected measuring the dielectric constant of partially-saturated high-plasticity clays. Partially-saturated high-plasticity clays exhibit high electrical conductivity, which affects measurement of matric suction that relies on electrical conductivity.

### 8.2.2 Soil behavior parameters

***Shear strength***

Fredlund and Morgenstern (1977) adopted Bishop (1977) definition of effective stress and recommended that two independent sets of measurements is necessary to describe the behavior of partially saturated soil. The first set of measurement describes the soil behavior with respect to the first stress variable ($\sigma$-$u_a$); and the second set of measurements describes the soil behavior with respect to the second stress variable ($u_a$-$u_w$). For example, the shear strength envelope of partially saturated soil following the Fredlund and Morgenstern (1977)'s ideology is described by Equation 8.3; where $\phi$' is the friction angle of the soil skeleton and $\phi'_b$ is an additional friction angle to capture the contribution of matric suction to shear strength.

$$\tau = \sigma - u_a \tan\varphi' + u_a - u_w \tan\varphi'_b \qquad \text{Equation 8.3}$$

Determining the shear strength parameters in Equation 8.3 requires control of confining stress and matric suction. Adding to the complications of accurately determining the matric suction, controlling the matric suction of partially saturated soil is a time consuming procedure; because, permeability of partially saturated soil decreases significantly as clay soils becomes less saturated.

***Stress strain behavior***

Alonso (1990) proposed a minimal experimental program that combines basic stress paths required to determine the parameters of the Basic Barcelona Model (Figures 8.3a, 8.3b, and 8.3c). The experimental program consists of:

1- Volumetric strain measurement corresponding to increase in the matric suction, followed by volumetric strain measurement corresponding to a cycle of isotropic hardening (Figure 8.3a).

2- Volumetric strain measurement corresponding to a cycle of matric suction variation, followed by volumetric strain measurement corresponding to a isotropic loading, followed by volumetric strain measurement corresponding to loading-unloading cycle followed by shear strain measurement corresponding to shearing to failure (Figure 8.3b).

3- Volumetric strain measurement corresponding to an increase in matric suction, followed volumetric strain measurement due to isotropic loading, followed by shear strain measurement corresponding to shearing to failure (Figure 8.3c)

Each test should be conducted at least three times at a range of stresses close to the anticipated stress levels to evaluate soil parameters. The applicability of adopting the BBM is challenged because of the complexity and time consuming tests. The following section presents an effective stress definition proposed by Lu and Likos (2006). Adopting Lu and

Likos (2006)'s definition of effective stress could bypass practitioners from relying on matric suction measurements and from running complicated laboratory measurements.

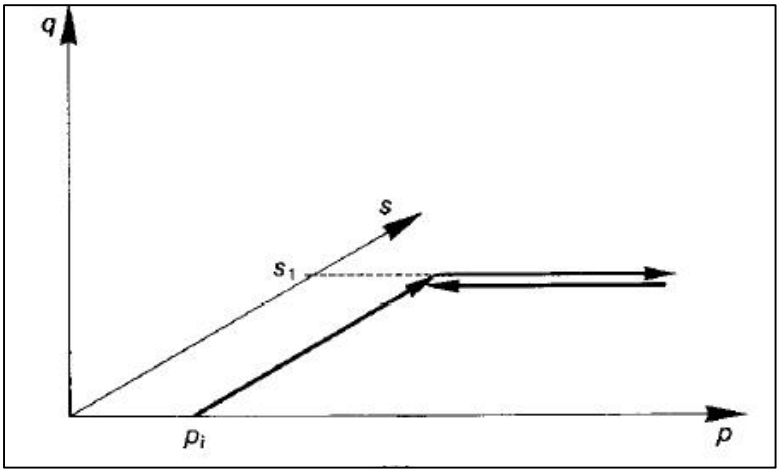


(a)

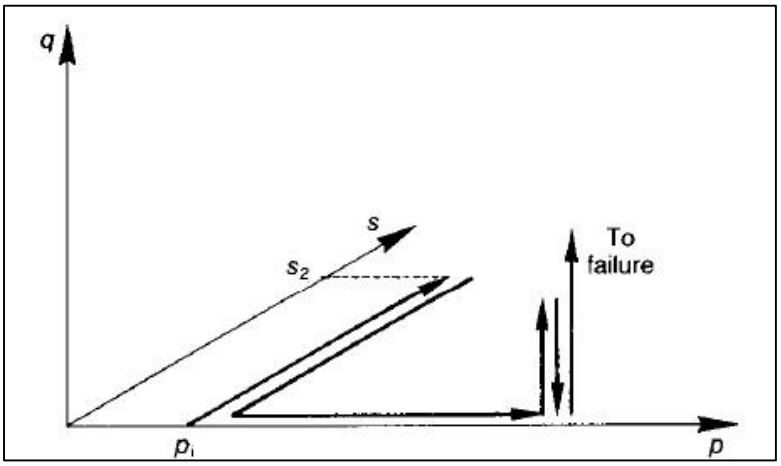


(b)

Figure 8.3 continued next page

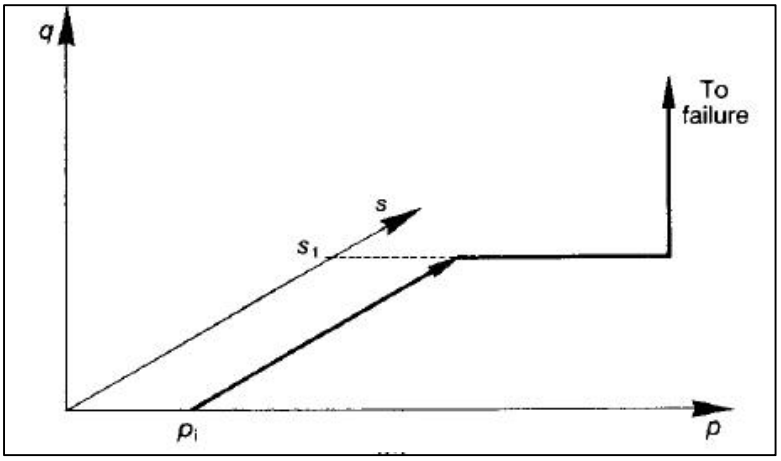


(c)

Figure 8.3: Tests required to determine the Basic Barcelona model parameters (Alonso et al 1990)

### 8.3 LU AND LIKOS (2006) EFFECTIVE STRESS DEFINITION

Lu and Likos (2006) proposed an effective stress definition that bypass practitioners from measuring the matric suction. They defined the effective stress according to Equation 8.4, where $\sigma_s$ is the termed as the "suction stress". Comparison between Equation 8.2 and Equation 8.4 shows that the suction stress is a different stress than the matric suction. The matric suction is multiplied by the $\chi$ coefficient to obtain the additional effective stress in the soil skeleton due to the pore-water and pore-air pressure, while, the suction stress is essentially an isotropic effective stress.

$$\sigma' = \sigma - u_a + \sigma_s \qquad \text{Equation 8.4}$$

The advantages of describing the effective stress due to partial saturation of soil in terms of an effective stress expression rather than in terms of $\chi$ coefficient and matric suction are: first, uncertainties associated with describing a unique function of the $\chi$ coefficient is avoided. Second, necessity of measuring the matric suction of partially saturated soil is also avoided. Third, effective stress terminology accounts for effective

stresses due to particle to particle attraction and repulsion forces other than capillary forces. Fourth, the behavior of partially saturated soil is described according to a single stress variable (effective stress) instead of two stress variables (total stress- air pressure, and matric suction), which simplifies the constitutive relations of the partially saturated soils.

Figure 8.4 and Figure 8.5 present schematic variations of inter-particle forces (e.g. Van der Waals attraction, capillary attraction, cementation, and double layer repulsion) with respect to the soil degree of saturation and the soil particle size, respectively. Lu and Likos (2006) concluded that the microscopic inter-particle stresses scaled up to a macroscopic effective stress i.e. the suction stress $\sigma_s$.

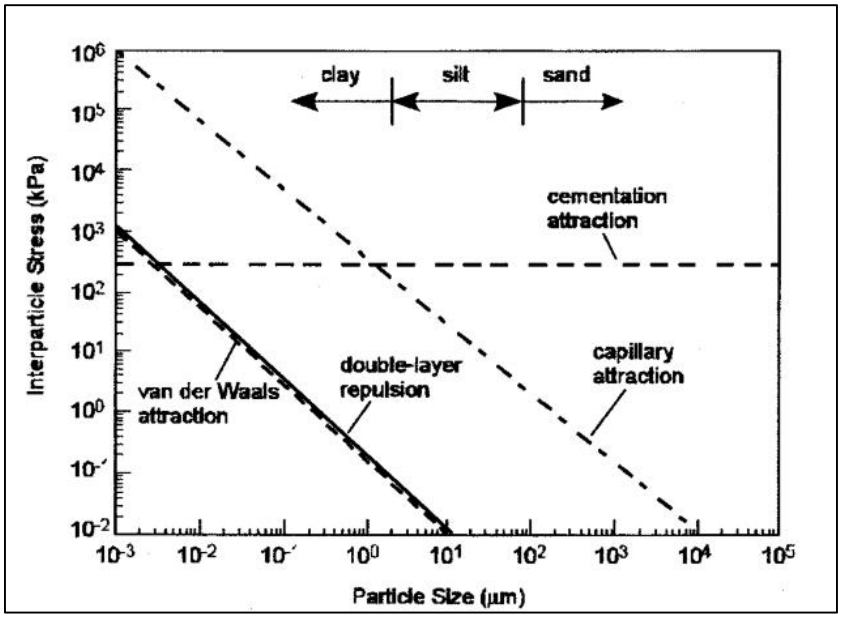


Figure 8.4: Schematic relationship between particle size and suction stress (Lu and Likos 2006)

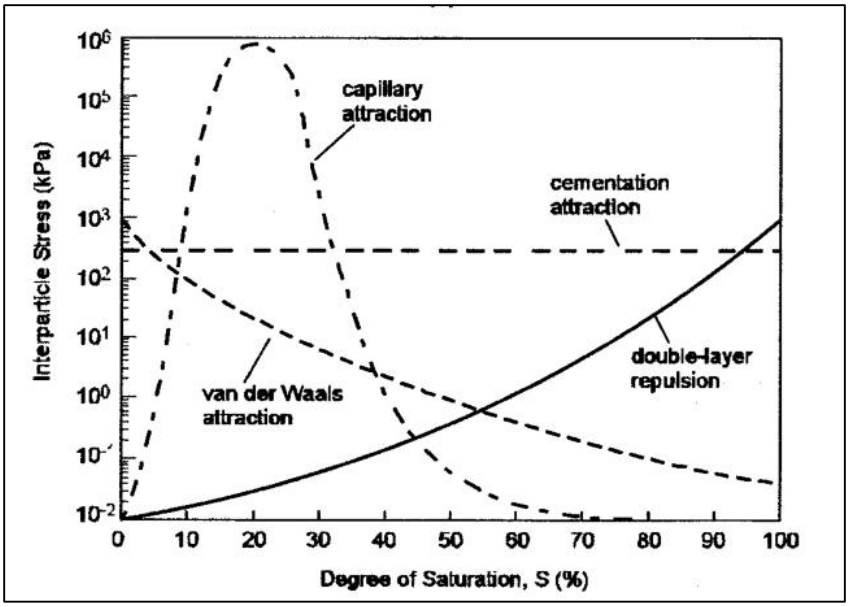


Figure 8.5: Schematic relationship between effective degree of saturation and suction stress (Lu and Likos 2006)

In order to implement the Lu and Likos (2006)'s definition in describing the effective stress of partially saturated soil, knowledge of the suction stress is required. However, unlike matric suction, suction stress cannot be measured; because, the suction stress is the internal soil skeleton effective stress. Section 8.4 presents Lu and Likos (2006)'s methodology of estimating the suction stresses of partially saturated soil.

## 8.4 ESTIMATION OF SUCTION STRESSES

Escario (1980) evaluated shear strength envelopes of the Madrid gray clay at different degrees of saturation (Figure 8.6). Results showed that the shear strength envelope depends on the degree of saturation of the soil. Lu and Likos (2006) extended shear strength envelopes beyond the apparent cohesion intercept i.e., y-axis. Figure 8.7 present a schematic shear strength envelope that extended beyond the apparent cohesion intercept and the shear strength envelope is extended to the effective stress axis i.e., x-axis.

Intersection of the shear strength envelope with the effective stress envelope i.e., tensile strength is plotted against matric suction measurement (Figure 8.7-quadrant III). Lu and Likos (2006) defined the relationship between the effective stress and the matric suction as the "Soil Suction Characteristic Curve" (SSCC).

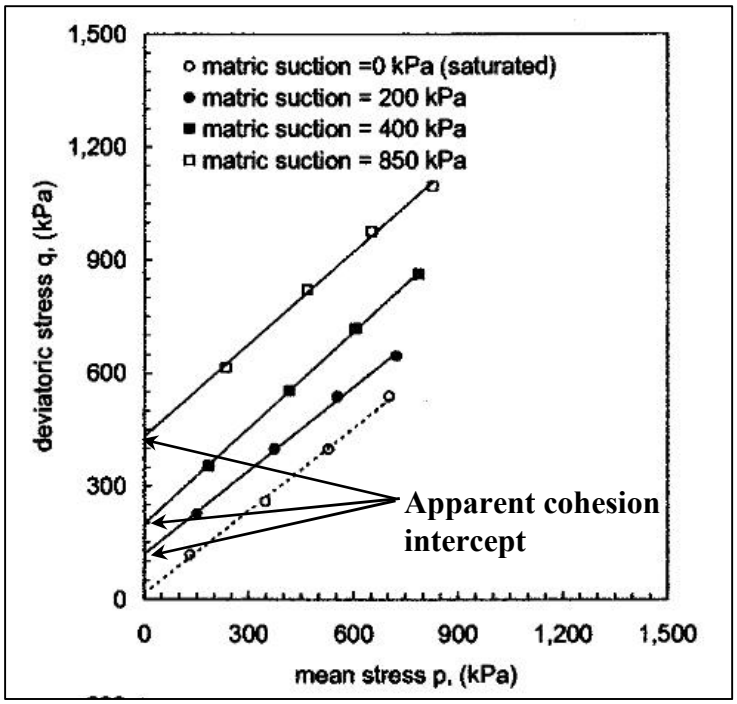


Figure 8.6: Mohr-coulomb failure criteria for Madrid gray clay under saturated and unsaturated conditions in p-q space (Escario 1980)

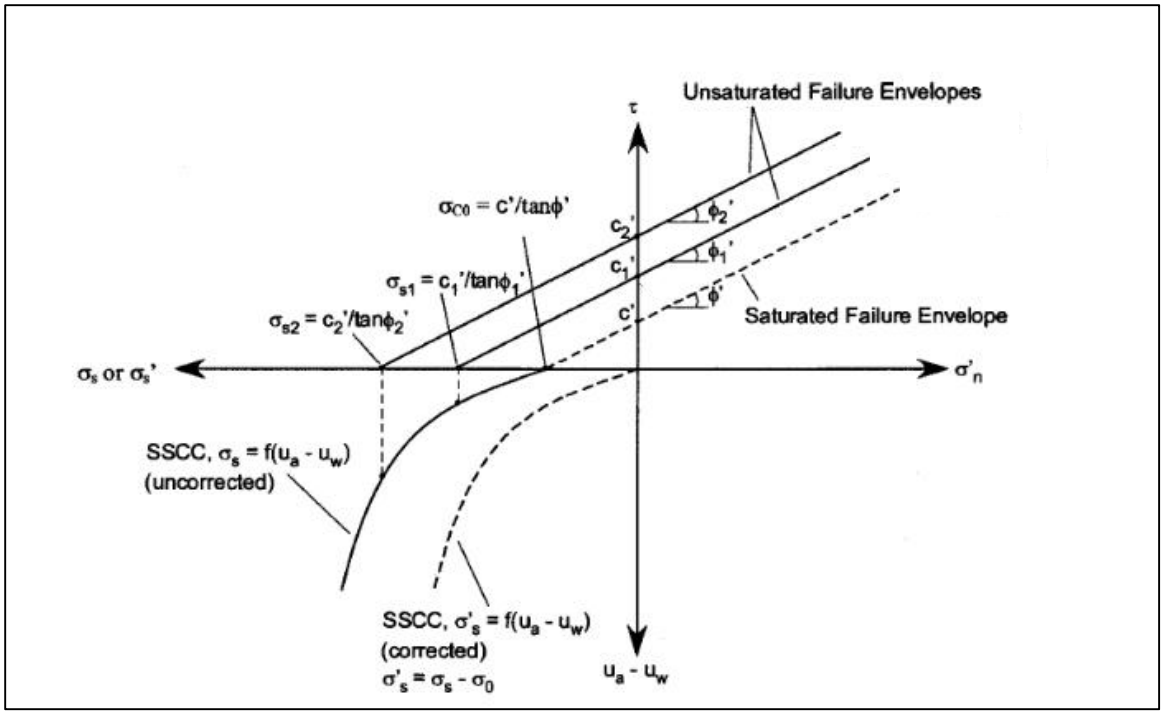


Figure 8.7: Illustrated methodology for quantifying suction stress characteristic curve from Mohr–Coulomb type failure experiments (Lu and Likos 2006)

Lu and Likos (2006) calculated the suction stresses from the shear strength measurements of the gray Madrid Clay that are presented in Figure 8.6, estimated a SSCC of the soil (Figure 8.7), and then described the shear strength envelope of these tests in terms of their new definition of effective stresses (Figure 8.8). In other words, Figure 8.8 presents the shear strength envelope obtained by Lu and Likos (2006) for the same shear strength measurements reported by Escario (1980) of the partially saturated gray Madrid Clay. The figure shows that the adopting Lu and Likos (2006)'s definition of effective stress results in a unique shear strength envelope for samples with different saturations levels. Defining a unique shear strength envelope of partially saturated soil is useful because it means that the effective stress in partially saturated soil could be inferred if the shear strength is measured and the unique shear strength envelope is known.

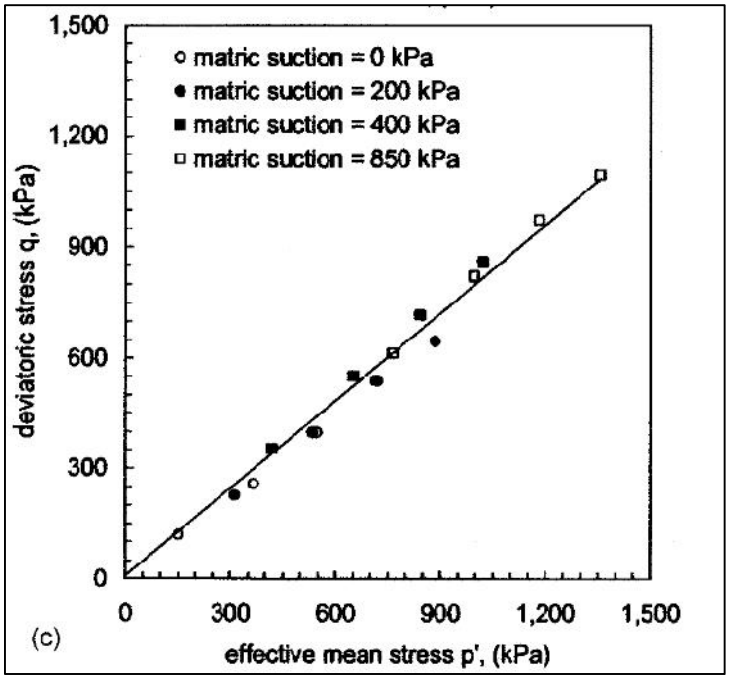


Figure 8.8: Mohr Coulomb failure for Madrid gray clay under saturated and unsaturated conditions in p'-q space (Lu and Likos 2006)

Lu and Likos (2006) stated that the SSCC relationship may also be described as a relationship between suction stress and the degree of saturation. Therefore, this ideology bypass practitioners from running complicated and time consuming suction controlled tests, and replace it with conventional laboratory shear strength testing procedures conducting water-content-controlled tests.

Adding to the advantages of describing the effective stress of partially saturated soil in terms of suction stress rather than the matric suction, presented in the previous section; Lu and Likos (2006) stated that adopting the suction stress ideology significantly enhances our capabilities of real-time field monitoring of partially saturated soil. Because, the current capabilities of measuring insitu water content far exceeds that of measuring the matric suction.

## 8.5 CLOSED-FORM EQUATION OF SUCTION STRESS

Lu et al (2010) presented the hypothesis that the change in energy of soil water from its free water state is mostly consumed in suction stress and establish a thermodynamic justification for a closed-form equation for effective stress in variably saturated soils. Further to presenting a thermodynamic justification of the hypothesis, their study reinterpreted available experimental results from the literature to validate the closed-form equation on the basis of experimental observations i.e., semi-quantitative validation.

Lu et al (2010) correlated the suction stress to the effective degree of saturation ($S_e$) adopting Van Genuchten model (1980)'s parameters (Equation 8.5), where $\alpha$ is the inverse of the air-entry pressure and n is the pore size distribution parameter. Figure 8.9 presents the range of the parameters adopted in the Lu et al. (2010) equation, calibrated for different soil types. The effective degree of saturation of partially saturated soil is calculated according to Equation 8.6, where $\theta$ is the volumetric moisture content, $\theta_r$ is the residual volumetric moisture content, $\theta_s$ is the saturation volumetric moisture content.

$$\sigma_s = -\frac{S_e}{\alpha}\left(S_e^{\frac{n}{1-n}} - 1\right)^{\frac{1}{n}} \qquad \text{Equation 8.5}$$

$$S_e = \frac{(\theta-\theta_r)}{(\theta_s-\theta_r)} \qquad \text{Equation 8.6}$$

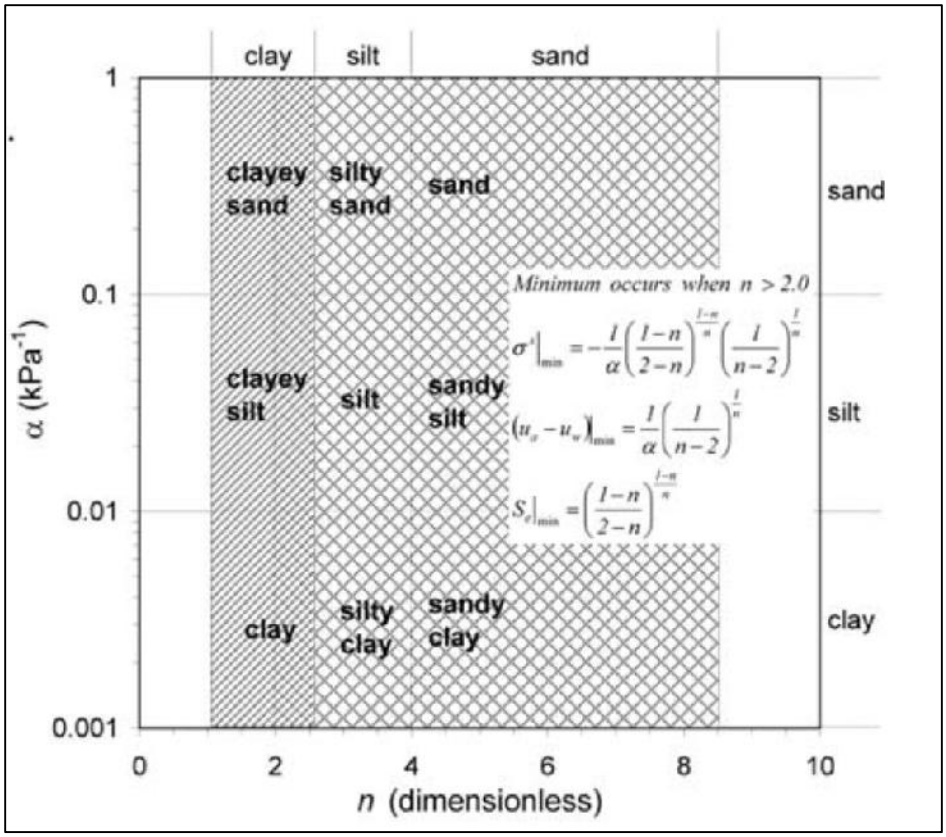


Figure 8.9: Closed-form equation correlation coefficients (Lu et al 2010)

Lu et al. (2010) presented the relationship between the matric suction and the suction stress for the soil used in the semi-quantitative validation of the closed-form solution. Figure 8.10 present a sample of the matric suction-suction stress relationships for different soils. The figure shows that, generally, the matric suction is less than the suction stress and that the relationship between matric suction and suction stress is not constant and is sensitive to the soil type.

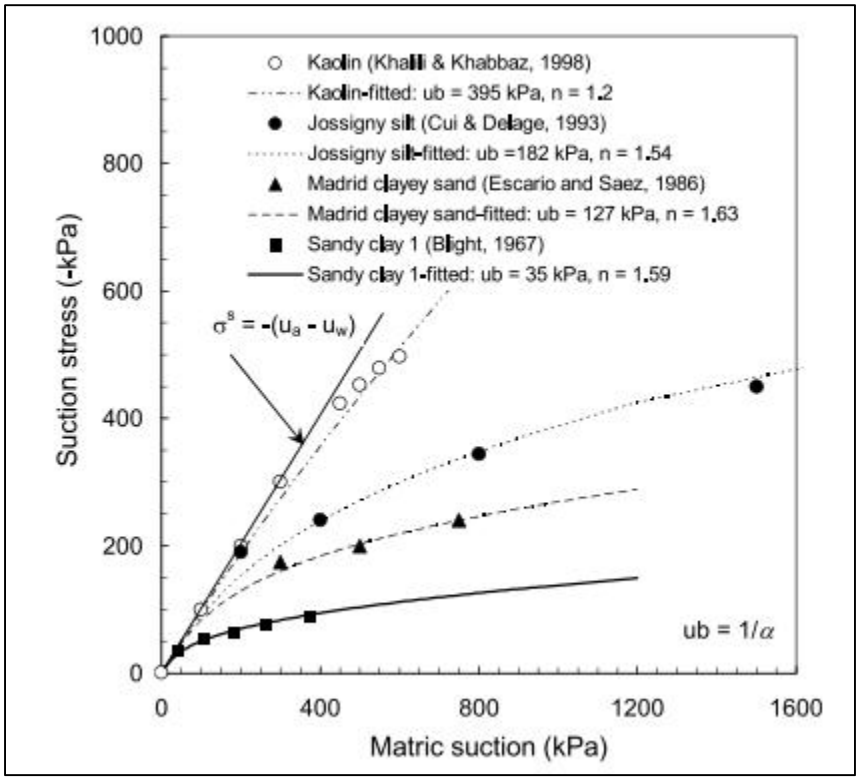


Figure 8.10: Semi-quantitative validation of the closed-form equation for effective stress, measured and fitted SSCCs for kaolin, Jossigny silt, Madrid clayey, sand and sandy clay soils (Lu et al. 2010)

## 8.6 ESTIMATION OF THE EFFECTIVE STRESS PROFILE FOR THE REESE WALL SITE

The objective of this chapter is to develop a framework that could be used to predict the swell potential of partially saturated soil. The framework attributes the soil swelling to the loss of effective stresses during the soil inundation. Sections 8.3 through 8.5 discussed the advantages, and methods of developing the relationship between the effective stress and the degree of saturation i.e., SSCC, that is essential in implementing the framework.

This section presents the development of the SSCC for the Reese wall site. The SSCC of the Reese wall site is estimated according to two approaches; first, Lu et al (2010) closed-form equation, second, undrained shear strength measurements.

### 8.6.1 Estimation of effective degree of saturation

Direct measurement of the soil degree of saturation are not possible, instead, the degree of saturation is calculated according to phase diagrams of soil with the knowledge of soil density and water content. The effective degree of saturation of the Reese wall site is estimated from the dry unit weight and water content profiles (Figure 8.11). The saturated volumetric moisture content ($\theta_s$) is calculated from phase diagrams at each soil increment, and the residual volumetric moisture content ($\theta_r$) is assumed to be constant and equal to the lowest value of volumetric moisture content.

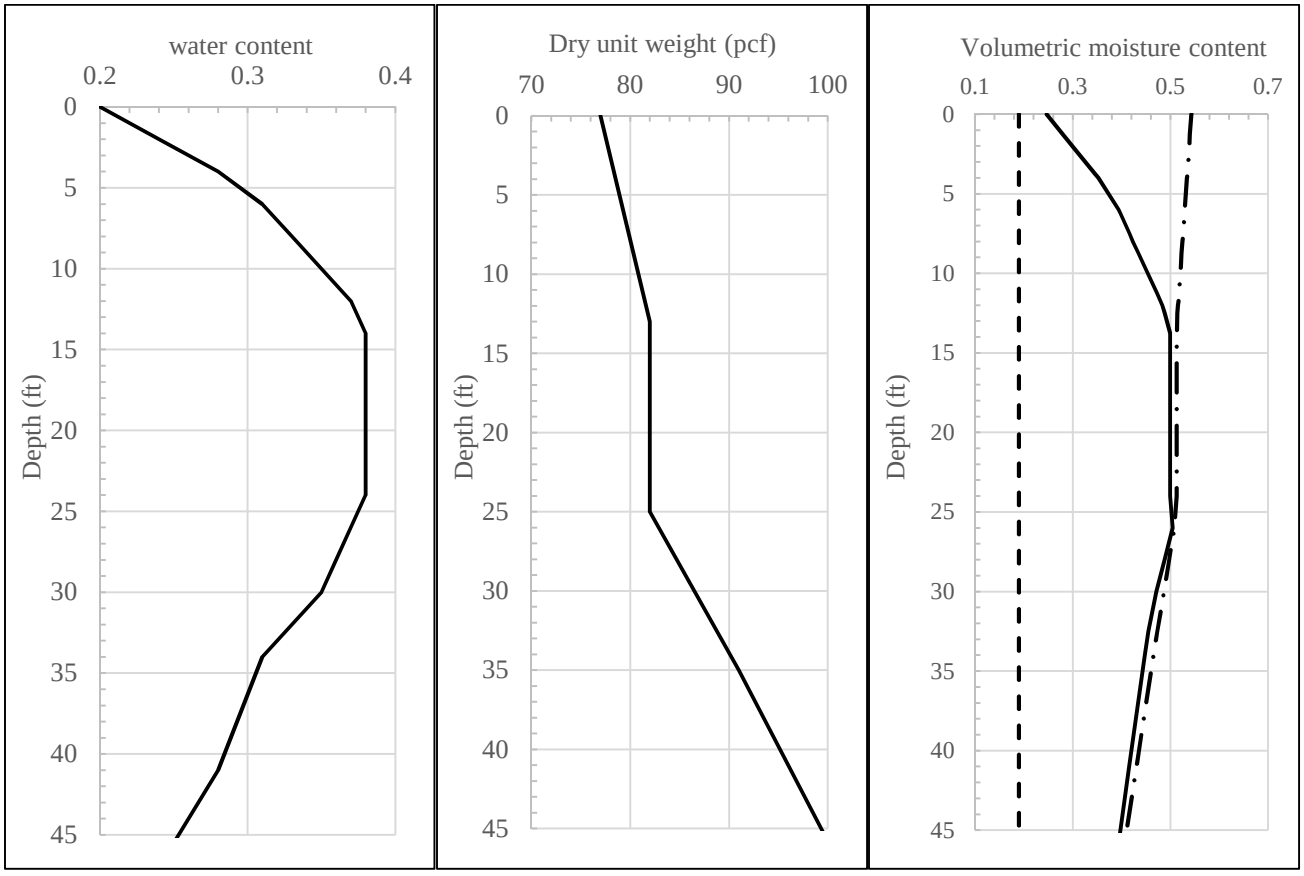


Figure 8.11: Estimation of the effective degree of saturation during site investigation conditions

The effective degree of saturation profile shows that active zone is approximately 15ft deep. At depths below 15ft the soil approaches full saturation; however, the volumetric moisture content along the investigated soil profile is continuously less than saturation volumetric moisture content.

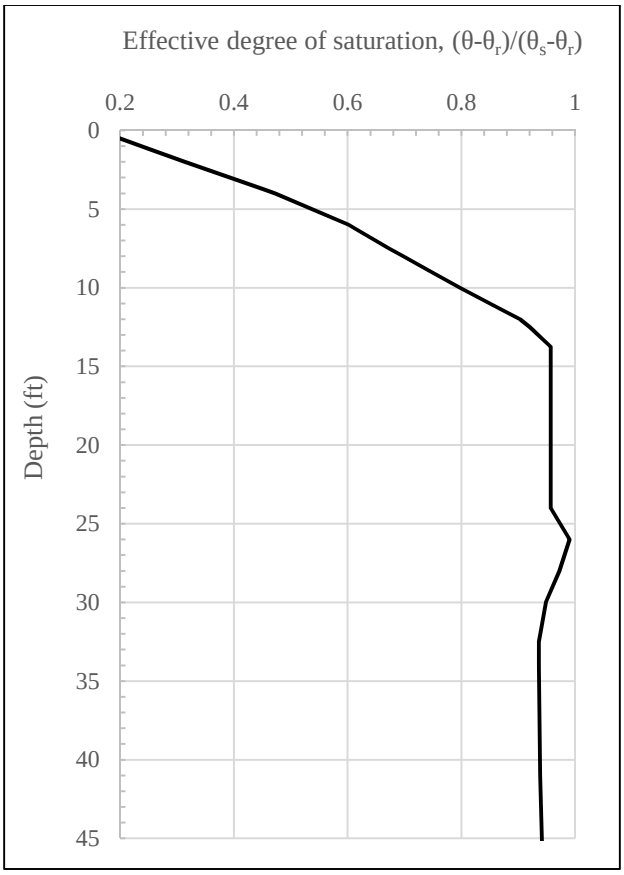


Figure 8.12: Volumetric moisture content profile with respect to residual and saturation volumetric moisture contents

### 8.6.2 Estimation of suction stress: Closed-form equation

Lu et al (2010)'s closed-form equation is based on the Van Genuchten (1980)'s model parameters. The parameters of the Van Genuchten (1980)'s model are obtained by

calibrating the model with Soil Water Retention Curve (SWRC) of similar soils reported by Kuhn and Zornberg (2006) of the Eagle Ford Clay; as well as SWRC reported by Puppala et al (2013), which estimated the SWRC four high plasticity clay soils of Texas, namely, El Paso clay, Houston clay, Fort Worth clay and Paris and San Antonio Clay. Figure 8.13 shows a comparison between the SWRCs of different soils in Texas.

The SWRC of the Eagle Ford Clay (Kuhn and Zornberg 2006) shows that the air-entry pressure is approximately 2000psf. The inverse of the air entry pressure is the $\alpha$ parameter in the Van Genuchten (1980)'s model.

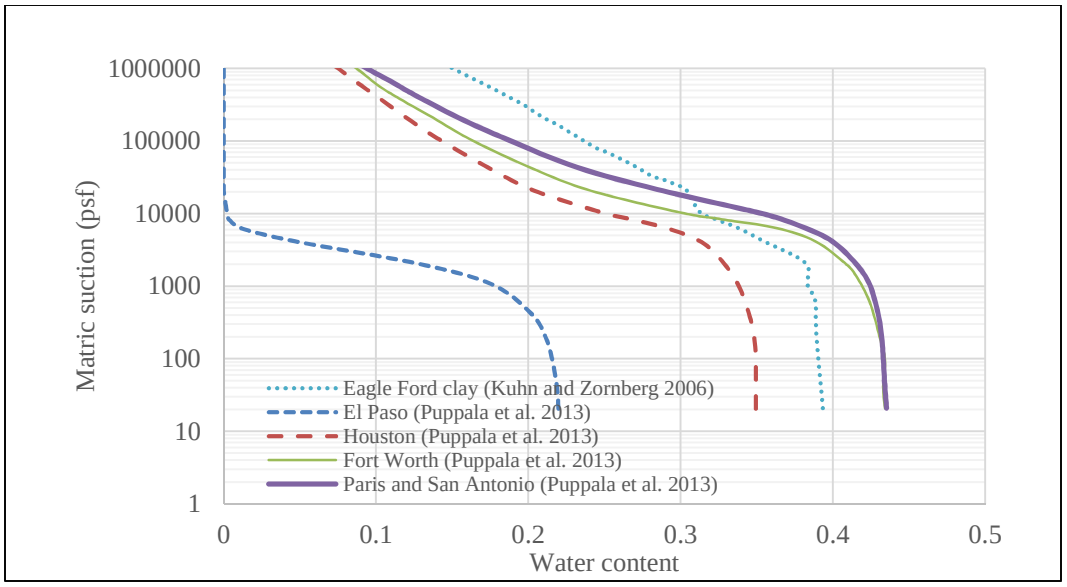


Figure 8.13: Soil Water Retention Curves of different soils in Texas

The n parameter in the Van Genuchten model controls the slope of the SWRC model. Figure 8.14 shows the calibration process of the Van Genuchten model with the SWRC of the Eagle Ford clay. The calibration process concludes that the Van Genuchten model best describes the estimates SWRC when $\alpha$ and n are 1/2000psf and 1.2, respectively.

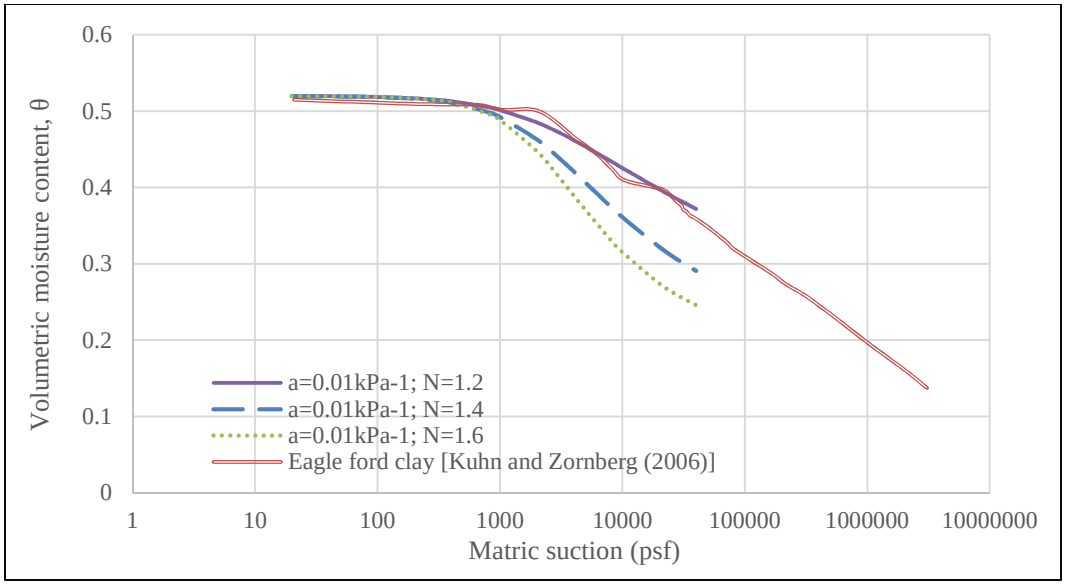


Figure 8.14: Comparison between SWRC estimated from laboratory measurements and SWRC adopted in the parametric analyses

### 8.6.3 Estimation of suction stress: Undrained shear strength measurements

Section 8.4 presented Lu and Likos (2006)' methodology of developing the SSCC of partially saturated soil from water-content controlled tests. Drained shear strength measurement of water-content-controlled tests for the Reese wall site were not conducted. Instead, undrained shear strength measurements are used to estimate the SSCC for the Reese wall site. This section presents the procedures adopted in estimating the SSCC from undrained shear strength measurements.

Unconsolidated Undrained triaxial and Texas Cone Penetration measurements were conducted to measure the undrained shear strength of the Reese wall site. The undrained shear strength of the soil could also be estimated according to the SHANSEP equation (Equation 8.7). The SHANSEP equation relates the undrained shear strength of overconsolidated soil to the undrained shear strength of the same soil in normally consolidated conditions ($S_{uNC}$) and the overconsolidation ratio (OCR); where $\sigma'_{OC}$ is the

effective stress at the overconsolidated state, $\sigma'_{NC}$ is the effective stress at the normally consolidated state, m is a correlation coefficient..

$$\frac{S_u}{\sigma'}_{OC} = \frac{S_u}{\sigma'}_{NC} \times OCR^m \qquad \text{Equation 8.7}$$

Rearranging the SHANSEP equation such that the effective stress is calculated as the dependent variable results in Equation 8.8; where, the undrained shear strength of the overconsolidated clay $Su_{OC}$ is obtained from shear strength measurements, preconsolidation effective stress is estimated from one-dimensional consolidation tests. Figure 8.15 presents a comparison between measured shear strengths and shear strengths predicting from the SHANSEP equation adopting typical values for the undrained shear strength to effective stress at normal consolidation ratio ($Su_{NC}/s'_{NC}$ =0.25) and the overconsolidation power coefficient (m=0.8).

$$\sigma'_{OC} = \left(\frac{S_{uOC}}{\frac{S_{uNC}}{\sigma'_{NC}} \times \sigma'_{precons}{}^m}\right)^{\frac{1}{1-m}} \qquad \text{Equation 8.8}$$

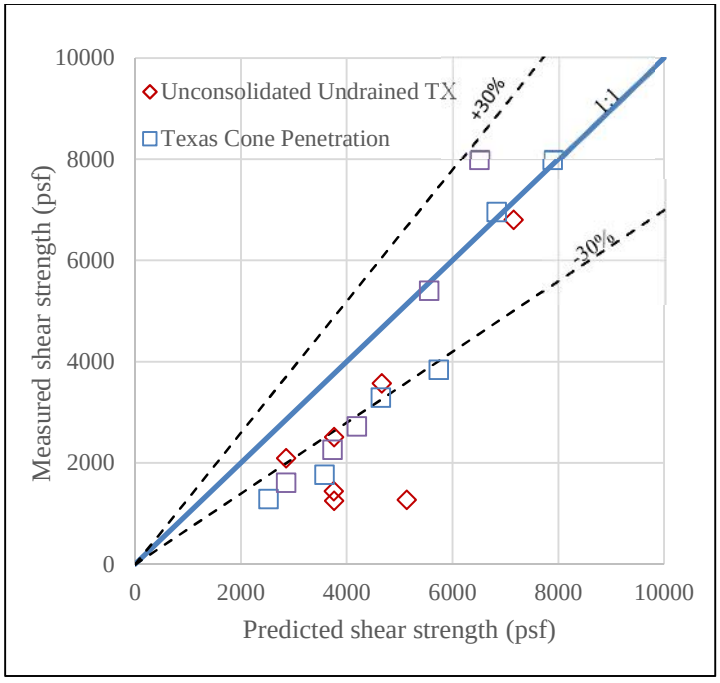


Figure 8.15: Measured undrained shear strength versus predicted undrained shear strength using uniform SHANSEP parameters ($Su_{NC}/\sigma$' and m)

Reese et al. (1975) measured the undrained shear strength of a site in close proximity to the Reese wall site (20 miles to the west of the Reese wall). The study showed that the shear strength profile of the Taylor clay formation follows a bilinear shear strength profile (Figure 8.16).

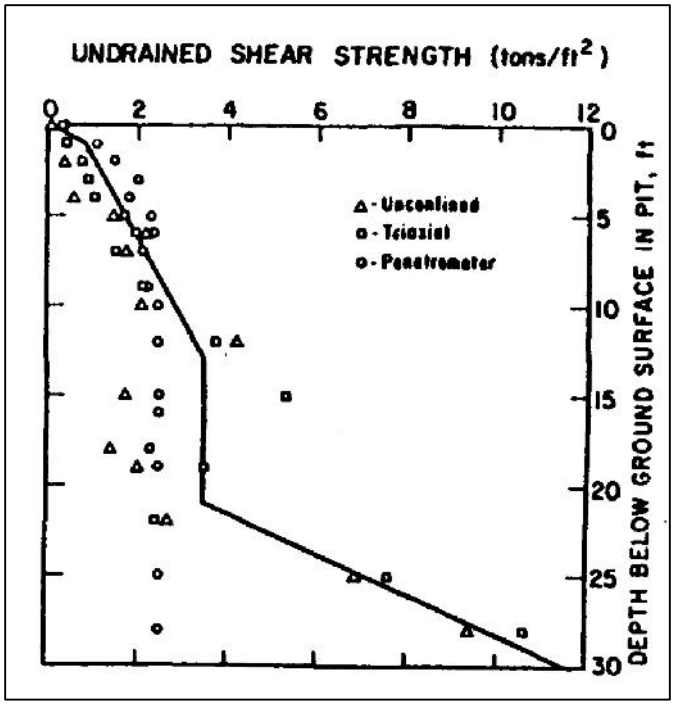


Figure 8.16: Undrained shear strength measurements in Manor, TX (Reese et al 1975)

Figure 8.17 presents a comparison between measured shear strengths and shear strengths predicting from the SHANSEP equation adopting different SHANSEP parameters of for the top 15ft and depths below 15ft. The undrained shear strength to effective stress at normal consolidation ratio ($Su_{NC}/s'_{NC}$) and the overconsolidation power coefficient (m) for the top 15ft of soil are 0.2 and 0.7, respectively; and, 0.22 and 0.8 for soil deeper than 15ft. Comparison between Figure 8.15 and Figure 8.17 shows that adopting variable parameters results in better agreement between the measured and predicted undrained shear strengths.

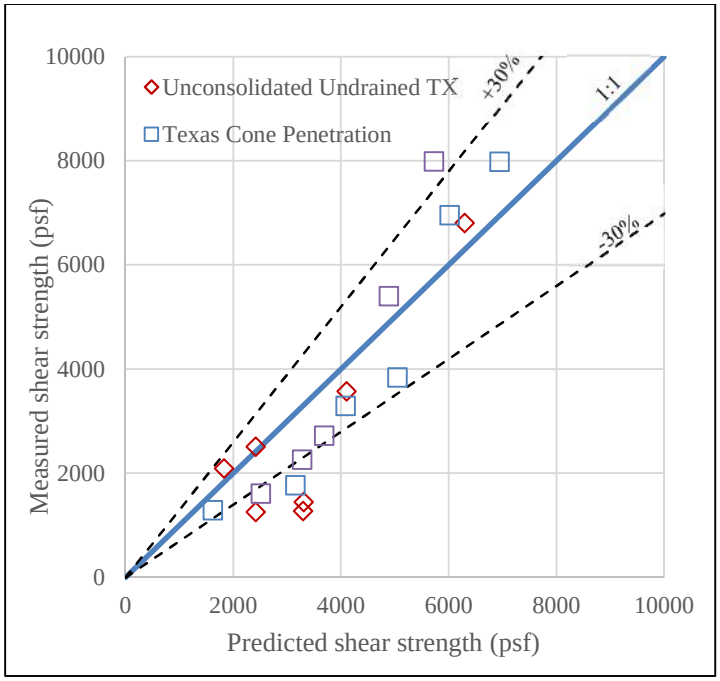


Figure 8.17: Measured undrained shear strength versus predicted undrained shear strength using bilinear SHANSEP parameters ($Su_{NC}/\sigma$' and m), threshold depth= 15ft

### 8.6.4 SSCC of the Reese wall site

Figure 8.18 presents the suction stress versus effective degree of saturation estimates for the Reese wall site using the two approaches proposed in sections 8.6.2 and 8.6.3. Upper and lower bounds of the Van Genuchten parameters for clay soil proposed by Lu et al (2010) (Figure 8.9) are adopted, such that the α coefficient ranges between 0.001 and 0.01kPa$^{-1}$ and the n coefficient ranges between 1.2 and 2.2. Suction stresses calculated from the UU and TCP undrained shear strength measurements are presented, and the depths from which the measurement are obtained are stated to qualitatively group soil depths with similar SSCCs. Two swell pressure test results are compared to the estimated suction stresses as well.

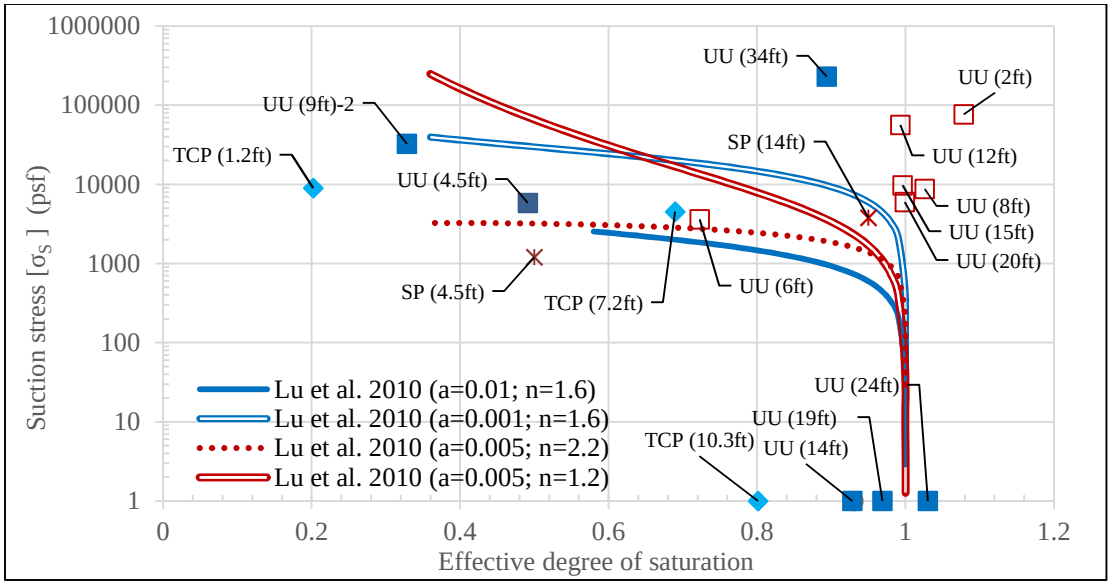


Figure 8.18: SSCC of Taylor clay estimated from (i) swell pressure tests (ii) UU tests (iii) TCP tests (iv) empirical equation

Results show that soil deeper that 20ft could have a different SSCC than shallower samples. Such that, the suction stress of soil shallower than 20ft is asymptotic with the full effective degree of saturation line, i.e., $S_e$=1, at a suction stress in the order of 1,000psf; while, the suction stress of soil samples deeper than 20ft, which are generally close to the saturation, are close to 10,000psf.

Estimates of suction stress of soil deeper than 20ft are not enough to interpolate a SSCC for soil deeper than 20ft. The soil depth prone to changes in the degree of saturation of the Reese wall is roughly 15ft. Therefore, suction stresses of the soil deeper than 20ft is assumed to be constant during wetting and drying conditions of the soil. The SSCC of the top 20ft of soil is considered to be described with the Lu at al. (2010) closed form equation with $\alpha$ and n parameters of 0.01kpa$^{-1}$ and 1.6, respectively.

Figure 8.19 presents the estimated effective vertical stress profile, suction stress profile, and the mean effective stress profile of the Reese wall site. The figure shows that during the site investigation conditions the suction stress was the major component of effective stresses for the top 10ft of soil. The mean effective stress is calculated based on the $k_0$ value estimated in section 6.1.

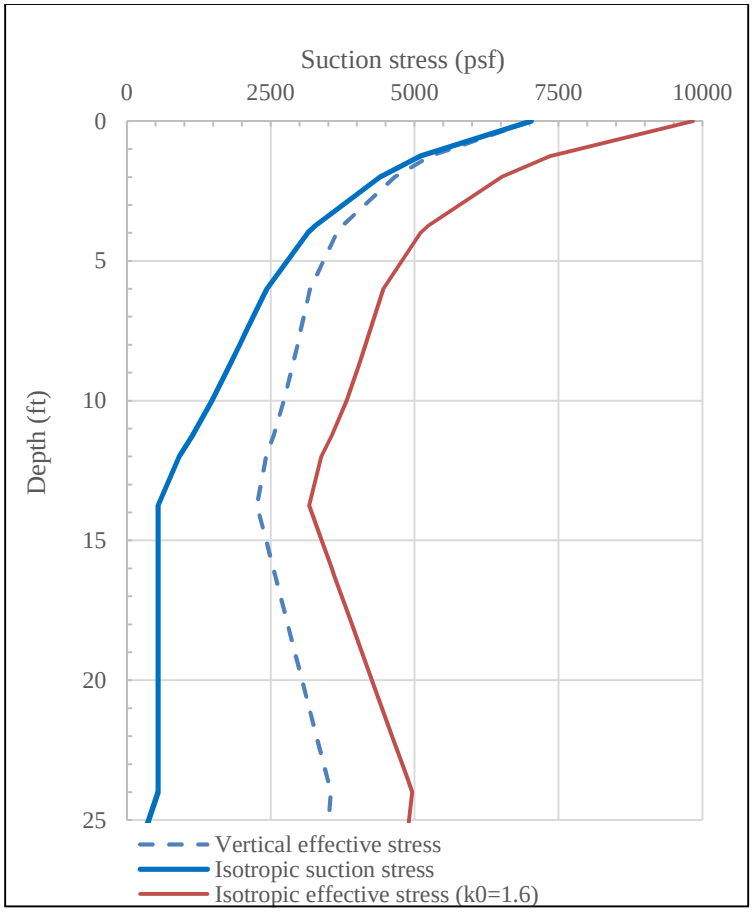


Figure 8.19: Effective stress profiles during site investigation conditions

## 8.7 ISOTROPIC HARDENING OF PARTIALLY SATURATED SOIL

Sections 8.1 through 8.6 presented a relationship that correlates the effective stress in partially saturated soil with the effective degree of saturation of partially saturated soils. Shibuya et al. 1997 correlated the soil stiffness to the mean effective stress of the soil (P'). The correlation presents the normalized maximum shear stiffness ($G_{max}/P'_r$) as a function of effective mean stress (P') and void ratio (e) (Equation 8.9), where $P'_r$ is a reference effective mean stress, and B is a constant calibration coefficient which depends on the soil type. As discussed in sections 8.1 through 8.6 the effective stress of the soil is a function of the degree of saturation of the soil. Therefore, the insitu stiffness measurements are only representative of the initial conditions at which the site investigation was conducted. This section presents the stiffness-stress relationship adopted in the numerical model to account for changes in the soil stiffness due to variation in the degree of saturation.

$$\frac{G_{max}}{P'_r} = B \times \frac{\left(\frac{P'}{P'_r}\right)^{0.5}}{1+e^{2.4}} \qquad \text{Equation 8.9}$$

Vardanega and Bolton (2013) complied measurements of normalized maximum shear stiffness versus confining stress of fully saturated silt and clay soils (Figure 8.20). The figure shows reasonable agreement of the Shibuya (1997)'s linear model with laboratory measurements.

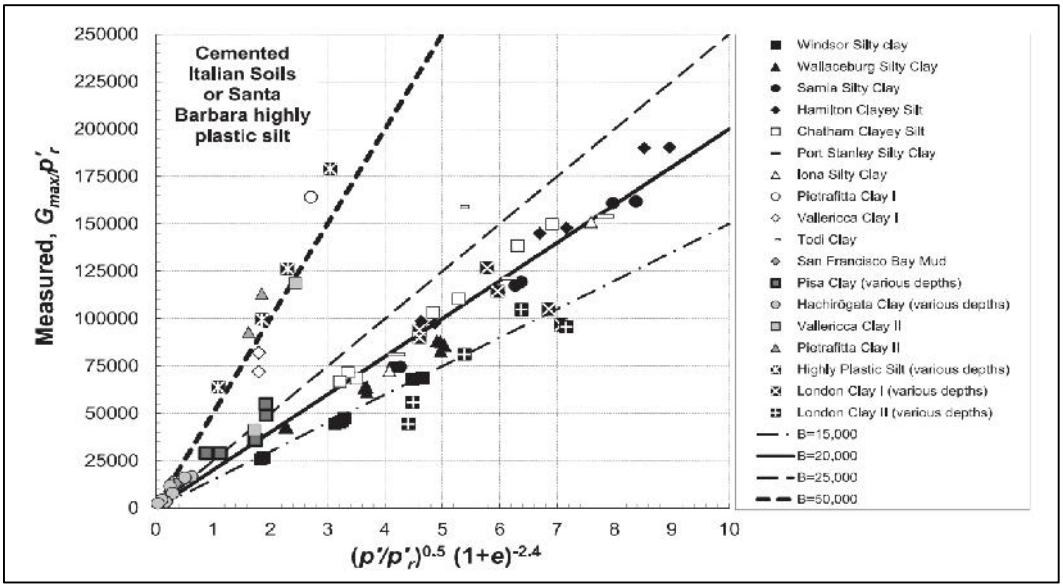


Figure 8.20: Shibuya et al 1997 isotropic hardening model for different soils (Vardanega and Bolton 2013)

Figure 8.21 presents a comparison between the London clay stiffness vs. stress measurements, reported by Vardanega and Bolton (2013) and the stiffness vs. stress obtained from the SASW measurements of the Reese wall site. The effective mean isotropic stress of the London clay soil is calculated according to Terzaghi (1923)'s definition of effective stress; because, the soil is fully saturated. But, the effective mean isotropic stress of the Reese wall site is calculated according to Lu and Likos (2006)'s definition of effective stress; because the SASW measurements are conducted on in-situ conditions where the soil is partially saturated. The effective stress of Reese wall site is estimated according to the SSCC developed in section 8.6.

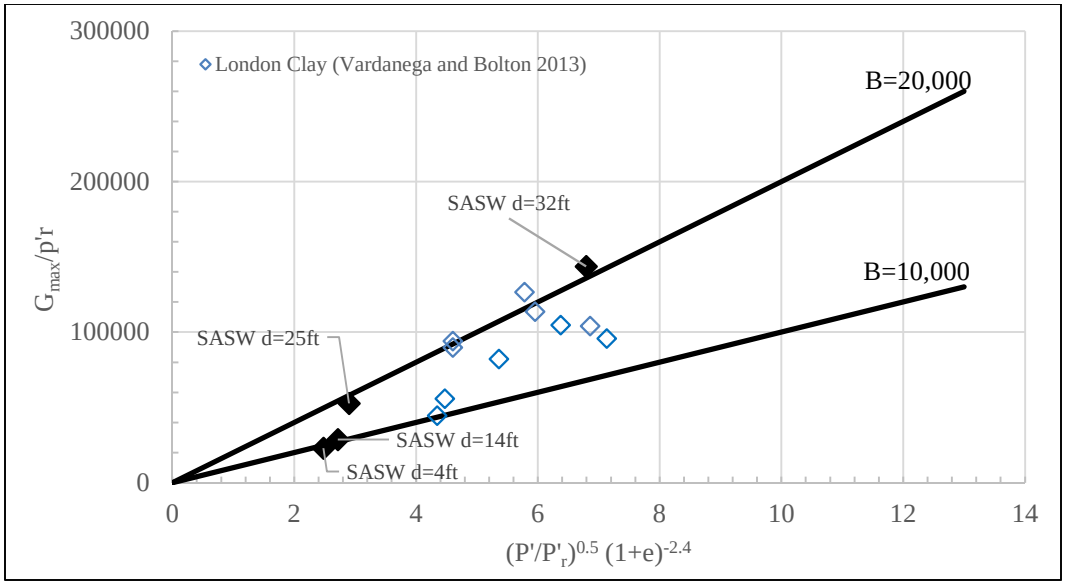


Figure 8.21: Calibration of the Shibuya et al. (1997) isotropic hardening model with: (i) SASW measurements (ii) London Clay measurements

The Shibuya et al. (1997) calibration coefficient (B) of the London clay ranges between 10,000 and 20,000. SASW measurements shows that the calibration coefficient of the Reese wall site ranges between the same bounds as the London Clay soil (Figure 8.21). The Shibuya et al. (1997) calibration coefficient adopted for the top 20ft of soil and soil deeper than 20ft are 10,000 and 20,000, respectively.

Large-strain stiffness is sensitive to variation in the effective stress as well as the small-strain stiffness. Therefore, the large-strain stiffness values calibrated with the UU measurements in section 6.1.3 are only representative of the saturation conditions at which the site investigation was conducted. The small strain-strain reduction/enlargement factor, i.e., $G_{max}(P'_{final})/ G_{max}(P'_{initial})$, calculated from the Shibuya et al. (1997) model is also adopted for the large-strain stiffness reduction/enlargement factor.

The following section experiments the validity describing the soil swell behavior of partially saturated soil by adopting the Lu and Likos (2006)'s definition to describe the

effective stress and adopting the Shibuya et al (1997) model to describe the stress-stiffness relationship.

## 8.8 IMPLEMENTING THE FRAMEWORK

The objective of this chapter is to develop a framework that could describe the behavior of partially saturated high-plasticity soil subjected to variation in the degree of saturation. Sections 8.1 through 8.6 presented the relationship between the effective stress and the degree of saturation of soil; section 8.7 presented the variation of the maximum small-strain stiffness with the variation of effective stress. This section present the technique of implementing the framework in a Finite Element Method software (PLAXIS). A numerical model of a one-dimensional swell test is simulated to evaluate the validity of the framework in describing the swell behavior of partially saturated soil subjected to inundation.

### 8.8.1 Analytically implementing the framework to estimate swell strains

***Laboratory measurements***

Table 8.1 presents the initial conditions of four accelerated swell-shrink tests. Samples are trimmed into a 1inch high consolidation ring, subjected to the vertical stresses ranging from 150psf to 4050psf, and then subjected to 5 cycles of wetting and drying. Test-results sample obtained from test #1 are presented in Figure 8.22.

Table 8.1: Summary of accelerated swell-shrink tests (Ellis 2011)

| Test # | Depth (ft) | Vertical stress (psf) | $\gamma_{total}$ | $W_{c,initial}$ (%) | $W_{c,min}$ (%) | $W_{c,max}$ (%) |
|---|---|---|---|---|---|---|
| 1 | 3-4 | 150 | 122.4 | 25.4 | 4.3 | 31.3 |
| 2 | 2-3 | 500 | 121.1 | 26.6 | 3.3 | 28.7 |
| 3 | 4-5 | 1000 | 123.1 | 26.7 | 4.3 | 28.4 |
| 4 | 5-6 | 4050 | 127.5 | 23.3 | 3.3 | 24.6 |

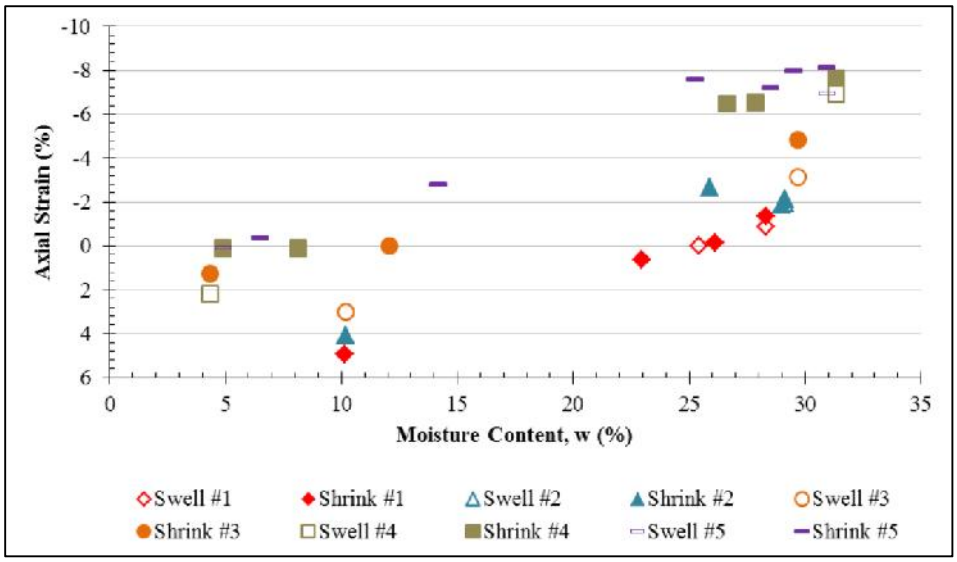


Figure 8.22: Strain Vs. moisture content of cyclic swell Test 1 (Ellis 2011)

Ellis (2011) estimated an average linear relationship between the axial strain and the soil moisture content (Figure 8.23). The figure shows that the slope of the strain versus moisture content relationship is roughly constant for different vertical stresses.

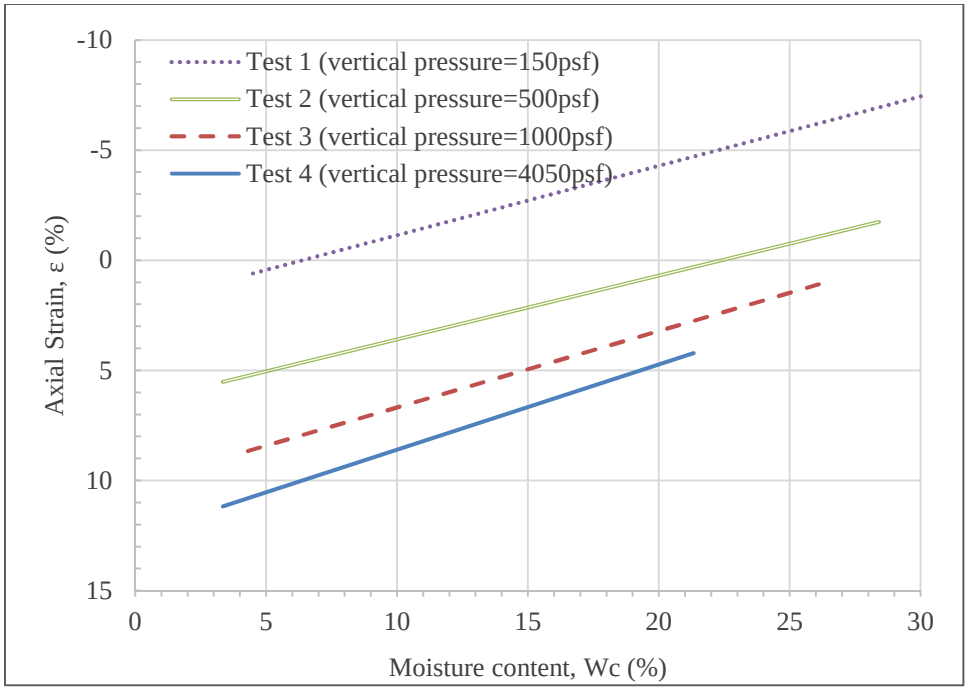


Figure 8.23: Summary of steady state shrink-swell behavior (Ellis 2011)

***Sample calculation***

Figure 8.24 presents the average linear relationship Ellis (2011) estimated from accelerated swell-shrink test #1. The figure shows the water content and axial strain measurements of the first swelling and shrinkage cycle. The following procedures presents an analytical estimate of the axial swelling strain. The estimation adopts the framework presented in sections 8.1 through 8.7, which described the effective stresses and the soil stiffness in terms of the soil saturation. The estimated relationship between the axial strain and the water content is also presented in Figure 8.24.

1- Calculate the initial volumetric moisture content from a phase diagram utilizing the initial water content and total unit weight.

2- Calculate the total unit weights of soil at the residual and saturated conditions by accounting for the measured changes in the axial strains, i.e., voids ratio.

3- Calculate the residual and saturated volumetric moisture contents.

4- Calculate the effective degree of saturation at the initial conditions.

5- Estimate the suction stress of the partially saturated soil using Lu et al. (2010) closed form equation, adopting the $\alpha$ and n parameters estimated in section 8.6.

6- Assume a reasonable Poisson ratio ($\nu$'=0.3 is adopted in this calculation); and calculate the constrained modulus from the measured $G_{max}$ and the assumed Poisson ratio.

7- Vary the moisture content incrementally, and calculate the volumetric moisture content for the new moisture content assuming that the total unit weight is constant after the variation of the soil moisture content.

8- Calculate the effective degree of saturation for the new moisture content.

9- Estimate the suction stress of the partially saturated soil for the new effective degree of saturation.

10- Estimate the shear stiffness for the suction stress calculated in step 9, using the Shibuya et al. (1997) model.

11- Calculate the constrained modulus equivalent to the shear stiffness calculated in step 10.

12- Calculate an average value of the constrained modulus over the inundation increment, i.e., average of the constrained moduli calculated in steps 6 and 10.

13- Calculate the difference in suction stress that took place during the inundation cycle, i.e., difference between suction stresses calculated in steps 5 and 9.

14- Calculate the axial strain due to the soil inundation increment by dividing the difference in the suction stress (step 13) by the average constrained modulus.

15- Calculate the new void ratio at the end of the inundation cycle, and update the shear stiffness of the soil according to the Shibuya et al. (1997) model.

16- Repeat steps 7 through 15.

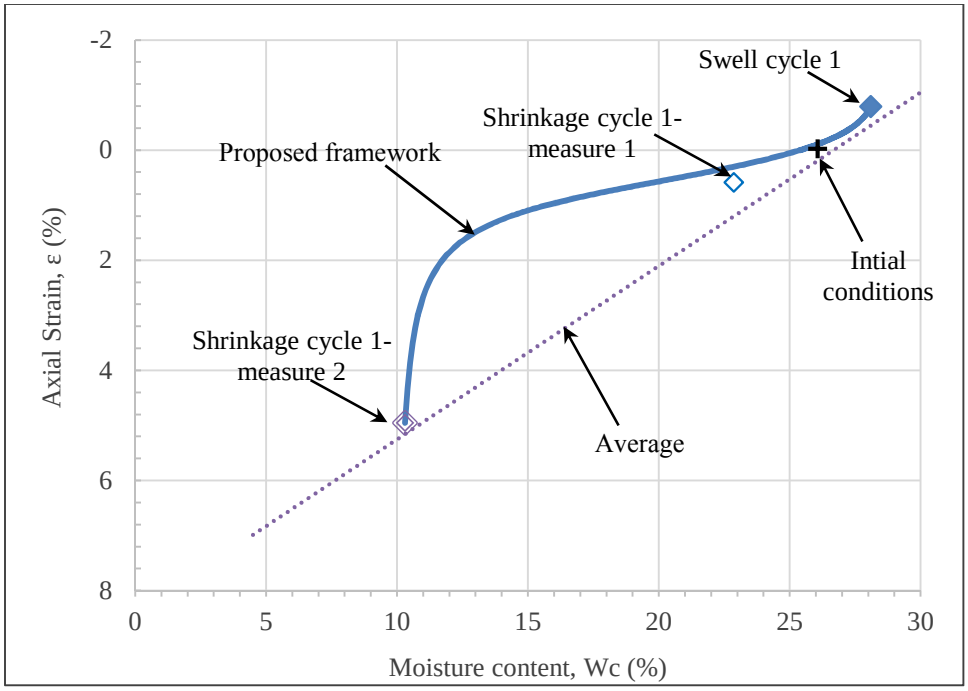


Figure 8.24: Summary of steady state shrink-swell behavior (normalizing axial strains to strains at the driest water content)

Figure 8.24 shows that the relationship of the axial strain versus the moisture content estimated according to the previous procedures agrees with the laboratory measurements. The proposed framework resulted in a nonlinear relationship between axial strain and water content. The framework suggests that the most significant axial strains are experienced when the soil is least saturated. The SSCC of the soil is a logarithmic relationship, such that the changes in the suction stresses of low saturation soils are orders of magnitude higher than the changes in suction stresses of high saturation soils.

Figure 8.25 presents the variation of the small-strain shear stiffness of the soil with the variation in moisture content. The figure shows the small-strain shear stiffness corresponding to the moisture conditions presented in Figure 8.24. The shear stiffness is calculated according to the Shibuya model described in section 8.7. Results show that the small strain stiffness of the soil is the most sensitive at saturation conditions close to the residual moisture conditions; i.e., driest conditions.

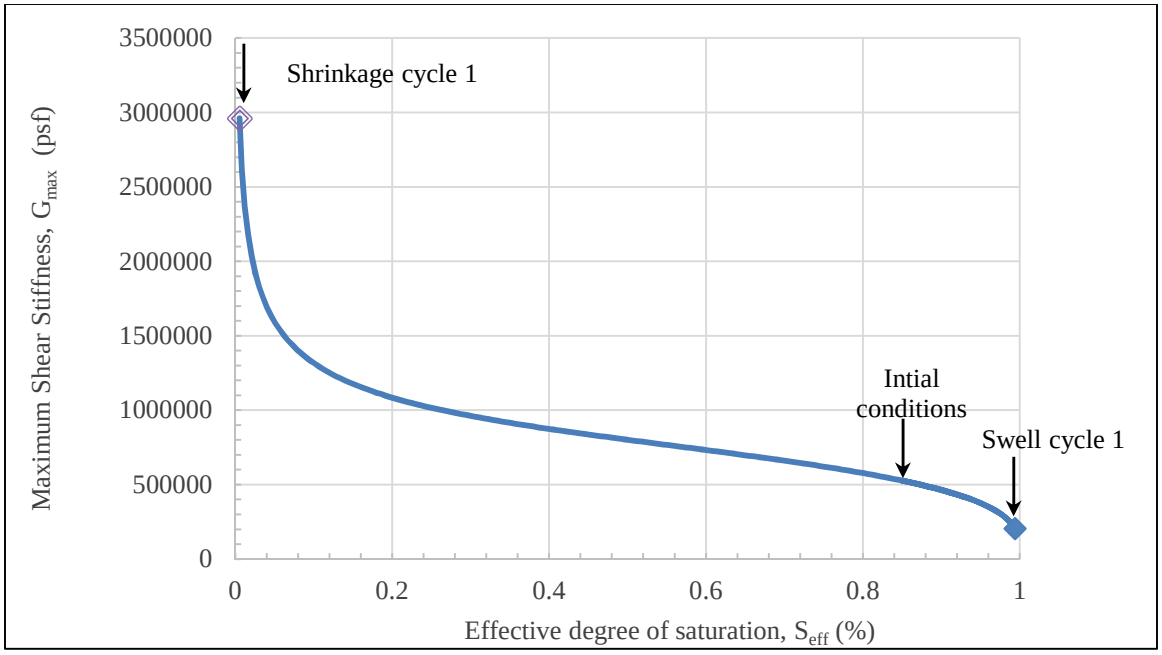


Figure 8.25: Relationship between small-strain shear stiffness and effective degree of saturation

### 8.8.2 Implementing the framework in a FE model to estimate swell strains

This section presents the default assumption adopted in PLAXIS, and the assumptions adopted in order to implement the suction stress school of thought rather than the matric suction school of thought.

***One-dimensional swell test***

Before implementing the framework in the Reese wall numerical model, the framework is evaluated with a simpler numerical model of a one-dimensional swell test. Results from a laboratory swell test are compared to a numerical model of the test that adopts the proposed framework. The laboratory swell test is a stress controlled test where the partially saturated soil is inundated and the corresponding strain is measured.

The soil in a one-dimensional oedometer cell behaves according to the soil constrained modulus. The soil constrained modulus is a function of the soil shear stiffness and Poisson ratio ($v$) (Equation 8.10). Wongsaroj et al (2004) measured the axial and radial strains of London Clay in triaxial compression tests. The study recommended a Poisson ratio of 0.3. Therefore, Poisson ratio ($v$=0.3) is adopted in modelling soil of the Reese wall site.

$$M = \frac{2G(1-v)}{1-2v} \qquad \text{Equation 8.10}$$

***Laboratory measurement***

Swell test is conducted on supposedly an undisturbed soil sample obtained from 9ft deep specimen. The sample thickness is 1inch, the initial void ratio of the soil sample is 1.1. A sitting load of 150psf was applied on the specimen, and the soil was inundated. The void ratio of the soil after inundation was 1.13, i.e., the axial swell strain of the soil sample is 14.3%, i.e., 0.143 inch (Figure 8.26).

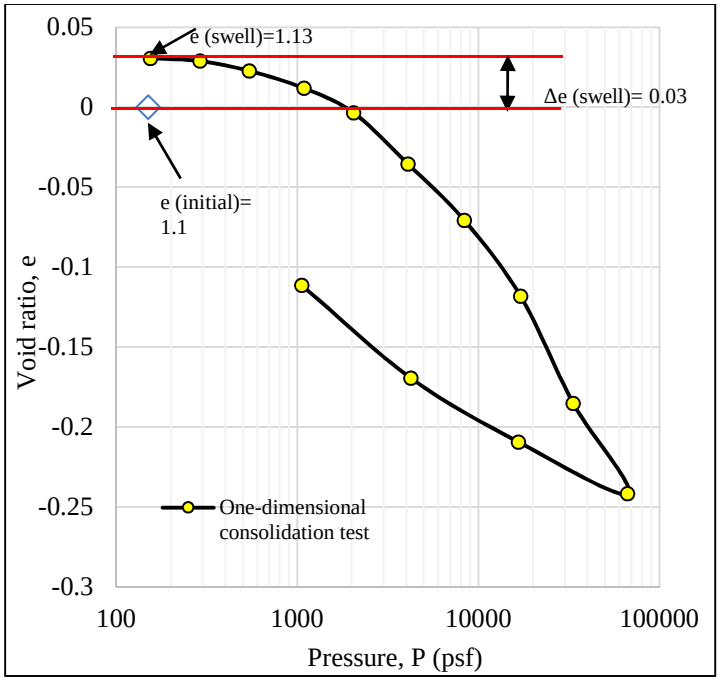


Figure 8.26: Swell strain test results of specimen obtained from 9ft deep sample

***PLAXIS Effective stress definition***

Bishop (1959)'s definition of effective stress is adopted in PLAXIS software to describe the effective stress of partially saturated soil. The $\chi$ coefficient is assumed to be equal to the effective degree of saturation of the soil, such that, the effective stress of partially saturated soil is described in PLAXIS with Equation 8.11.

$$\sigma' = \sigma - u_a + S_{eff}(u_a - u_w \qquad \text{Equation 8.11}$$

Pufahl (1982) suggested that the pore-air pressure could be considered as negligible; this recommendation is adopted in PLAXIS. Therefore the effective stress of partially saturated soil is reduced in PLAXIS to Equation 8.12. Effective degree of saturation is calculated in PLAXIS according to the Van Genuchten Model; therefore, the

boundary condition of partially saturated soil in PLAXIS can be described in term of either the pore-water pressure or the degree of saturation.

$$\sigma' = \sigma + S_{eff}(u_w \quad \text{Equation 8.12}$$

***Assumptions adopted in PLAXIS***

In order to implement the suction stress school of thought rather than the matric suction school of thought three assumption are adopted in the FE model. First, the partially saturated soil is assumed to be fully saturated in the numerical model, i.e., a boundary condition of S=1 is assigned to the partially saturated soils. This means that the effective stress in PLAXIS are described according to Equation 8.13. Second, the relationship between the soil saturation and the matric suction is suppressed and replaced with a user-defined boundary condition, i.e., boundary condition of the pore-water pressure is required as an input in the numerical model.

$$\sigma' = \sigma + u_w \quad \text{Equation 8.13}$$

Lu and Likos (2006)'s definition of effective stress is revisited in Equation 8.14. Comparison between Equation 8.13 and Equation 8.14 shows that the pore-water pressure ($u_w$) boundary condition could be adopted as a surrogate for the suction stress. In other words, the pore-water pressure boundary conditions are assigned the same value of the suction stress estimated from the water content measurements; and the effective stress generated in PLAXIS is thereby described according to Lu and Likos (2006)'s effective stress definition.

$$\sigma'_{\text{Lu \& Likos}} = \sigma + \sigma_s \quad \text{Equation 8.14}$$

It is important to mention that the numerical model is not intended to describe the behavior of partially saturated soil with respect to time. In other words, a permeability coefficient (k) higher than the actual partially saturated soil permeability coefficient is adopted to ensure that full consolidation is reached when the pore-water pressure boundary condition is changed.

***Numerical model***

The Shibuya et al. (1997) calibration coefficient (B) was estimated from insitu SASW measurements of the Reese wall site (Figure 8.21). The shear wave velocity of the swell test soil sample is probably affected by sampling disturbance, which would variate the Shibuya (1997) calibration coefficient for laboratory samples. Stokoe et al (2004) studied the ratio between field shear wave velocity ($V_{s,\ field}$) and laboratory shear wave velocity ($V_{s,\ lab}$) (Figure 8.27). The shear wave velocity of the top 15ft of soil is approximately 300m/s. The corresponding ratio of the lab to field shear wave velocities ($V_{s,\ lab}/\ V_{s,\ field}$) is approximately 0.8. According to Stokoe et al. (2000) the $G_{max,\ lab}/\ G_{max,\ field}$ ratio, corresponding to a $V_{s,\ lab}/\ V_{s,\ field}$ ratio of 0.8, is approximately 0.65. Therefore, the Shibuya et al. (1997) calibration coefficient for the soil sample tested in the one-dimensional oedometer test is assumed to be 6,500 rather than 10,000.

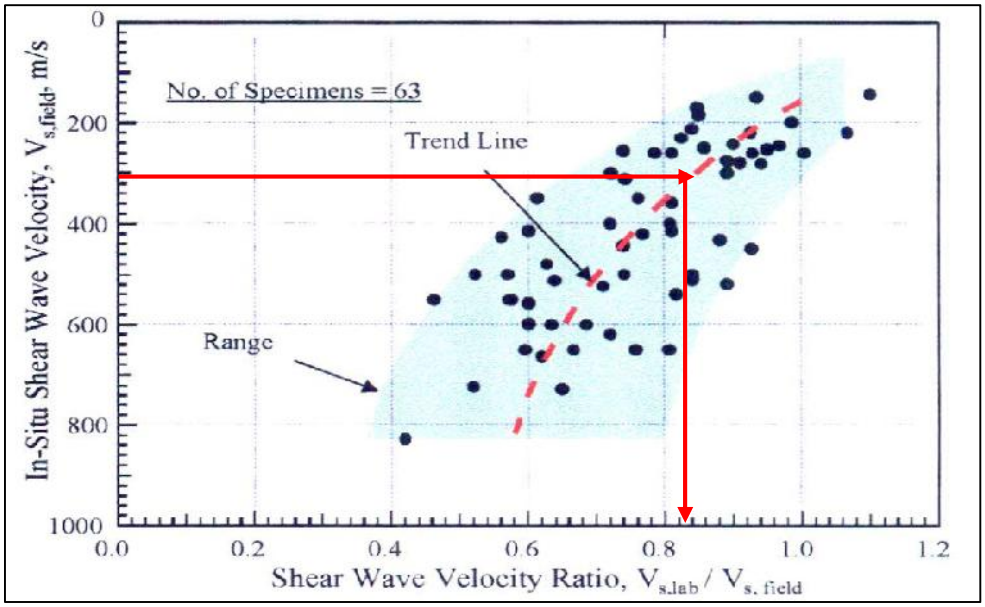


Figure 8.27: Shear wave velocity ratio as a function of measured shear wave velocity (Stokoe et al. 2000)

The One-dimensional Oedometer test is modeled in plane-strain conditions by increasing the width to height ratio such that the adopted width to height ratio of the numerical model is 20:1, and the height of the numerical model is the same as the height of the laboratory sample (Figure 8.28). The side displacement boundary conditions are restrained in the horizontal direction, and, the base displacement boundary condition is restrained in the vertical direction. The sitting load of 150psf is applied as boundary conditions to the top surface. The soil is assumed to be fully saturated as discussed previously. According to the effective degree of saturation profile presented in Figure 8.12, the effective degree of saturation profile at depth of 9ft is $S_e$= 0.75. According to the SSCC presented in Figure 8.18 the suction stress of an effective degree of saturation of $S_e$=0.75 is $\sigma_s$=2100psf.

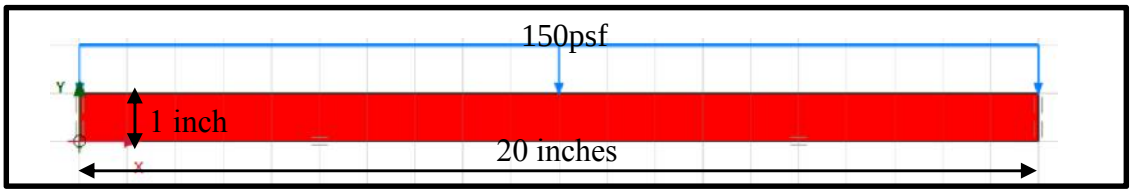


Figure 8.28: Finite Element model of one-dimensional swell test

The framework is implemented in the FE model following two approaches. The first approach adopts incremental changes of the soil degree of saturation, i.e. the change in the effective degree of saturation is divided into increments, the suction stress and the soil stiffness are calculate after each incremental change of the effective degree of saturation, and the soil properties and boundary conditions are updated with the calculated values. The second approach adopts an average value of soil stiffness, where the soil properties are calculated based on the average effective degree of saturation of initial and final saturation conditions.

i- Incremental analysis

The incremental swell test is simulated by 9 incremental changes of the degree of saturation. Figure 8.29 presents the SSCC adopted for the top 20ft of soil. Points "1" through "9" plots the path of partially saturated soil as the soil becomes more saturated. Point "1" presents the initial conditions of the partially saturated soil, i.e., conditions during the site investigation, and point "9" is assumed to be the maximum degree of saturation the soil can reach. The maximum degree of saturation is probably less than 100%; because, high-plasticity clay requires back pressurizing to reach full saturation.

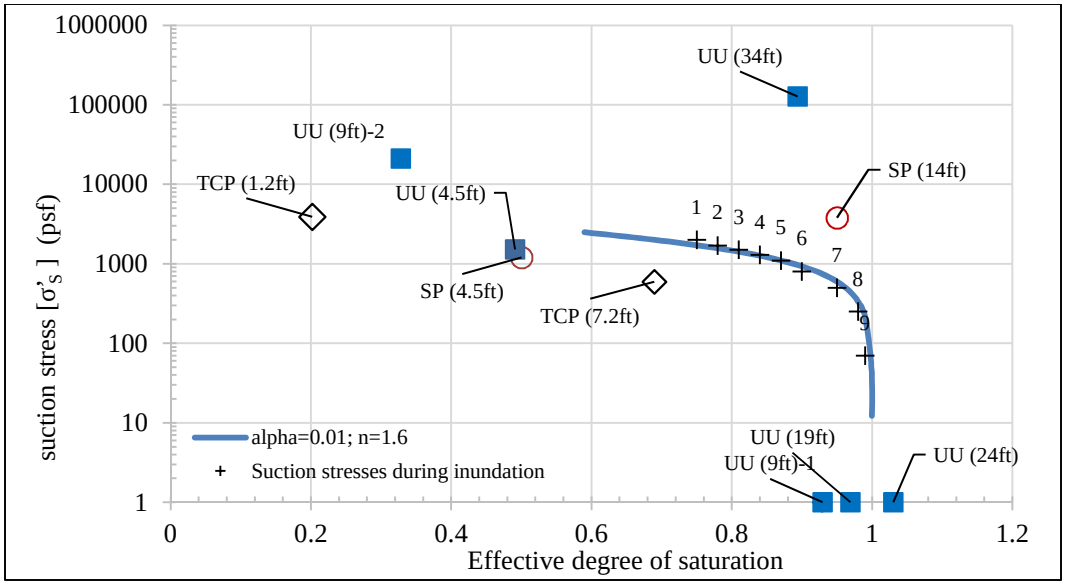


Figure 8.29: Suction stress for incremental analysis

Figure 8.30 presents the Shibuya et al. (1997) stress-stiffness hardening model adopted for the swell test. The figure accounts for the stiffness reduction due to sample disturbance. The stiffness of the partially saturated soil at points "1" through "9" are estimated according to the adopted Shibuya et al. (1997) model. As previously mentioned the change in the large-strain stiffness ($E_{50}$) due to changes in the effective stress is equally factorized as the small-strain stiffness ($G_{max}$).

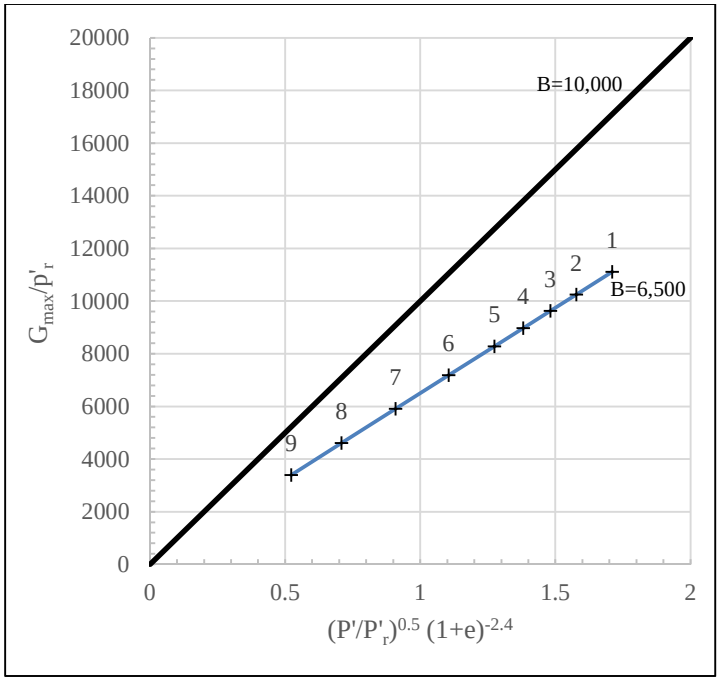


Figure 8.30: Shear stiffness inputs at various suction stress increments

The following presents the steps of implementing the framework in stages 1, 2 and 2C of the numerical model. The number in parenthesis refers to the point at which the soil property or boundary condition refers to.

Stage 1 [Initial state]

1- Estimate the suction stress equivalent to effective degree of saturation (1) according to the adopted SSCC.
2- Assign full saturation condition to the soil.
3- Estimate the soil stiffness according to the Shibuya et al. (1997) model, and assign it to material conditions (1)
4- Assign pore-water boundary condition equal to the estimated suction stress (1).
5- Generate initial stresses according to a $k_0$ procedure.

Stage 2 [$S_e(1)$ to $S_e(2)$]

1- Estimate the suction stress equivalent to effective degree of saturation (2) according to the adopted SSCC.
2- Estimate the soil stiffness according to the Shibuya et al. (1997) model, and assign it to material conditions (2).
3- Run Plastic analysis

Stage 2C [$S_e$(1) to $S_e$(2)]

1- Assign pore-water boundary condition equal to the estimated suction stress (1).
2- Run Consolidation analysis

Table 8.2 presents the description and the analysis type of the numerical model stages. First, the initial stresses are generated according to a $k_0$-procedure. The adopted $k_0$ value is previously discussed in section 6.1. Before the incremental change in the suction stress is applied, the material properties are updated in a plastic deformation analysis. Then a consolidation stage is analyzed where the boundary condition of the suction stress is modified (i.e. the pore-water pressure boundary condition in PLAXIS is changed). As previously mentioned, the numerical model is not intended to describe the behavior of partially saturated soil with respect to time. Thus, the permeability coefficient is increased to ensure that the suction stress is fully implemented in the soil.

Table 8.2: Stages and analysis type of the swell test numerical model

| Stage No. | Stage description | Analysis type | Stage No. | Stage description | Analysis type |
|---|---|---|---|---|---|
| 1 | - Material (1)<br>- $u_w$ (1)<br>- $k_0$= 1.6 | $k_0$ procedure | 6 | - Material (6)<br>- uw (5) | Plastic |
| 2 | - Material (2)<br>- uw (1) | Plastic | 6C | - Material (6)<br>- $u_w$ (6) | Consolidation |
| 2C | - Material (2)<br>- $u_w$ (2) | Consolidation | 7 | - Material (7)<br>- uw (6) | Plastic |
| 3 | - Material (3)<br>- uw (2) | Plastic | 7C | - Material (7)<br>- uw (7) | Consolidation |
| 3C | - Material (3)<br>- uw (3) | Consolidation | 8 | - Material (8)<br>- uw (7) | Plastic |
| 4 | - Material (4)<br>- uw (3) | Plastic | 8C | - Material (8)<br>- uw (8) | Consolidation |
| 4C | - Material (4)<br>- uw (4) | Consolidation | 9 | - Material (9)<br>- uw (8) | Plastic |
| 5 | - Material (5)<br>- uw (4) | Plastic | 9C | - Material (9)<br>- uw (9) | Consolidation |
| 5C | - Material (5)<br>- uw (5) | Consolidation | | | |

Figure 8.31 presents contour lines of the predicted ultimate vertical swell (i.e. swell at point "9") using the incremental variation of saturation approach. The figure shows results of a 1.5inch strip at the mid span of the model. The predicted axial swell at the top of the sample is 0.13inch. The predicted axial swell shows reasonable agreement with the swell measured in the laboratory (0.143inch).

The soil swell predicted in the numerical model is due to the loss of the suction stress (implemented in the model as pore-water boundary condition). As the soil effective degree of saturation increases, the internally confining stress, i.e. the suction stress, is lost and the soil swells. Agreement between the measured and predicted soil swell means that adopting a framework that describe the changes in the effective stress due to variation of

the soil degree of saturation could be used to describe the swelling behavior of partially saturated soil subjected to variation in the degree of saturation.

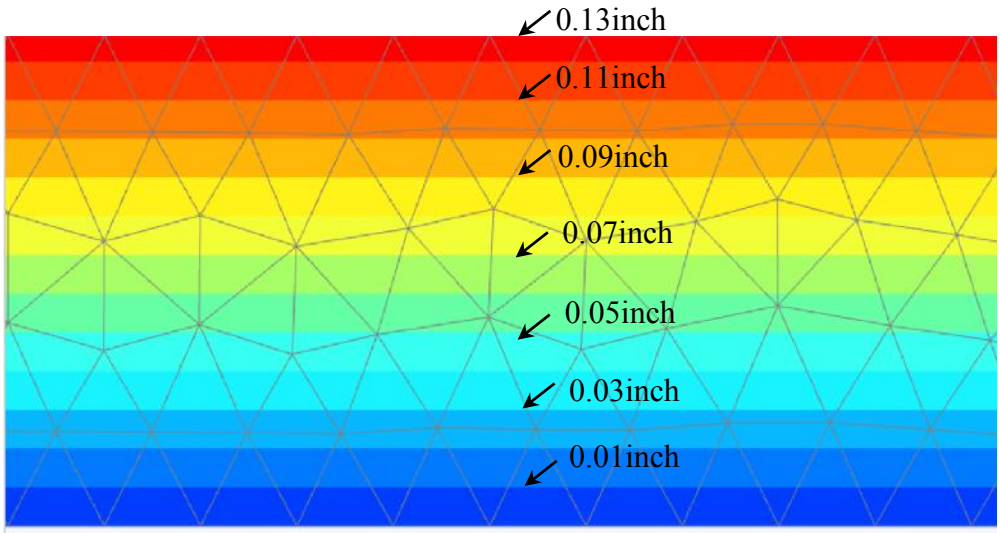


Figure 8.31: Incremental-analysis predictions of vertical swell during the final stage of inundation (i.e. point "9")

ii- Average analysis

Incrementing the variation of the effective degree of saturation could be a tedious process; specially, when the numerical model simulates a soil profile where variation of the effective degree of saturation is a function of soil depth; therefore, a more robust analysis is experimented in this section. Instead of analyzing the behavior of the soil after each incremental change of the effective degree of saturation, average soil properties are adopted and the change in the effective degree of saturation is assumed to take place in one increment.

Unlike the incremental analysis the variation in the suction stress is modelled in a single stage. Figure 8.32 presents the initial and final conditions of the partially saturated

soil and the condition at which the average soil properties are calculated. Point "1" presents the initial conditions of the partially saturated soil and point "9" is assumed to be the maximum degree of saturation the soil can reach. Point "5" is the midpoint of the change of the effective degree of saturation, such that the initial degree of saturation i.e. point "1" is 0.75 and the final degree of saturation i.e. point "9" is approximately 1, and the effective degree of saturation at point "5" is 0.87.

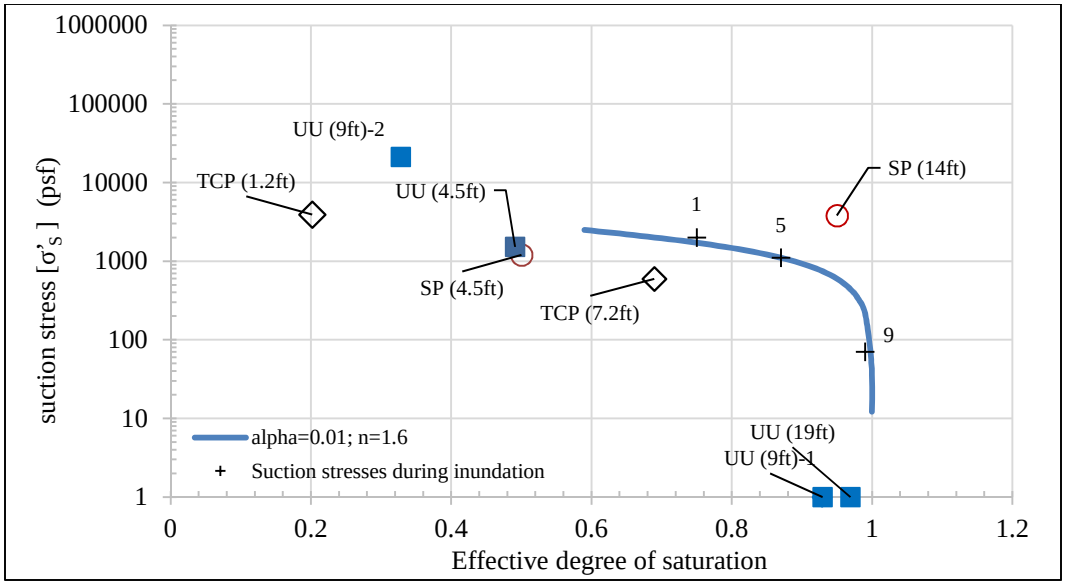


Figure 8.32: Suction stress for average analysis

Figure 8.33 presents the initial and final conditions in the Shibuya et al. (1997) model and the conditions at which the average properties are calculated. Figure 8.34 presents contour lines of the predicted ultimate vertical swell (i.e. swell at point "9") using the average soil properties approach. The figure shows results of a 1.5inch strip at the mid span of the model. The predicted axial swell at the top of the sample is 0.156inch. The

predicted axial swell shows reasonable agreement with the swell measured in the laboratory (0.143inch).

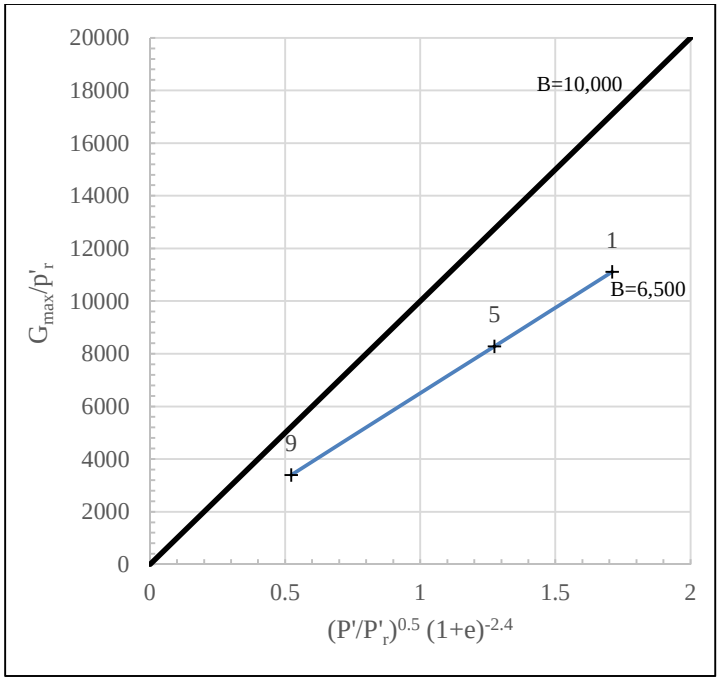


Figure 8.33: Shear stiffness inputs at various suction stress increments

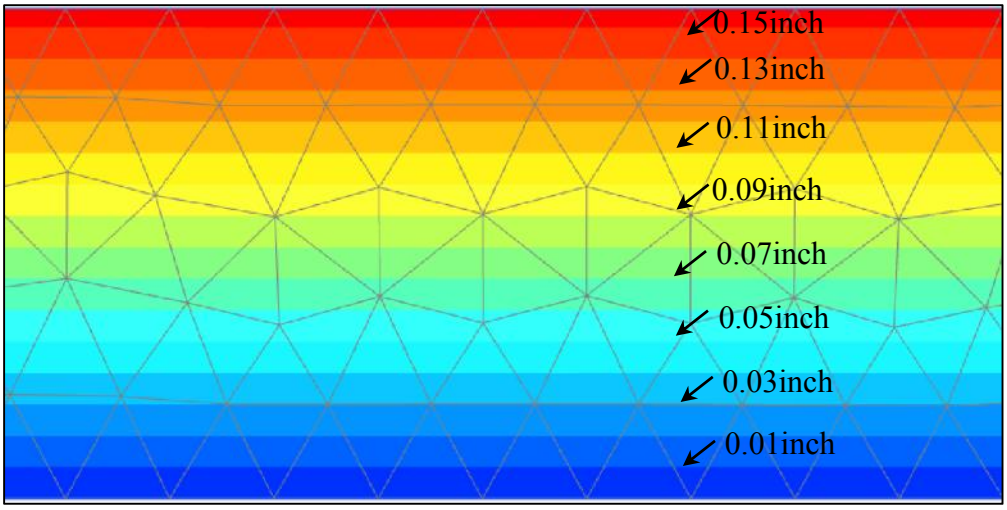


Figure 8.34: Average-analysis predictions of vertical swell during the final stage of inundation (i.e. point "9")

This chapter presented a framework proposed in this study that could be adopted to describe the behavior of partially saturated soil. First, the framework was implemented analytically in a spread sheet and was compared to laboratory measurements of an accelerated swell-shrink test. Comparison showed that the framework could reasonably predict swell strains. Second, the framework was implemented in a Finite Element model of a one dimensional test. Comparison between measured and predicted swell strain tests suggests that the assumptions adopted in the Finite Element model is acceptable and yield reasonable results. The following chapter implements the framework for the more complicated problem of the Reese wall.

# CHAPTER 9: LONG-TERM BEHAVIOR: THE REESE WALL (FINITE ELEMENT MODEL)

This chapter implement the framework developed in chapter 8 in the numerical model of the Reese wall. Section 9.1 presents the soil input properties adopted for the Reese wall numerical model. Section 9.2 compares between the measured wall behavior during cycle and the predicted wall behavior adopting the framework presented in Chapter 8. Section 9.3 segregates the factors causing additional deflection during long-term behavior. Walls retaining partially saturated soil that are subjected to variation in the soil saturation, undergo several changes during the transition to the more critical long-term conditions. These changes are described as follows:

1- Dissipation of the excavation induced pore-water pressure.

2- Changes in the active side soil properties due to changes in the soil saturation.

3- Changes in the passive side soil properties due to loss of confining stress.

4- Changes in the hydrostatic pressure due to changes in the ground water table.

## 9.1 SOIL INPUT PROPERTIES

During the transition of a wall from the short-term to the long-term conditions the soil properties on the active side changes with respect to the changes in the soil degree of saturation. In other words, the soil properties measured during the site investigation are not constant and depends on the soil saturation level. Soil properties changes on the passive side of the wall changes with respect to the changes in the confining pressure of the wall. This section discusses these changes and the procedures followed to extrapolate the soil properties measured during the site investigation to the soil properties expected for conditions different than the site investigation conditions.

### 8.1.1 Active side

***Total unit weight***

The active side of the wall is subjected to variation in soil water content, the framework, presented in chapter 8, suggested that the soil effective stresses are described in terms of the effective degree of saturation using the SSCC. The effective degree of saturation is calculated as a function of the volumetric moisture content ($\theta$) the residual volumetric moisture content ($\theta_r$) and the saturation volumetric moisture content ($\theta_s$). Direct measurement of the volumetric moisture content of partially saturated soil are not available for the Reese wall site, instead the volumetric moisture content is estimated from total unit weight estimates and water content measurements for different wetting and drying cycles. Water content measurements are available during different wetting and drying stages, total unit weight measurements are only available from the undisturbed soil samples obtained during the site investigation works. Total unit weight measurements obtained during the site investigation are only representative of the soil during the site investigation saturation conditions, and cannot be used in estimating the effective degree of saturation of the soil at different stages.

Figure 9.1 presents a comparison between estimated total unit weight profiles during different wetting and drying cycles. Total unit weight profiles estimated for the wetting and drying conditions are extrapolated from the site investigation profiles, following the framework previously presented in Chapter 8.

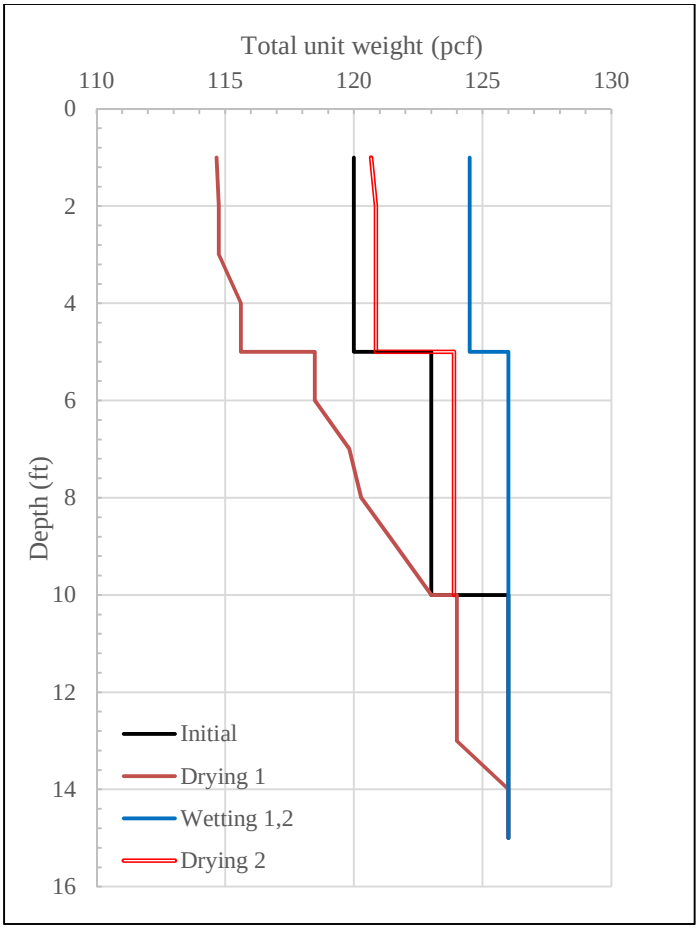


Figure 9.1: Comparison between total unit weight profiles on the active side during wetting and drying stages

***Water content***

The water content of the Reese wall site is measured periodically during wetting and drying cycle. This section presents the water content measurements before the wall construction, and, during cycles of wetting and drying.

***Water content: Before wall construction***

Figure 9.2 presents the water contents measurements during the initial site investigation works (January 12$^{th}$ 2010). Although the piezometers indicate that the natural

ground water table is 8ft below the ground surface, the water content measurements of the top 15ft indicate the soil below the natural ground water table might be partially saturated. Comparison between water content measurements from different boreholes suggests that spatial variation of water content is insignificant.

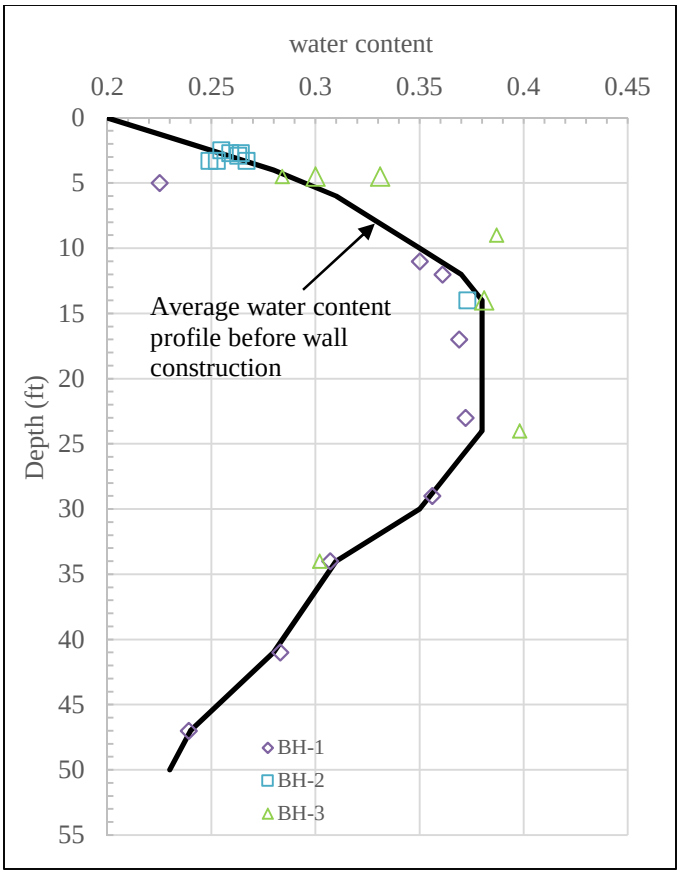


Figure 9.2: Water content measurements before wall construction (Jan-12-2010)

Figures 9.3 through 9.6 presents the water contents measured during wetting and drying cycles. Variation in the water content within the same stage of wetting or drying could be attributed to three factors. First, the spatial variation due to proximity of a source

of water; second, presence of dissection cracks and fissures that have permeability parameter different than intact soil; third time dependent characteristics of soil.

Consistency of water content measurements from different boreholes during the initial site investigation suggests water contents are not affected by a nearby source of water. Therefore, the variability of the water contents during the drying conditions are due to the heterogeneity of water content due to the presence of a random structure of cracks. The lower envelope of the measured water contents during drying stages are assumed to represent the water content of the soil; because lower envelope measurements are probably the samples least affected by the water with desiccation cracks and fissures.

However, during inundation stages, the spatial variation is evident; because the inundation pond is providing a continuous source of water. Besides, all the water content measurement samples during inundation phases are obtained from outside the inundation pond (for workability reasons). Therefore the high envelope of the measured water contents during inundation stages are assumed to represent the water content of the soil in within the inundation pond.

***Water content: First natural moisture fluctuation***

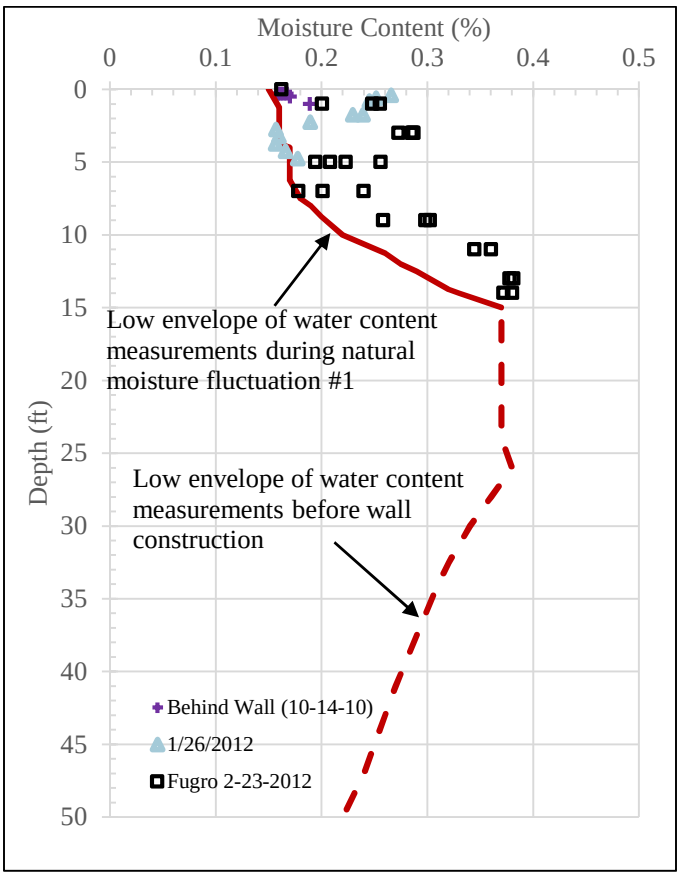


Figure 9.3: Water content measurements during first natural moisture fluctuation (Oct-1-2010 to May-3-2012)

***Water content: First inundation cycle 1***

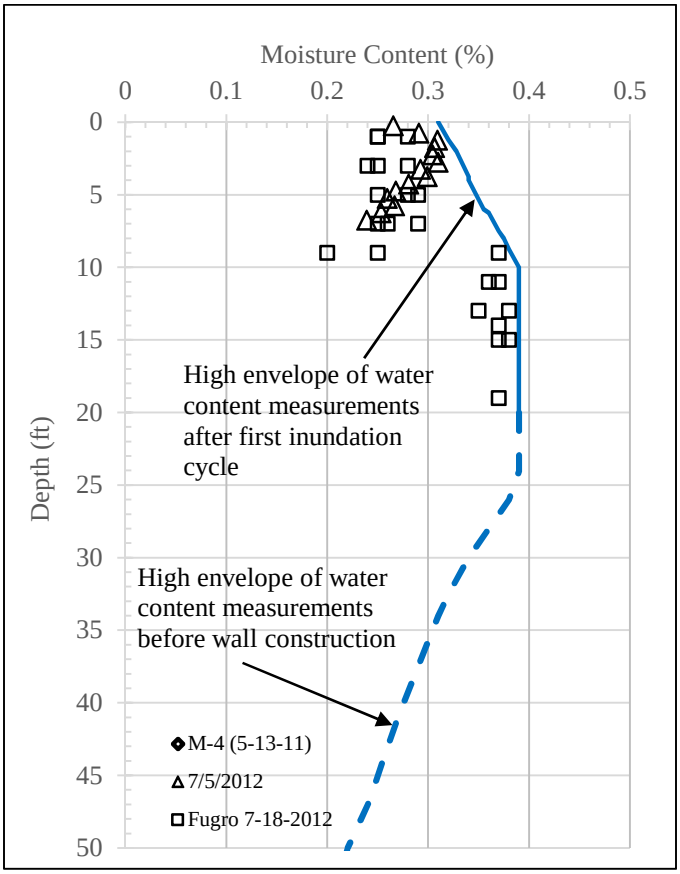


Figure 9.4: Water content measurements during first inundation cycle

***Water content: Second natural moisture fluctuation***

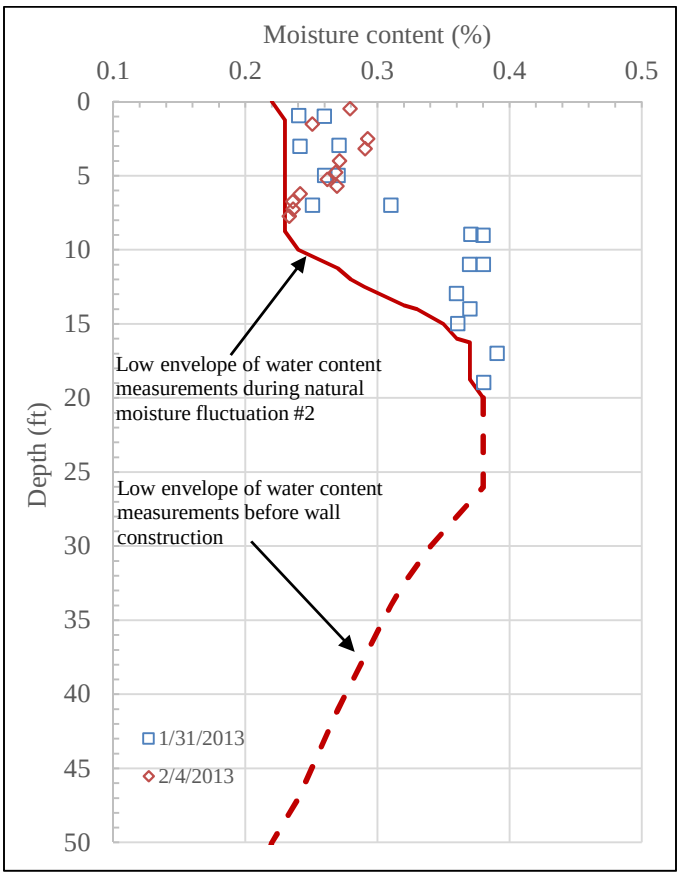


Figure 9.5: Water content measurements during second natural moisture fluctuation

***Water content: Second inundation cycle 2***

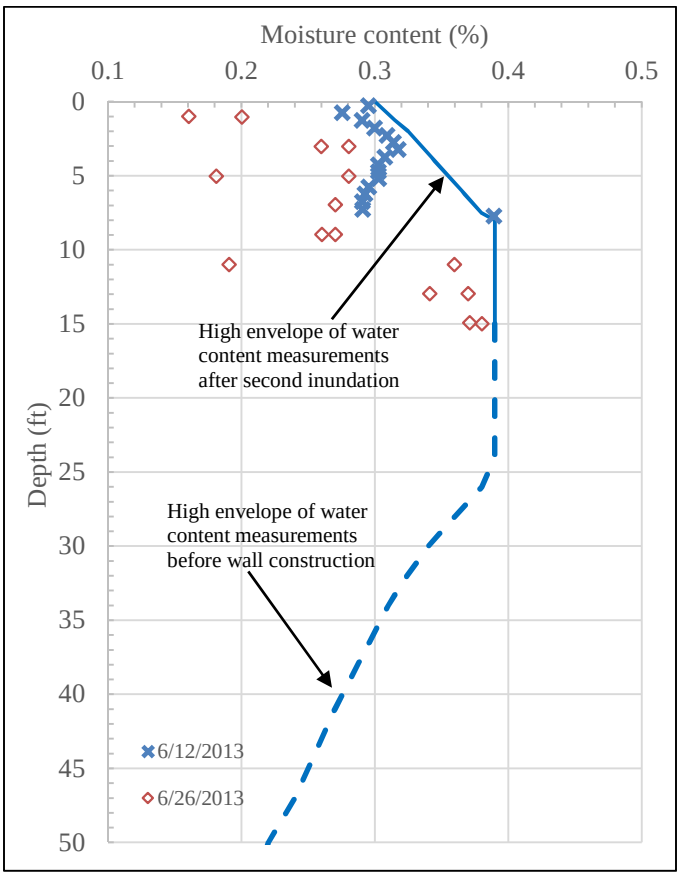


Figure 9.6: Water content measurements during second inundation cycle

Figure 9.7 presents a comparison between water content profiles during different stages of wetting and drying. The figure shows that variability of the water content is limited to the top 15ft of soil, i.e., the active zone of the Reese wall site is 15ft deep.

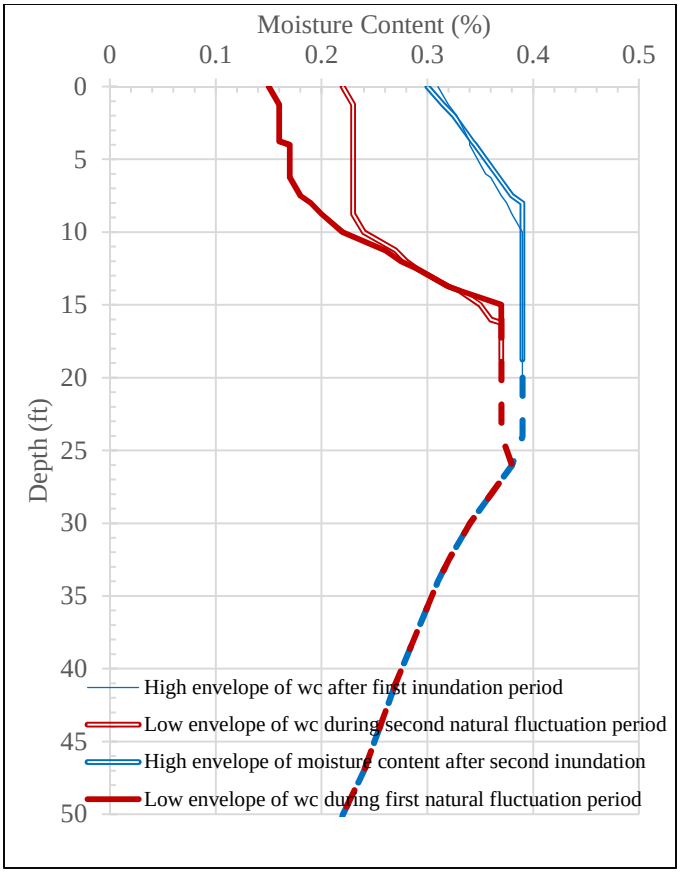


Figure 9.7: Comparison between water content profiles (i) Natural fluctuation period 1 (ii) Inundation period 1 (iii) natural fluctuation period 2 (iv) Inundation period 2

***Effective degree of saturation***

Figure 9.8 presents the estimated effective degree of saturation profiles on the active side of the wall, during different wetting and drying conditions. The profiles are estimated from the water content measurements and the estimated dry unit weight profiles. The lowest envelope of effective degrees of saturation is estimated during the first natural moisture fluctuation cycle. The highest envelope is estimated during the inundation cycles, the two inundation cycles result in similar effective degree of saturation profiles. The variation of the effective degree of saturation is evident at the top 15ft of soil. At the ground

surface, the effective degree of saturation varies between 0.05 and 0.51; and, the effective degree of saturation during site investigation is 0.18.

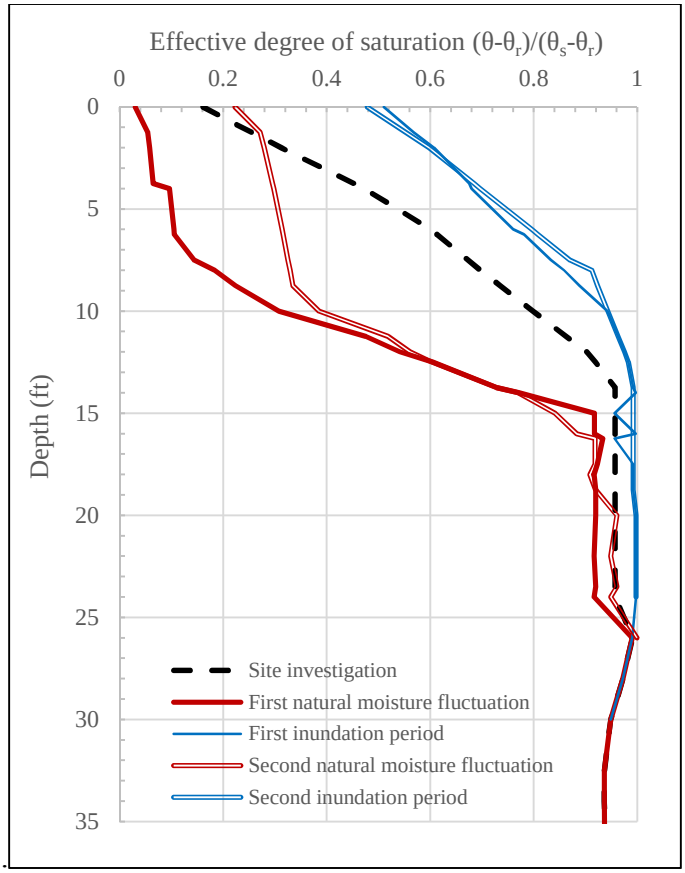


Figure 9.8: Comparison between effective degree of saturation profiles on the active side during wetting and drying stages

***Suction stress***

On the active side of the wall, the total stress over the pore-air pressure ($\sigma$-$u_a$) is constant during wetting and drying cycles; because, no additional loads are applied or removed. Therefore; Figure 9.9 presents the only variable component of effective stress, the suction stress. The figure presents the suction stress profile during different wetting and

drying cycles. The profile is generated by estimating the suction stresses corresponding to effective degree of saturation profiles presented in Figure 9.8, using the adopted SSCC presented in Figure 8.18. The variation of the suction stress is evident at the top 15ft of soil; however, minute changes in the effective degrees of saturation of soil deeper than 20ft results in significant changes in suction stress; because a different SSCC is adopted for soil deeper than 20ft (as discussed in section 8.6).

Changes in the degree of saturation below 25ft was assumed negligible and soil deeper than 25ft is assumed to have constant suction stress during wetting and drying conditions. At the ground surface, the suction stress varies between 3,000psf and 15,000psf; while, the suction stress during the site investigation stage is 7,000 psf. The suction stress during wetting and drying conditions decreases with depth, until a depth 15ft where different stages of wetting and drying show an approximately equal suction stress.

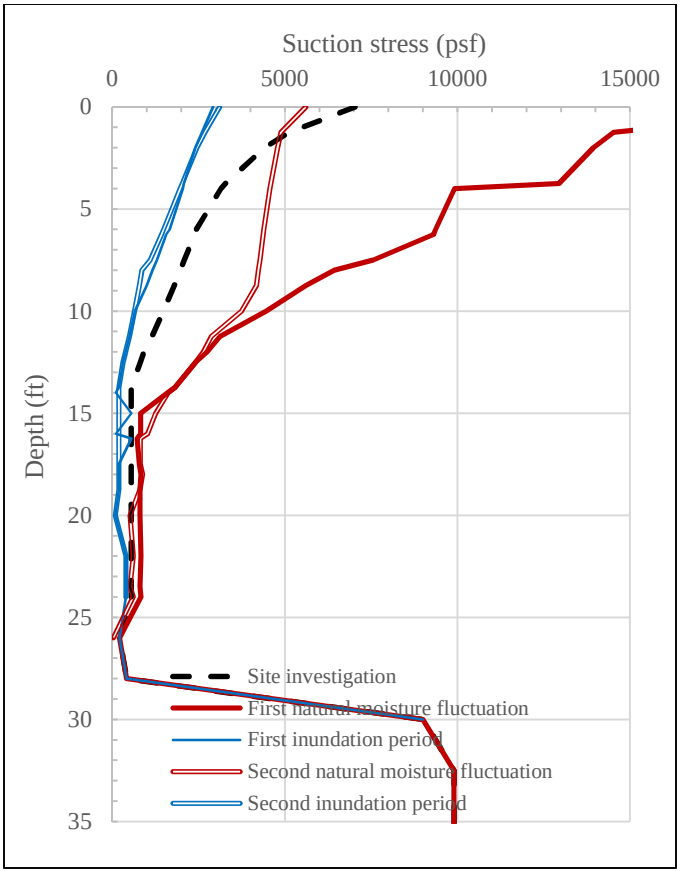


Figure 9.9: Suction stress profiles on the active side during wetting and drying stages

***Soil stiffness***

Section 8.8 presented two different approaches for analyzing the behavior of partially saturated soils during variation of the degree of saturation; namely the incremental analysis and the average analysis. The average analysis adopted soil properties based on an average condition of effective degree of saturation. Figures 9.10 through 9.11 presents the soil properties calculated based on the initial, final, and average soil conditions for each wetting and drying stage. The low water content envelops of the drying conditions and high water content envelopes of the wetting conditions presented in Figures 9.2 through 9.6.

***Soil stiffness: First natural moisture fluctuation***

Figure 9.10 presents the average stiffness profile adopted in numerical model during the first natural moisture fluctuation cycle. The FE input profile is calculated as the average between the initial soil properties calculated at the initial site investigation conditions, and the final soil properties calculated at the low envelope of the first natural moisture fluctuation conditions i.e., driest conditions. As described in Chapter 7 the soil stiffness is calculated as a function of the effective stress on the soil. Variation of the soil stiffness with the variation of the effective stress during the first natural moisture fluctuation cycle seems to be limited to the top 7ft of soil. The small-strain shear stiffness at the ground surface varies between 6.0E+5 psf to 1.1E+6 psf.

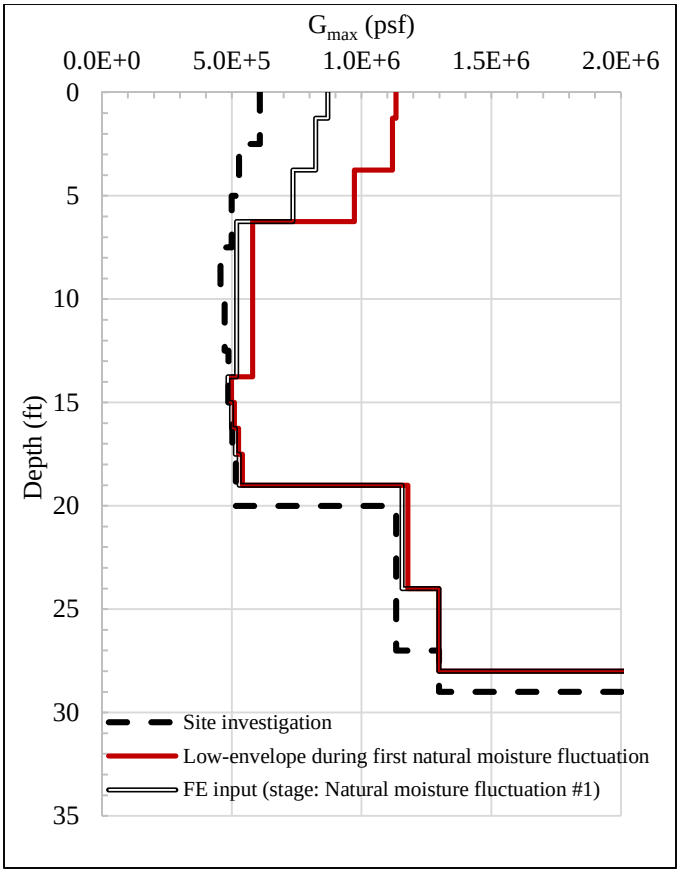


Figure 9.10: Small-strain shear stiffness profiles on the active side during: (i) Site investigation (ii) Low bound during first natural moisture fluctuation (iii) FE input profile

Figure 9.11 presents the average large strain-stiffness profile adopted in numerical model during the first natural moisture fluctuation cycle. The stiffness profile is calculated by reducing the large-strain stiffness with the same stiffness reduction calculated from the Shibuya et al. (1997) due to the increase of effective stresses during the first inundation cycle.

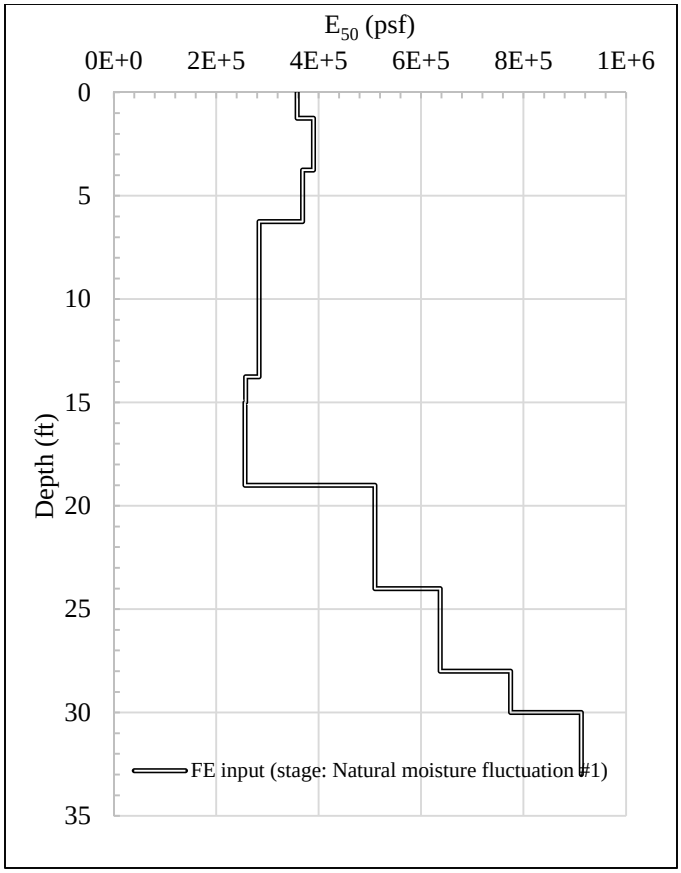


Figure 9.11: Large-strain shear stiffness profiles on the active side during adopted in the FE model during the first natural moisture fluctuation cycle

***Soil stiffness: First inundation cycle***

Figure 9.12 presents the average stiffness profile adopted in numerical model during the first inundation cycle. The FE input profile is calculated as the average between the initial soil properties calculated at the low envelope of the first natural moisture fluctuation conditions i.e., first driest conditions, and the final soil properties calculated at the high envelope of the first inundation cycle conditions i.e., first wettest conditions. This cycle is associated with largest variation of stiffness. Variation of the soil stiffness with the variation of the effective stress during the first wetting cycle seems to be limited to the top

7ft of soil. The small-strain shear stiffness at the ground surface varies between 4.0E+5psf and 1.1E+6psf.

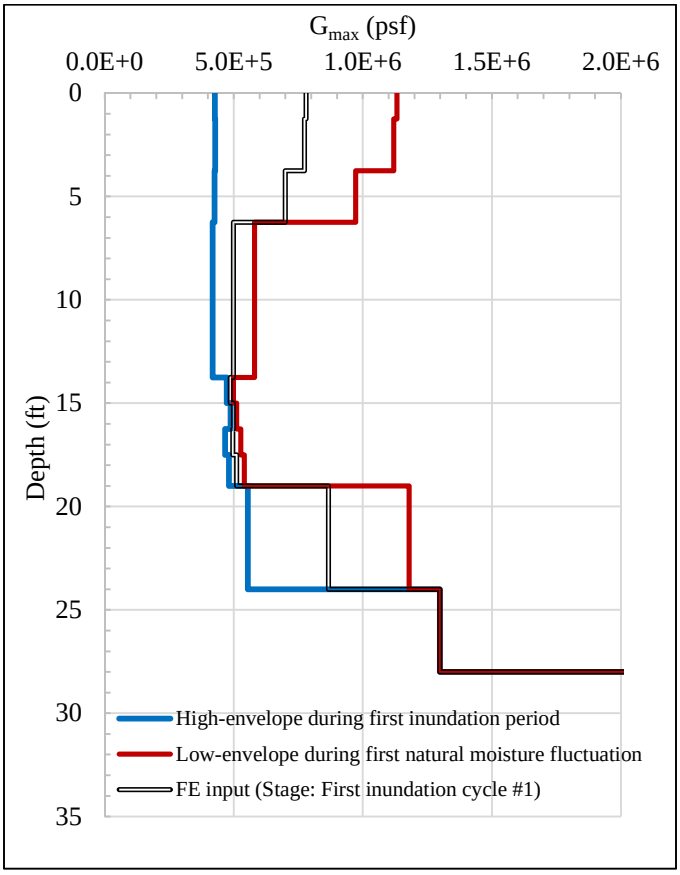


Figure 9.12: Small-strain shear stiffness profiles on the active side during: (i) Low-bound during first natural moisture fluctuation (ii) High-bound during first inundation period (iii) FE input profile

Figure 9.13 presents the average large strain-stiffness profile adopted in numerical model during the first inundation cycle. The stiffness profile is calculated by reducing the large-strain stiffness with the same stiffness reduction calculated from the Shibuya et al. (1997) due to loss of effective stress during the first inundation cycle.

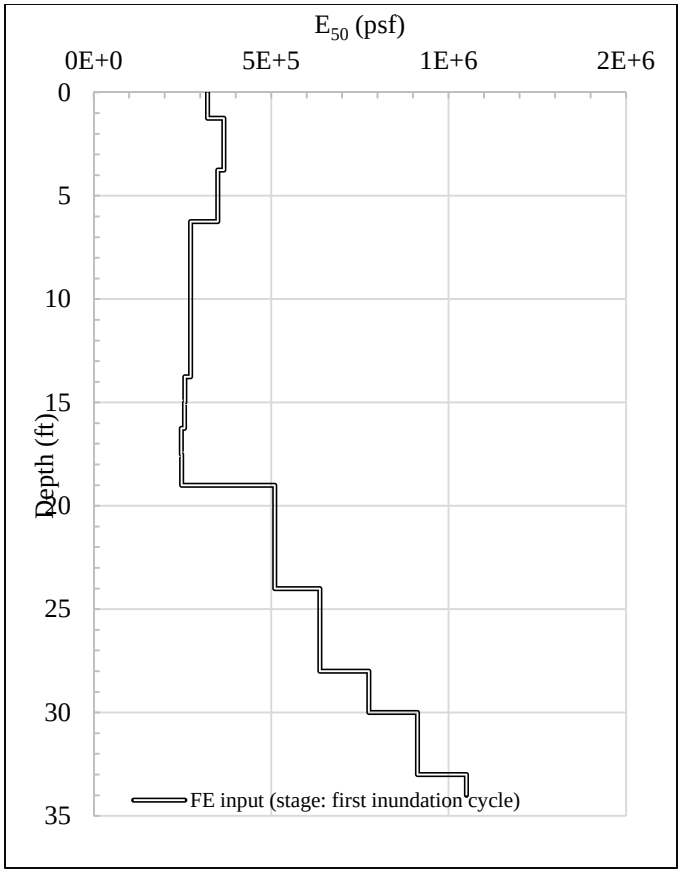


Figure 9.13: Large-strain shear stiffness profiles on the active side adopted in the FE model during the first inundation cycle

***Soil stiffness: Second natural moisture fluctuation***

Figure 9.14 presents the average stiffness profile adopted in numerical model during the second natural moisture fluctuation cycle. The FE input profile is calculated as the average between the initial soil properties calculated at the high envelope of the first inundation cycle conditions i.e., first wettest conditions, and, the final soil properties calculated at the low envelope of the second natural moisture fluctuation conditions i.e., second driest conditions. The small-strain shear stiffness at the ground surface varies between 4.0E+5psf and 6.0E+5psf.

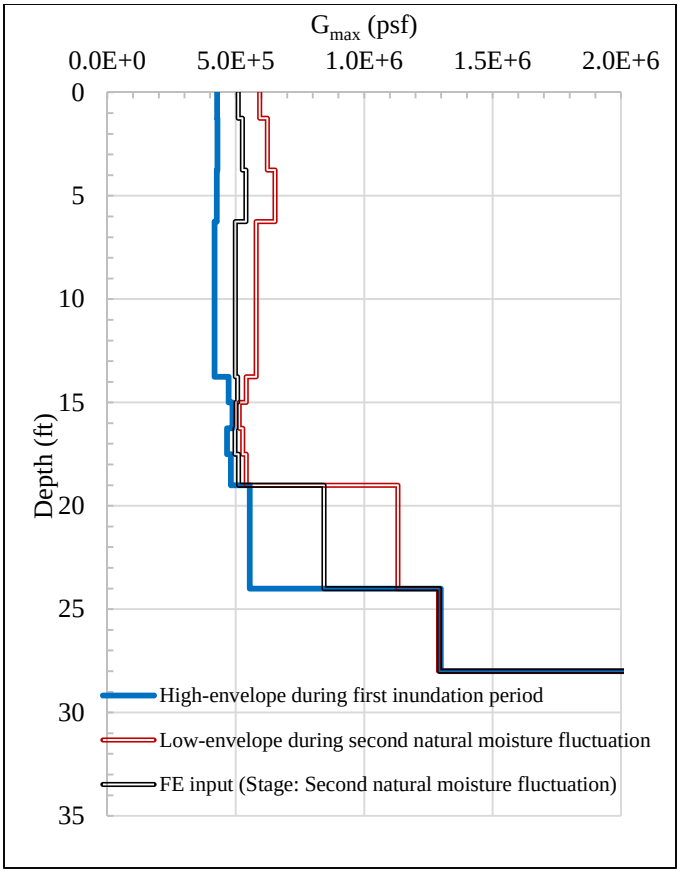


Figure 9.14: Small-strain shear stiffness profiles on the active side during: (i) High-bound during first inundation period (ii) Low-bound during second natural moisture fluctuation (iii) FE input profile

Figure 9.15 presents the average large strain-stiffness profile adopted in numerical model during the second natural moisture fluctuation cycle. The stiffness profile is calculated by increasing the large-strain stiffness with the same stiffness reduction calculated from the Shibuya et al. (1997) due to gain of effective stress during the natural moisture fluctuation cycle.

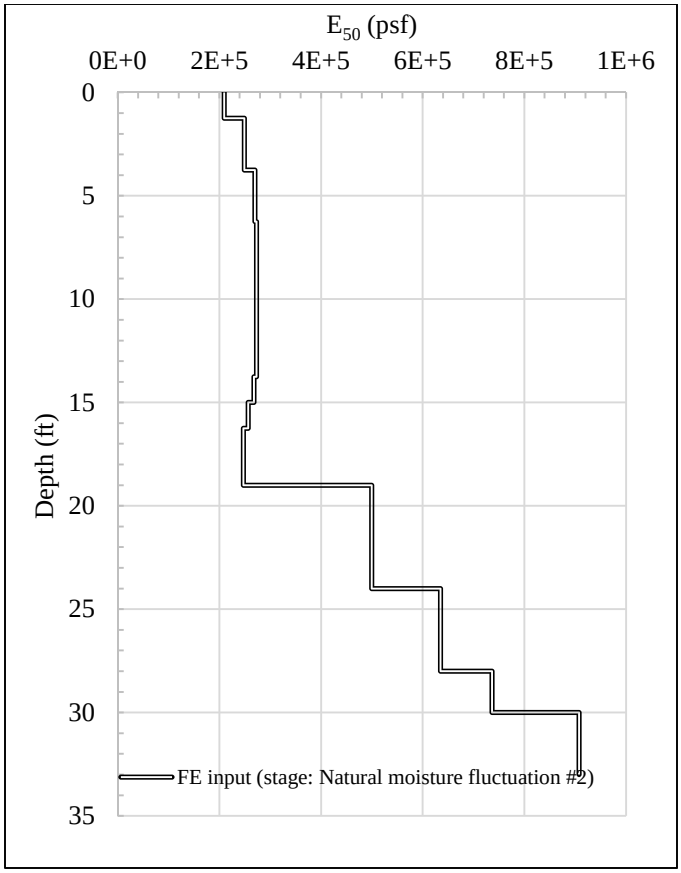


Figure 9.15: Large-strain shear stiffness profiles on the active side adopted in the FE model during the second natural moisture fluctuation cycle

***Soil stiffness: Second inundation cycle***

Figure 9.16 presents the average stiffness profile adopted in numerical model during the second wetting cycle. The FE input profile is calculated as the average between the initial soil properties calculated at the low envelope of the second natural moisture fluctuation conditions i.e., second driest conditions, and the soil properties calculated at the high envelope of the second inundation cycle conditions i.e., second wettest conditions. The small-strain shear stiffness at the ground surface varies between 4.3E+5psf and 6.0E+5psf.

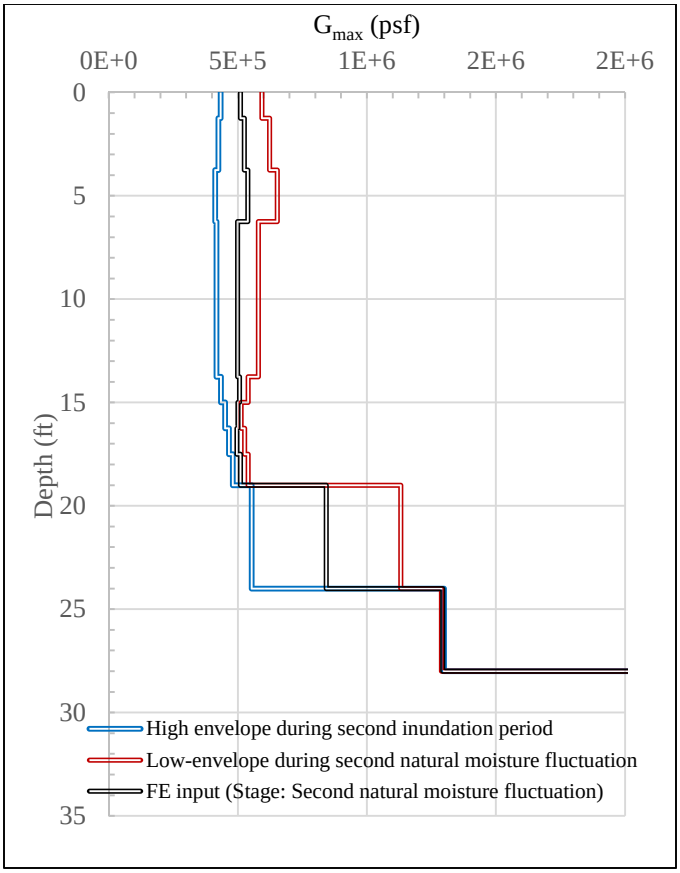


Figure 9.16: Small-strain shear stiffness profiles on the active side during: (i) Low-bound during second natural moisture fluctuation (ii) High-bound during second inundation period (iii) FE input profile

Figure 9.17 presents the average large strain-stiffness profile adopted in numerical model during the second inundation cycle. The stiffness profile is calculated by reducing the large-strain stiffness with the same stiffness reduction calculated from the Shibuya et al. (1997) due to gain of effective stress during the natural moisture fluctuation cycle.

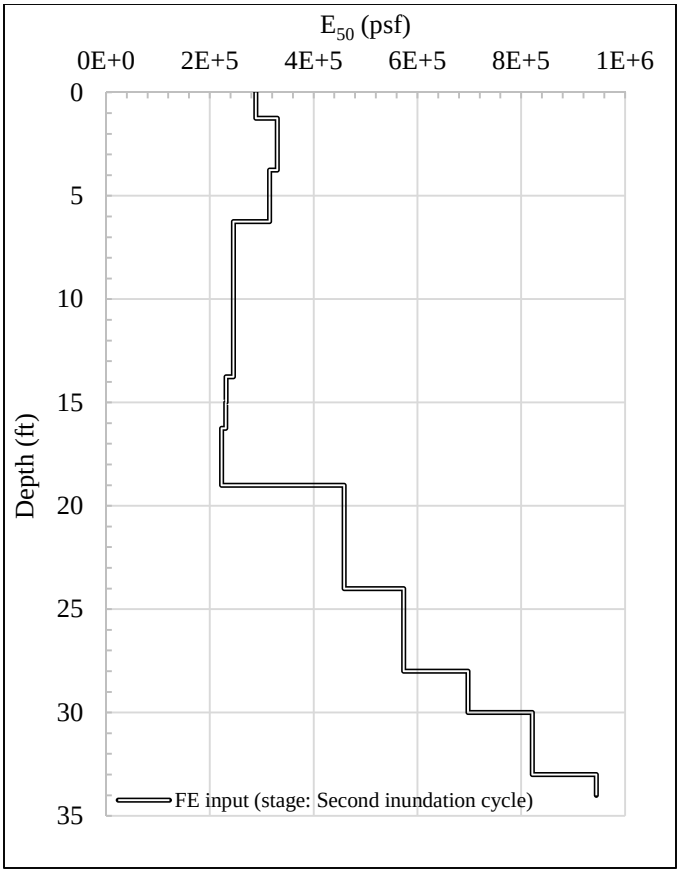


Figure 9.17: Large-strain shear stiffness profiles on the active side adopted in the FE model during the second inundation cycle

### 8.1.2 Passive side

On the passive side of the wall, the effective stress of the soil varies because of two reasons, namely, changes in the total stress and changes in the suction stress. However, the effective degree of saturation of the soil on the passive side of the wall is assumed to be constant in the numerical model of the Reese wall, because of three reasons. First, the excavation level is deeper than the natural ground water table of the Reese wall site (8ft deep). Second, water from the inundation pond reached to the excavation side during both inundation cycles, and the water was continuously pumped out of the excavated side. Third,

water content measurements are insufficient to estimate the effective degree of saturation during different wetting and drying stages. Therefore, the soil properties on the passive side is assumed to be variating only due to changes in the total stress, i.e. excavation of soil.

During the long-term conditions, soil on the excavated side of the wall, i.e., passive side, loses the confining stresses of the excavated soil. According to the Shibuya et al (1997) model, presented in section 8.7, the soil stiffness is sensitive to the soil void ratio. Change in the void ratio due to soil excavation is estimated by evaluating the excavation induced pore-water pressure and the recompression index of the soil ($C_r$).

Figure 9.18 presents the excavation induced pore-water pressure profile predicted from the numerical model; such that, the profile is computed at the end of the excavation stage. The profile shows that the excavation induced pore-water pressure is maximum at the excavation elevation and decreases with depth. The maximum excavation induced pore-water pressure is approximately 2000psf at the excavation elevation (-15ft), and decreases to 250psf at the elevation of the wall toe (-35ft).

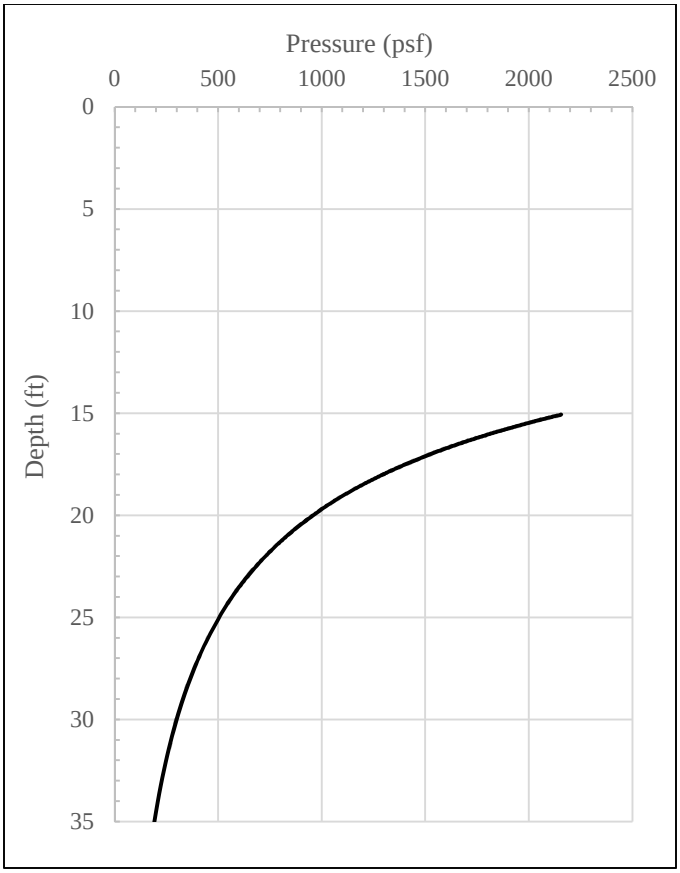


Figure 9.18: Excavation induced pore-water pressure profile on the passive side

Ellis (2011) measured the soil recompression index of four soil samples. Table 9.1 presents the measured recompression index values. A recompression index value of 0.1 is assumed for the soil and the variation in the void ratio is calculated. Figure 9.19 presents the change in the void ratio due to the loss of the excavation induced pore-water pressure. The maximum decrease in the void ratio is 0.03, and takes place at the excavation level, the deeper the soil the less significant the change in the void ratio due to the loss of the excavation induced pore-water pressure. The change in the void ratio is almost negligible at the level of the wall toe. Figure 9.20 presents a comparison between the void ratio of the soil before and after the loss of the excavation induced pore-water pressure.

Table 9.1: Recompression index of the Reese wall site (Ellis 2011)

| Depth (ft) | $C_r$ |
|---|---|
| 6-8 | 0.033 |
| 4-5 | 0.103 |
| 4-5 | 0.112 |
| 13-15 | 0.150 |

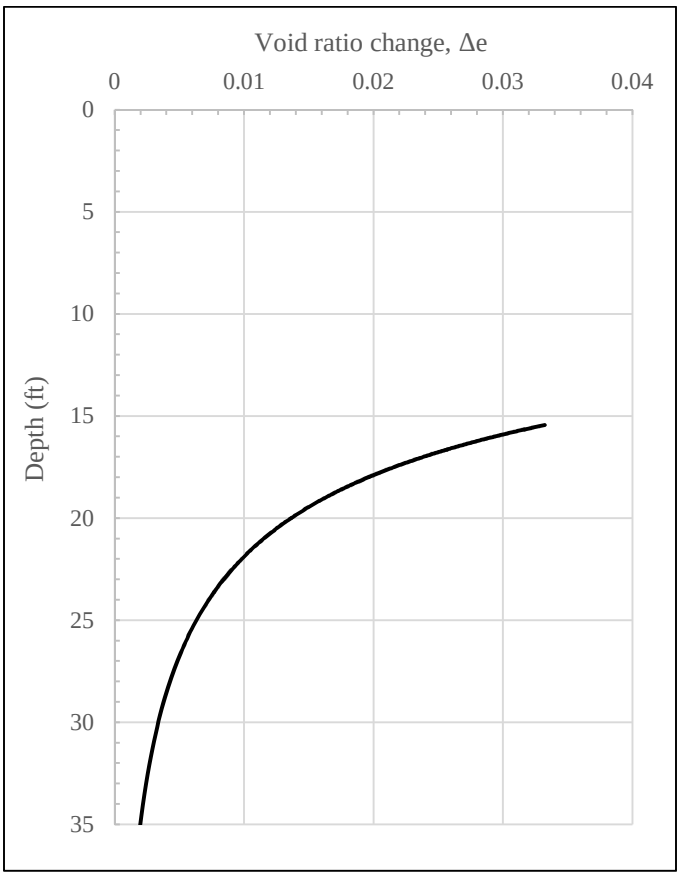


Figure 9.19: Excavation induced change in voids ratio on the passive side

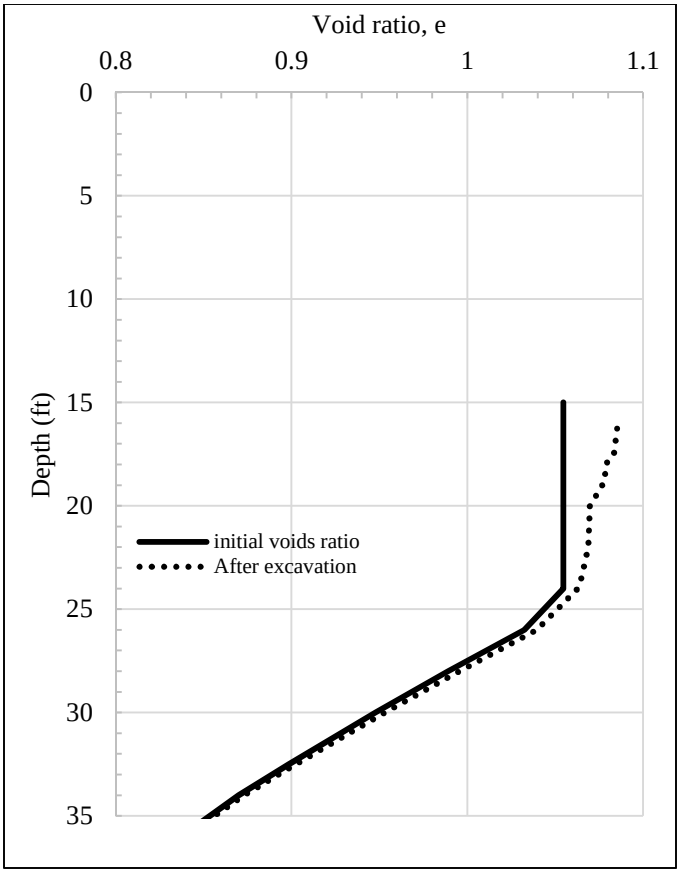


Figure 9.20: Comparison between void ratio profiles on the passive side before and after excavation

Figure 9.21 presents the small-strain stiffness profiles before excavation and after the dissipation of the excavation induced pore-water pressure. The small strain stiffness profiles are estimated according to the Shibuya et al (1997) model adopting the void ratio profiles presented in Figure 9.20. The variation of the effective stress due to consolidation of the excavation induced pore-water pressure sensitive to time dependent properties, such a permeability and time interval. Therefore, changes in soil properties on the passive side of the wall is assumed to take place gradually in different stage. Section 9.2 discusses the assumptions adopted for time dependent characteristics of the model.

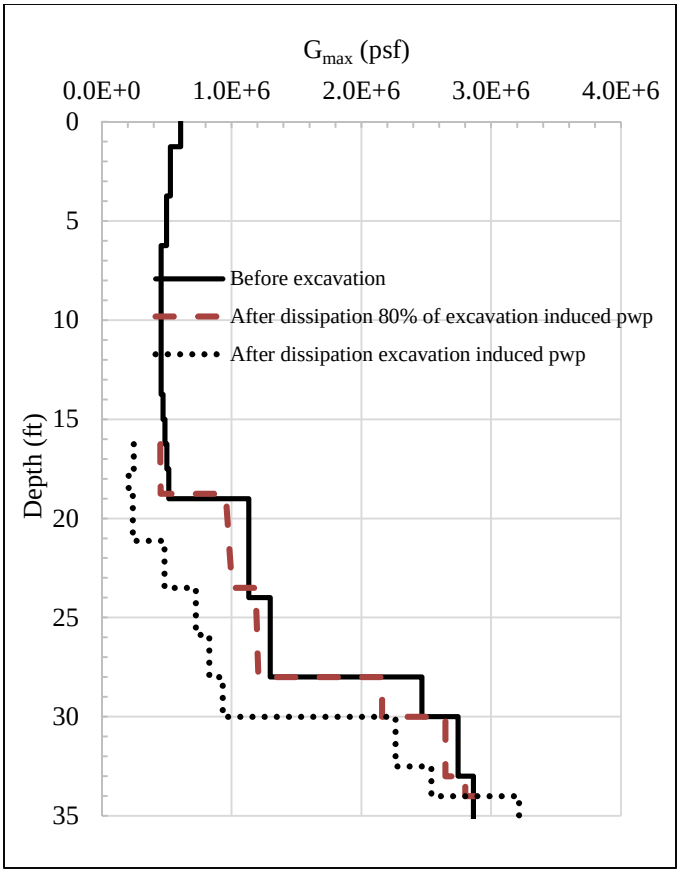


Figure 9.21: Comparison between Small-strain shear stiffness profiles on the passive side before excavation and after the dissipation of the excavation induced pore-water pressure

Figure 9.22 presents the average large strain-stiffness profile adopted in numerical model during the second inundation cycle. The stiffness profile is calculated by reducing the large-strain stiffness with the same stiffness reduction calculated from the Shibuya et al. (1997) due to the loss of effective stress lost during the dissipation of the excavation induced pore-water pressure.

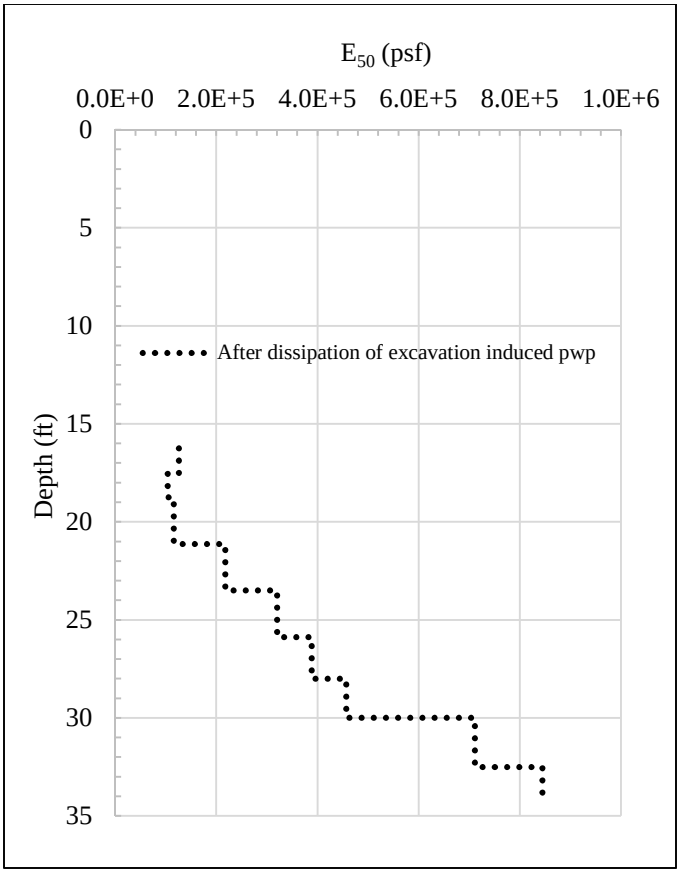


Figure 9.22: Large-strain shear stiffness profiles on the passive side adopted in the FE model during the second inundation cycle

## 9.2 CONSTRUCTION STAGES AND PREDICTED WALL RESPONSE

### 9.2.1 Free water pressure

Section 8.8 presented the methodology of implementing the developed framework into the PLAXIS software. The implementation adopted the pore-water pressure as a surrogate for the suction stress. The partially saturated soil in the Reese wall site is believed to sustain two schemes of pore-water pressures. First, the inter-particle pore-water pressure which is function of capillary pressure, double layer repulsion, etc., second, the pore-water pressure due to the free water within the random structure of cracks (Figure 9.23). The two

schemes of pore-water pressure are applied separately in the Rees wall numerical model, such that the inter-particle pore-water pressure is applied as isotropic pore-water pressure and the free water pressure is applied as loads on the wall.

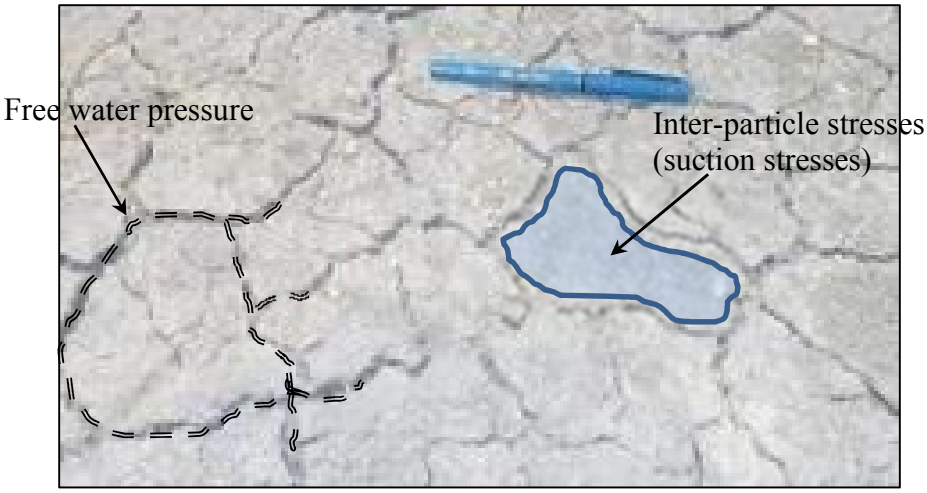


Figure 9.23: Pore-water pressure systems in partially saturated soil

The pressure applied on the wall from the free water at different wetting and drying stages are estimated from the piezometric measurements. Figure 9.24 presents the piezometric measurements 7.3ft and 15.1ft behind the wall, during the second inundation cycle. Piezometric measurements show that the free water pressure on the retained side of the wall is less than the hydrostatic pressure, approximately 65% of the hydrostatic pressure (Figure 9.25). The free water pressure is less than hydrostatic; because, the water is flowing downwards and towards the excavated side on the active side, and flows upward on the passive side. This flow of free water induces downward seepage force on the soil in retained side and upward force on the soil in passive side. These seepage forces are calculated and accounted for in the numerical model.

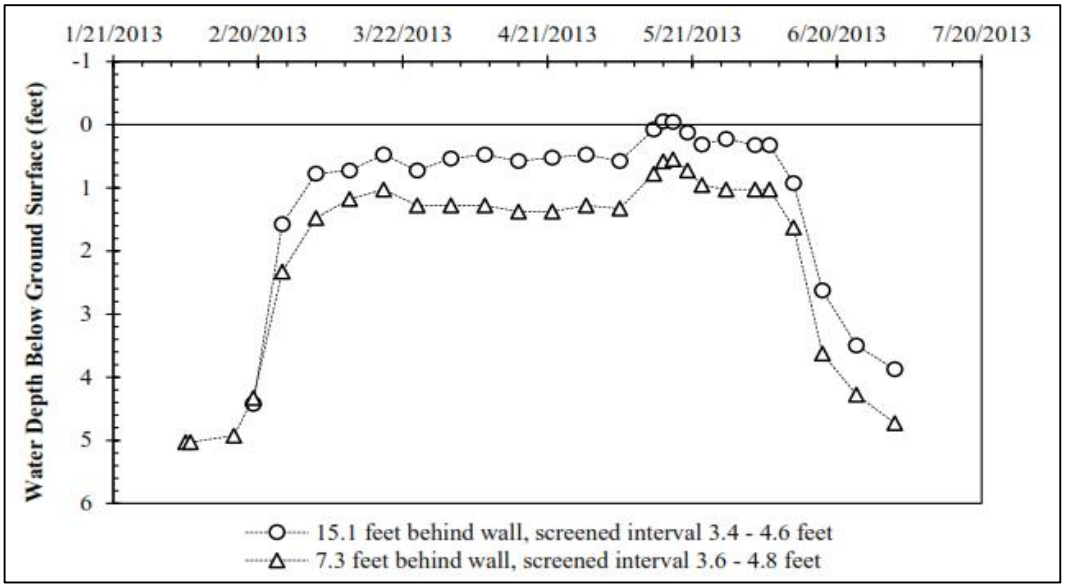


Figure 9.24: Data from shallow screened stand pipe piezometers during second inundation cycle (Brown 2013)

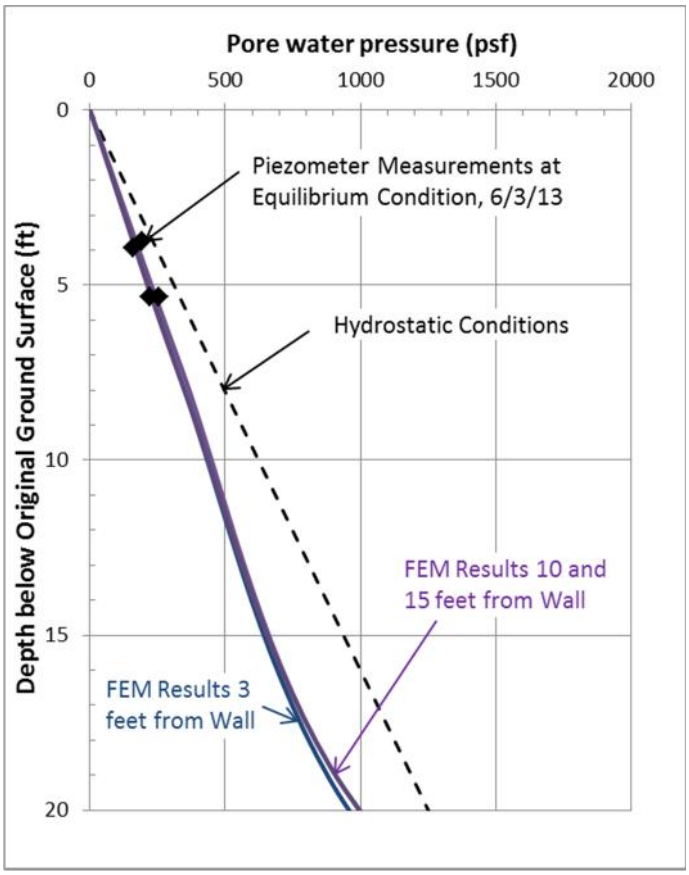


Figure 9.25: Comparison between hydrostatic water pressure piezometer measurements and FE prediction (Brown et al 2013)

### 9.2.2 Consolidation of excavation induced pore-water pressure

As previously mentioned, the soil permeability coefficient input parameters are adjusted to ensure that the input suction stress are completely imposed on the soil skeleton at the end of consolidation stages. This assumption results in expediting the consolidation of the excavation induced pore-water pressure. To account for the fact that consolidation takes place over both inundation cycles, percentages of consolidation is assigned to both inundation stages according to the wall deflection (Figure 9.26). The figure presents measured maximum wall deflection during the monitoring period. The maximum wall

deflection after the short-term conditions is 1inch, the maximum wall deflection after the second inundation cycle is 5inches. The 4inches additional deflection that took place during the transition from the short-term conditions to the long-term condition occurred during both inundation cycles. Such that during the first inundation cycle the wall deflected additional 3 inches, and during the second inundation cycle the wall deflected additional 1inch. The ratio of additional deflection is assumed to be consistent with the ratio of consolidation of excavation induced pore-water pressure. Such that during the first inundation cycle 80% of the excavation induced pore-water pressure is assumed to dissipate and during the second inundation cycle 20% of the excavation induced pore-water pressure is assumed to dissipate. Figure 9.26 shows an approximated average water content of the top 10ft of soil. Increase in the average water content measurements complies with the propagation of the wall deflection.

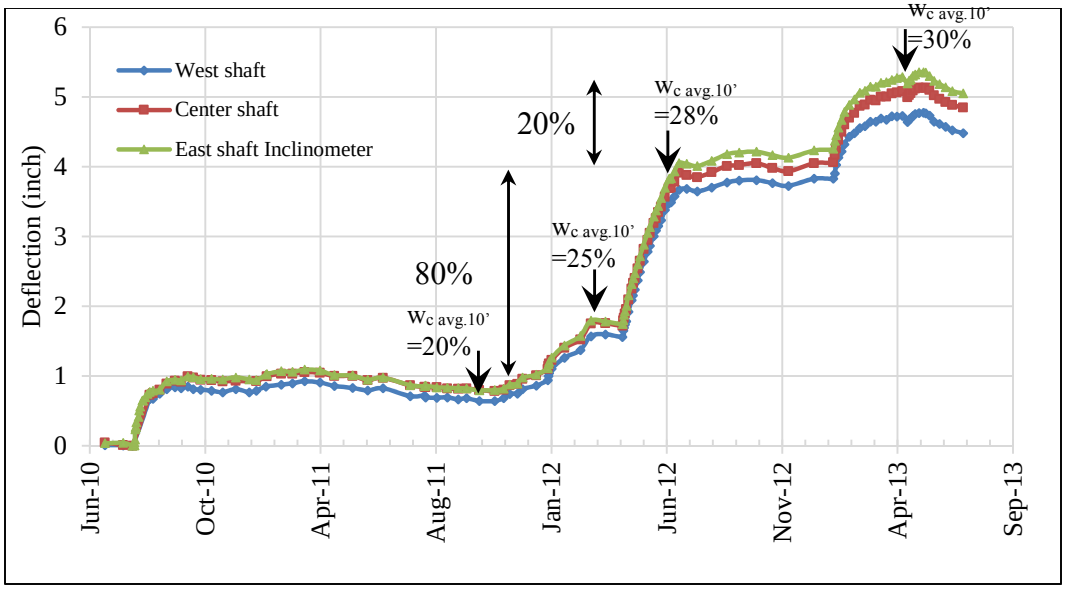


Figure 9.26: Maximum wall deflection propagation during cycles of wetting and drying

### 9.2.3 Numerical model stages

Figure 9.27 presents the timeline of wetting and drying cycles of the Reese wall site. These cycles of wetting and drying are simulated in the numerical model by 15 stages, Table 9.2 presents the description and calculation type of these stages. Stages 5, $5C_S$, and 5FW simulates the Reese wall conditions during the first natural moisture fluctuation cycle. Stages 6, $6C_S$, 6FW, and $6C_{Ex\text{-}pwp}$ simulates the Reese wall conditions during the first inundation cycle. Stages 7, $7C_S$, and 7FW simulates the Reese wall conditions during the second natural moisture fluctuation cycle. 8, $8C_S$, 8FW, and $8C_{Ex\text{-}pwp}$ simulates the Reese wall conditions during the second inundation cycle.

Stages followed by "$C_S$" denote consolidation stages where the strains are computed due to the changes in the pore-water pressure input, i.e., suction stress, as discussed in section 8.8. Stages followed by "FW" denote stages where the pressure from the free-water is imposed. Stages followed by "Ex-pwp" denote stages consolidation stages where the excavation induced pore-water pressure dissipates. Assigning the pore-water pressure according to the suction stress does not neutralize the excavation induced pore-water pressure; because, PLAXIS software distinguishes between the excess pore-water pressure and the steady-state pore-water pressure.

Figures 9.28 through 9.41 present the numerical model of the Reese wall at the end of the natural moisture fluctuation and inundation cycles, and present a comparison between measured and predicted deflection and bending moment profiles. Changes in the color of the soil indicates changes in the soil properties.

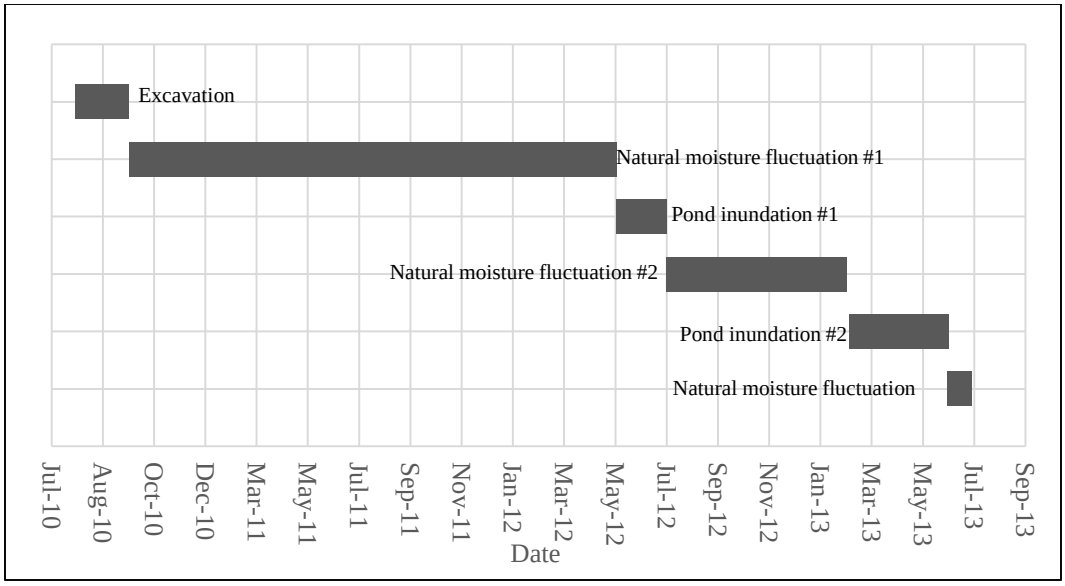


Figure 9.27: Construction activities timeline

Table 9.2: Stages of the long-term behavior of the Reese wall

| Stage | Description | Calculation type |
|---|---|---|
| 5 | Material change | Plastic |
| $5C_S$ | Natural moisture fluctuation #1 | Consolidation |
| 5FW | Hydrostatic pressure (-8ft) | Plastic |
| 6 | Material change #2 | Plastic |
| $6C_S$ | Inundation period #1 | Consolidation |
| 6FW | Constant x Hydrostatic pressure | Plastic |
| $6C_{Ex\text{-}pwp}$ | Consolidation 80% | Consolidation |
| 7 | Material change | Plastic |
| $7C_S$ | Natural moisture fluctuation #2 | Consolidation |
| 7FW | Hydrostatic pressure (-8ft) | Plastic |
| 8 | Material change | Plastic |
| $8C_S$ | Inundation period #2 | Consolidation |
| 8FW | Constant x Hydrostatic pressure | Plastic |
| $8C_{Ex\text{-}pwp}$ | Consolidation 100% | Consolidation |
| $8_{Seepage}$ | Seepage forces | Plastic |

***First natural moisture fluctuation***

Figure 9.28 presents the numerical model during the first natural moisture fluctuation cycle (stage 5FW). 8ft deep tension crack is modeled on the retained side to suppress tension stresses pulling the wall backwards toward the retained side. The free water pressure is assigned as hydrostatic pressure at elevation of (-8ft). Small-strain and large-strain stiffness profiles on the active side of the wall adopted in simulating the first

natural moisture fluctuation cycle were presented in Figures 9.10 and 9.11, respectively. The soil stiffness on the passive side is assumed to be equal to the measured during site investigation conditions.

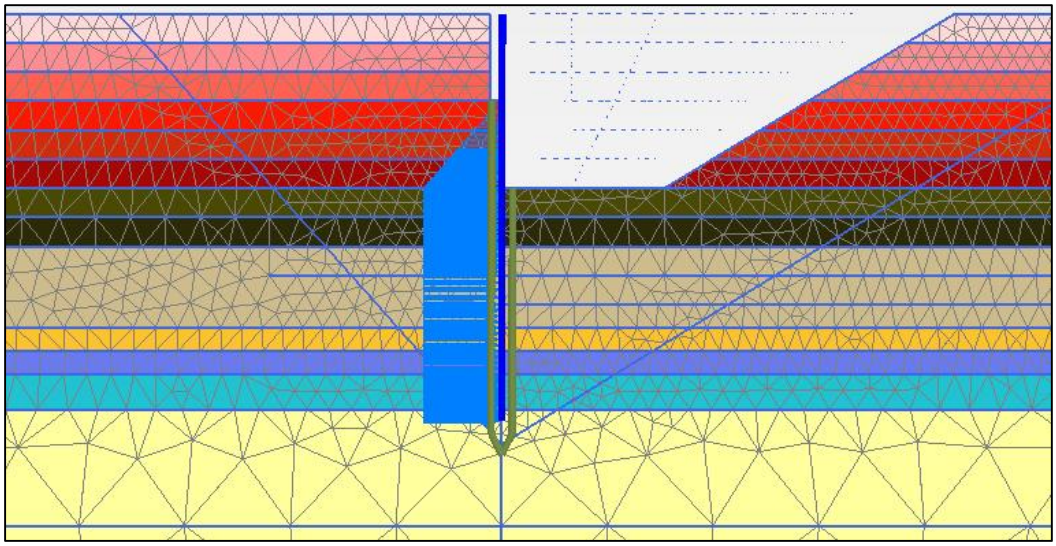

Figure 9.28: FE model stage (5FW): Soil conditions during natural moisture fluctuation #1 with hydrostatic pressure at 8ft below ground surface

Figure 9.29 presents a comparison between measured and predicted wall deflection profiles. The maximum measured wall deflection, i.e., deflection at the wall top during the first natural moisture fluctuation cycle is 0.64inch; while the maximum predicted wall deflection is 0.75inch. The maximum measured wall deflection during short-term conditions was 0.9inch, i.e., the Reese wall moved back-wards toward the retained side during the first natural moisture fluctuation cycle. Deflection toward the retained side could be attributed to the significant increase in the magnitude of suction stress during the first natural moisture fluctuation cycle. Increase in the suction stress internally confines the soil

which means that the soil exerts less stress on the external retaining system, i.e., retaining wall. Second, increase in the suction stress increases the soil stiffness.

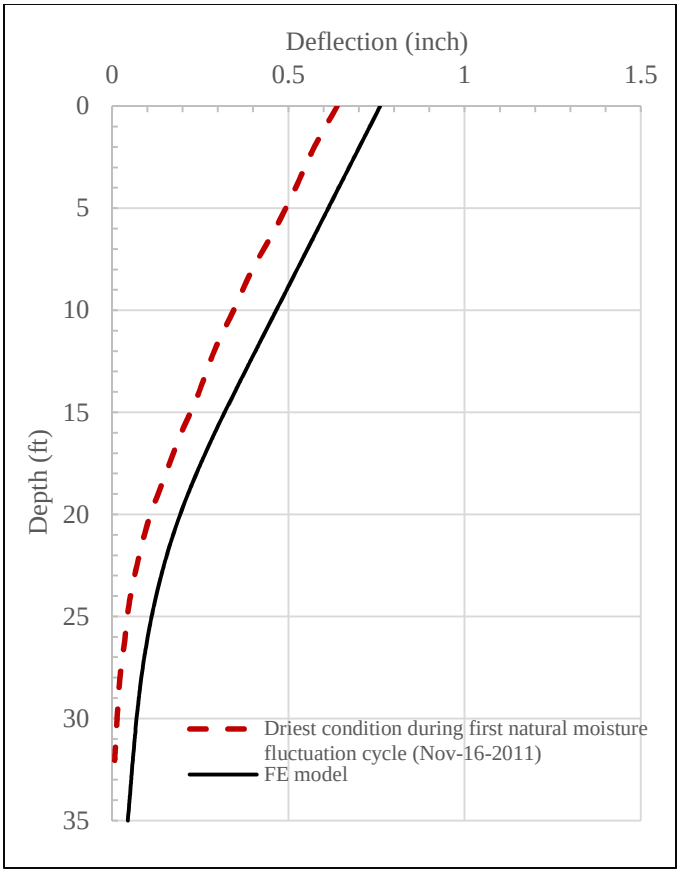


Figure 9.29: Comparison between measured and predicted deflection profiles due to first drying cycle

Figure 9.30 presents a comparison between measured and predicted wall bending moment profiles. The maximum bending moment during the first natural moisture fluctuation cycle is measured 5ft below the excavation depth. The maximum measured bending moment of 25,000lb.ft per shaft is almost equal to the maximum predicted bending moment. The maximum measured bending moment during short-term conditions was

approximately 40,000lb.ft per shaft, i.e., the maximum bending moment decreased during the first natural moisture fluctuation of the Reese wall site.

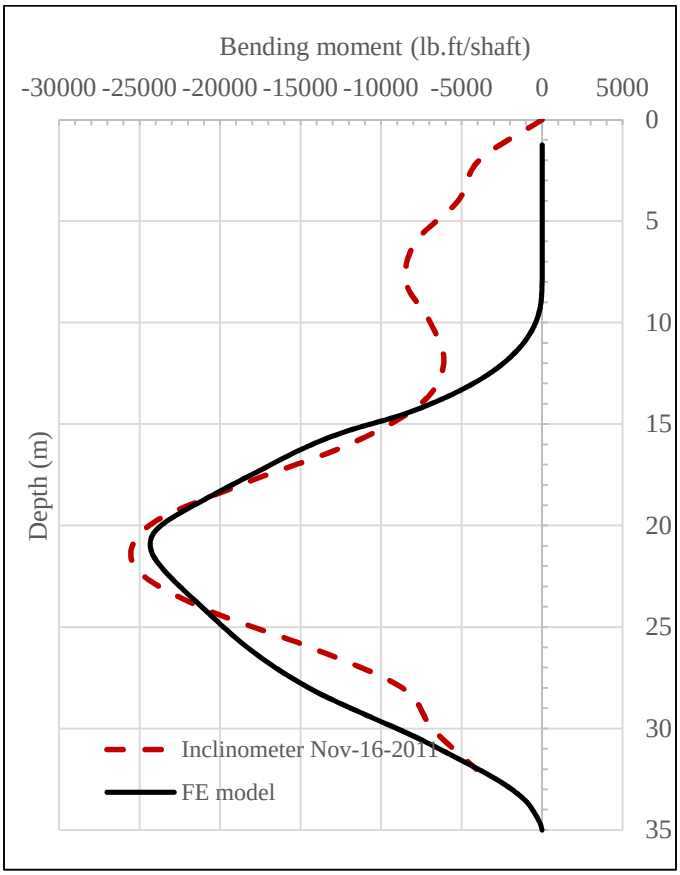


Figure 9.30: Comparison between measured and predicted bending moment profiles due to first natural moisture fluctuation cycle

***First inundation cycle***

At the beginning of the first inundation cycle (May-6-2013) the Reese wall site experienced extreme rainfall conditions, and the excavated side was filled with runoff water (Figure 9.31). The water in the excavated side was pumped out; however, 1.5ft of scoured soil filled the excavation bed, i.e., the excavation depth after the extreme rainfall and the removal of water is 13.5ft rather than 15ft.

Figure 9.31: Reese wall site conditions after severe rainfall, May 6 2013 (Brown 2013)

To account for the weight of the 1.5ft scour soil in the numerical model, an overburden pressure of 180psf is applied at the excavation level; and, to account for the lateral pressure induced by the 1.5ft scour soil in the numerical model, a triangular pressure of 180psf, i.e., $k_0$=1, is applied on the retained side of the wall at depths between 13.5ft and 15ft (Figure 9.32).

Figure 9.32 presents the numerical model at the end of the first inundation cycle (stage $6C_{Ex\text{-}pwp}$). Stage $6C_{Ex\text{-}pwp}$ is characterized as the stage when 80% of the excavation induced pore-water pressure dissipates, the retained side of the wall is subjected to a factorized hydrostatic pressure where the ground water table rises to the ground surface, and 80% of the changes in the soil properties on the passive side are accounted for. Small-strain and large-strain stiffness profiles on the active side of the wall adopted in simulating the first inundation cycle were presented in Figures 9.12 and 9.13, respectively. Small-

strain and large-strain stiffness profiles on the passive side of the wall adopted in simulating first inundation cycle were presented in Figures 9.21 and 9.22, respectively.

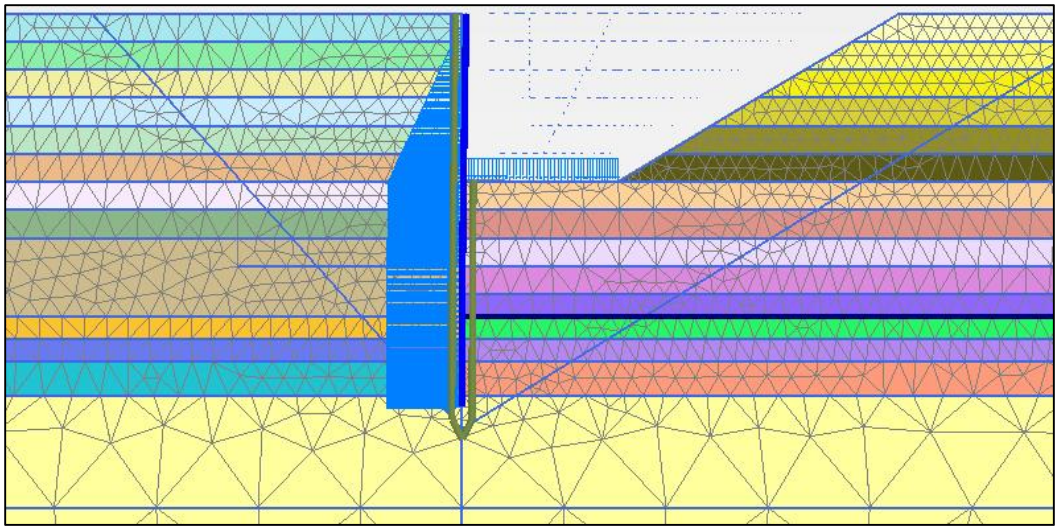

Figure 9.32: FE model stage(6CEx-pwp): Soil conditions during inundation cycle #1 with hydrostatic pressure at ground surface, assuming 80% consolidation of excavation induced pore-water pressure

Figure 9.33 presents a comparison between measured and predicted wall deflection profiles at the end of the first inundation cycle. The predicted deflection profile shows good agreement with the measured wall deflection profile. The maximum measured wall deflection is 3.6inches; while the maximum predicted wall deflection is 4.4inches. The additional deflection of the Reese wall during the transition from the dry state to the wet state is attributed to five factors. First, loss of internally confining suction stress which causes additional stresses on the wall, second, additional hydrostatic pressure due to the rise of the ground water table, third, loss of soil stiffness on the active side due to loss of effective stress, fourth, dissipation of excavation induced pore-water pressure, fifth, loss of soil stiffness on the passive side due to loss of overburden pressure.

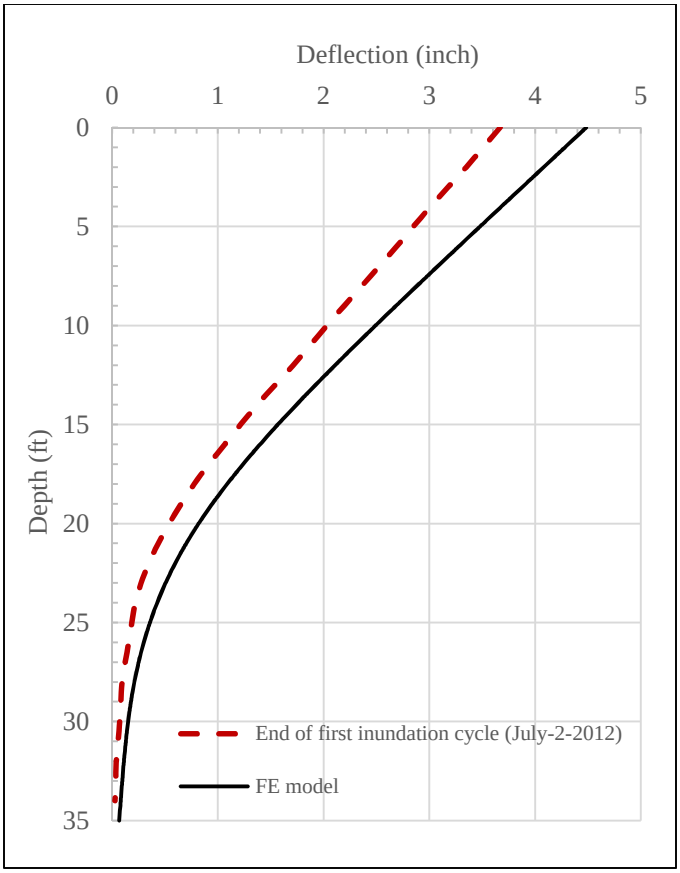


Figure 9.33: Comparison between measured and predicted deflection profiles due to First inundation cycle

Figure 9.34 presents a comparison between measured and predicted wall bending moment profiles during the first inundation cycle. The maximum bending moment is measured 5ft below the excavation bed. The predicted bending moment profile shows good agreement with the measured profile, such that the maximum measured and predicted bending moment are approximately 160,000lb.ft per shaft.

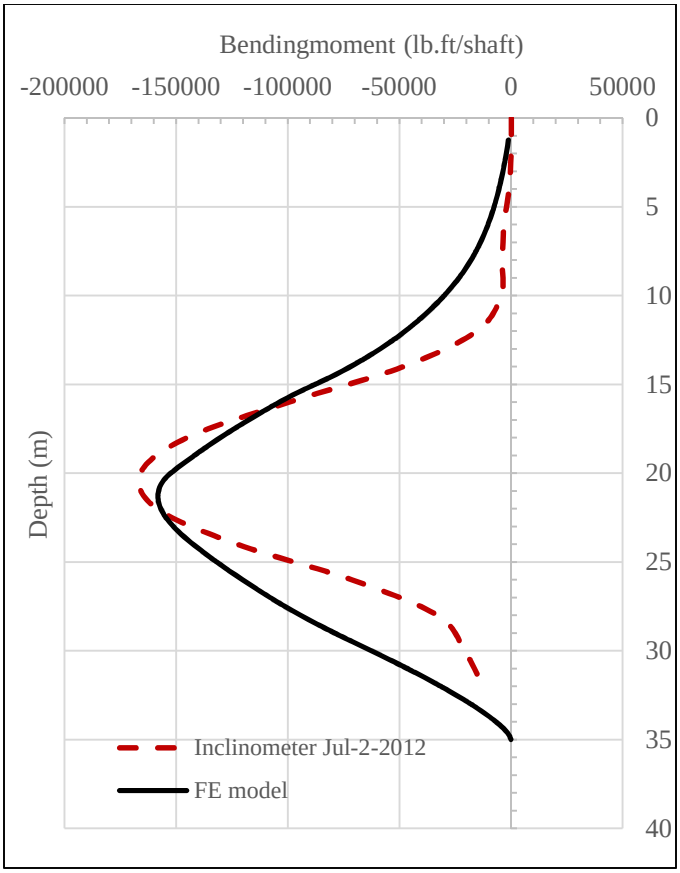


Figure 9.34: Comparison between measured and predicted bending moment profiles due to first inundation cycle

***Second natural moisture fluctuation***

Figure 9.35 presents the numerical model at the end of the second natural moisture fluctuation cycle (stage 7FW). The free water pressure is assigned as hydrostatic pressure at elevation of (-8ft). Small-strain and large-strain stiffness profiles on the active side of the wall adopted in simulating the second natural moisture fluctuation cycle were presented in Figures 9.14 and 9.15, respectively.

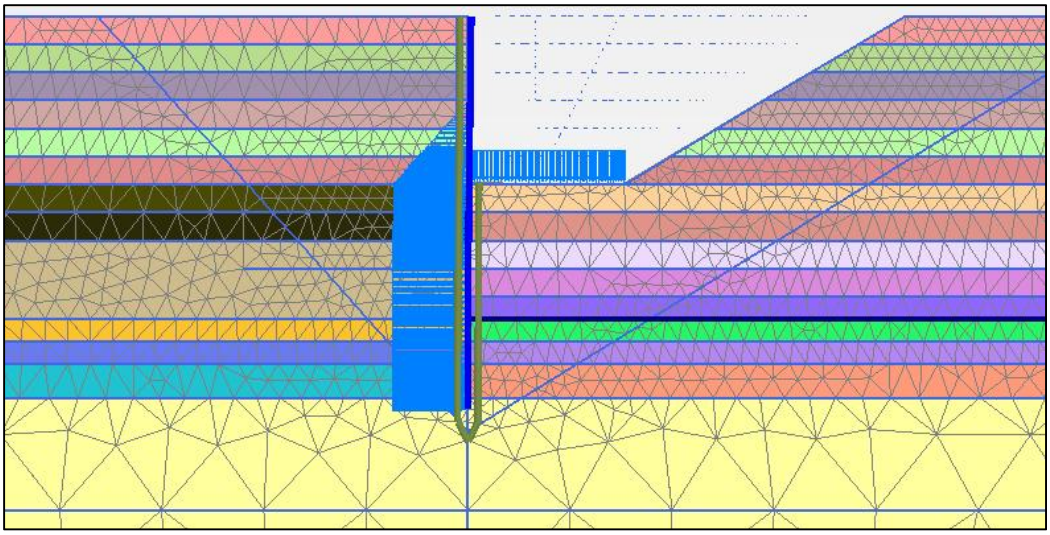

Figure 9.35: FE model stage(7FW): Soil conditions during natural moisture fluctuation #2 with hydrostatic pressure 8ft below ground surface

Figure 9.36 presents a comparison between measured and predicted wall deflection profiles at the end of the natural moisture fluctuation cycle. The predicted wall deflection profile shows good agreement with the measured wall deflection profile. The maximum measured wall deflection is 4inches; while the maximum predicted wall deflection is 3.8inches.

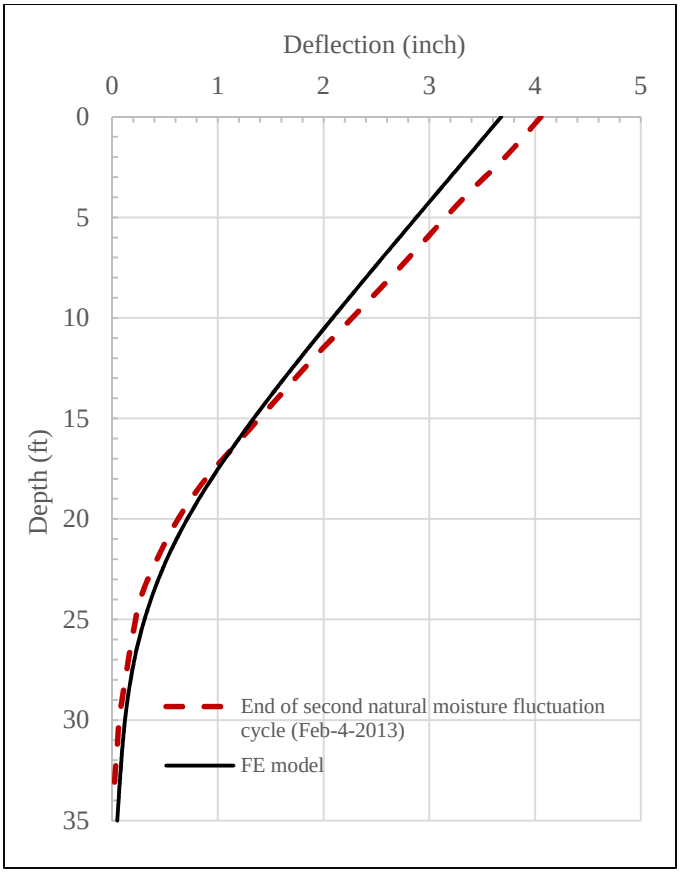


Figure 9.36: Comparison between measured and predicted deflection profiles due to Second drying cycle

Figure 9.37 presents a comparison between measured and predicted wall bending moment profiles during the second natural moisture fluctuation cycle. The maximum bending moment is measured 5ft below the excavation bed. The predicted bending moment profile shows reasonable agreement with the measured profile. The maximum measured bending moment is 170,000lb.ft per shaft; while, the maximum predicted bending moment is 130,000lb.ft per shaft.

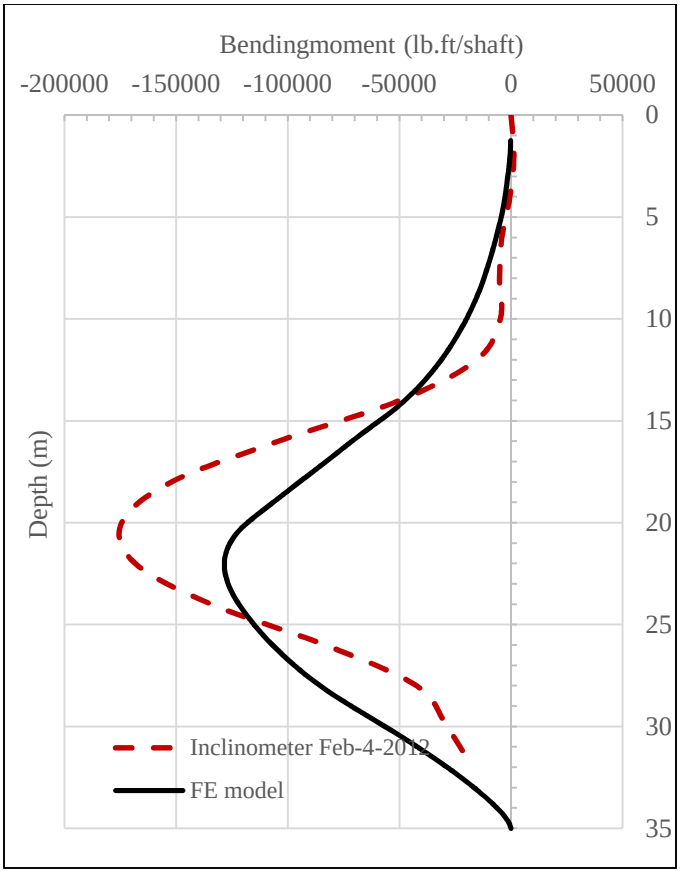


Figure 9.37: Comparison between measured and predicted bending moment profiles due to second drying cycle

***Second inundation cycle***

Figure 9.38 presents the numerical model at the end of the second inundation cycle (stage $8C_{Ex\text{-}pwp}$). Stage $8C_{Ex\text{-}pwp}$ is characterized as the stage when 100% of the excavation induced pore-water pressure dissipates, the retained side of the wall is subjected to a factorized hydrostatic pressure where the ground water table rises to the ground surface, and 100% of the changes in the soil properties on the passive side are accounted for. Small-strain and large-strain stiffness profiles on the active side of the wall adopted in simulating the second inundation cycle were presented in Figures 9.16 and 9.17, respectively. Small-

strain and large-strain stiffness profiles on the passive side of the wall adopted in simulating first inundation cycle were presented in Figures 9.21 and 9.22, respectively.

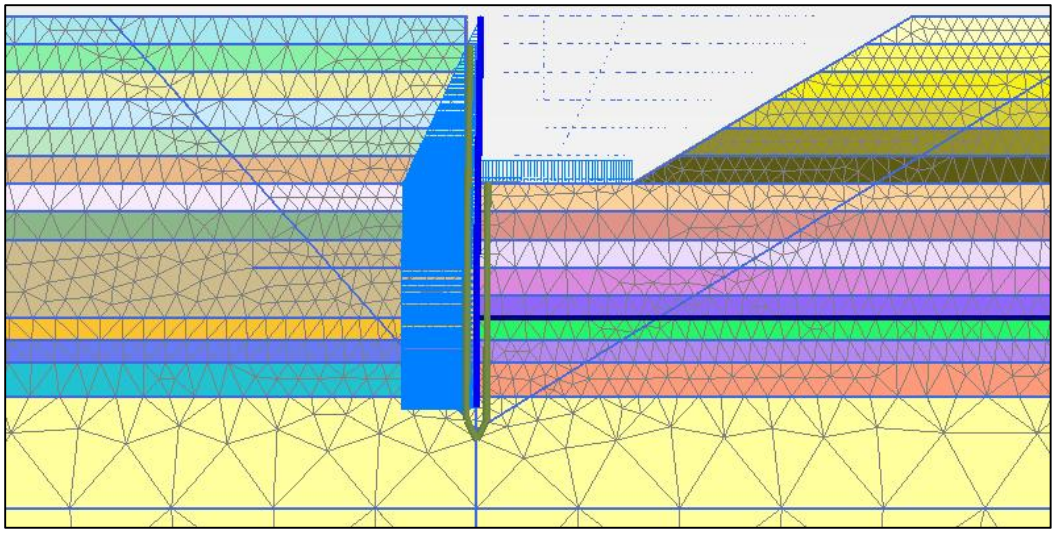

Figure 9.38: FE model stage (8CEx-pwp): Soil conditions during inundation cycle #2 with hydrostatic pressure at ground surface, assuming 100% consolidation of excavation induced pore-water pressure

Figure 9.39 presents a comparison between measured and predicted wall deflection profiles at the end of the second inundation cycle. The predicted deflection profile shows good agreement with the measured wall deflection profile. The maximum measured wall deflection is 5inches; while, the maximum predicted wall deflection is 4.6inches.

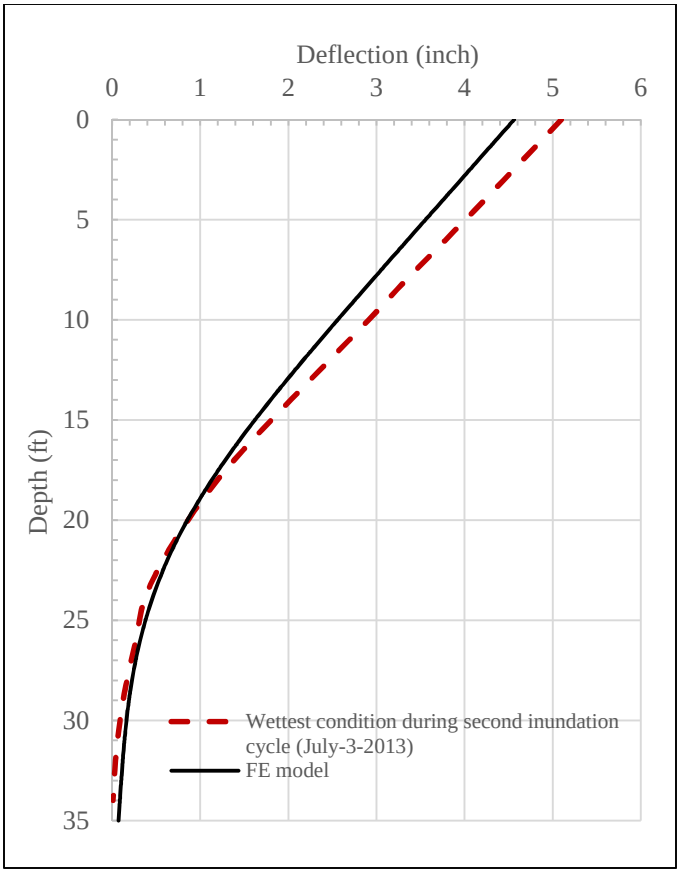


Figure 9.39: Comparison between measured and predicted deflection profiles due to Second inundation cycle

Figure 9.40 presents a comparison between measured and predicted wall bending moment profiles during the second inundation cycle. The maximum bending moment is measured 6ft below the excavation bed. The predicted bending moment profile shows reasonable agreement with the measured profile. The maximum measured bending moment is 210,000lb.ft per shaft; while, the maximum predicted bending moment is 160,000lb.ft per shaft.

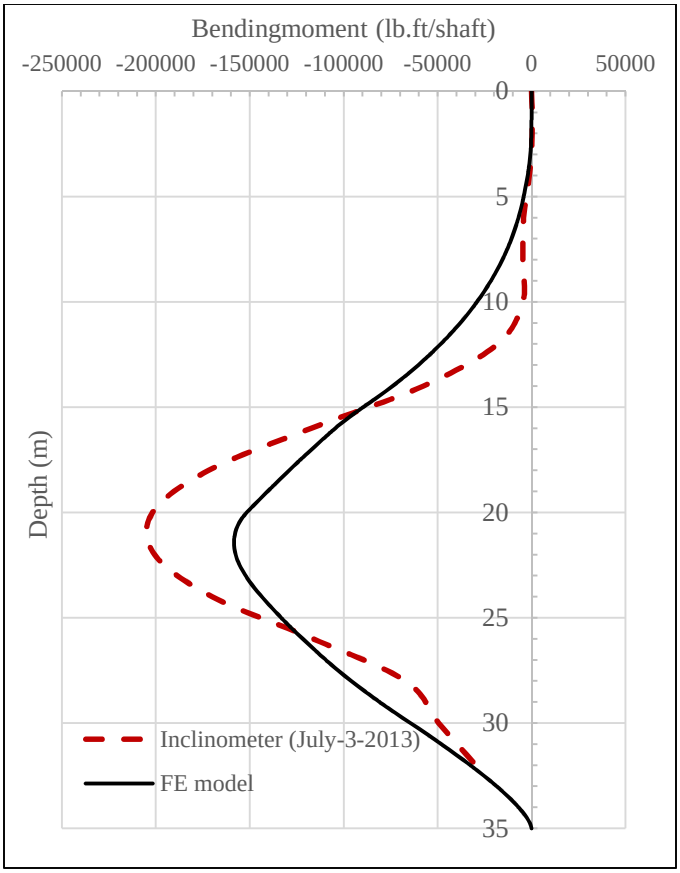


Figure 9.40: Comparison between measured and predicted bending moment profiles due to second inundation cycle

***Seepage forces***

Figure 9.41 presents the numerical model during seepage of water from the inundation pond to the excavated side (stage $8_{Seepage}$). The retained side of the wall is subjected to a factorized hydrostatic pressure where the ground water table rises to the ground surface, and 100% of the changes in the soil properties on the passive side are accounted for. Small-strain and large-strain stiffness profiles on both active and passive sides are the same as the previous stage. The wall does not experience any additional deflection or bending moment due to the seepage forces from the flow of free water.

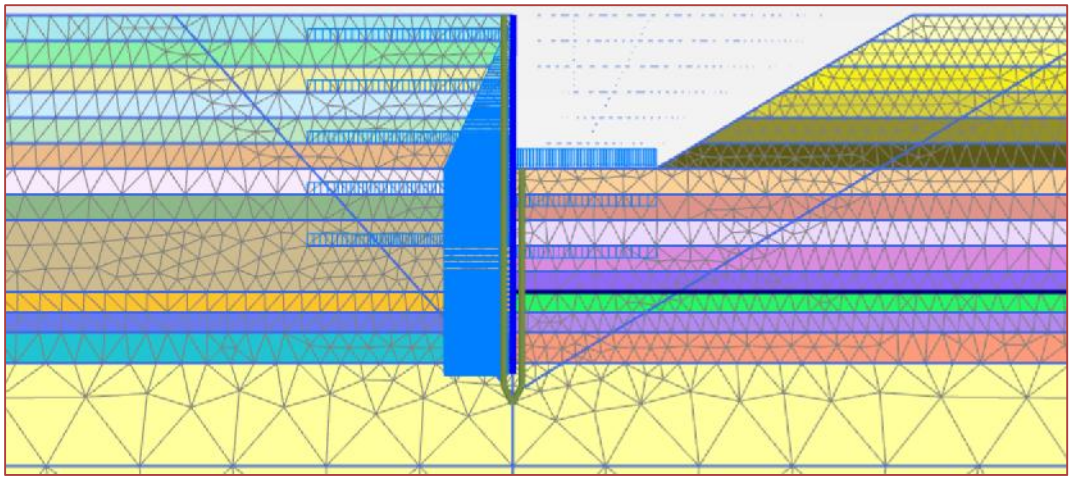

Figure 9.41: FE model stage(8): Soil conditions during natural moisture fluctuation #2 with hydrostatic pressure 8ft below ground surface, assuming 100% consolidation of excavation induced pore-water pressure and accounting for seepage forces and thermal expansion

## 9.3 SENSITIVITY OF WALL BEHAVIOR TO FACTORS GOVERNING LONG-TERM CONDITIONS

During the propagation of the Reese wall from short-term conditions to long-term conditions the wall simultaneously experience additional loads and changes in the soil properties. After comparing the predicted deflection and bending moment profiles to the measured profiles (Section 9.2), the developed numerical model is manipulated to segregate the deflection contribution of each long-term condition. Segregation of the long-term behaviors in the numerical model could be misleading; because, in reality, the long-term behaviors affect the wall simultaneously during the transition from short-term conditions to long-term conditions. Therefore, the percentage of contribution of each long-term behavior presented in Table 9.3 are for guidance only and the actual contribution of each behavior might vary.

Table 9.3 presents the segregated contribution of the wall deflection due to each of the factors discussed earlier. The short-term deflection of the Reese wall account for 20%

of the total wall deflection. Dissipation of the excavation induced pore water pressure, i.e., conventional long-term condition, accounts for 30% of the total wall deflection. It is important to mention that changes in the soil properties are not accounted for in the deflection calculation due to the dissipation of excavation induced pore-water pressure. Loss of confining stress and loss of stiffness accounts for 40% of the total deflection of the wall. The wall behavior is more sensitive to the loss of stiffness on the passive side than the loss suction stress on the active side, such that, the loss of stiffness on the passive side accounts for 25% of the total wall deflection; while, the loss of suction stress on the active side accounts for 15% of the total wall deflection. The free water pressure on the retained side of the wall accounts for 10% of the total wall deflection and the seepage forces caused by the flow of water downward on the active side and upward on the passive side is in significant to the wall deflection.

Table 9.3: Sensitivity of the Reese wall deflection to long-term behaviors

| Behavior | $\Delta_{behavior}/\ \Delta_{total}$ |
|---|---|
| Short-term behavior | 20% |
| Dissipation of excavation induced pwp. | 30% |
| Loss of effective stress (Active side) | 15% |
| Loss of effective stress (Passive side) | 25% |
| Hydrostatic pressure | 10% |
| Seepage pressure | 0% |

This chapter implemented the framework (presented in Chapter 8) in a numerical model of the Reese wall. The numerical model of the Reese resulted in predicted deflection and bending moment profiles that are in reasonable agreement with the measured profiles.

The match between the measured and predicted profiles suggests that the swell strain of soil can be attributed to the loss of suction stress and loss of soil stiffness.The following chapter tests the sensitivity of the framework to key parameters; and, projects the conditions of the Reese wall to conditions other than the actual conditions of the Reese wall site.

# CHAPTER 10: SENSITIVITY ANALYSES OF WALL BEHAVIOR DURING LONG-TERM CONDITIONS

This chapter extrapolate the numerical model of the Reese wall to cases different than the actual field conditions. The objective of this chapter is to study the sensitivity of the long-term behavior of walls to the construction season of walls. The chapter also presents sensitivity of the predicted behavior of the Reese wall to uncertainty in the adopted soil properties such as the Shibuya hardening coefficient B, and parameters describing the SSCC.

## 10.1 Sensitivity of Wall Behavior to Construction Season

This section discusses the sensitivity of the Reese wall behavior to the construction season. This section compares between the predicted results of walls constructed during three seasons, namely: wall constructed during the actual construction season, i.e., the Reese wall; a wall constructed during the driest conditions; finally, a wall constructed during the wettest conditions. The free water pressure, i.e., the piezometric line in the three cases are equal, for both short-term and long-term conditions. Thus this section is intended to illustrate the sensitivity of walls deflection to variability of the initial soil conditions, keeping the free water boundary conditions the same.

Figure 10.1 presents a comparison between suction stress profiles during the actual, driest and wettest conditions. The figure shows that constructing the wall during driest and wettest conditions varies the initial effective stresses, i.e., suction stresses in the soil. Higher initial suction stresses means higher initial soil stiffness during the short-term conditions; and, more severe loss in the soil stiffness during long-term conditions.

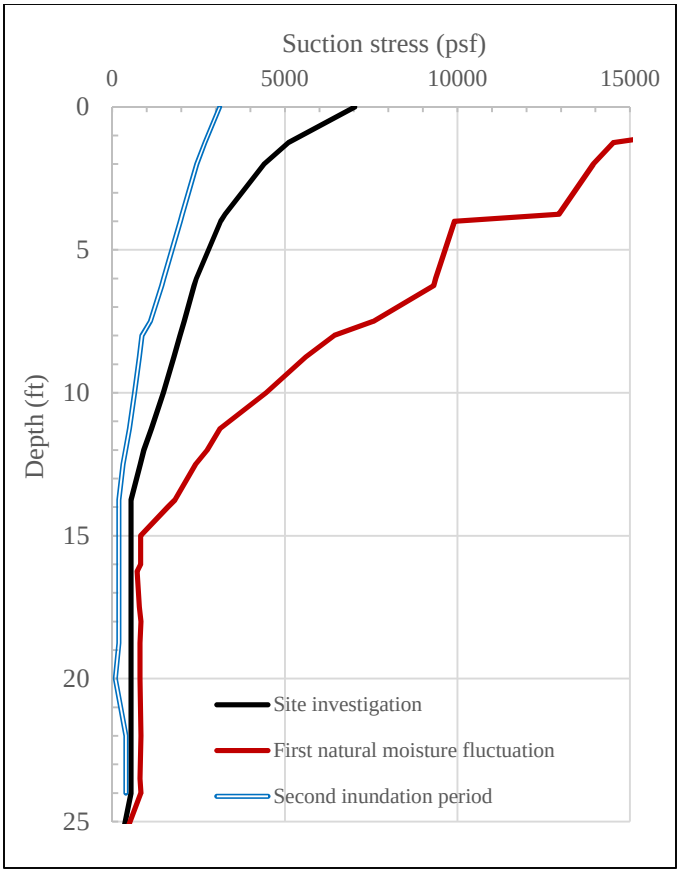


Figure 10.1: Comparison between initial suction stress profiles during (i) actual construction season (i) dry construction season (ii) wet construction season

### 10.1.1 Deflection

Figures 10.2 and 10.3 present the predicted deflection profiles of the Reese wall, considering different construction seasons, for short-term and long-term conditions, respectively. Figure 10.2 shows that for the short-term conditions, constructing the Reese wall during the dry season reduces the wall deflection with a negligible reduction. However, constructing the Reese wall during the wettest construction season increases the maximum wall deflection from 1.1inch to 1.3inch.

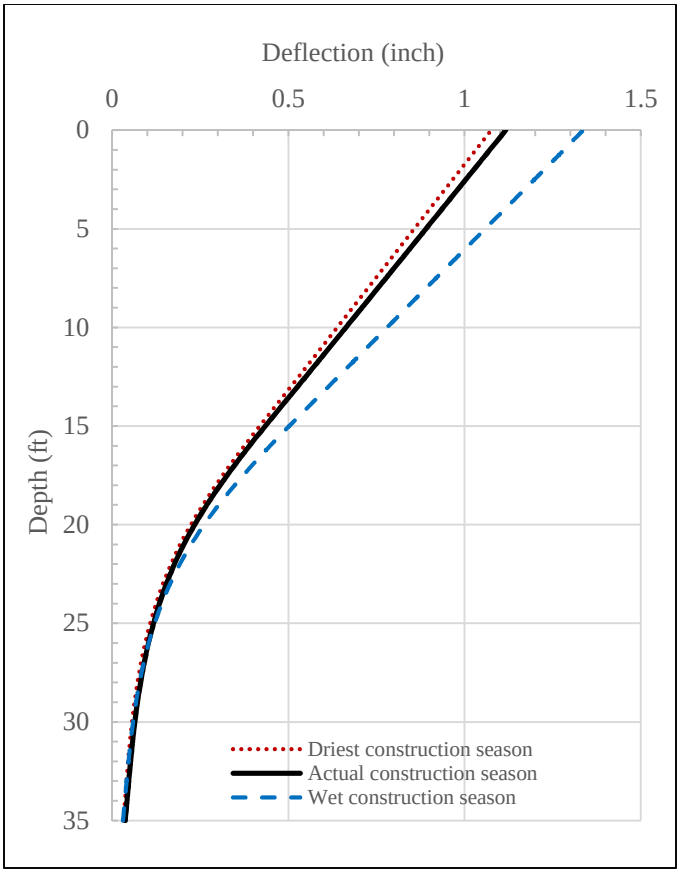


Figure 10.2: Predicted short-term deflection profiles of walls constructed during: (i) actual construction season (i) dry construction season (ii) wet construction season

Figure 10.3 shows that for the long-term conditions, constructing the Reese wall during the dry season reduces the predicted wall deflection from 4.5inches to 3.8inches. While, constructing the Reese wall during the wettest season increases the maximum wall deflection from 4.5inches to 5.5inches.

In conclusion the deflection of walls could be sensitive to the construction season, such that constructing walls during a dry season would increase the deflection of walls during the long-term conditions. On the other hand, constructing walls during a wet season

could decrease walls deflection during the long-term conditions; and, increase the short-term deflection.

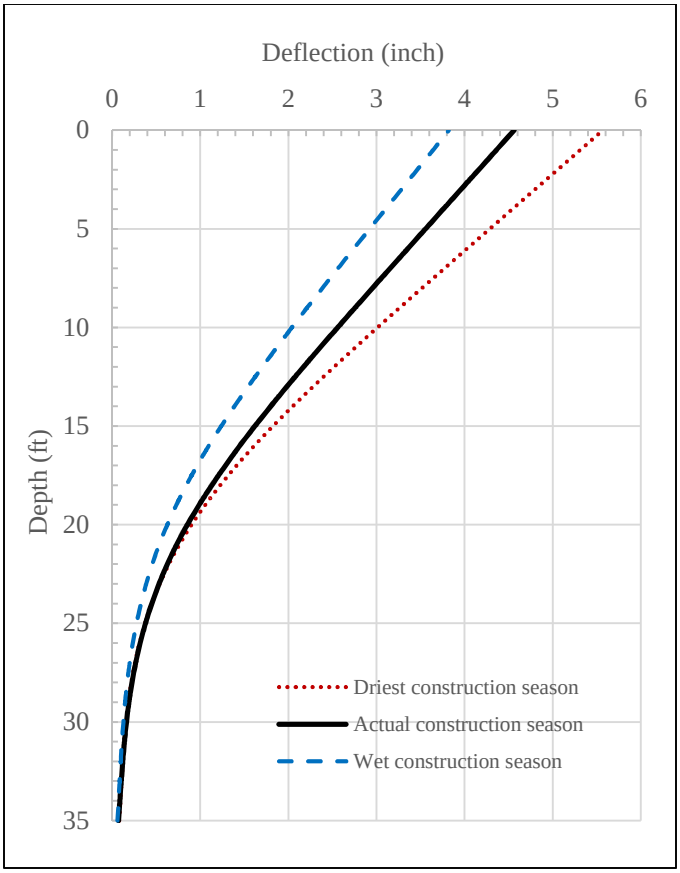


Figure 10.3: Predicted long-term deflection profiles of walls constructed during: (i) actual construction season (i) dry construction season (ii) wet construction season

### 10.1.2 Bending moment

Figures 10.4 and 10.5 present the predicted bending moment profiles of the Reese wall, considering different construction seasons, for short-term and long-term conditions, respectively. Figure 10.4 shows that for the short-term conditions, constructing the Reese wall during the dry season reduces the maximum bending moment with a negligible

reduction. While, constructing the Reese wall during the wettest construction season increases the maximum bending moment from 44,000lb.ft/shaft to 57,000inch.

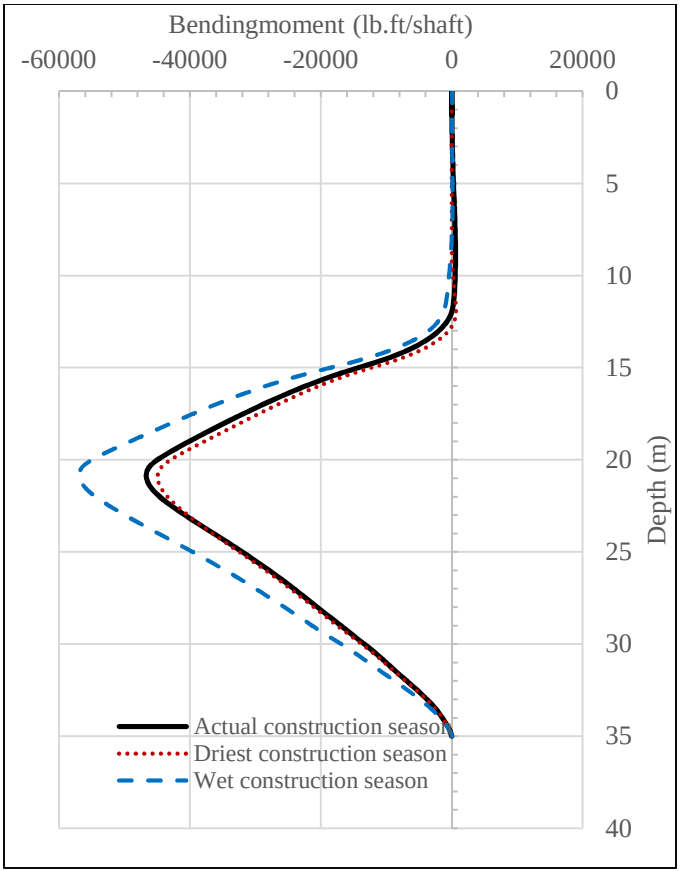


Figure 10.4: Predicted short-term bending moment profiles of walls constructed during: (i) actual construction season (i) dry construction season (ii) wet construction season

Figure 10.5 shows that for the long-term conditions, constructing the Reese wall during the dry season increases the maximum bending moment from 160,000lb.ft/shaft to 210,000lb.ft/shaft. While, constructing the Reese wall during the wettest construction season decreases the maximum bending moment from 160,000lb.ft/shaft to 140,000lb.ft/shaft.

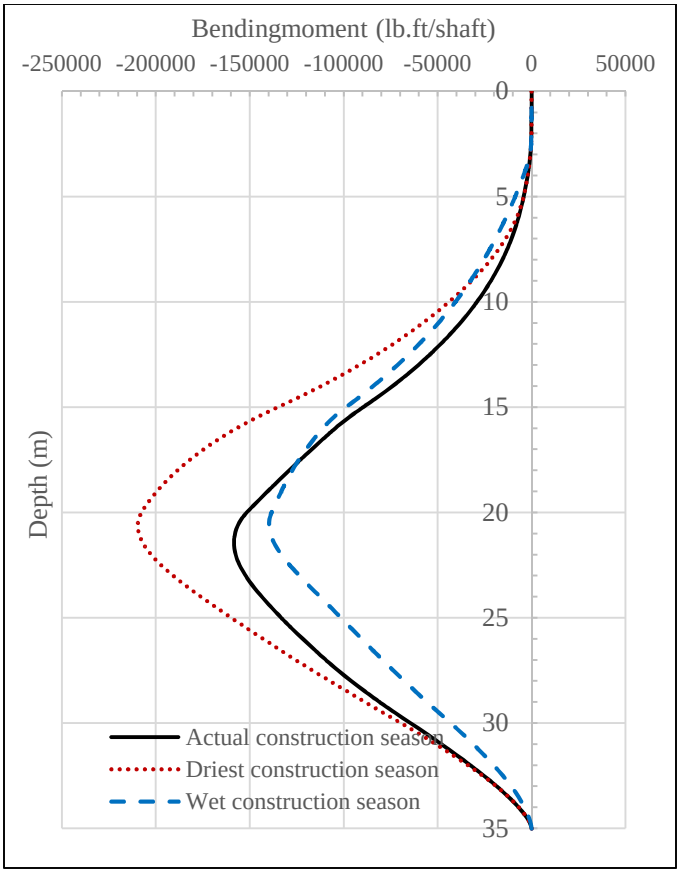


Figure 10.5: Predicted long-term bending moment profiles of walls constructed during: (i) actual construction season (i) dry construction season (ii) wet construction season

In conclusion the bending moment of walls could be sensitive to the construction season, such that constructing walls during a dry season would increase the bending moment of walls during long-term conditions. While, constructing walls during a wet season could decrease the bending moment of walls during the long-term conditions; and, increase the bending moment of walls during short-term conditions.

## 10.2 Sensitivity of Wall Behavior to Soil Properties

This section discusses the sensitivity of the Reese wall behavior to the adopted soil properties adopted in the Shibuya numerical model. First, the sensitivity of the wall behavior to the Shibuya (1997) isotropic hardening parameter B is evaluated. Second, the sensitivity of the wall behavior to the SSCC is evaluated.

### 10.2.1 Shibuya hardening coefficient B

Figure 8.21 presented the calibration of the Shibuya (1997) equation with the SASW measurements from the Reese wall site, and from London Clay measurements obtained from the literature. Different B values were adopted for the soil shallower than 20ft and soil deeper than 20ft, the adopted B values are 10,000 and 20,000 for the top and bottom soils, respectively.

Figure 10.6 presents the sensitivity of the Reese wall maximum deflection to the B value of the top 20ft. The figure presents the deflection during short-term and long-term conditions for B values ranging between 7,000 and 13,000. Other parameters such as the SSCC, initial and final suction stresses are kept constant. The figure shows that the maximum wall deflection during both short-term and long-term conditions decreases as the value of B increases. The figure shows that the short-term wall deflection is not very sensitive to the Shibuya isotropic hardening coefficient; such that, the short-term maximum deflections are 1.2inch and 0.7inch for B values of 7,000 and 13,000, respectively. The maximum wall deflection during long-term conditions are more sensitive to the B value than the short-term deflections. The long-term maximum deflections are 6inches and 3.7inches for B values of 7,000 and 13,000, respectively.

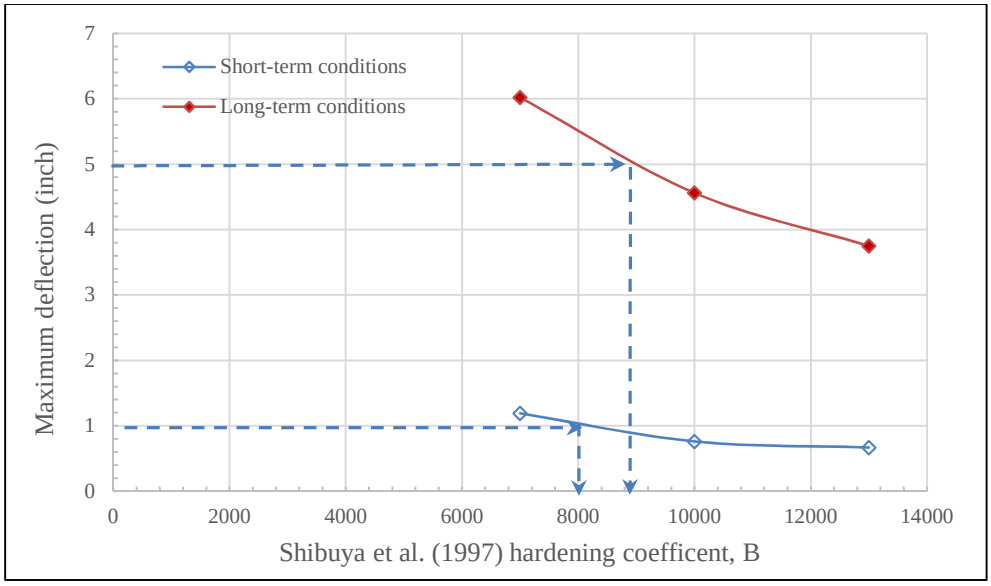


Figure 10.6: Sensitivity of maximum wall deflection to Shibuya hardening coefficient, B, during: (i) driest conditions (ii) wettest conditions

Figure 10.7 presents the same data presented in Figure 11.6 in term of normalized wall deflection. The long-term normalized deflections are 0.034 and 0.021 for B values of 7,000 and 13,000, respectively.

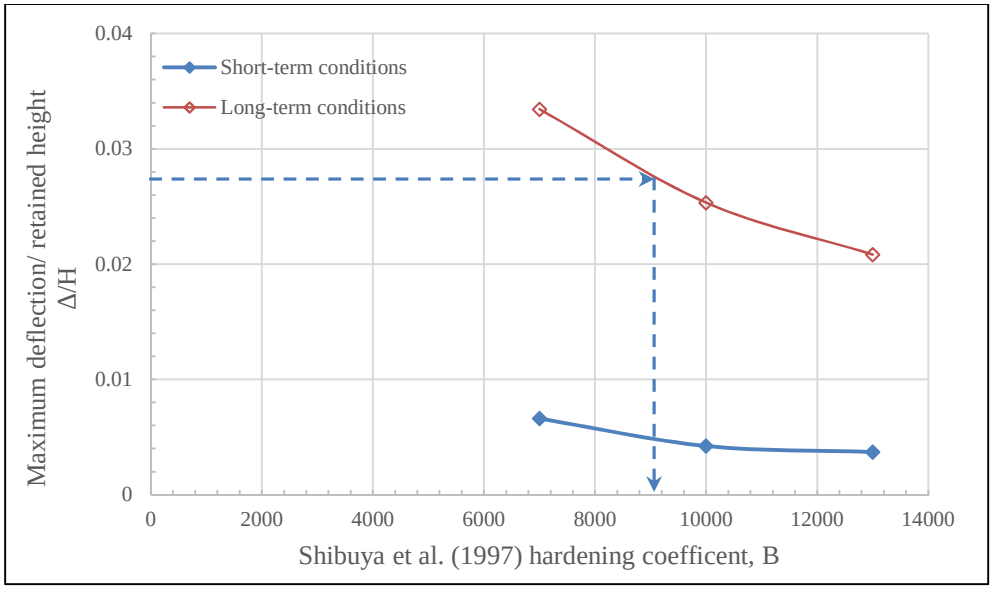


Figure 10.7: Sensitivity of normalized maximum wall deflection to Shibuya hardening coefficient, B, during: (i) driest conditions (ii) wettest conditions

Figure 10.8 presents the sensitivity of the Reese wall maximum bending moment to the B value of the top 20ft. The figure presents the bending moment during short-term and long-term conditions for B values ranging between 7,000 and 13,000. The figure shows that the maximum bending moment during both short-term and long-term conditions decreases as the value of B increases. During the short-term conditions, the maximum bending moment of the Reese wall is 36,000lb.ft/shaft; and, the predicted bending moments assuming B values of 7,000 and 13,000 are 40,000lb.ft/shaft and 20,000lb.ft/shaft, respectively. During the long-term conditions, the maximum bending moment of the Reese wall is 200,000lb.ft/shaft; and, the predicted bending moments assuming B values of 7,000 and 13,000 are 210,000lb.ft/shaft and 130,000lb.ft/shaft, respectively.

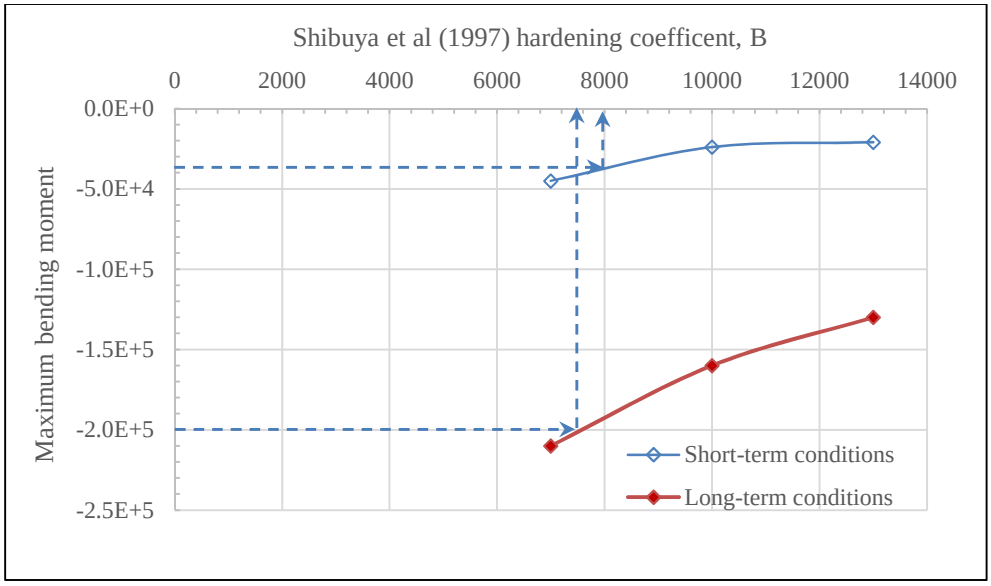


Figure 10.8: Sensitivity of maximum bending moment to Shibuya hardening coefficient, B, during: (i) driest conditions (ii) wettest conditions

Figure 10.9 presents the same data presented in Figure 10.8 in term of normalized bending moment. The long-term normalized maximum bending moments are 0.052 and 0.032 for B values of 7,000 and 13,000, respectively.

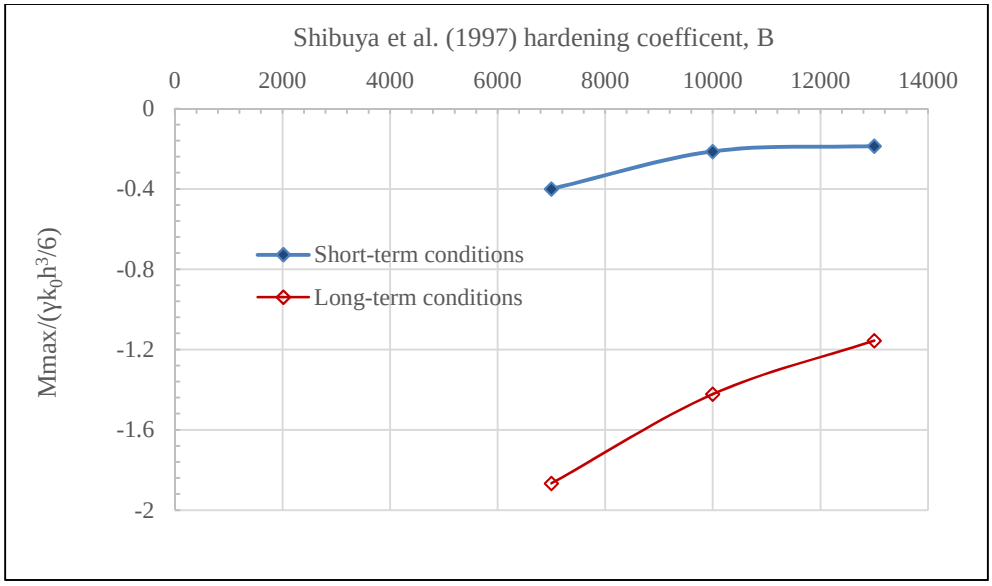


Figure 10.9: Sensitivity of normalized maximum bending moment to Shibuya hardening coefficient, B, during: (i) driest conditions (ii) wettest conditions

The B value adopted in the numerical model was estimated according the SASW measurement of the Reese wall site and data obtained from the literature of the London Clay (Figure 8.21). Figures 10.6 and 10.8 presented the predicted maximum deflections and bending moments for different B values, respectively. The figures show the B values corresponding to the measured maximum deflection and bending moment of the Reese wall. In conclusion the B value adopted for the top 20ft soil is considered reasonable.

### 10.2.2 Soil Suction Characteristic Curve

Section 8.6 presented the development of the SSCC for the Reese wall soil. The section presented the SSCC estimated from undrained shear strength measurements and the closed-form solution. It was recommended a more reliable SSCC could be estimated from drained shear strength measurements of water-content controlled tests. To assess the

necessity of obtaining a more reliable SSCC estimate, the sensitivity of the predicted deflection and bending moment to the SSCC is discussed in this section.

Figure 10.10 presents different SSCCs adopted in the Reese wall numerical model. The SSCCs are estimated from the Lu et al. closed form equation, which describes the curve with the Van Genuchten (1980)'s parameters α, and n. As previously discussed in section 8.5, α coefficient is the inverse of the air entry pressure and n depends on the porosity of the soil and governs the slope of the SWRC beyond air-entry pressure. The α value measured for the Eagle Ford clay and adopted in the Reese wall numerical model is kept constant because all the SWRCs presented in Figure 8.13 showed close air-entry pressures for different soils around Texas. Thus different SSCC are estimated by varying the n parameter between 1.2 and 1.6. Different SSCC means that the effective stress change due to the changes in the soil degree of saturation follows a different path, and that the initial suction stresses are also different. Other parameters are kept constant while studying the sensitivity of the wall behavior to the SSCC.

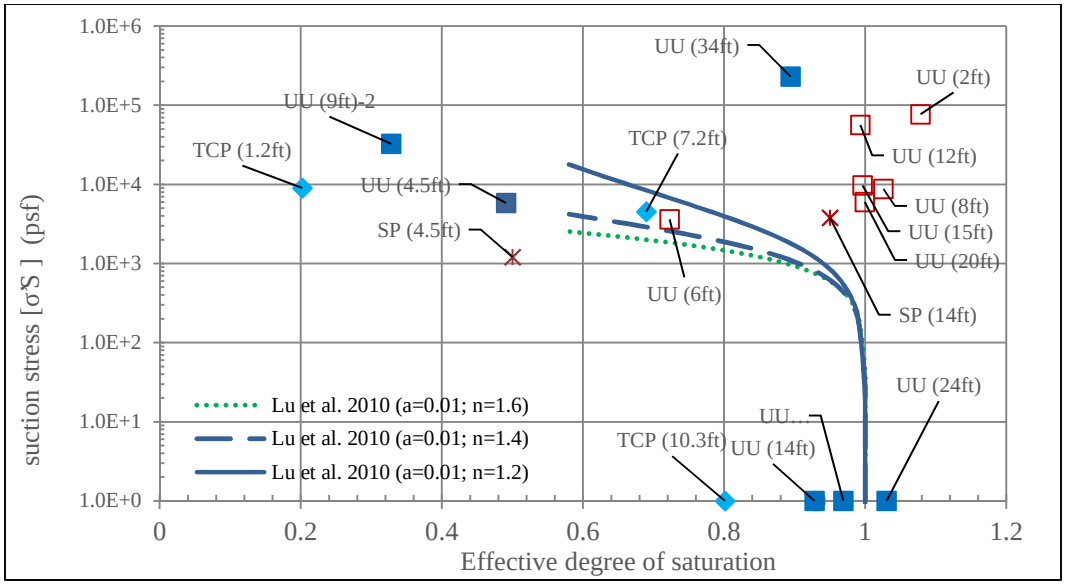


Figure 10.10: Comparison between SSCC estimated from laboratory measurements and SSCC adopted in the parametric analyses

Figure 10.11 presents the sensitivity of the Reese wall maximum deflection to the Van Genuchten parameter n of the top 20ft of soil. The figure presents the deflection during short-term and long-term conditions for n values ranging between 1.2 and 1.6. The figure shows that the short-term wall deflection is not sensitive to the SSCC. Adopting different SSCC controls the initial suction stress, which consequently controls the initial soil stiffness. The short-term deflections estimated from different SSCC are the same.

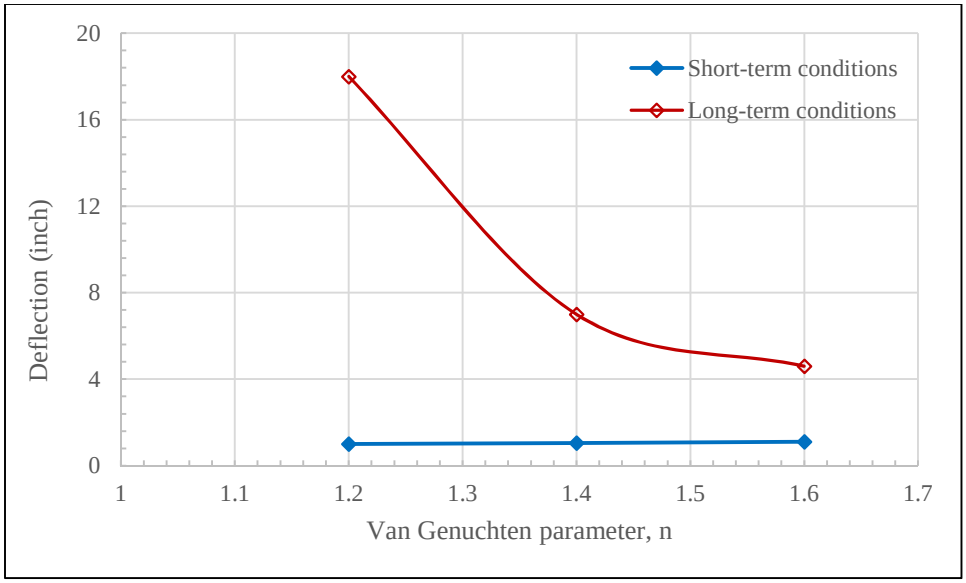


Figure 10.11: Sensitivity of maximum deflection during short-term and long-term conditions to the soil suction characteristic curve

The figure shows that the long-term wall deflection is sensitive to the SSCC. Adopting different SSCC means that the suction stresses lost during the consolidation stages are different. The smaller the n parameter, the higher the suction stresses are for the same effective degree of saturation; and, the higher the changes in suction stresses due to changes in effective degree of saturation. The higher the variation of suction stress, the more dramatic the soil stiffness changes; and, the more significant the change of retaining pressure on the wall. The maximum deflection during long-term conditions ranges from 18inches to 5inches for n values ranging from 1.2 to 1.6, respectively.

Figure 10.12 presents the sensitivity of the Reese wall maximum bending moment to the Van Genuchten (1980)'s parameter n of the top 20ft of soil. The figure presents the maximum bending moment during short-term and long-term conditions for n values ranging between 1.2 and 1.6. The figure shows that the short-term maximum bending moment is not sensitive to the SSCC. The maximum bending moment during long-term

conditions ranges from 600,000lb.ft/shaft to 160,000lb.ft/shaft for n values ranging from 1.2 to 1.6, respectively

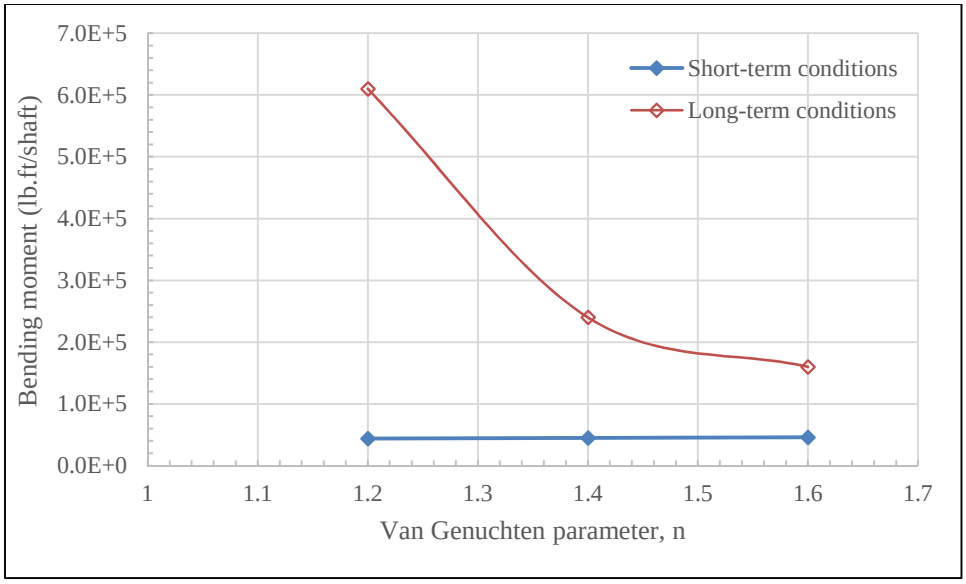


Figure 10.12: Sensitivity of maximum bending moment during short-term and long-term conditions to the soil suction characteristic curve

Long-term deflections as high as 18inches is probably unrealistic; because, the soil is probably cracked in tension before reaching high suction stresses corresponding to low effective degrees of saturation. Section 9.2 showed that the zone of influence of the suction stresses is bounded by the cracks around a soil cluster. At suction stresses higher than the cracking suction stress, any increase in suction stresses is not continues throughout the soil continuum and the volumetric straining associated with changes in the effective degree of saturation goes to the tension cracks. To account for development of tension cracks at a certain suction stress, a SSCC with an upper limit is adopted (Figure 10.13). The Figure presents two SSCC, with and without the suction limit. Both SSCC are estimated according to the Lu et al. (2010) closed form equation, adopting an n parameter of 1.2. The maximum

suction stress of the SSCC adopted in the numerical model of the Reese wall, i.e., n=1.6, was 3,000psf. To be consistent with the in terms of the maximum possible suction stress, the same maximum suction stress value is adopted for the SSCC calculated using N value of 1.2.

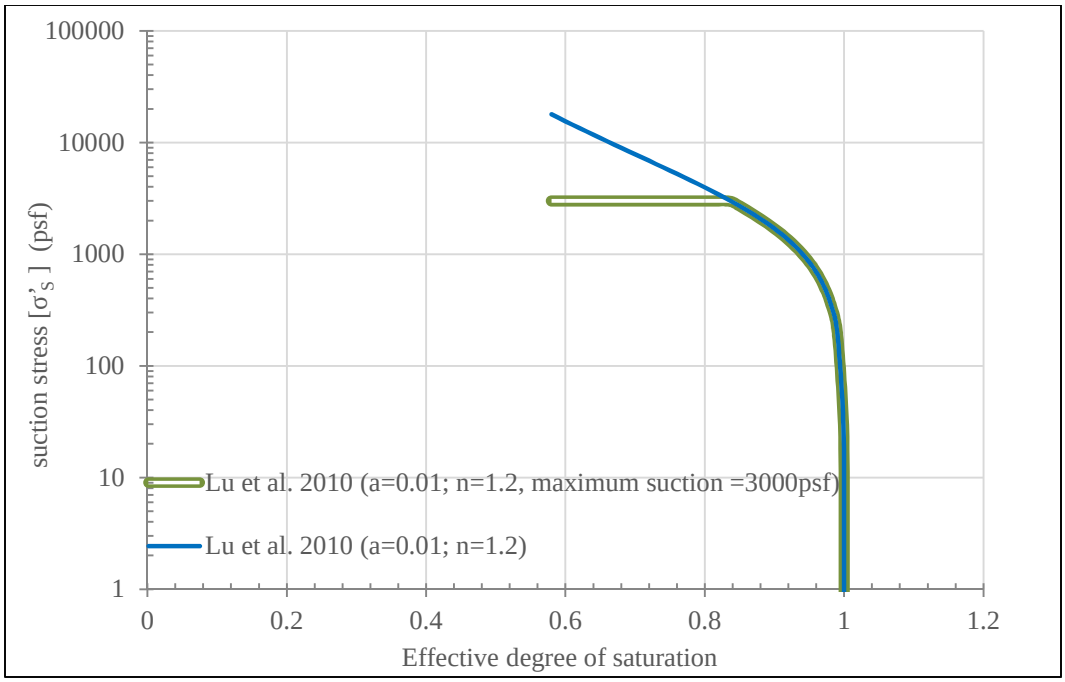


Figure 10.13: Soil Suction Characteristic Curves with and without maximum suction (a=0.01, n=1.2)

Figure 10.14 presents a comparison between the measured long-term deflection profile of the Reese wall and predicted wall deflection profiles assuming (i) continuous SSCC, a=0.01, n=1.6 (ii) SSCC, n=1.6, a=0.01, with maximum suction stress=3,000psf. As shown in Figure 10.11, the predicted maximum wall deflection assuming a continuous SSCC is 18inch; while, the predicted maximum wall deflection assuming a SSCC with a maximum suction stress of 3,000psf is 5inches. Therefore, it is suggested that defining a

maximum suction stress value, that accounts for soil cracking is important in describing the behavior of walls in partially saturated soils.

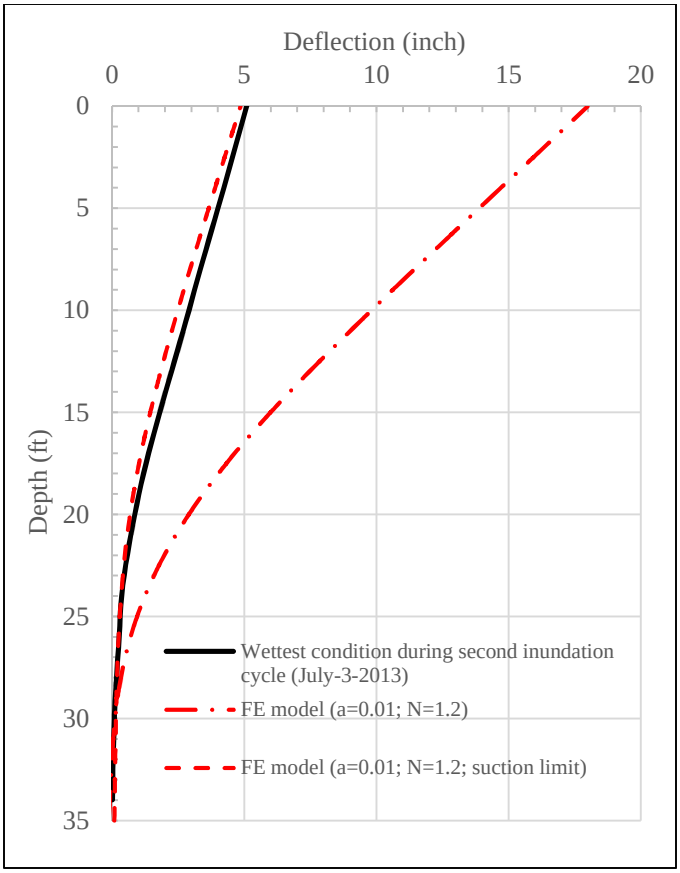


Figure 10.14: Sensitivity of applying suction cap on long-term deflection profile

Figure 10.15 presents a comparison between the measured long-term bending moment profile of the Reese wall and predicted wall bending moment profiles assuming (i) continuous SSCC, a=0.01, n=1.6 (ii) SSCC, n=1.6, a=0.01, with maximum suction stress=3,000psf. As shown in Figure 10.12, the predicted maximum bending moment assuming a continuous SSCC is 600,000lb.ft/shaft; while, the predicted maximum bending moment assuming a SSCC with a maximum suction stress of 3,000psf is 200,000lb.ft/shaft.

Therefore, it is suggested that defining a maximum suction stress value, that accounts for soil cracking, is important in describing the behavior of walls in partially saturated soils.

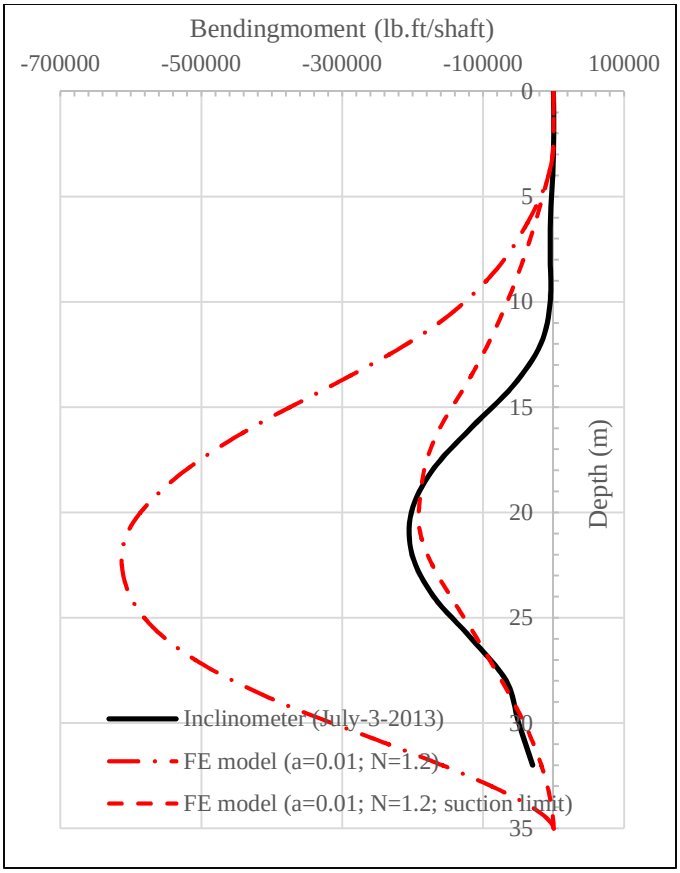


Figure 10.15: Sensitivity of suction cap on long-term bending moment profile

### 10.3 Sensitivity of Wall Behavior to Wall Design Parameters

This section discusses the sensitivity of the Reese wall behavior to the wall design parameters. First, the sensitivity of the wall behavior to the embedment ratio is evaluated. Second, the sensitivity of the wall behavior to bending stiffness is evaluated.

### 10.3.1 Embedment ratio

Figure 10.16 presents the sensitivity of the normalized wall deflection to the wall embedment ratio d/h. The analyses are conducted adopting the same bending stiffness of the Reese wall. As previously mentioned, the embedment ratio of the Reese wall is 1.33; comparing the normalized deflections corresponding to d/h ratios of 1.33 and 2 suggests that building a deeper wall does not reduce the maximum wall deflection. The same conclusion was observed for short-term conditions. However, building a shallower wall with embedded depth of 7.5ft, i.e. d/h=0.5, increases the long-term deflection of the wall. Such that the normalized deflection increase to 0.0355, i.e., 6.4inches.

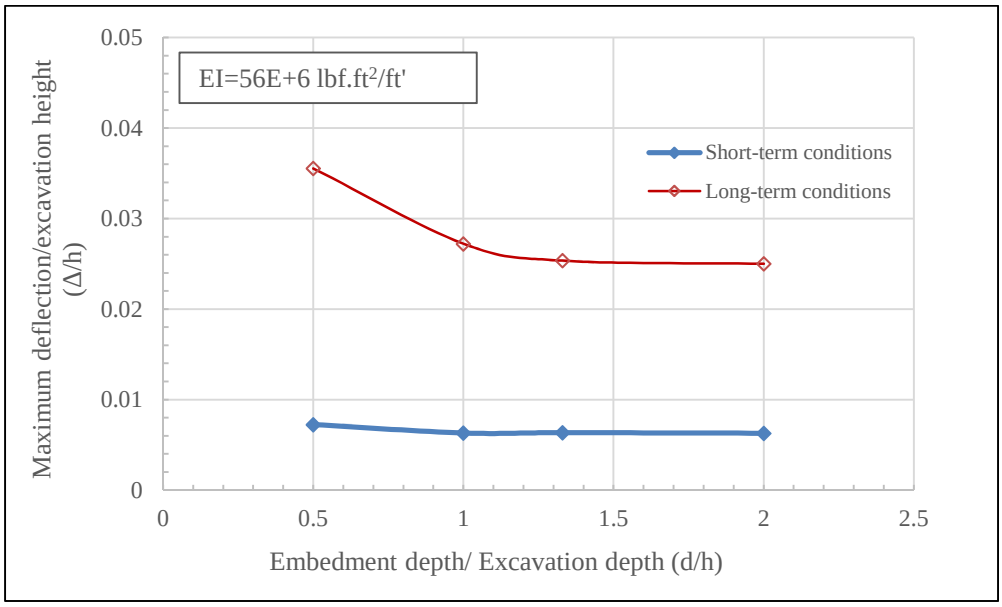


Figure 10.16: Sensitivity of normalized maximum wall deflection to wall embedment ratio during: (i) Short-term conditions (ii) Long-term conditions

Figure 10.17 presents the sensitivity of the normalized bending moment to the wall embedment ratio d/h. The analyses are conducted adopting the same bending stiffness of the Reese wall. As previously mentioned, the embedment ratio of the Reese wall is 1.33;

comparing the normalized bending moments corresponding to d/h ratios of 1.33 and 1 suggests that building a shallower wall could reduce the normalized bending moment by approximately10%; however, Figure 10.16 showed that building a shallower wall could increase the wall deflection by approximately 10%.The design engineer is supposed to compromise between the maximum bending moment which translates to cost of reinforcement and the serviceability requirements.

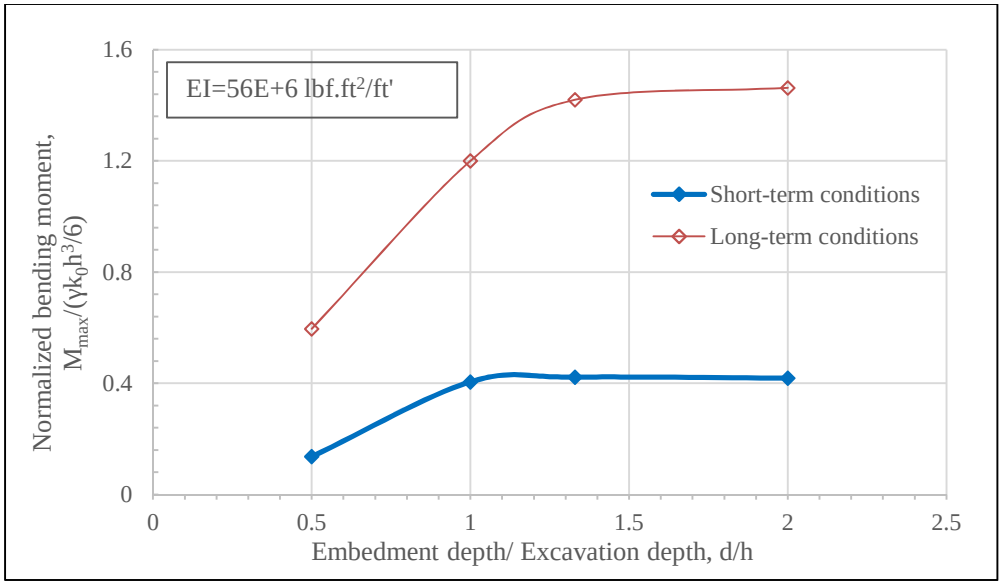


Figure 10.17: Sensitivity of normalized maximum bending moment to wall embedment ratio during: (i) short-term conditions (ii) long-term conditions

### 10.3.2 Wall stiffness

Figure 10.18 presents the sensitivity of the normalized wall deflection to the wall bending stiffness, EI. The analyses are conducted adopting the same embedment ration of the Reese wall. The bending stiffness per foot run along the wall is varied between 2.2E+7 lb.ft$^2$/ft and 28E+7 lb.ft$^2$/ft, where the Reese wall bending stiffness is 5.6E+7 lb.ft$^2$/ft. Comparing the normalized deflections corresponding to EI values of 5.6E+7 lb.ft$^2$/ft and

28E+7 lb.ft$^2$/ft suggests that building a wall three times stiffer than the Reese wall, i.e., diameter =36inches with the same steel reinforcement ratio, could decreases the long-term deflection of the wall by 20%.

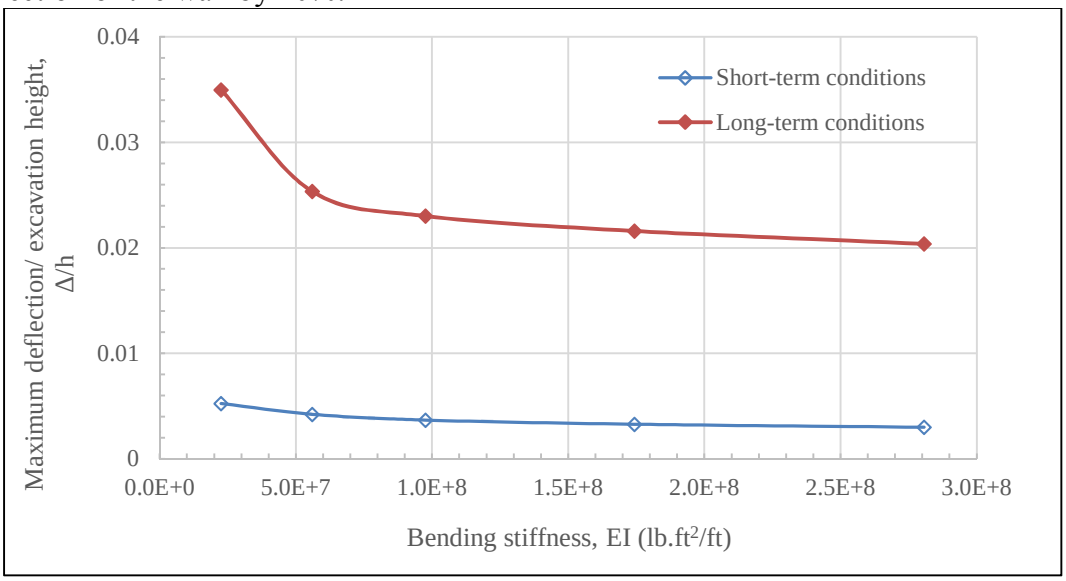


Figure 10.18: Sensitivity of normalized maximum wall deflection to wall stiffness during: (i) short-term conditions (ii) long-term conditions

This chapter first discussed the sensitivity of walls behavior to the construction seasons. The study suggested that walls constructed during dry season are susceptible to higher swelling strains than walls constructed during wet season. Second, the study showed that the deflection and bending moment predictions are sensitive to the parameters adopted in the framework, such as, the Shibuya et al. (1997) model and the soil suction characteristic curve. Further laboratory measurements are required to better evaluate the soil suction characteristic curve of the soil. Third, the study shows that the long-term behavior of the wall is not very sensitive to the wall embedment beyond an embedment ratio of 1. The following chapter summarized this research study and compiles the conclusions obtained.

# CHAPTER 11: CONCLUSIONS AND RECOMMENDATION

The main objective of this study is to advance the prediction of the deflection and bending moment of a drilled shaft retaining wall, retaining highly expansive clay during short-term (undrained) and long-term (drained) conditions. In this chapter, a summary of the research study, conclusions, and recommendations for future work are presented.

## 11.1 SUMMARY OF RESEARCH STUDY

In earlier research (Brown et al. 2013), a full-scale wall (the Reese wall) was built and monitored for four years. The Reese wall was designed according to the current TXDoT procedures, which do not distinguish between temporary and permanent walls. The Reese wall was constructed prior to a record drought season, and it was subjected to two cycles of man-made inundation with ponded surface water over four years. The deflections and bending of the wall were monitored, and the properties of the clay were measured at different times.

In this dissertation, a numerical model of the Reese wall was simulated using the finite element method software, PLAXIS. The model simulated the construction sequence and the wetting and drying cycles. A hardening small-strain model available in PLAXIS software was adopted for the model. The small-strain stiffnesses were obtained from Spectral-Analysis-of-Surface-Waves (SASW) conducted on the Reese wall site, and, the large-strain stiffnesses were obtained from unconsolidated undrained triaxial tests.

For long-term conditions, framework was developed to describe the behavior of partially saturated soils subjected to variations in the degree of saturation. The framework describes the effective stress of partially saturated soil according to Lu and Likos (2006) definition of effective stresses. The effective stress definition does not rely on soil matric suction; but, rather attempts to infer the effective stress in partially saturated soils from

compressibility and shear strength measurements. The framework describes the effective stresses in partially saturated soils according to a relationship between the effective stress and the effective degree of saturation termed "Soil Suction Characteristic Curve". The Soil Suction Characteristic Curve was estimated for the soil at the site of the Reese wall from consolidation and shear strength measurements of soil with known moisture contents and dry densities. The developed framework was adopted in the Reese wall numerical model to describe the behavior of the wall during cycles of wetting and drying.

The numerically-predicted Reese wall behavior was compared to the actual measured behavior. In addition, the Reese wall conditions were extrapolated to different conditions in parametric analyses. The parametric analyses tested the sensitivity of the walls to different factors such as: construction seasons, wall embedment ratio, wall stiffness, and soil properties.

## 11.2 CONCLUSIONS

The goal of this research is to advance our understanding of the behavior of partially saturated high-plasticity clays, often referred to as expansive clay, in soil-structure interactions. The conclusions of this study focus on the prediction of the wall behavior by comparing the predicted wall behavior to the actual behavior. In this section conclusions based on the comparison between actual and predicted behavior of the wall during short-term and long-term conditions are presented.

### 11.2.1 Short-term conditions

Short-term conditions of the wall are defined as conditions immediately after the completion of excavation works. The behavior of the Reese wall during short-term conditions was predicted via analytical and finite element methods. Based on comparisons

between actual and predicted behaviors as well as the parametric analyses, the conclusions of the behavior of walls during short-term conditions include:

1- The Reese wall movement during the short-term conditions did not exhibit a point of fixity. A point of fixity is characterized as a point that experiences zero lateral movement but experiences rotation. Field measurements and numerical analyses of the Reese wall showed that the entire profile of the wall experienced movements in one direction, towards the excavated side.

2- The shear strain mobilized during short-term conditions in numerical analyses did not exceed an absolute strain of 0.002; the mobilized shear strain corresponded to a stiffness reduction of approximately 40% and 20% for soil above and below 15feet, respectively. The maximum mobilized shear strain was experienced at the mid third of the retained height.

3- Predicting the deflection of the Reese wall adopting a constitutive model that accounts for the small strain stiffness and stiffness non-linearity resulted in reasonable agreement between the measured and predicted profiles. Predicting the deflection of the Reese wall adopting a linear-elastic perfectly plastic constitutive model considering the small strain stiffnesses of the soil underestimates the deflection and bending moment profiles of the Reese wall. Predicting the deflection of the Reese wall adopting a linear-elastic perfectly plastic model considering the large strain stiffnesses measurements or correlations overestimates the deflection and bending moment profiles of the Reese wall.

4- The maximum deflection of an open-cut excavation could be less than the maximum deflection of the Reese wall. The presence of the wall reduces the

bulging deformation mechanism of the wall and uniforms the movement, such that the maximum deflection is experienced at the top of the wall and the deflection decreases with depth. An open-cut model predicted a maximum deflection of 0.68inch at the mid third of the retained height; while, the maximum deflection of the Reese wall was 0.95inch at the top of the wall.

5- The parametric analysis of the $k_0$ value showed that the behavior of walls during short-term conditions is highly sensitive to the $k_0$ value.

6- The construction season could affect the short-term behavior of walls. Two numerical models were compared: one assuming dry construction and excavation season and the other assuming wet construction and excavation season. The wall constructed during the driest condition predicted less deflection and bending moment profiles than a wall constructed during a wet construction season.

7- The short-term behavior of the Reese wall is relatively insensitive to deeper embedment depth of the wall. However, the predicted maximum deflection of a wall shallower than the Reese wall (40% of the Reese wall embedment depth) is 15% higher than the maximum deflection of the Reese wall. The predicted maximum bending moment of a wall shallower than the Reese wall (40% of the Reese wall embedment depth) is 50% lower than the maximum bending moment of the Reese wall.

8- The short-term behavior of the Reese wall is slightly sensitive to the wall bending stiffness. Building a wall three times stiffer than the Reese wall is predicted to produce 25% decrease in the maximum deflection.

9- An analytical method which solves the lateral and rotational equilibrium equations for two unknown, namely, the mobilized shear strength, and the location of the point of fixity, reasonably estimates the maximum short-term deflection of the Reese wall but overestimates the maximum bending moment. The analytical method predicts that the maximum bending moment occurs at a deeper cross section of the wall, which is attributed to adopting a stress profile that describes the kinematics of the wall movement as rotation about a point of fixity. The analytical method is highly sensitive to the evaluation of the undrained shear strength of the soil.

### 11.2.2 Long-term conditions

The long-term conditions are defined as the conditions when the groundwater reaches steady state. Transition of pore-water pressure from short-term to long-term conditions include the dissipation of the shear induced pore-water pressure on the active side, dissipation of the excavation induced pore-water pressure on the passive side, in addition to any changes in the pore-water pressure due to changes in the degree of saturation. The most critical long-term condition is the condition when the surrounding soil is the most saturated; therefore, the "long-term condition" expression is used to refer to the condition where the excavation induced and shear induced pore-water pressures dissipated and the soil is in the most saturated condition.

The behavior of the Reese wall during long-term conditions was predicted via analytical and finite element methods. The finite element method adopted a framework that describes the effective stresses in partially saturated soil without the matric suction, instead, effective stresses in partially saturated soil is inferred from shear strength measurements.

Based on comparisons between actual and predicted wall behaviors as well as parametric analyses, the conclusions of the behavior of walls during long-term conditions include:

1- Comparison between the measured swelling/shrinkage strains from one-dimensional Oedometer tests and the predicted swelling/shrinkage strains resulted in reasonable agreement between actual measurements and predictions. A framework was developed to predict the swelling/shrinkage behavior of partially saturated soils. The framework relies on two soil properties, namely the relationship between effective stresses of partially saturated soil and the effective degree of saturation, and the relationship between the soil stiffness with effective stresses and voids ratio. The framework was evaluated by comparing the swelling/shrinkage predicted according to the framework to swelling/shrinkage measured in a one-dimensional Oedometer test.

2- Comparison between the field measurements of the Reese wall deflection and bending moment profiles and the finite element model predictions showed good agreement during different wetting and drying cycles. The developed framework could be implemented in a finite element model to predict the behavior of the Reese wall during drying and wetting cycles.

3- The short-term deflection of the Reese wall accounted for 20% of the total wall deflection. The finite element model was used to segregate the causes of additional long-term deflection. Dissipation of the excavation induced pore water pressure on active and passive sides, i.e., conventional long-term condition, accounted for 30% of the total wall deflection. Loss of confining stress and loss of stiffness on active and passive sides accounted for 40% of the total deflection of the wall. The wall behavior is more sensitive to the loss of

confining stresses and stiffness on the passive side than the loss effective stress and stiffness on the active side; the loss of stiffness on the passive side accounted for 25% of the total wall deflection; while, the loss of suction stress on the active side accounted for 15% of the total wall deflection. The free water pressure on the retained side of the wall accounted for 10% of the total wall deflection.

4- The construction season could affect the long-term behavior of walls. Two numerical models were compared: one assuming dry construction and excavation season and the other assuming wet construction and excavation season. The wall constructed during the driest condition predicted more deflection and bending moment profiles than a wall constructed during a wet construction season.

5- The parametric analysis of the slope coefficient showed that the behavior of walls during long-term conditions is relatively sensitive to the B coefficient. The framework relies on a hardening equation that relates the maximum shear stiffness to the effective stress and voids ratio (Shibuya 1997) in a linear relationship model. The slope of the linear relationship was estimated for the Reese wall site according to Spectral Analysis of Surface Waves measurements and a slope coefficient of 10,000 was adopted in the analysis. The slope of the line was varied in a parametric analysis and the deflection and bending moment of wall were predicted for slope coefficients. The selected slope coefficient was considered acceptable since it matched the predicted and measured deflection and bending moment profiles.

6- Results showed that the predicted behavior of the Reese wall is sensitive to the relationship between effective degree of saturation and effective stress. The relationship between the effective degree of saturation and effective stress, referred to in the study as the Soil Suction Characteristic Curve was estimated for the Reese wall site according to Lu et al. (2010) closed form equation. The closed form equation, described in terms of Van-Genuchten (1980) parameters, reasonably matched the estimates of the suction stresses from undrained shear strength measurements and swell tests adopting Van-Genuchten parameters of n=1.6 and $\alpha$=0.01psf$^{-1}$. The SSCC was varied in a parametric analysis and the wall behavior was predicted accordingly. Analyses showed that accounting for loss of soil coherence at high suction stresses would suppress overestimating the wall deflection.

7- The long-term behavior of the Reese wall is relatively insensitive to deeper embedment depth for the wall. However, the predicted maximum deflection of a wall with shallower embedment (40% of the Reese wall embedment depth) is 30% higher than the maximum deflection of the Reese wall. The predicted maximum bending moment of a wall with shallower embedment (40% of the Reese wall embedment depth) is 60% more than the maximum bending moment of the Reese wall.

8- The long-term deflection of the Reese wall is relatively insensitive to increasing the bending stiffness for the wall; such that, the predicted maximum deflection of a wall three times stiffer than the Reese wall is 20% less than the maximum deflection of the Reese wall. However, the long-term deflection of the Reese wall is sensitive to decreasing the bending stiffness; such that, the predicted

maximum deflection of a wall with half the bending stiffness of the Reese wall is 30% more than the deflection of the Reese wall.

9- An Analytical method which solves the lateral and rotational equilibrium equations for two unknown, namely, the mobilized friction angle, and the location of the point of fixity, overestimates the mobilized friction angle and the maximum deflection and underestimates the maximum bending moment, because the mobilized friction angle method adopts kinematics of wall movement that did not match the observed kinematics of the Reese wall.

## 11.3 RECOMMENDATION FOR FUTURE WORK

Comparison between measured and predicted long-term deflections provided useful insights for developing a framework that described the behavior of soils subjected to variation in the degree of saturation. This framework relies on two soil properties that are not captured by common site investigation works, namely, the isotropic hardening properties of soil and the relationship between suction stress and effective degree of saturation.

While some generalizations can be made about the isotropic hardening properties of the Reese wall soil from the Spectral Analysis of Surface Waves, more thorough evaluation of the isotropic hardening properties of partially saturated soil is required. Adopting a unified effective stress variable rather than two stress variables, for partially saturated soil could be followed to simplify such tests. This could be done by measuring the isotropic hardening properties of fully saturated soils subjected to confining stresses equivalent to the anticipated suction stresses.

The relationship describing the variation of suction stresses as a function of the effective degree of saturation, i.e., the Soil Suction Characteristic Curve (SSCC), was

evaluated based on undrained shear strength measurements. Parametric analyses showed that the behavior of the predicted behavior is sensitive to adopted SSCC relationship. More robust evaluation of the SSCC could be obtained by measuring the drained shear strength of partially saturated soils with variable degrees of saturations. In other words, evaluating the relationship between the apparent cohesion intercept and the degree of saturation.

# References


Adil Haque, M. Bryant, J. (2011) “Failure of VERT Wall System: Forensic Evaluation and Lesson Learned” Geo-Frontiers 2011: Advances in Geotechnical Engineering Pp 3487-3496.

Alonso, E. Gens, A. Josa, A. “A constitutive model for partially saturated soils” Geotechnique Vol. 40(3) Pp 405-430.

Bishop, A. Blight, G. (1963) “Some Aspects of Effective Stresses in Saturated and Partially Saturated Soils” Geotechnique London Vol. 13 Pp 177-197.

Bocking, K.A., and Fredlund, D.G. (1980). “Limitations of the axis translation technique,” Proceedings of the 4th International Conference on Expansive Soils, Denver, CO, Pp. 117-135.

Bolton, M.D. (1990) “The design of stiff insitu walls retaining overconsolidated clay, part 1, short term behavior”. Ground Engineering Vol. 23(1) Pp 34- 39.

Bozbey and Togrol (2010) “Correlation of standard penetration test and pressuremeter data: a case study from Istanbul, Turkey” Bulletin of Engineering Geology and the Environment Vol. 69(4) Pp 505-515.

Brooker, E., Ireland, H. (1965) “Earth Pressures at Rest Related to Stress History” Canadian Geotechnical Journal Vol. 2(1) Pp 1-15.

Brown, A.C. (2013) “The behavior of drilled shaft retaining walls in expansive clay soils” Ph.D. Dissertation, The University of Texas Austin.

Corey, A., (1957). “Measurement of water and air permeability in unsaturated soil,” Proceedings of the Soil Science Society of America, Vol. 21, No. 1, pp. 7-10.

Dakshanamurthy, V., V. Raman (1973) “A simple method of identifying an expansive soil” Soils and Foundations, 13, Pp 97-104.

Dellinger, G. (2011) “The Use of Time Domain Reflectometry Probes for Moisture Monitoring of a Drilled Shaft Retaining Wall in Expansive Clay” M.S. Thesis, The University of Texas at Austin.

Ellis, T. (2011). “A Subsurface Investigation in Taylor Clay” Master’s Thesis, The University of Texas at Austin.

Escario, V. (1980). “Suction controlled penetration and shear tests.” Proc., 4th Int. Conf. on Expansive Soils, Vol. 2, Denver, Pp 781–797.

Fredlund, D. Morgenstern N. “Stress State Variables for Unsaturated Soils” Journal of the Geotechnical Engineering Division (ASCE) 1977; 103(GT5) Pp 447–466.

Fredlund, D., and Rahardjo H. (1993). “Soil mechanics for unsaturated soils,” John Wiley & Sons, New York, 560p.

Gasparre, A., Nishimura, N., Minh, A., Coop, M., Jardine, R., (2007) “The Stiffness of London Clay” Geotechnique 57, Pp 33-47.

Hardin, B., Drnevich, V. (1972b) “Shear Modulus and Damping in Soils: Measurement and Parameter Effects- Terzaghi Lecture” Journal of Soil Mechanics Foundation Division 986 Pp 603–624.

Hilf, J., (1956). “An investigation of pore-water pressure in compacted cohesive soils,” Ph.D. Dissertation, Technical Memorandum No. 654, U.S. Department of the Interior, Bureau of Reclamation, Design and Construction Division, Denver, Colorado.

Hong, G. (2008). “Earth Pressures and Deformations in Civil Infrastructure in Expansive Soils” Ph.D. dissertation, Texas A&M University.

Imai T 1977 “P-and S-wave velocities of the ground in Japan” Proc. 9th Int. Conf. on Soil Mechanics and Foundation Engineering vol.2 Pp 127–32.

Jafari, M., Shafiee, A., Ramzkhah, A., (2002) “Dynamic properties of the fine grained soils in south of Tehran” J. Seismology and Earthquake. Eng. 4 Pp 25–35.

Jardine, R., Symes, M., and Burland, J. (1984). “The measurement of soil stiffness in the triaxial apparatus” Géotechnique, 34(3) Pp 323–340.

Jennings, J., Burland, J. (1962) “Limitations to The Use of Effective stress in Partially Saturated Soils” Geotechnique Vol. 12 (2) 125-144.

Kayyal, M., Wright, S. (1991) “Investigation of Long-term Strength properties of Paris and Beaumont Clays in Earth Embankments” Research Report 1195-2F, Center for Transportation Research, The University of Texas at Austin.

Koutrouvelis, Iraklis. (2012). “Earth Pressures Applied on Drilled Shaft Retaining Walls in Expansive Clay during Cycles of Moisture Fluctuation” Master's Thesis, The University of Texas at Austin.

Kuhn, J., Zornberg, J. (2006) “Field Suction and Effect of Cracking in Highly Plastic Clay” FHWA/TX-07/0-5202-2.

Kulhawy, F., Jackson, C., Mayne, P., (1989) "First-Order Estimation of $K_0$ in Sands and Clays" Foundation Engineering: Current Principals and Practices, ASCE, New York Pp 121-134.

Ladd, C., (1960). "Mechanics of swelling of compacted clays," Highway Research Board Bulletin No. 245, National Research Council, pp. 10-26.

Lee, S. (1990) "Regression models of shear wave velocities" J. Chinese Institute of Engineers. Vol.13(5) Pp 19–32.

Long, M. (2001) "Database for Retaining Wall and Ground Movements due to Deep Excavations" Journal of Geotechnical. Geoenvironmental. Engineering. Vol.127 Pp 203-224.

Lu, N. Likos, W. (2006) "Suction stress characteristic curve for unsaturated soil". Journal of Geotechnical and Geoenvironmental Engineering; ASCE.

Lu, N. Godt, J. Wu, Wu, D. (2010) "A Closed-form Equation for Effective stress in Unsaturated Soil" Water Resources Research Vol. 46.

Lytton, R. (2007) "Design of Structures to Resist the Pressures and Movements of Expansive Soils". Texas A&M University.

Mayne, P., Kulhawy, F., (1988) Discussion of "Independence of Geostatic Stress from Overconsolidation in Some Beaufort Sea Clays" Canadian Geotechnical Journal Vol. 25(3) Pp 617-621.

Ohya S, Imai T, Matsubara M (1982) "Relationship between N value by SPT and LLT pressuremeter results" Proceedings of 2nd European Symposium on Penetration Testing, Vol 1, Amsterdam, The Netherlands, 24–27 Pp 125–130.

Olson, R. (1963). "Effective stress theory of soil compaction," Journal of Soil Mechanics and Foundations Division, ASCE, Vol. 89(2), Pp. 27-45.

Olson, R., Langfelder, L., (1965). "Pore water pressures in unsaturated soils," Journal of Soil Mechanics and Foundations Division, ASCE, Vol. 91, No. SM4, Pp. 127-150.

Osman, A.S., and Bolton, M.D. (2004) "A new design method for retaining walls in clay" Canadian Geotechnical Journal 41(3), 451-466.

Pitilakis, K., Raptakis, D., Lontzetidis, K., Vassilikou, T., Jongmans, D., (1999) "Geotechnical and geophysical description of Euro-Seistests, using field and laboratory tests, and moderate strong ground motions" Journal of Earthquake. Engineering. 3 Pp 381–409.

Poulos, H. Davis, E. (1980) “Pile Foundation Analysis and Design” The University of Sydney.

Pufahl, D. Fredlund, D. Rahardjo, H. (1983) “Lateral earth pressures in expansive clay soils” Canadian Geotechnical Journal Vol 20 Pp 228-241.

Puppala, A., Manosuthikij, T., Chittoori, B. (2013) “Swell and shrinkage characterizations of unsaturated expansive clays from Texas” Engineering Geology Journal Vol. 164 Pp 187-194.

Reese, L. C. & Van Impe, W. F. (2001). Single piles and pile groups under lateral loadings. A. A. Balkema, Rotterdam.

Salem (2006) “Stiffness of Unsaturated Compacted Clays at Small Strains” Ph.D. thesis, The University of Texas at Austin, Austin, Texas, U.S.A.

Schanz, T. Vermeer, P. Bonnier, P. (1999) “The hardening soil model: Formulation and verification” Beyond 2000 in Computational Geotechnics – 10 Years of PLAXIS Balkema.

Seed, H. B., Woodward, R. J., Jr. and Lundgren, R. (1962) “Prediction of swelling potential for compacted clays” J. ASCE, Soil Mechanics and Foundation Division, Vol. 88, No. SM-3, Part I, Pp. 53-87.

Shibuya, S., Hwang, S. C., and Mitachi, T. (1997). “Elastic shear modulus of soft clays from shear wave velocity measurement.” Geotechnique, Vol.47(3), Pp 593–601.

Skempton, A. (1961) “Horizontal stresses in over-consolidated Eocene clay” 5th International Conference of Soil Mechanics, Paris, 351-357.

Skempton, A. Petley, D. (1967) “The Strength Along Structural Discontinuities in Stiff Clays” Proceedings of the Geotechnical Conference Oslo. 29-46.

Skempton, A. W. (1970). “First-Time Slides in Over-Consolidated Clays.” Géotechnique Vol. 20(3) Pp 320-324.

Smith, R. Smith, D. Griffin, J. (2009). “Top-Down Construction of a Bridge in Clay Shale” American Society of Civil Engineers Conference Proceedings. 337, 76, 598-605.

Stark, T., and Eid. H. (1997). “Slope stability analyses in stiff fissured clays.” Journal of Geotechnical and Geoenvironmental Engineering 123(4), 335-343.

Stokoe K. H., II, and J. C. Santamarina (2000). “Seismic-wave-based testing in geotechnical engineering” International Conference on Geotechnical and

Geological Engineering, GeoEng 2000, Melbourne, Australia, November, Pp 1490- 1536.

Terzaghi, Karl (1943), Theoretical soil mechanics, John Wiley & Sons, Inc., p. 265.

TxDOT (2009). Cantilver Drilled Shaft Wall Design.

TxDOT Geotechnical Manual. (2012). Texas Department of Transportation, Bridge Division, Austin, Texas.

Van Genuchten, M. (1980) "A Closed-form Equation for Predicting the Hydraulic Conductivity of Unsaturated Soils" Soil Science Society of America Journal Vol.44 Pp892-898.

Vardanega, P. Lau, B. Lam S. Haigh, S. Madabhushi S. Bolton, M. (2012) "Stiffness of clays and silts: normalized shear modulus and shear strain" Journal of Geotechnical and Geoenvironmental Engineering; ASCE. 139.9: 1575-1589.

Vardanega, P. and Bolton, M. (2013) "Stiffness of clays and silts: normalized shear modulus and shear strain" Journal of Geotechnical and Geoenvironmental Engineering 139.9: 1575-1589.

Weather Underground (2013). http://www.wunderground.com/.

Wongsaroj, J. Soga, K. Yimsiri, S. Mair, R. "Stiffness Anisotropy of London Clay and its Modelling: Laboratory and Field" Advances in Geotechnical Engineering: The Skempton Conference 2004, Thomas Telford, London.

Wright, S (1969) "A Study of Slope Stability and the Undrained Shear Strength of Clay Shales" Ph.D. thesis, University of California, Berkeley, California, U.S.A.

Wright, S., (2005) "Evaluation of Soil Shear Strengths for Slopes and Retaining Wall Stability Analyses with Emphasis on High Plasticity Clays" FHWA/TX-06/5-1874-01-1.

Wright, S. Zornberg, J. Aguettant, J. (2007) "The Fully Softened Shear Strength of High Plasticity Clays" FHWA/TX-07/0-5202-3.

Whittle, A. Kavvadas, M. (1994) "Formulation of MIT-E3 Constitutive Model for Overconsolidated Clays" Journal of Geotechnieal Engineering, Vol. 120 No. 1 173-198.

Wongsaroj, J., Soga, K., Yimsiri, S. and Mair, R.J. (2004) "Stiffness anisotropy of London Clay and its modelling: Laboratory and Field. Advances in Geotechnical Engineering" The Skempton Conference, Thomas Telford, London.

Wright, S. and Duncan (1972) "Analyses of Waco Dam Slide" Journal of Soil Mechanics and Foundation division Vol 98 (SM9): Pp 869-877.

Zornberg, J., Kuhn, J., Wright, S. (2007) "Determination of Field Suction Values, Hydraulic Properties, and Shear Strength in High PI Clays" FHWA/TX-07/0-5202-1.

# Vita

Ali Fawzi Helwa was born in Giza, Egypt, in 1987, the son of M. Fawzi Helwa and Hoda Shaaban. After graduating from Manor House IGCSE high school, he enrolled in the Faculty of Engineering at Cairo University in September 2004. He earned his Bachelor of Science in Civil Engineering with highest honors in July 2009. Ali started his graduate studies at Cairo University in September 2009 specializing in geotechnical engineering. In July 2012, he received his Master of Science in Civil Engineering with distinction under the supervision of Professors Mostafa Mosaad and Manal Salem. Ali started his doctoral studies at the University of Texas at Austin in August 2012.

Email address: Ali.f.helwa@gmail.com

This dissertation was typed by the Author.